Thermal Control of Gas Turbine Casings for Improved Tip Clearance

MyeongGeun Choi

St Catherine's College

Oxford

A thesis submitted in partial fulfilment of the requirements of the degree of

Doctor of Philosophy at the University of Oxford, Michaelmas term, 2015.

Department of Engineering Science

University of Oxford

Parks Road, Oxford OX1 3PJ

Thermal Control of Gas Turbine Casings for Improved Tip Clearance

A thesis submitted in partial fulfilment of the requirements of the degree of Doctor of Philosophy in the University of Oxford, Michaelmas Term 2015

MyeongGeun Choi
St Catherine's College

Abstract

A thermal tip clearance control system provides a robust and flexible means of manipulating the closure between the casing and the rotating blade tips in a jet engine, reducing undesirable tip leakage flows. This may be achieved using an impingement cooling scheme on the external casing of the engine in conjunction with careful thermal management of internal over-tip seal segment cavity. For a reduction in thrust specific fuel consumption, the mass flow rate of air used for cooling must be minimised, be at as low a pressure as possible and delivered through a light weight structure surrounding the rotating components in the turbine.

This thesis first characterises the effectiveness of a range of external impingement cooling arrangements in typical engine casing closure system. The effects of jet-to-jet pitch, number of jets, inline and staggered alignment of jets, arrays of jets on flange, on an engine representative casing geometry are assessed through comparison of the convective heat transfer coefficient distributions in a series of numerical studies. A baseline case is validated experimentally. The validation data allowed the suitability of different turbulence closure models to be assessed using a commercial RANS solver. Importantly for each configuration the thermal contraction of an idealised engine casing is predicted using thermo-mechanical finite element models, at a series of operating conditions representing engine idle to maximum take-off conditions.

Cooling is provided by manifolds attached to the outside of the engine. The assembly tolerance of these components leads to variation in the standoff distance between the manifold and the casing. For cooling arrangements with promising performance, the study is extended to characterise the variation in closure with standoff distance. It is shown that where a sparse array of non-interacting jets is used the system can be made tolerant of large build misalignments.

The casing geometry itself contributes to the thermal response of the system, and, in an additional study, the effect of casing thickness and circumferential thermal control flanges are investigated. Restriction of the passage of heat into the flanges was seen to be dramatically change their effectiveness and slight necking of the flanges at their root was shown to improve the performance disproportionally.

High temperature secondary air flowing past the internal face of the engine casing tends to heat the casing, causing it to grow. Experimental and numerical characterisation of a heat transfer within a typical over-tip segment cavity heat transfer is presented in this thesis for the first time. A simplified modelling strategy is proposed for casing and a means to reduce the casing heat pickup by up to 25 % was identified.

The overall validity of the modelling approach used is difficult to validate in the engine environment, however limited data from a test engine temperature survey became available during the course of the research. By modelling this engine tip clearance control system it was shown that good agreement to the temperature distribution in the engine casing could be achieved where full surface external heat transfer coefficient boundary conditions were available.

Acknowledgement

It was great privilege for me to be able to study in the University of Oxford, and I would like to thank my supervisor Prof David Gillespie who provided this opportunity and helped me provide wholehearted support. His guidance, patient, and encouragement throughout the course of my research are truly appreciated. I also would like to thank to Prof Peter Ireland who offered much useful advice and scientific insight toward the work presented in the thesis. Special thanks must go to Dr Leo Lewis from Rolls-Royce, Derby whose knowledge of all aspects of the practical engineering challenges involved with tip clearance control, and the relative importance of different aspects of the project has been vital to its progress. It would have been impossible to complete my doctorate journey without their exceptional support.

I would like to acknowledge Rolls-Royce, the Technology Strategy Board, and the Aerospace Technology Institute, UK for providing the funding for the research and bursary, and St Catherine's College's Overseas Scholarship for the additional financial support and benefits they have provided. Their support is greatly appreciated.

Table of Contents

Nomenclature

Symbols

c	specific heat capacity ($kg^{-1}K^{-1}$)
d	impingement hole diameter (mm)
htc	heat transfer coefficient ($Wm^{-2}K^{-1}$)
EARSM	explicit algebraic Reynolds stress model
I	manifold thickness (mm)
k	thermal conductivity ($Wm^{-1}K^{-1}$)
l,r	spatial coordinate 2 (mm)
L	casing length (mm)
Ma	Mach number
$\dot{m}$	mass flow rate (kgs^{-1})
Nu	Nusselt number, hd/k
P	pressure, Pa
Pr	Prandtl number, $c\mu/k$
q''	heat flux (Wm^{-2})
R	casing radius (mm)
RANS	Reynolds-averaged Navier-Strokes
Re	Reynolds number, $\rho ud/\mu$
RSS	root sum square
S	distance along casing wall (mm)
SST	shear stress transport
t	time (s)
T	temperature (K)
th	casing thickness (mm)
x,y,z	spatial coordinate 1 (mm)
y^+	dimensionless wall distance

Greek

δ	increment in a variable
μ	dynamic viscosity ($kgm^{-1}s^{-1}$)
ρ	density (kgm^{-3})

Subscripts

avg	overall area averaged
e	Engine
g	driving gas
hook	point of casing liner attachment
m	Model
n	Number
ref	Reference
span	spanwise averaged
surf	Surface

Abbreviations

EXP	Experiment
OP	operating condition
TCC	turbine casing cooling
TLC	transient liquid crystal

Chapter 1 Introduction

One of the key ways to improve the efficiency of the gas turbine is by actively managing the undesirable flow between the turbine casing and high speed rotating blade tips. The existence of thermal and centrifugal expansions of the rotor and casing mean that aerodynamic design of the rotor tip can never, by itself, optimise this flow at cruise conditions. The use of active heating or cooling of the engine casing is an attractive design solution to allow the casing diameter to be changed, and thus to reduce the aerodynamic blade tip losses. Furthermore, the active system provides a means of maintaining these tight clearances as the engine deteriorates with time in service. In this chapter, the motivation for this research, the scope of work, thesis structure and published outcomes from the research are introduced.

1.1 Research Motivation

The International Panel on Climate Change has estimated that aviation is responsible for around 3.5 % of manmade climate change, and without improvements in technology this could rise to between 5 and 15 % by 2050 **(IPCC, 2007)**. The aviation industry has long recognised the challenge, and the Advisory Council for Aeronautical Research in Europe **(ACARE, 2011)** established a long-term target of 75 % reduction in fuel burn or CO_2 emissions, 65 % in perceived noise, and 90 % in landing/take-off NO_x emissions by year 2050, relative to year 2000 levels. The engine contribution to these goals is defined as a reduction in CO_2 emissions by 30 % and NO_x by 75 %. **Figure 1.1** shows one of leading aero engine maker's progress on reduction in fuel burn with indication of the ACARE Flightpath 2050 target.

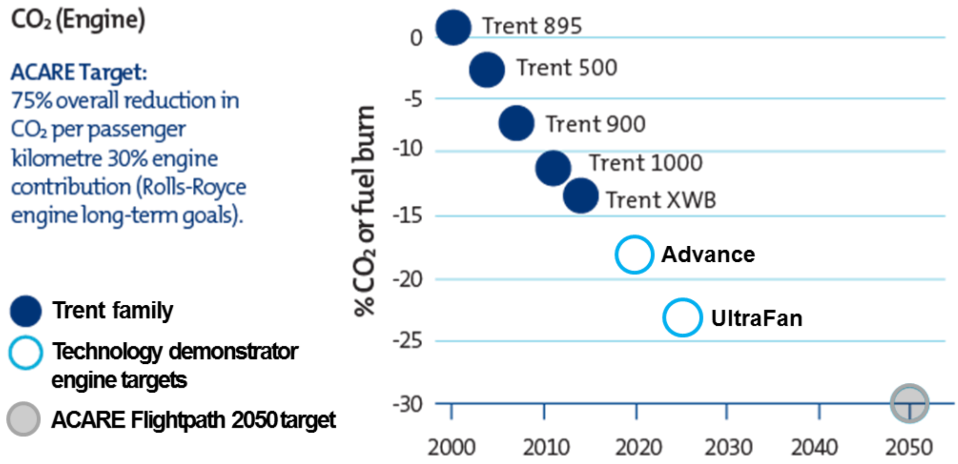

Figure 1.1 Rolls-Royce's progress on reduction in fuel burn with contribution towards ACARE 2050 fuel consumption target (Rolls-Royce, 2011).

All engine manufacturers have employed the combined strategy of large increases in operating pressures and temperatures to improve engine efficiency and power to weight ratio. These improvements are illustrated in **Figure 1.2**.

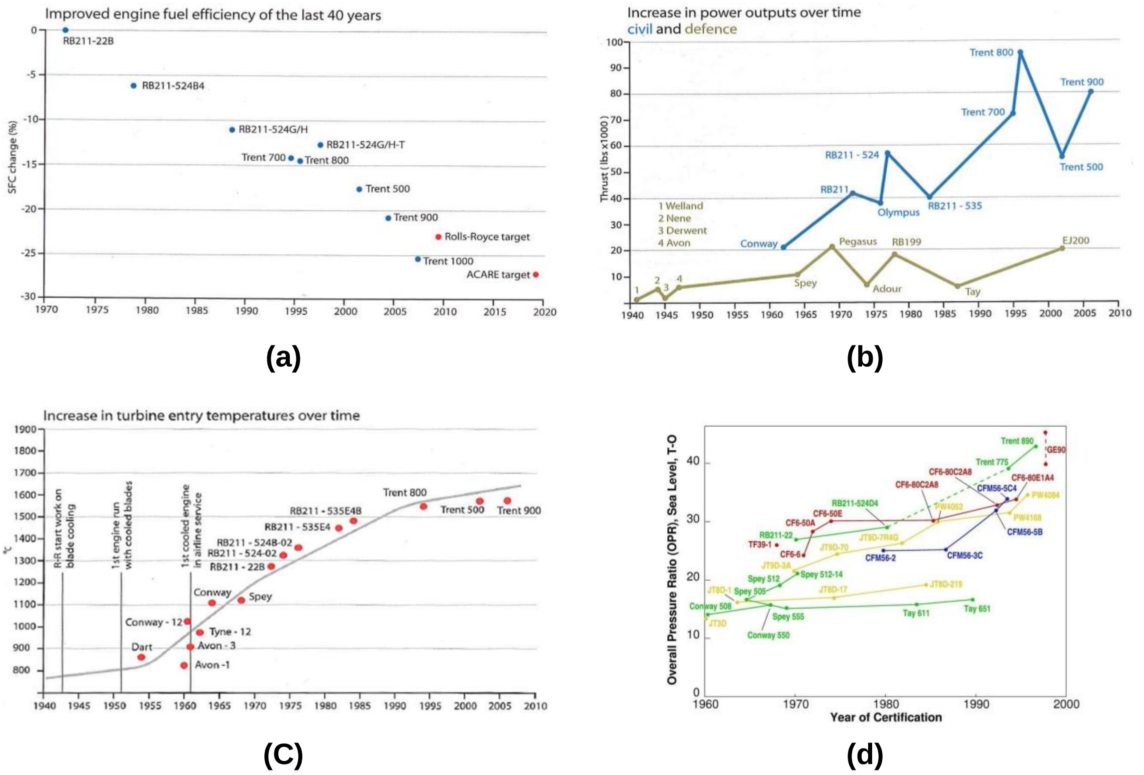

Figure 1.2 (a) Improved engine fuel efficiency (Rolls-Royce, 2005), (b) Increased in power outputs (Rolls-Royce, 2005), (c) Increased in operating temperature (Rolls-Royce, 2005), and (d) Increased in overall pressure ratio over time (Gunston, 1998).

A simplified gas turbine engine cycle can be used to outline the trends driving changes in performance. The temperature-entropy (T-s) diagram in **Figure 1.3** represents the working process: a fixed amount of air is compressed (1) → (2), heated (2) → (3), expanded in turbine stages (3) → (4) and cooled (4) → (1). The power of turbine stages is translated to drive the compressor and the rest output is used to drive the fan or produce net power $\dot{W}_{net}$ which is equal to $\dot{W}_{turb.} - \dot{W}_{comp.}$. The net power output of the simple gas turbine cycle can be written as a function of pressure ratio r_p (= P_2/P_1) and temperature ratio T_3/T_1, when the mass flow of fuel in the gas flow is negligible compared to that of air,

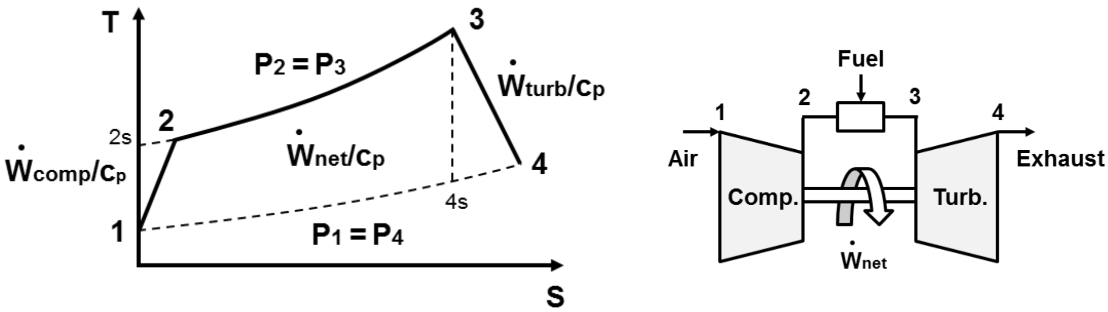

Figure 1.3 Temperature and entropy diagram for simple gas turbine cycle.

$$\dot{W}_{net} = \dot{m}_{air} c_p (\dot{W}_{turb.} - \dot{W}_{comp.})$$
$$= \dot{m}_{air} c_p T_1 \left(\frac{T_3}{T_1} \left(1 - \frac{1}{r_p^{\frac{\gamma-1}{\gamma}}} \right) \eta_{turb.} - \frac{r_p^{\frac{\gamma-1}{\gamma}} - 1}{\eta_{comp.}} \right) \quad (1.1)$$

where isentropic efficiency of compressor and turbine stages are defined as

$$\eta_{comp.} = \frac{T_{2s} - T_1}{T_2 - T_1} \quad \text{and} \quad \eta_{turb.} = \frac{T_3 - T_4}{T_3 - T_{4s}} \ . \quad (1.2)$$

Note that nowadays the efficiencies of compressor and turbine stages in a modern gas turbine are likely to be around 90 % **(Cumpsty, 1997)**.

The efficiency of the cycle can be as written as the ratio of net power out to the heat transfer rate to working gas flow,

$$\eta_{cycle} = \frac{\dot{W}_{net}}{\dot{m}_{air} c_p (T_3 - T_2)}$$
$$= \frac{\dot{W}_{net}}{\dot{m}_{air} c_p T_2 \left(\frac{T_3}{T_1} - \frac{r_p^{\frac{\gamma-1}{\gamma}} - 1}{\eta_{comp.}} \right)} \ . \quad (1.3)$$

Figure 1.4 shows the non-dimensional net power output and cycle efficiency, relative to the 100 % ideal compressor and turbine stages or both stages at 90 %. To obtain large power output and high cycle efficiency it is essential to operate at high values of T_3/T_1 with an adapted operating pressure range. The pressure in HP turbine in modern large civil engine have ended up at about 1:50 ratio, for instance RR Trent XWB = 52.1:1 **(Rolls-Royce, 2015)**, and the allowable temperature extends of the blade is upto 1400 K and 2000 K for the working gas **(EASA, 2013)**.

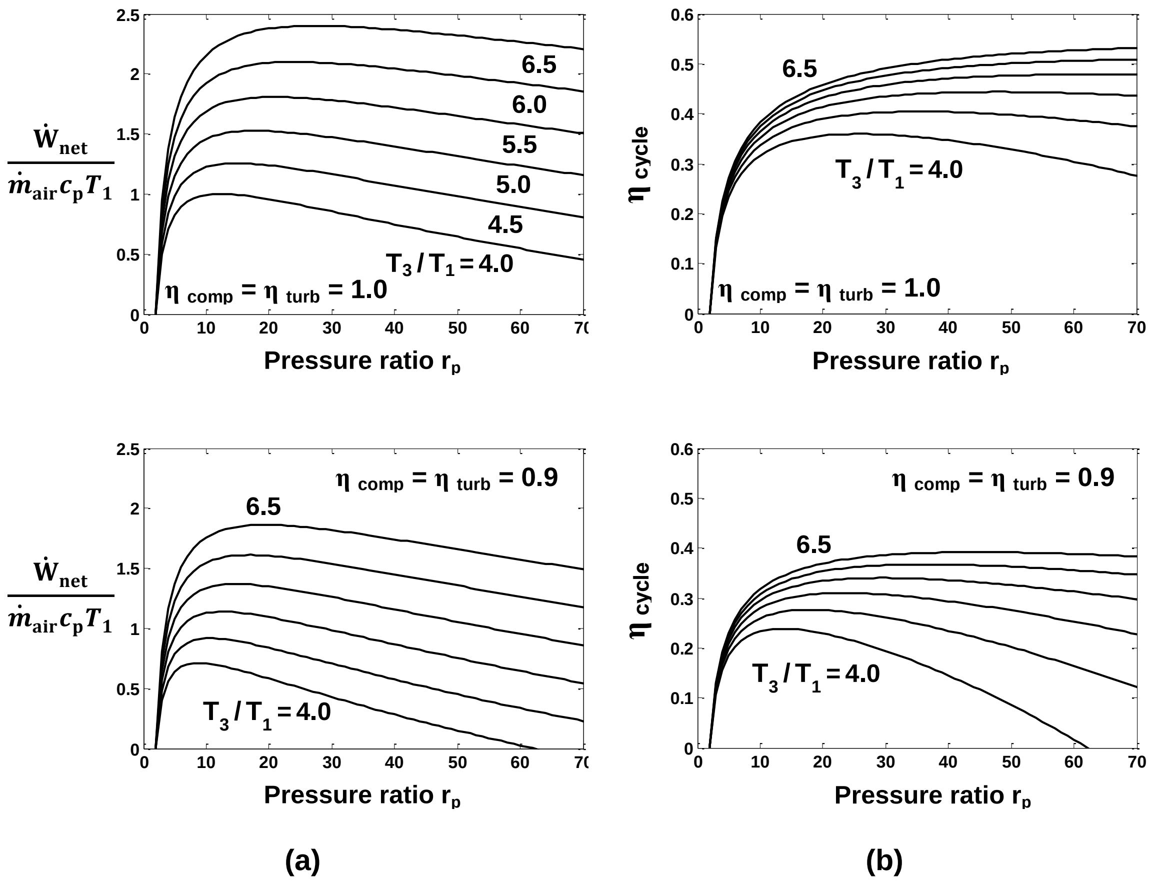

Figure 1.4 (a) Non-dimensional power and (b) cycle efficiency of an idealised gas turbine for different temperature ratio and pressure ratio.

However, limits in such improvements are now being reached because of the plateau in material technology and the need to use sustainable, available and relatively cheap materials for construction. Improvements in other areas such as undesirable leakage flows are now seen as a key way of improving performance. Prolonging the life of efficient engines reduces the environmental impact of their construction and reduces maintenance costs for manufacturers who typically sell the engine on a ‘power by the hour’ basis.

Minimizing undesirable blade tip leakage flow is crucial to improve turbine performance, where a tip clearance with a height of 0.5 - 1.5 % blade span exists between the rotors and casing liner. The blade design in modern high pressure turbines fall into two categories: a shrouded or an unshrouded blade. The unshrouded design is widely employed for a reduction in weight, low stress, and advanced cooling of the blade. The over-tip leakage flow is driven by the inherent pressure difference between the blade pressure side surface and suction side surface and is dominated by the vortex shed near the blade tip (see **Figure 1.5**).

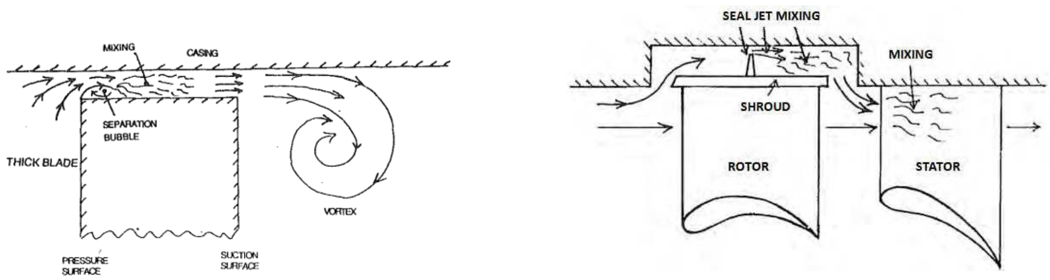

Figure 1.5 Flow over the tip gap for an unshrouded and shrouded blade (Denton, 1993).

The size of tip gap translates almost linearly to a loss in stage efficiency in the turbine (see **Figure 1.6 (a)**) and an increase in flow instability, particularly in the compressor stages. Here the tip leakage has been shown to be the key contributor to aerodynamic loss (see **Figure 1.6 (b)**). Many previous workers have attempted to optimise the tip or shroud geometry to minimise such losses, but generally a range of tip gaps must be accommodated as there are changing thermal and centrifugal rotor and casing growths throughout the engine cycle.

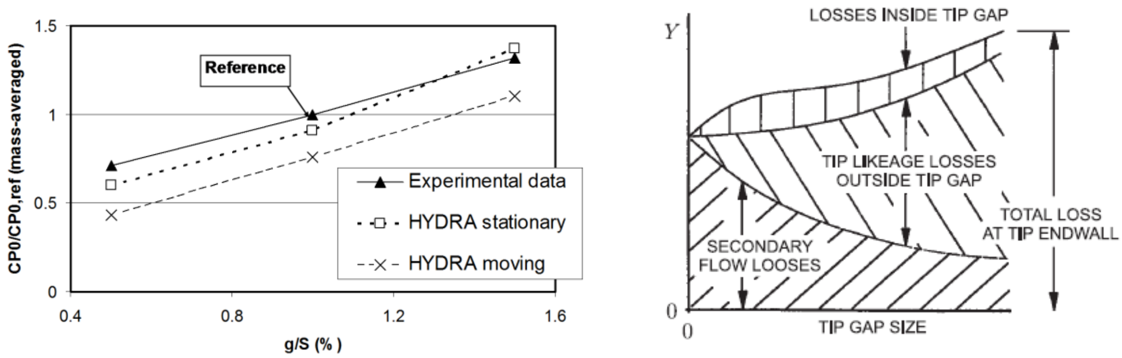

(a) (b)

Figure 1.6 (a) Total pressure loss variation with tip gap magnitude (O'Dowd, 2010) and (b) a tentative diagram of contribution of loss components (Yaras and Sjolander, 1992).

During a typical jet engine cycle, as shown in **Figure 1.7**, there is a continual change in the blade tip to liner clearance because of changes in thermal and mechanical loads on the rotating and stationary casing structures. The system is highly complicated as high operating temperatures require active cooling of the turbine blades and their surrounding casing. While the tip gap should be minimised for the best aerodynamic performance, with active control, the cold build clearance, (a), is set by a transient minimum expected clearance, (b), typically encountered at the end of runway or the top of climb conditions. At cruise, (c), a larger tip clearance is encountered and this may be reduced by active clearance control.

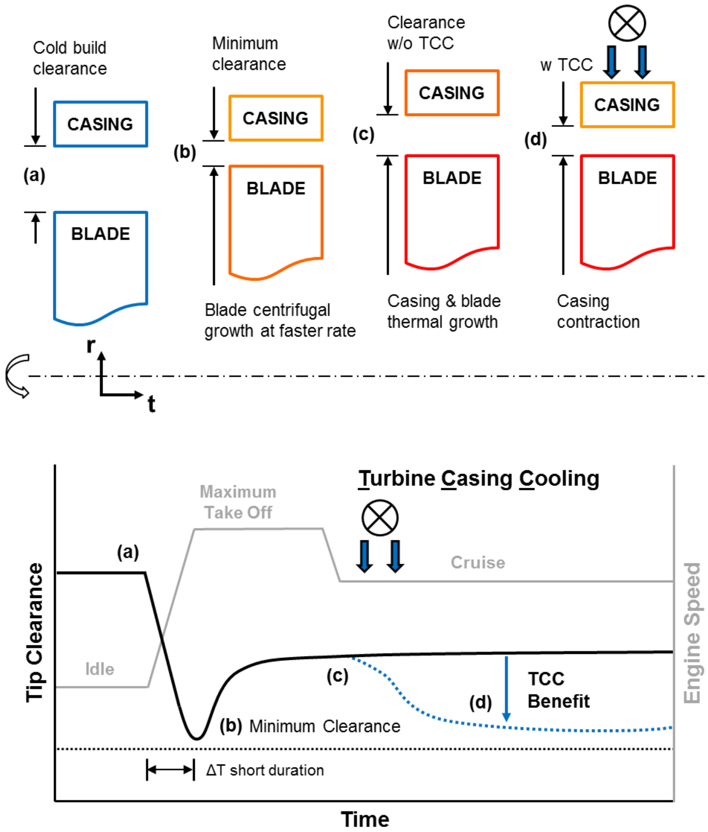

Figure 1.7 Potential tip clearance improvement induced by turbine casing thermal control system, after Lattime and Steinetz (2004).

While most of the operating time is spent at cruise conditions, this is not usually aligned to the point of minimum clearance. The problem is complicated: an increase in engine speed results in a decrease in clearance due to the centrifugal growth of the rotor, but an increased clearance from the increased internal pressure. Additionally slower thermal response occurs with different time constants in the stationary and rotating parts; as the core engine temperature rises the casing generally expands at a faster rate than the rotor due to the casing having a smaller volume than the rotor disc. This tends to increase the clearance and hence reduces engine efficiency and increases transient specific fuel consumption.

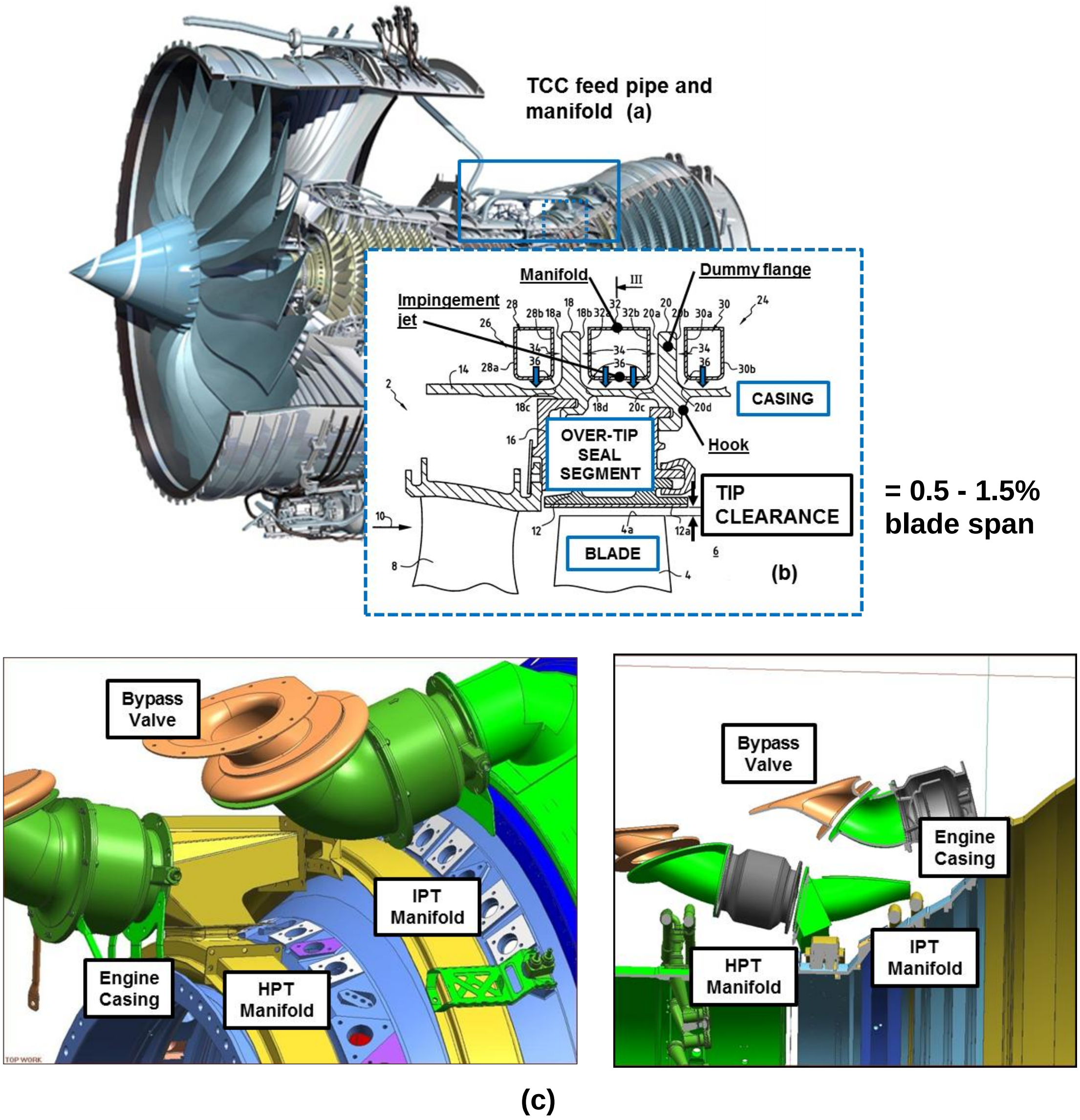

Figure 1.8 HPT casing configuration on (a) a typical large civil engine (Rolls-Royce, 2011) and (b) a radial cross-section through a typical manifold (Amiot et al., 2007), and (c) a close up view of a high and intermediate pressure turbine external casing (Rolls-Royce, 2011).

A desire to control the clearance actively must be paid off against the dangers of introducing unreliable systems into the jet engine. A turbine thermal tip clearance control system offers a robust solution by manipulating casing temperature, where corresponding radial contraction is translated to the casing liner for tight tip running: in the event of system failure the gap reopens passively allowing the plane to continue to fly. This can be achieved primarily through controlling the impingement of cool air taken from the early compressor stage onto the external casing in conjunction with considerable thermal management onto the internal casing. A typical system with its radial cross section through an annular manifold is illustrated in **Figure 1.8**. Cooling air are ducted through the external manifold and then directed through a set of small diameter holes in the bottom wall of manifold to impinge onto the external casing wall. The over-tip seal segments which offer passages of a relatively hot and high pressure air are mounted on this wall via pairs of internal hooks. The low stiffness of the seal segments means that any casing contraction is directly translated to a reduction of tip clearance and hence tight tip running. The manifold arrangement studied in the current research is included as **Figure 1.9**. The system is created from a ring main with which feeds 6, 60 degree segments shown in the right hand diagram. The segments are supported at each end, meaning that as the temperature of the casing increases with respect to the manifold, the region between the flanges is likely to be pulled towards the target surface. More details of external manifold and internal over-tip seal segment cavity can be found in the following section 3.2.1 and 3.3.1 respectively.

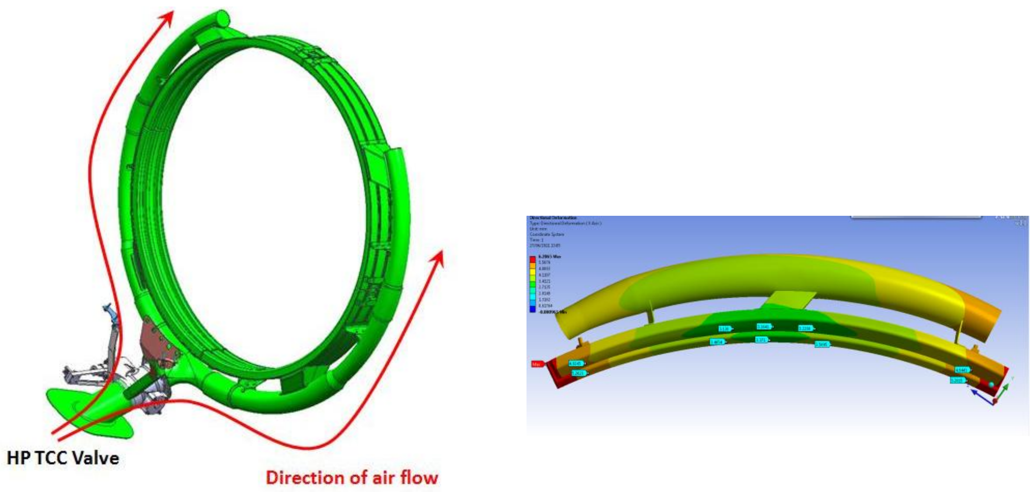

(a) (b)

Figure 1.9 Rolls-Royce XWB manifold, showing (a) the main control valve and (b) individual 60^{o} sector of cooling manifold.

Historically, the CFM56-2 engine introduced on re-engined Boeing 707 aircraft in 1982 first employed active tip clearance control, while the CFM56-5A was one of the first civil engines to employ modulated clearance control on both high and low pressure turbines **(CFM International, 2011)**. And now such systems have been employed to provide means of tip clearance control by all major aero-engine manufacturers, however design philosophies are still evolving. The thermal control system scheduling in today's engine is very reliant on an understanding of the casing thermal boundary conditions. Some aspects of this technology, for example the component thermal expansion coefficient, are well understood; others, particularly the heat transfer coefficient (*htc*), which depends upon an understanding of complex gas flow patterns, are currently highly uncertain. In current practice, engine designers make use of *htc* derived from empirical correlations with user-specified multiplying factors or modified correlations as the reference in the design stage. Such an approach may result in significant discrepancies when temperature predictions are compared to a hot engine thermocouple survey. The combination of small changes in local *htc* distributions by changing cooling arrangement or the cooled area may also have a substantial impact on the casing contraction achieved.

The key drivers of the system are only partially understood: the steady-state position is known to depend on a trade-off between the heat transfer coefficients from the inner and outer surfaces, while the speed of the transient behaviour is determined by the area weighted total of the external and internal heat transfer coefficients. The engine designers may also be multiply constrained by other engine requirements: weight of the system, source of cooling air, temperature of the spent air, stiffness of the casing, maximum stress in components, ability to manufacture, reliability of control scheme, build tolerance etc. Those considerations make the development of the effective thermal control system for tip clearance quite challenging. In spite of the difficulty of modelling such a sensitive system the motivation for the research is high: with an approximately 0.3 - 0.4 % reduction in specific fuel consumption at cruise available from 0.25 mm reduction in tip clearance **(Rolls-Royce, 2011)**.

1.2 Research Focus and Thesis Outline

The aim of present research is to improve understanding of the thermal response of the casing to realistic thermally induced heat fluxes while proposing improved cooling systems. By understanding how the outer (cold) and inner (hot) side of the casing affect both steady-state and transient clearances, it is hoped to establish the ideal heat transfer levels from a continuous control point of view, and the means to achieve this. This is a multi-dimensional environment, where achieving a desirable *htc* cannot be considered independently of the required coolant mass flow rate, manifold size and weight. An improved system has the possibility to increase jet engine efficiency by whole of points accordingly, however, its reliability and robustness to geometric tolerances are of equal importance.

To achieve these goals the tip clearance control system can be broken down into several component stages:

- the flow within the cooling manifold;
- the external cooling of the casing driven by the cooling and casing geometry;
- the casing metal temperature distribution, affected by the casing geometry;

- the internal heating of the casing driven by the internal flow and casing geometry.

Aspects of each of these processes are considered further in this thesis at different levels of detail. Many component design choices beyond the influence of this research, such as the casing material and thickness, are considered as constants within the system, and data from Rolls-Royce who have sponsored the research are used.

A key emphasis in this thesis has been to optimise the cooling performance per unit cooling mass flow, linking this directly to casing closure (rather than heat transfer coefficient), see **Figure 1.10**. To achieve this, a wide range of computational fluid dynamics and finite element modelling coupled impinging array cooling simulations have been conducted with engine representative geometrical details and operating conditions. The transient liquid crystal heat transfer technique has been used to validate the heat transfer coefficient distributions obtained for some of the designs at large scale. The numerical approach using industry best practice in a systematic manner, has allowed many design solutions to be assessed. Within the CFD studies, the relative performance of different turbulence models for predicting the jet impingement flow and heat transfer seen in the thermal control systems has been evaluated by comparing these to available benchmark data and the experimental results. The results acquired through CFD provide component wall heat transfer coefficients over several critical operating points and understanding of the effect of external impingement cooling manifold stand-off distance from the target casing wall on heat transfer coefficient: one of key issues facing engine designers in the early design stage. These data, when used as boundary conditions in thermo-mechanical models, predict the casing thermal displacement profile.

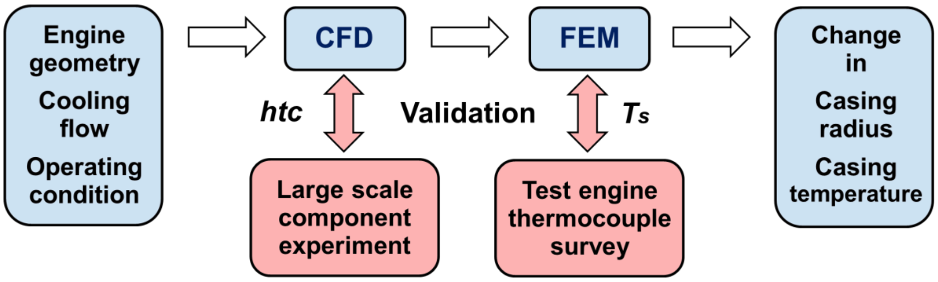

Figure 1.10 A simplified work flow for present turbine casing cooling research.

The geometry of the casing itself has considerable influence on the contraction achieved. Several design parameters such as thickness of the casing, the axial length of casing cooled, the height of the circumferential webs, and detail of their interface with the main engine casing were examined with an aim of identifying how engine weight could be reduced, and what features must be protected.

At equilibrium the casing temperature and closure is dictated by both the external and internal heat transfer. Extensive modelling has been conducted to characterise heat transfer from the NGV and segment coolant flows for a typical engine design. Historically these components have never been designed with consideration of the heat transfer to the casing. The modelling approach was validated by comparing predictions to validation data, generated within the current research programme by other workers, at the lowest engine representative mass flow rates.

The remainder of the thesis is structured as listed below. Chapter 2 provides a review of relevant work by other workers on thermal clearance control systems. Chapter 3 describes the experimental technique used for the investigation of an external impingement cooling manifold geometry and an internal over segment cavity geometry. Chapter 4 describes the use of CFD and FE analysis to investigate a very wide range of case cooling (and heating) geometries. Chapter 5 presents the cooling heat transfer coefficient distributions on the external casing from both experiment and CFD analysis together with corresponding casing thermal closures. Chapter 6 presents the FE analyses investigating a parametric range of variation in the local casing geometry including the dummy flange. Chapter 7 presents the heating heat transfer coefficient distributions on the internal casing from both measurement and CFD analyses. In Chapter 8 an alternative cooling scheme was analysed to allow the casing temperature predictions to be compared to the results of a test engine temperature survey. The casing contraction for this case was also determined for comparison to the current design. A summary of the work, conclusions and recommendations for future work are drawn in Chapter 9.

1.3 Contribution of Thesis

The main contributions of the work reported in this thesis are as follows:

- The external cooling flows are investigated, and in addition the interaction of the casing with the flow in over segment cavities seen in a typical engine casing closure system is characterised.
- The parametric study using a range of external impingement cooling arrangement has resulted in the best embodiment of the thermal control system.
- A detailed investigation of the effect of impingement cooling manifold standoff distance on external casing heat transfer and thermal closure was performed and the results show that the improved performance of the *htc* system occasionally leads to small changes in the closure available.

- An extensive parametric study of casing thermal closure for sets of different local casing features allows the importance of other geometric features, in particular the relative value of stiffening dummy flanges which surround the external casing at the location of the HP disc.
- The impact of small exit leakages flows in seal segment on the inner surface of engine casing heat transfer was examined and it suggests a route to reduce modelling complexity.
- An alternative inlet hole position in the over segment cavity is proposed to reduce level of the casing wall heat transfer leading to less thermal dilatation of casing, thereby tightening tip clearance can be expected.
- The current modelling technique which is suitable for coupled optimization of the cooling arrangement and casing local geometric features was validated against engine representative experimental data.

1.4 Publications

The research has been presented at two international conferences and, at the time of writing, papers have been accepted for two further presentations next year. A paper entitled "The Effect of Impingement Jet Heat Transfer on Casing Contraction in a Turbine Case Cooling System" **(Choi et al., 2014)** was presented at the ASME Turbo Expo 2014, Dusseldorf, Germany. It describes experimental and numerical investigation of a typical engine casing closure system with external impingement cooling scheme as presented in Chapter 8. A paper entitled "The Relative Performance of External Casing Impingement Cooling Arrangements for Thermal Control of Blade Tip Clearance" was presented at the ASME Turbo Expo 2015, Montreal, Canada. It has been reproduced in the ASME Journal of Turbomachinery **(Choi et al., 2016)**. This work is detailed in Chapter 5. Two further papers are expected on the effect of cooling manifold standoff distance on casing external heat transfer and thermal closure, and numerical characterisation of the flow distribution and thermal closure in a high temperature model engine representative thermal tip clearance control system.

Chapter 2 Literature Review

This chapter provides a literature review focussing on the turbine thermal clearance control systems. There are limited descriptions of such systems in the literature and these are discussed. This section is followed by a review of existing research on turbine tip clearance control system together with the relevant patent survey. The end of the chapter looks at some studies of impingement cooling systems. It is noted that the amount of previous work in this field is vast, however, a rather small amount number of papers are relevant to the high offset distances, sparse arrays and low Reynolds numbers typical of casing cooling schemes used in tip clearance control systems.

2.1 Research on Tip Clearance Evaluation

Understanding of running tip clearances and the thermo-mechanical behaviour of engine casing is important to improve thermal clearance control systems. Several previous workers have attempted to evaluate running clearances by means of numerical and analytical models. Some of the modelling techniques are transferable to the present research.

Kypuros et al. (2003) published some of the earliest open literature work describing a reduced order dynamic clearance model for tip clearance prediction. This was developed by **Luo et al. (2010)** to include some of nonlinearities in the model achieving higher fidelity prediction results. Similarly **Giovannetti et al. (2008)** proposed a procedure for the evaluation of seal clearance and the clearance reduction available using abadable seals in a casing liner.

As computing power has increased 3D FE modelling of the engine casing to predict local tip clearances has become feasible as a design tool, with some recent work presented by **Benito et al. (2008)** and **Arkhipov et al. (2009)**. These studies are limited by the fidelity of the local external casing cooling as crudely imposed bulk thermal boundary conditions are applied on the external casing. Notably because of the large number of design variables included in the model each simulation took about a day to complete. These workers conclude that a whole engine clearance prediction can be labour-intensive and the time required for optimisation studies using such an approach is subject to computing resources. Reduced order and 2D modelling approaches remain popular and **Bozzi et al. (2012)** more recently presented a simple procedure for calculating component thermal loads for running clearances. **Luca et al. (2012)** calculated running clearance based on a combination of 2D and 3D analysis, reducing the computation time required for each iteration. **McElhaney (2008)** draws attention to the importance of local mounting features causing distortion of the casing: he notes that the dependency of the clearance to local geometries is not negligible, and an axisymmetric approach must only be undertaken once the significance of local features has been assessed.

2.2 Research on Tip Clearance Control System

There are two main possible mechanisms for control of blade tip clearance: thermal shrinking of the casing and mechanical actuation of liner segments. The latter is a novel concept that makes use of mechanical actuators to control the radial position of over-tip seal segments relative to the casing thereby setting blade tip clearance. **Lattime et al. (2004)** at NASA Glenn Research Centre designed and developed a test rig equipped with hydraulic actuators for a proof of concept demonstration. **Steinetz et al. (2005)** and **Taylor et al. (2006)** evaluated the performance of the overall system leakage control, the actuation rates to position seal carriers and the accuracy of the clearance sensors at ambient/high temperature and pressurised conditions. The system has potential benefit of addressing the fast response of the engine casing using direct sensor feedback, allowing the engine to run at a desired optimum running clearance. However, mechanical systems are subject to secondary sealing, increased weight and complexity to the overall engine design. Additionally the operational reliability of clearance measuring systems that need to survive under the high temperatures experienced is still questionable. They may have a significant role to play in industrial gas turbines where more intermittent running will be required in the future.

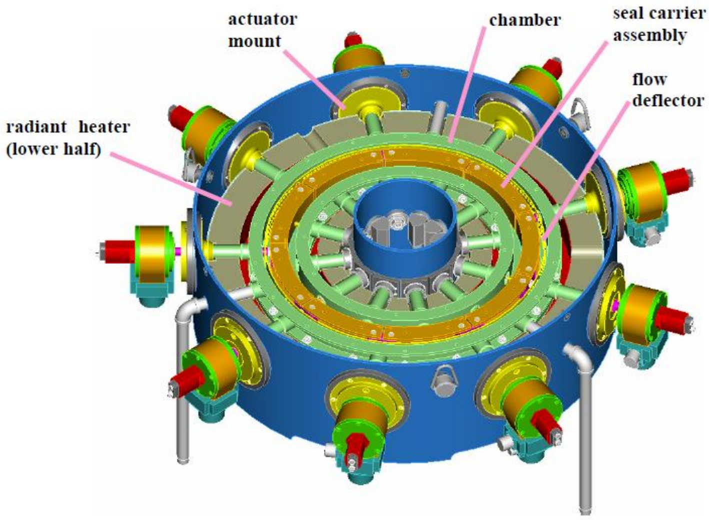

Figure 2.1 Overview of the NASA TCC facility with the housing lid removed (Lattime et al., 2004).

The thermal control system, on the other hand, offers a more reliable and practical solution stage by shrinking the entire outer casing to close the tip clearance, through the controlled impingement of relatively cheap low pressure external cooling air and internal secondary air, used for other purposes in the engine. The potential pitfalls of the thermal system are its relatively slow transient behaviour due to the casing's the large thermal mass and limited (/large) cold build clearance setting. This is a result of there currently being no clearance measurement system on the engine, resulting in an open loop control system. Impingement cooling schemes have proved to provide high heat transfer to the outer casing to allow improved tip clearance. They are suitable for schemes where there is a plentiful supply of air at a relatively low feed pressure and high driving gas temperature difference, due to their high local heat transfer coefficients. There is an enormous body of literature on impingement jet heat transfer for various engine applications, but few papers which deliver any detailed analysis concerning the relevant thermal control mechanisms. The geometrical aspect of turbine casing cooling and its flow conditions differ from other impingement cooling applications with less confinement and very large standoff distances and these merit new research beyond that found in the current literature.

Andreini et al. (2013) present some of the first academically published characterisation of a tip clearance control manifold. A highly idealised version of an impingement cooling manifold is used in the presence of a bypass flow seen in a low pressure turbine. The work involved experimental survey, by means of a liquid crystal technique, replicating in real scale a sector of 15^o of a bypass duct with five circular manifolds (each consisting of a single streamwise row of jet holes drilled at 90^o to the main passage; with a streamwise jet-to-jet spacing of s/d = 12) installed in an open-loop suction type wind tunnel (see **Figure 2.2**), and numerical simulations of these setups. They evaluated the heat transfer coefficient and the adiabatic effectiveness distributions at different manifold pressure ratios (P_{in}/P_{out} = 1.05, 1.10, and 1.15) and undercowl flow regimes (Re_{duct} = 40000, 60000, and 80000).

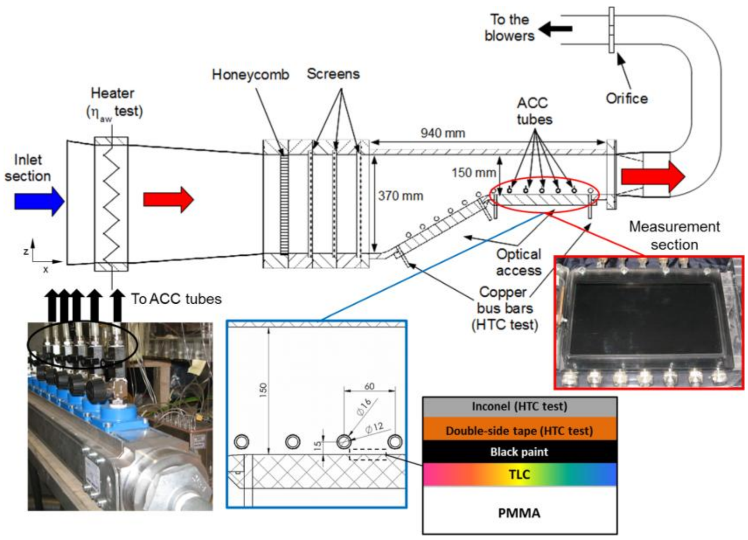

Figure 2.2 Overview of the experimental arrangement set by Andreini et al. (2013) at the University of Florence.

Andreini and Da Soghe (2012), **Da Soghe et al. (2012, 2015)** and **Da Soghe and Andreini (2013)** carried out numerical simulations using various casing cooling hole geometries on an isolated cylindrical manifold (see **Figure 2.3**). Two pressure ratios were considered: P_{in}/P_{out} = 1.01 and 1.65. An empirical correlation was developed for the prediction of the impingement holes discharge coefficient as a function of local pressure ratio, the length to diameter ratio of jet hole (*I*/*d*), and local mass velocity ratio, providing data with a maximum error of 4.5%.

$$C_d = 0.745(\Delta P)^{\alpha} g\left(\frac{I}{d}\right)\left(1 - 0.1262(31)^{-8(\frac{G_j}{G_c})^{0.1124}}\right) \tag{2.1}$$

where α and $g\left(\frac{I}{d}\right)$ are

$$\alpha = 0.0124\left(\frac{I}{d}\right)^2 - 0.117\left(\frac{I}{d}\right) + 0.379 \tag{2.2}$$

$$g\left(\frac{I}{d}\right) = -0.0204\left(\frac{I}{d}\right)^2 + 0.129\left(\frac{I}{d}\right) + 0.826. \tag{2.3}$$

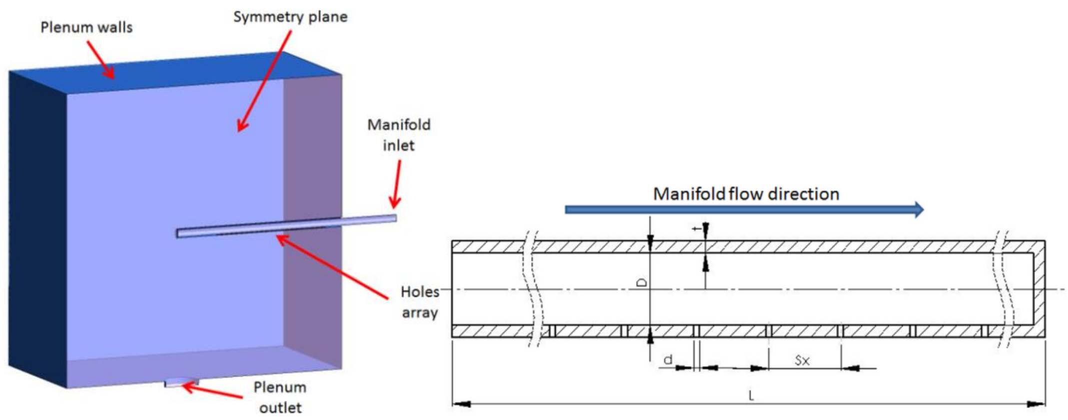

Figure 2.3 Typical computational domain set by Da Soghe and Andreini (2013).

Ahmed et al. (2010, 2011, 2012) determined heat transfer coefficient and discharge coefficient by changing cooling hole configurations of low pressure turbine casing manifolds. The investigations covered the effect of different hole diameters, different length to diameter ratio of jet holes and various hole shapes (cylindrical, elliptic, convergent and divergent conical as shown in **Figure 2.4**). All tests were conducted at a constant jet Reynolds number of 7500. They showed the discharge coefficients are nearly constant in the incompressible flow regime (Ma < 0.3) when the circular holes at constant length were compared and this C_d can be increased by increasing the hole length.

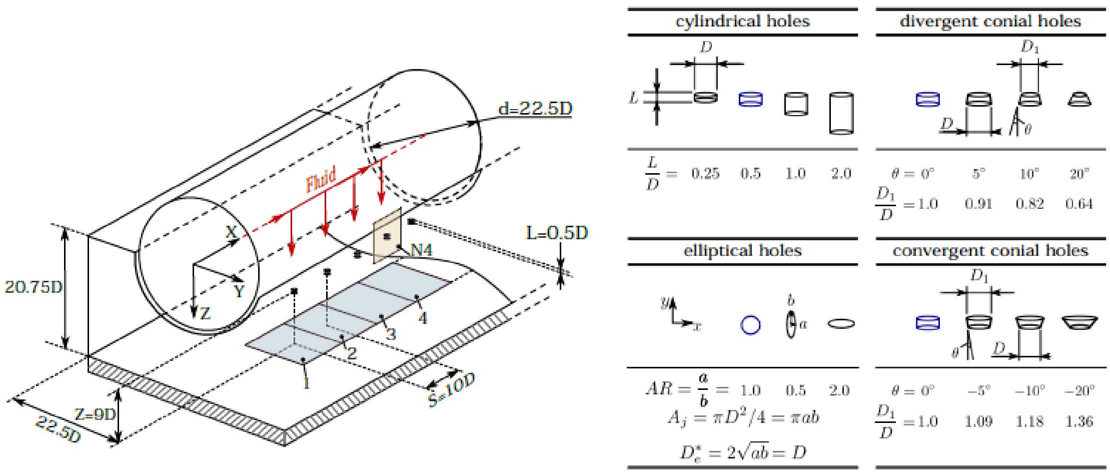

Figure 2.4 Different nozzle shapes applied to the study by Ahmed et al. (2011).

Most previous heat transfer research associated with thermal clearance control relied on numerical simulations and occasionally that coupled with scaled cold flow measurement. There are very few full scale investigations conducted in a high temperature environment to determine engine casing thermal behaviour.

An important area of tip clearance control research is the transient response of engine casing to instantaneous change in boundary conditions seen, for example during an acceleration or deceleration of the aircraft engine.

Dann et al. (2012, 2014) carried out engine representative thermal condition tests using a haded HPT/IPT casing employing an idealised cooling manifold arrangement to determine both the extent and variation in the contraction in a typical tip casing control arrangement at the Loughborough University. The inner side of the casing was held at a temperature of 600 - 900 K inferred from the hot uncombusted working gas flow in an engine. In the experiment this was achieved using a set of electric radiant heaters. Internal pressure effects were not taken into account in the study. They performed the displacement measurement using a laser triangulation sensor in the presence of external impingement cooling air over the outer wall at mass flow rate of 0.1 - 0.4 kg/s being delivered in a step-like manner when the heated casing reached a plateau in temperature. The rig allowed the thermal clearance control of the casing to be measured when real effects such as the radiative heating of the cooling manifold are present. It provides some of the best validation data for full engine models of casing closure (see **Figure 2.5**).

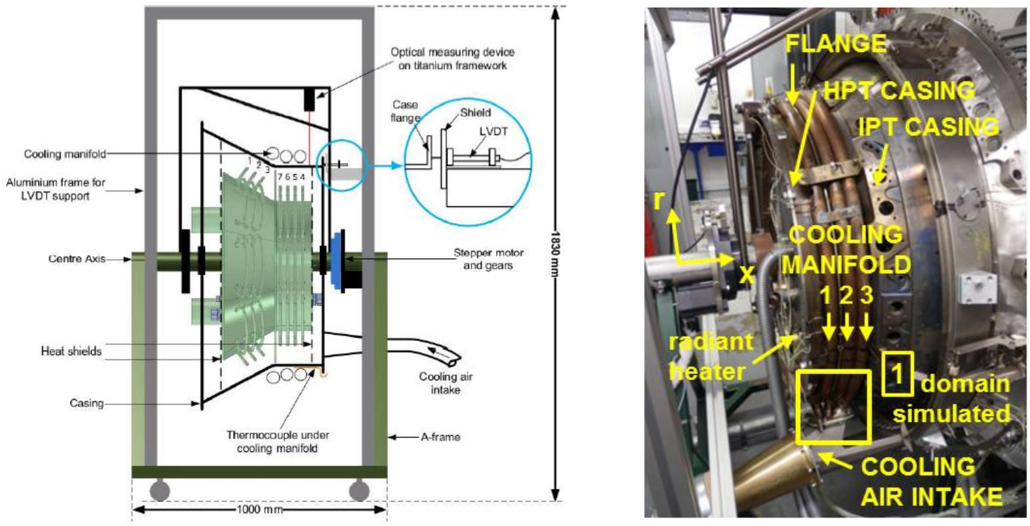

(a)

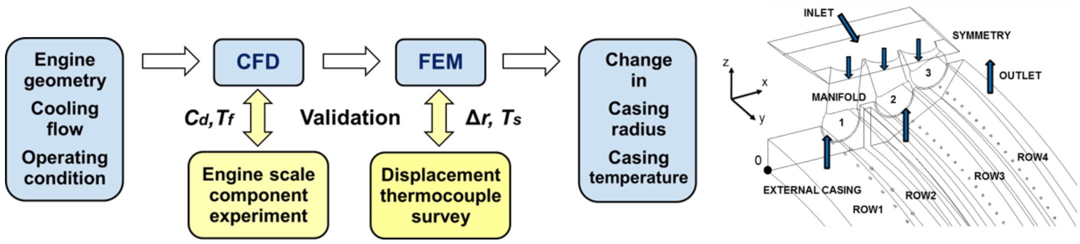

(b)

Figure 2.5 (a) Overview of the engine representative casing thermal test conducted by Dann et al. (2012, 2014) at Loughborough University and (b) a possible validation process.

More recently, **van Paridon et al. (2015)** and **Dann et al. (2016)** designed and developed a transient heat transfer test facility capable of reproducing an engine representative secondary air flow system i.e. at cruise temperature, pressures and mass flow rates, allowing advanced understanding of casing thermals. The test facility mainly consists of the flow system connecting to a compressed air supply, using electric heaters at a power of 407 kW to heat 0.6 kg/s and 13.5 bar of the working gas up to 650 K, and the test section inside the pressure vessel separated into an internal and external cavity. Change in asymmetric and axisymmetric casing positions in both quasi-steady and transient condition can be measured. The test facility can also be used to assess the impact of internal seal leakages on casing thermals which may be complementary to the present research in Chapter 7, though no data are yet available.

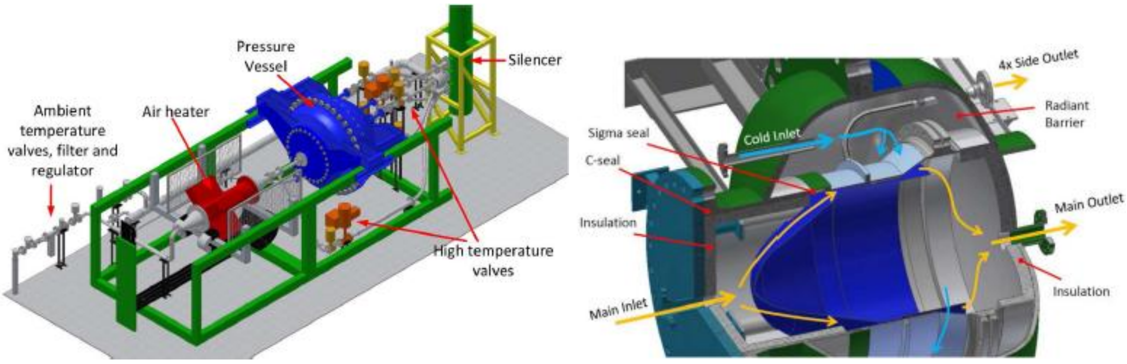

Figure 2.6 Overview of the transient heat transfer facility for casing thermals designed by van Paridon et al. (2015) at Osney Laboratory, University of Oxford.

Other literature in this area, for instance **Knipser et al. (2009)** provides general overview of the subject and **Amiot et al. (2007)**, **Bucaro et al. (2009)**, **Estridge et al. (2009)**, and **Lewis and Blidmark (2013)** present patented casing cooling configurations which lack validation. **Saroi (2014)** claimed in his patent that external impingement cooling manifold to casing wall distance can be altered using a spacer above manifold mounting features. This should allow optimized impingement jet to target casing wall distances to be achieved later in an engine's life to increase the tip clearance closure, thus maintaining engine performance.

Lewis and Bacic (2011) have proposed a further refinement of the tip clearance control system by installing a heat shield positioned inside the internal cavity (see **Figure 2.7**). This reduces the rate of internal heat transfer to the casing. A benefit, perhaps a primary benefit of the system is that it allows secondary hot flow to be ducted through the shield to improve the transient response during a step climb reacceleration. This allows tighter clearances to be deployed at cruise conditions.

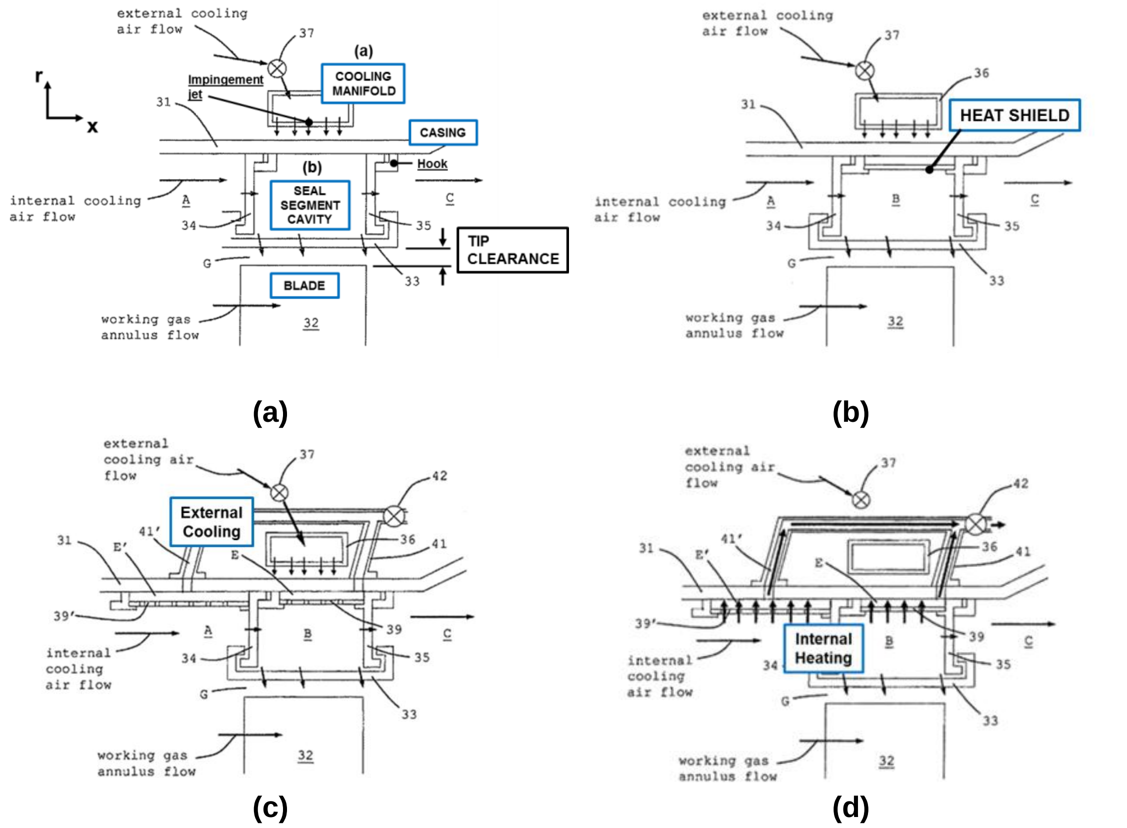

Figure 2.7 Typical cross section of turbine casing cooling arrangement (a) with or (b) without heat shields, and a concept of (c) external cooling during cruise and (d) internal heating during a step climb reacceleration, Lewis and Bacic (2011).

As an alternative to a thermal system, **Justak and Doux (2009)** introduce a self-acting air seal onto casing. This was designed to use aerodynamic force created by pressure drop across the turbine section to move the seal towards the blade tips to a preset position. This may allow the operating clearance to be maintained without contacting the blades. **Lewis (2014)** presented a concept paired system with a mechanical actuator linked to a case cooling apparatus.

2.3 Earlier Impingement Cooling

Impingement cooling systems have been identified as a method with the potential to provide the high rates of heat transfer needed for rapid heat removal. Due to its high heat transfer rates near the stagnation point, impinging jets have been used in many engineering applications where heating or cooling processes are required, from paper drying, food cooling, plastic film softening and in the current context the cooling of gas turbine nozzle guide vanes.

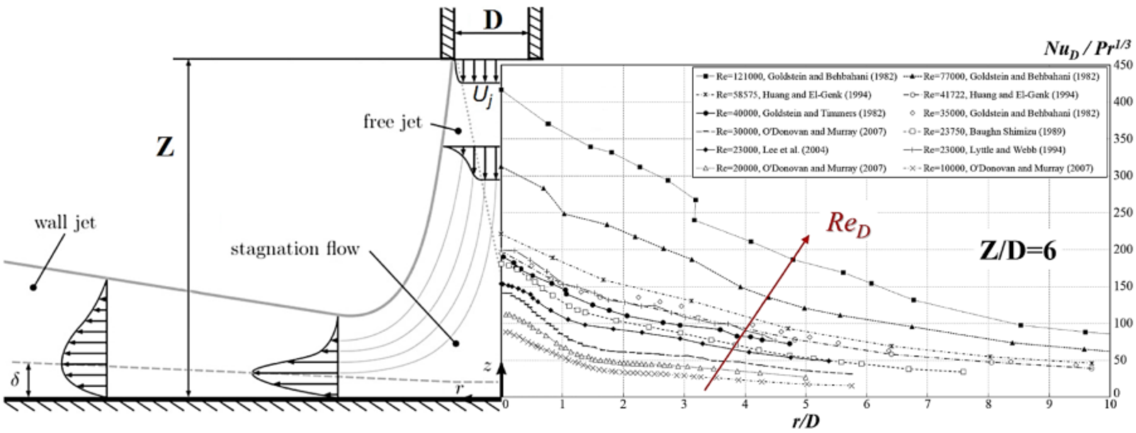

Figure 2.8 Local heat transfer (in Nusselt number) distributions under a single impingement jet, Terzis et al. (2015).

Single Jet. A single impingement jet flow can be divided into four main regions: the potential core and the developing zone, both within the free jet, the stagnation zone, and the wall jet. As jet traverses the space between the nozzle and the target surface, the shear layer thickens and the potential core becomes progressively narrower. The potential core ends when there is entrainment of flow to the jet axis (z/d = 5 - 6). **Lucas et al. (1992)** observed that the extent of potential core can be reduced with jet confinement due to additional flow entrainment. The developing zone, where the jet velocity is in inverse proportion to the distance from the nozzle exit, only exists at large jet-to-target spacing. In the stagnation zone, the jet direction changes from an axial to radial direction through a stagnation point, thus the static pressure increases as the flow slows towards zero velocity. **Popiel et al. (1980)** found that the stagnation heat transfer was directly proportional to $Re^{0.5}$. The wall jet parallel to the target surface accelerates from the stagnation point, but when due to continuity considerations this acceleration reduces the flow undergoes transition from a laminar to a fully turbulent flow and the local Nusselt number in the developing wall jet becomes proportional to $Re^{0.7\text{-}0.8}$ (**Yan et al., 1992**).

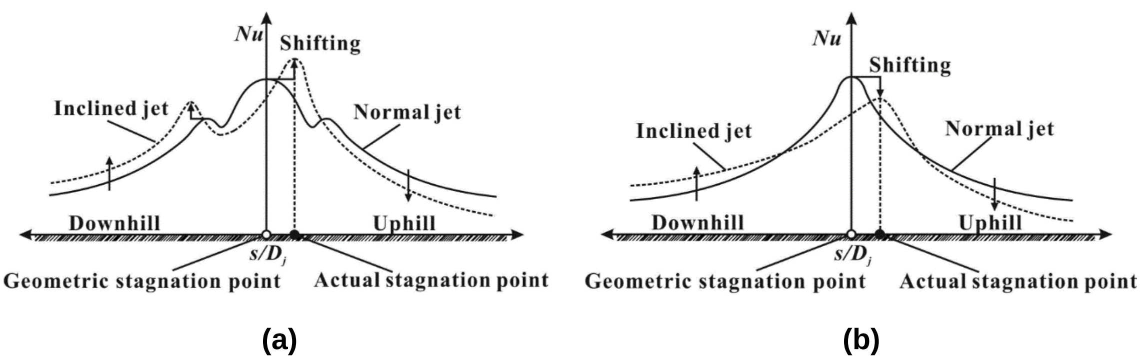

Figure 2.9 Schematic summary of lateral heat transfer distribution of a single normal jet and an oblique jet on a flat plate (a) for a small offset distance and (b) for a large offset distance, Wang et al. (2014).

Wang et al. (2014) depicted that lateral heat transfer distributions of a single jet for a short or a large standoff distance. At a short offset distance secondary enhancement occur in the local heat transfer coefficient increasing the area averaged values as shown in **Figure 2.9**. **San and Lai (2001)** found those second maxima at the jet-to-target spacing z/d less than 1, and **O'Donovan and Murray (2007)** reported that the secondary peak at $z/d < 2$ is due to an abrupt increase in turbulence in the wall jet.

Oblique Jet. For an oblique jet the position of maximum heat transfer moves away from the geometric centre of the jet axis toward the compression side of the wall jet. It was seen by **Beltaos (1976)** who investigated in an oblique jet in the range of jet Reynolds number from 35,000 to 100,000 and jet-to-target spacing *p*/*d* of 15 – 47. **Sparrow and Lovell (1978)** measured local heat transfer to an oblique impinging jet at low (10,000 or less) jet Reynolds numbers with the jet-to-target spacing *p*/*d* of 7 – 15 and also reported the shift along the axis of symmetry. **Yan and Saniei (1997)** studied the flow of an oblique impinging jet at the Reynolds numbers of 10,000 and 23,000. The jet angle of 90^{o}, 75^{o}, 60^{o} and 45^{o}, and the jet-to-target spacing *p*/*d* of 2, 4, 7 and 10 were tested. They showed that the shift is more pronounced with a smaller oblique angle (larger jet inclination) and a smaller jet-to-target distance. **Goldstein and Franchett (1988)** carried out heat transfer experiments for a jet impinging at different oblique angles of 90^{o}, 60^{o}, 45^{o} and 30^{o} with two Reynolds numbers of 10,000 and 23,000. They populated a correlation for an average Nusselt numbers over areas of interest. In the correlation, Nusselt number can be expressed as a function of Reynolds number, jet to target spacing *p*/*d* and the angle of impingement jet

$$\frac{\mathrm{Nu}}{\mathrm{Re}^{0.7}} = A\, exp^{-(B+C\cos\phi)(r/D)^{m}}. \tag{2.4}$$

where r and ϕ are cylindrical coordinates for correlation of contours of constant Nu. The constants A, B, C, D and E are obtained from **Table 2.1**.

Table 2.1 Coefficients for heat transfer correlation of Goldstein and Franchett (1988).

ϕ	A			B	C	E		
	p/d = 4	p/d = 6	p/d = 10			p/d = 4	p/d = 6	p/d = 10
90°	0.159	0.155	0.123	0.37	0.0	0.0	0.0	0.0
60°	0.163	0.152	0.115	0.40	0.12	0.8	0.6	0.9
45°	0.161	0.146	0.107	0.47	0.23	1.2	1.0	1.5
30°	0.136	0.124	0.091	0.54	0.34	1.5	1.4	1.9

Arrays of Jets. It is more common that arrays of jets are used in real applications. The heat transfer of arrays of jets is affected by additional interaction to neighbouring jets prior to impingement and upwash fountain (see **Figure 2.10**). The jet-to-jet interaction is mainly attributed by the growing shear layer of an adjacent jet. This interference would weaken the strength of jets and eventually degrade the magnitude of heat transfer. The jet fountain is formed by the two adjacent wall jets encountered in between resulting in heated air recirculation and flow entrainment.

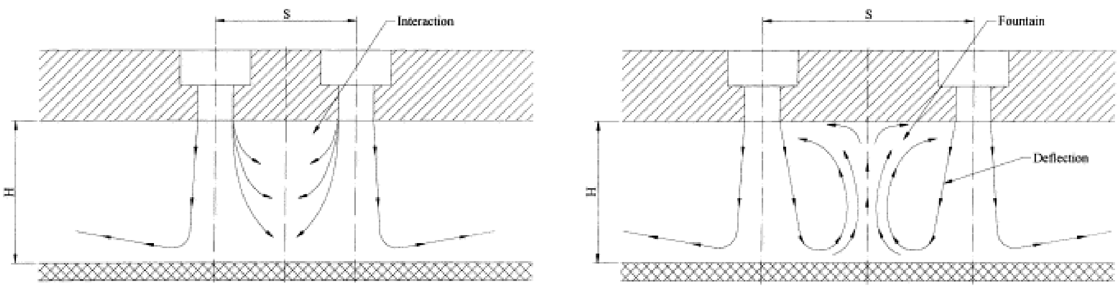

(a) **(b)**

Figure 2.10 (a) Jet to jet interaction prior to impingement and (b) upwash fountain in a multijet impingement, San and Lai (2001).

Goldstein and Seol (1990) studied a single impingement row and produced a heat transfer correlation in spanwise averaged, streamwise resolved values which has been widely used as an industrial standard correlation,

$$\mathrm{Nu} = \frac{2.9\ \mathrm{Re}^{0.7} e^{-0.09(\frac{x}{d})^{1.4}}}{22.8 + (\frac{x_n}{d})(\frac{z_n}{d})^{0.5}}\ . \tag{2.5}$$

The correlation is valid in the range: $x_n/d = 4 – 8$, $z_n/d = 2 – 8$, $x/d = 0 – 6$ and $\mathrm{Re}_{jet} = 10000 – 40000$. It should be noted that the correlation does not take into account the effects of crossflow or jet confinement.

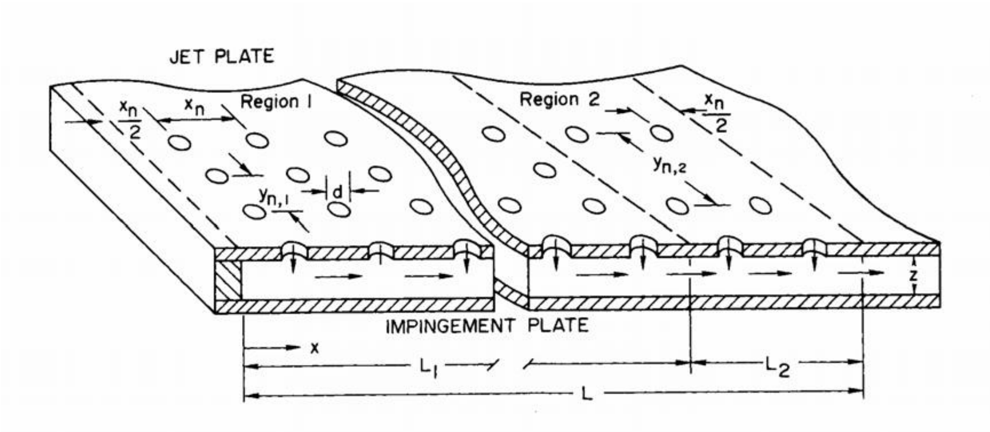

Figure 2.11 Schematic diagram of confined array impingement cooling, Florschuetz et al. (1981).

Florschuetz et al. (1981) conducted an extensive study of impingement jet heat transfer and developed heat transfer correlations for jets in inline and staggered arrays, which has been the basis for jet impingement research. The correlation considers the extensive geometric parameters (jet-to-jet spacing in streamwise direction x_n, jet-to-jet spacing in spanwise direction y_n, jet-to-target spacing z_n, jet hole diameter d) and flow field parameters (jet Reynolds number Re_{jet}, ratio of the jet-to-crossflow mass velocity G_c/G_j, Prandtl number Pr) for an averaged Nusselt number to be applied to an area extending $–y_n/2d$ to $+y_n/2d$ by $–x_n/2d$ to $+x_n/2d$, centred on the geometric jet axis.

$$\mathrm{Nu_{patch}} = \alpha \mathrm{Re_{jet}}^{m} \mathrm{Pr}^{1/3} \left(1 - \beta \left(\frac{z_n}{d} \frac{G_c}{G_j}\right)^{n}\right) \tag{2.6}$$

with the constants expressed as geometric functions:

$$\alpha, \beta, m, n = C \left(\frac{x_n}{d}\right)^{n_x} \left(\frac{y_n}{d}\right)^{n_y} \left(\frac{z_n}{d}\right)^{n_z} \tag{2.7}$$

where the constants C, n_x, n_y and n_z are obtained from the following table.

Table 2.2 Florschuetz correlation constants for inline and staggered arrays

	Inline pattern				Staggered pattern			
	C	n_x	n_y	n_z	C	n_x	n_y	n_z
α	1.180	-0.944	-0.642	0.169	1.870	-0.771	-0.999	-0.257
m	0.612	0.059	0.032	-0.022	0.571	0.028	0.092	0.039
β	0.437	-0.095	-0.219	0.275	1.030	-0.243	-0.307	0.059
n	0.092	-0.005	0.599	1.040	0.442	0.098	-0.003	0.304

The correlation is valid in the range: x_n/d = 5 – 15, y_n/d = 4 – 8, z_n/d = 1 – 3 and $\mathrm{Re_{jet}}$ = 5000 – 50000. In addition, many correlations have been presented for the heat transfer coefficients by others, and these have been well summarised in **Jambunathan et al. (1992)**, **Gillespie (1996)**, and **Zuckerman (2005)**.

Baily and Bunker (2002) tested impinging jet arrays with the jet-to-jet spacings *x*/*d* and *y*/*d* of 3, 6 and 9. The jet-to-target spacing *z*/*d* was varied from 1.25 to 5.5 and the jet Reynolds numbers was ranged from 14,000 to 65,000. They found that the Florschuetz correlation overpredicted the patch area averaged values for an array of *x*/*d* = 3 and *y*/*d* = 3 and an array of *x*/*d* = 9 and *y*/*d* = 9 (both are outside the range of the correlation). When *x*/*d* = 6 and *y*/*d* = 6 (within the range of the correlation) the Florschuetz correlation closely predicted to the experimental results they compared.

Metzger et al. (1979) reported area averaged heat transfer coefficients for inline and staggered impingement arrays where the jet-to-jet spacing are $x/d = 5$, 10 and 10, and $y/d = 4$, 6 and 8. They showed that the averaged values for the inline pattern are somewhat higher than those for the staggered counterparts as per the Florschuetz correlation. **Van Treuren et al. (1993)** investigated for a single confined inline and staggered array of jets for jet-to-target spacings z/d = 1, 2 and 4 at the jet Reynolds numbers ranging from 10,000 to 40,000. They also found that superior of the inline pattern and overprediction of the Florschuetz correlation for all offset levels.

Obot and Trabold (1987) evaluated impingement heat transfer on three different crossflow schemes at the jet Reynolds numbers ranging from 1,000 to 21,000. The particular geometry covered the jet-to-jet spacings x/d of 10, 10 and 5.6 and y/d of 8, 4 and 4, and jet-to-target spacing z/d ranging from 2 to 12. They reported that the largest heat transfer enhancement was seen under the minimum crossflow scheme at narrow jet-to-target spacings due to the crossflow degrades the uniformity and the level of the heat transfer. At larger jet-to-target spacing the magnitude of heat transfer and the uniformity were gradually degraded while the dependency of the crossflow was less important.

Brevet et al. (2002) studied impingement heat transfer for an array of x/d = 10 and y/d = 2 and an array of x/d = 10 and y/d = 10. The jet-to-target spacing was varied z/d = 1, 2, 5 and 10 and the jet Reynolds numbers ranging from 3,000 to 20,000 were tested. The results showed that the optimum jet-to-target spacing in terms of area averaged heat transfer is within the range from 2 to 5.

Xing et al. (2010, 2013) made a comparison for various jet to target spacings *z*/*d* = 1 – 5 of inline and staggered arrays of jets at three different crossflow schemes with the jet Reynolds numbers ranging from 15000 to 35000. They reported that at the minimum crossflow scheme (two axial exits in opposite direction) array with jet-to-target spacing *z*/*d* = 2 performed the best in terms of overall area averaged heat transfer coefficients. However, if it narrowed down to the three middle rows at the minimum crossflow cases which barely affected by jet-induced crossflow (or none of crossflow) the local heat transfer increases linearly as the jet-to-target spacing *z*/*d* decreases 5 to 1.

Huber and Viskanta (1994) studied the effect of jet to jet spacing and jet-to-target spacing on heat transfer to an inline array at *x*/*d* and *y*/*d* of 4, 6 and 8, and *z*/*d* of 0.25, 1 and 6. They reported that the jet-to-jet spacing *x*/*d* and *y*/*d* = 4 is the most efficient because a large fraction of the target surface is covered by the stagnation region and the influence of the low heat transfer coefficients associated with the wall jet region are minimised. The low jet-to-target spacing *z*/*d* = 0.25 and 1.0 resulted in significant enhancement of the magnitude and the uniformity compared to *z*/*d* = 6.0 case.

San and Lai (2001) investigated the effect of jet to jet spacing under staggered arrays. The jet to jet spacing was varied from 4 to 16 and the jet to target spacing from 2 to 5. They observed that for the lowest standoff distance *z*/*d* = 2 they tested the jet fountain between adjacent jets was more important and the jet-to-jet spacing *x*/*d* = 8 was the most desirable. For a higher jet-to-target distance *z*/*d* = 5, the jet shear layer expansion was more dominant and it was relieved as the jet-to-jet spacing was further increased to 6 while the spacing *x*/*d* over 6 the fountain effect became more dominant.

Goodro et al. (2007, 2008) studied the effect of Mach numbers and temperature ratio on heat transfer using a jet array of x/d and y/d of 8 at various jet hole diameters ranging from 3 to 20 mm. They showed that the Florschuetz correlation provides a closed fit to the measurement data at the low Mach range 0.16 and 0.21 showing no evidence for Mach number dependency, but a large derivation was found at the high Mach number at 0.74. It is known that the typical Mach numbers encountered in turbine casing cooling systems for tip clearance control are generally in a very low range where the flow is essentially incompressible. The heat transfer rate decrease as the temperature increases from 1.06 to 1.73. They reported that this was because the degradation of local turbulent transport in impingement flow as the temperature ratio increased.

There have been a number of studies on heat transfer and flow characteristic of impingement jet array; the effect of nozzle geometry, jet-to-jet spacing, jet-to-target spacing, crossflow, Mach number, oblique angle etc. have been studied and reviewed. However, a rather small amount number of papers are relevant to the high offset distances, sparse jet arrays and low Reynolds numbers typical of turbine casing cooling schemes used in tip clearance control systems.

Furthermore, many numerical studies have been conducted to evaluate the performance of turbulence models through comparisons with experimental results. **Craft et al. (1993)** utilized four turbulence models including k-ε and RSM to compare with experimental results. More recently, **Zuckerman et al. (2005, 2007)** utilized turbulence models including the realizable k-ε and the v^2-f for numerical accuracy assessment for a single jet. They showed that the v^2-f model which developed to accurately capture the turbulence boundary layer by **Durbin (1991)** provided better prediction of impingement jet heat transfer to experimental data. It is noted that the EARSM model is similar in formulation to the v^2-f model and will be considered in the current programme. **Ibrahim et al. (2005)** conducted CFD analysis for jet impingement heat transfer with a single jet and arrays of jets using the standard k-ε model, the k–ω model, and the v^2-f model. They reported the v^2-f model comes into the closest agreement to the measured data set for a single jet, but for multiple jets the v^2-f model behind the ranking and did not reproduce some features seen in the experiment. It is noted that SST k–ω developed by **Menter (1994)** which combines the standard k–ω model model for use sub-layer and the standard k-ε model away from layers will be implemented in this research. **Elebiary and Taslim (2012)** reported their numerical predictions of impingement jet heat transfer using the realizable k-ε model in conjunction with the enhanced wall treatment were in a reasonable agreement with their measured data. It is known that the realizable k-ε model is suitable for complex shear flows involving locally transitional flows and this will also be turned on in the current programme.

2.4 Summary

Few items of literature directly refer to the thermal clearance control problem. Those which do are frequently broad brush reviews of the subject or patented configurations which lack any scientific validation. Those thermal systems employing impingement cooling schemes have been reviewed along with a general review of earlier impingement jet studies. Experience of reliable turbulence models for RANS modelling was saught to determine the strategy employed in this thesis. Although the number of existing impingement cooling studies is more or less limitless, it is also clear from these that the thermal performance is very sensitive to the impingement cooling geometry and exit flow conditions. Thus characterising the cooling systems to be employed is one of the key challenges of the current research.

Chapter 3 Experimental Test Rigs and Measurement Techniques

This chapter details the experimental test rigs and techniques used to provide baseline data for the validation of heat transfer coefficient distributions for the computational heat transfer studies reported in this thesis. The heat transfer technique used was the transient liquid crystal technique, which has been developed at Oxford over the last 30 years. It is particularly appropriate where full heat transfer coefficient distributions are required on internal surfaces and is described in some detail. The baseline geometries used for both the external and internal surfaces of the engine casing are described: externally this is a cooling system concept used by a number of engine manufacturers for tip clearance control, internally a generic design typical of those used in a previous Rolls-Royce engine. Dimensional scaling required for the experiment are described. Along with details of the measurement technique an uncertainty analysis of the measurement using a perturbation method is reported.

The remainder of the chapter describes the development of two experimental test rigs both of which will use the transient liquid crystal technique to measure local heat transfer coefficient distributions in impingement flow driven test geometries. This is first described followed by the general dimensional analysis, scaling and embodiment of each of the test rigs.

3.1 Transient Liquid Crystal Technique

The transient liquid crystal (TLC) technique has become the primary means of determining local heat transfer coefficients in jet impingement research as full surface temperature measurements can be made easily on complex internal geometries. **Ireland and Jones (2000)** reviewed the use of TLC with a special emphasis on recent developments in the field. **Tapanlis (2011)** investigated heat transfer of a simple turbine casing impingement cooling system using the TLC technique to calculate local heat transfer coefficient distributions. There are very many descriptions of TLC techniques in the literature, however, as here the author has used the technique without its further development, the discussion is limited to the implementation currently in use at the Osney Thermo-Fluids Laboratory.

TLCs react to changes in temperature by selectively reflecting the visible spectrum of circularly polarised light over a limited temperature range dependent on their chemical composition. With increasing temperature, TLCs coating a transparent thermally insulating plate i.e. a Perspex model enter their chiral nematic phase, reflect red through blue light, once again becoming transparent at higher temperatures where the isotropic phase is entered and the liquid crystals melt – here the liquid crystals are held in a microencapsulation of gelatine so no material is lost from the surface. Provided the liquid crystal coating is carefully applied to the model surface, the process is repeatable, although there may be hysteresis between heating and cooling events. In general liquid crystal coatings are applied in aqueous solution using an aerosol spray gun. Care is taken to apply a smooth coating no more than 20 - 30 μm in thickness, with a further layer of backing ink of approximately 10 μm thick. This layer can be considered to be thermally thin, though the maximum heat flux must be limited to < 20 kW/m^2 to ensure accurate colour play. The colour plays of the reflected light on the TLC coated surfaces are recorded using video cameras. The hue or intensity signals from the RGB sensors can be used in subsequent analyses, while surface thermocouples are used to provide surface temperature histories for calibration purposes. Both surface and gas thermocouples provide boundary conditions for transient *htc* analyses. In the case of surfaces with complex curvature coatings of multiple narrow band liquid crystals (displaying colour full colour play over ~1 ^{o}C) are preferred to wide band liquid crystals as they are less affected by the viewing angle. For such liquid crystals the green intensity signal provides an excellent contiguous signature throughout a transient test.

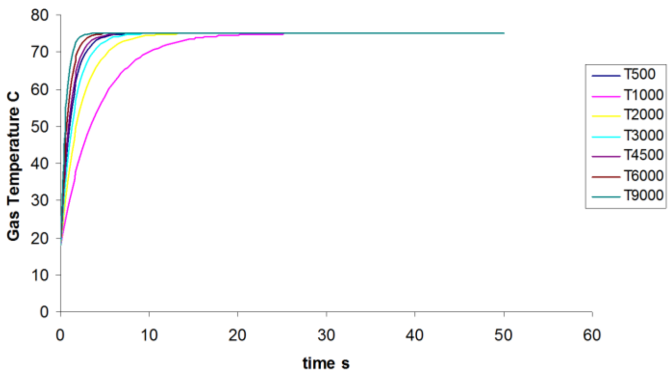

Figure 3.1 Predicted heater response for jet Reynolds number 2000 and 6000 (for U_{plenum} with air).

Typical tests are conducted by establishing initial cold flow conditions, which are isothermal with the walls of the experiment. When the test begins, the gas temperature is rapidly raised, at Oxford this involves the use of a heater mesh **Gillespie (1996)** which allows the plenum temperature, from which air to the impinging jets are supplied, to be suddenly changed without the need for a complicated bypass arrangement. **Figure 3.1** shows the predicted heater mesh response for present experiment in the following section 3.2 2, using an empirical correlation below.

$$T_{\mathrm{gas}} = T_{\mathrm{o}} + \Delta T_{gas} e^{\frac{-t}{\tau}} \tag{3.1}$$

$$\text{where } \tau = 0.111\, \mathrm{U}_{\mathrm{plenum}}^{-0.914} \tag{3.2}$$

The local *htc* is evaluated analytically by solving the 1D Fourier equation for a semi-infinite solid, **Equation 3.3**, using surface temperature history events determined from the liquid crystal colour play (1D validity will be considered in the uncertainty analysis). In the analysis the radiative heat transfer at the surface is considered negligible such that the heat convected to the surface equals the heat conducted into the solid, **Equation 3.4**. Further boundary conditions are isothermal initial conditions **Equation 3.5**, and that the solid is planar and semi-infinite **Equation 3.6**.

$$\frac{d^2T}{dx^2} = \frac{k}{\rho c}\frac{dT}{dt} \tag{3.3}$$

$$k\frac{dT}{dt} = htc(T_{gas} - T_s) \tag{3.4}$$

$$T_{x=0,t} = T_i \tag{3.5}$$

$$T_{x=\infty,t} = T_i \tag{3.6}$$

For **Equation 3.6** to remain valid at time = t_{max}, **Schultz and Jones (1973)** determined the minimum thickness wall required, x as **Equation 3.7**.

$$x = 4\sqrt{\frac{k}{\rho c_p} t_{max}} \tag{3.7}$$

For a reliable test a maximum test time of at least 30 seconds is desirable. Under these boundary conditions if the inlet gas temperature is modelled as a series of ramps of slope m_i, the surface temperature history can be calculated by **Equation 3.8** where beta (β) is given by **Equation 3.9**, as developed by **Ling et al. (2004)**. This may be solved by regression, however, a globally minimised solution can be found by generating a series of surface temperature responses for a given thermal product, $\sqrt{\rho c k}$. For Perspex $\sqrt{\rho c k} = 569 \pm 29 \frac{\sqrt{W}}{m^2 K}$ **Ireland (1987)**.

$$T_s = T_o + \sum_{i=1}^{n} m_i t \left(1 - \frac{2}{\beta_i} + \frac{1 - \exp(\beta_i^2)\mathrm{erfc}(\beta_i)}{\beta_i^2}\right) \tag{3.8}$$

$$\text{where } \beta_i = \frac{htc\sqrt{(t - t_i)}}{\sqrt{\rho c k}} \tag{3.9}$$

$$\text{and } m_i = \frac{\Delta T_{gas,\infty,i}}{\Delta t_i} \tag{3.10}$$

In the current studies these calculated temperature histories are then transformed into green intensity histories using an *insitu* temperature *vs*. intensity calibration. These theoretical intensity histories are directly compared with the experimental green intensity history at each pixel location to determine the *htc* value using a weighted least squares comparison. An *htc* map can then be established. A more detailed description of TLC technique can be found in THTAC: Transient Heat Transfer Analysis Code for Liquid Crystal Experiments at The University of Oxford: Updated GUI Driven Software, **McGilvray and Gillespie (2010)**. A flowchart showing the method of solution is given in **Figure 3.2**.

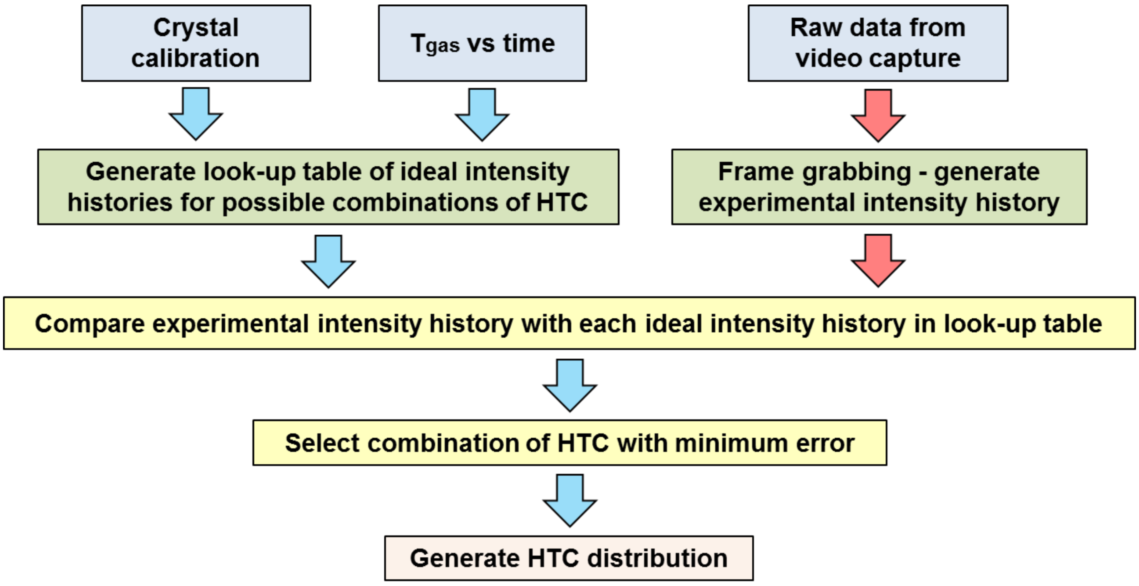

Figure 3.2 Method of Solution of Transient Liquid Crystal Tests.

3.2 External Casing Impingement Cooling Manifold

The TLC technique was applied to a model of a casing cooling manifold, impinging onto an external casing as described below. The results of the testing are presented in a subsequent chapter.

3.2.1 External Casing Baseline Cooling Geometry

Figure 3.3 shows a radial cross section through an idealised external casing cooling manifold configuration, typical of those adopted by leading large civil engine manufacturers for thermal tip clearance control. Three hollow ring manifolds surround the external casing mounted on either side of two circumferential thermal control flanges. Cooling air, taken from an early compressor stage and ducted through the manifold, are directed through a multiplicity of small diameter holes in the bottom wall of manifold to impinge onto the external casing wall (shown in cartoon format below the casing geometry). The over-tip seal segments are mounted on this wall via pairs of internal hooks. The impingement jets are used to change the temperature of the casing and, because of thermal contraction, the clearance between casing liner and the blade tips. The low stiffness of the over-tip seal segments means that any casing contraction is directly linked to a reduction of tip clearance and hence tight tip running. The thermal control flanges (‘dummy’ flanges) play a key role in the system by providing easily cooled additional thermal mass with a more tortuous conduction path from the internal heated surfaces.

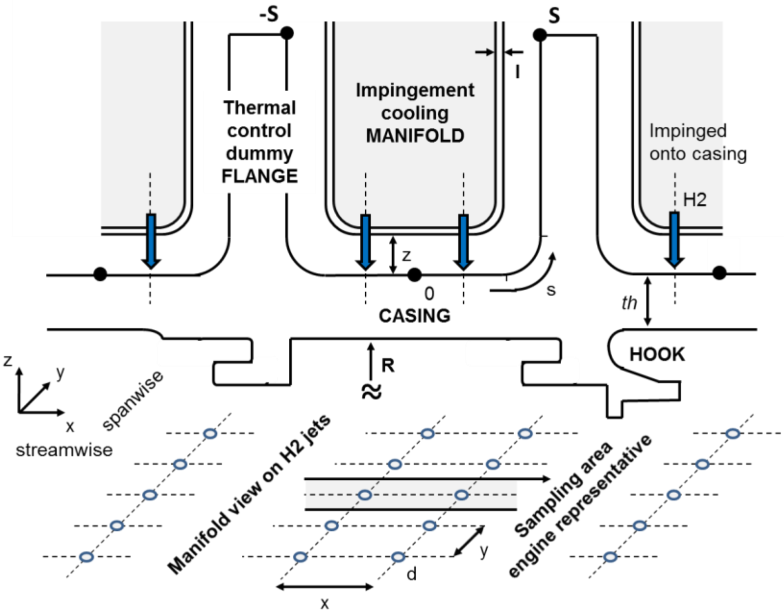

Figure 3.3 External Casing Impingement Cooling Manifold, adapted from (Rolls-Royce, 2011).

Operating conditions representative of Idle, Cruise, and Maximum take-off conditions were specified based on air system analyses by Rolls-Royce and two further conditions were chosen to represent Cruise and Maximum take-off with a worn engine where the control valve to the system is in a fully open configuration. These are listed in **Table 3.1**.

Table 3.1 External engine casing coolant flow condition (Rolls-Royce, 2011).

	$\dot{m}_{total}$	$\dot{m}_{single}$	$P_{manifold}$, kpa	$T_{manifold}$, K	Re_{jet}
Idle, new engine	0.0184	$\frac{\dot{m}_{total}}{2000}$, kg/s	101.3	290	540
MTO, new engine	0.0835		110.2	352	2120
Cruise, new engine	0.0789		36.4	285	2360
Cruise, valve fully-open	0.1910		49.5	285	5710
MTO, valve fully-open	0.3937		110.2	352	10000

3.2.2 Development of Impingement Manifold Model

A transient heat transfer test facility was developed to simulate the central manifold of a baseline configuration, henceforth called the *H2* configuration. While three manifolds are arranged axially around the casing, these are of very similar design with flow exiting upstream and downstream partially confined by the dummy flange walls. Thus, symmetry conditions are applied to the model in the central region. A schematic of the test rig is depicted in **Figure 3.4**.

The scaling factor was determined through dimensional analysis. A full dimensional analysis of an impingement system is described in **Chambers et al. (2003)**. The variables considered are shown in **Equation 3.11**

$$q'' = \emptyset\left(x, y, z, I, d, R_{fillet}, n, \rho, \mu, \mathrm{c}, \mathrm{k}, T_{gas}, T_{suf}, u\right) \tag{3.11}$$

and may be written in non-dimensional form as

$$Nu = \frac{q''d}{\Delta T\ \mathrm{k}} = \frac{htc\ d}{\mathrm{k}} = \emptyset\left(\frac{x}{d}, \frac{y}{d}, \frac{z}{d}, \frac{I}{d}, \frac{R_{fillet}}{d}, n, \frac{\rho u d}{\mu}, \frac{G_j}{G_c}, \frac{T_{gas}}{T_{suf}}, \frac{\frac{1}{2}u^2}{\mathrm{c}T}, \frac{\frac{1}{2}u^2}{\mathrm{c}\Delta T}\right) \tag{3.12}$$

In the current range of experiments, where the velocity is low, Mach number effects can be ignored ($Ma_{engine} < 0.3$). As buoyancy effects and cross flow are expected to be very small the gas to wall temperature ratio can also be ignored. Thus *htc* expressed as Nusselt number is treated as a function of jet Reynolds number (Re = 6000 and 2000), Prandtl number and geometric scaling (x/d = 11.7, y/d = 5.2, z/d = 1 - 6, I/d = 0.58, $\frac{R_{fillet}}{d} \sim 0$).

The rig scale could then be determined by the desire for a maximum test time of ~60 seconds, and a need for measurable *htc* during transient tests, at maximum heat flux levels compatible with the thermochromic liquid crystal employed. (A gas temperature rise of up to 50 ^{o}C was assumed.) Using values from the literature for stagnation point heat transfer **(Popiel et al., 1982)**, an approximately fourteen times scale model was chosen for the experiment. This made the internal wall thickness 10 mm, and Perspex sheets were used for all flat wall sections. Curved sections of the rig, namely, the fillets of the dummy flange and the manifold plenum was machined from MDF wooden sections except for a transparent window section on the dummy flange fillet which was CNC machined from a Perspex block 50 mm thick.

The impingement array of the baseline configuration consists of 2 streamwise rows by 5 spanwise (circumferential) rows. The target surface in the model is planar even though in the engine it is clearly a hoop of large radius, ~370 times that of the impingement jet hole diameter. This level of curvature has been shown to cause insignificant changes to the heat transfer coefficient by impingement (**Bunker and Metzger, 1990**). The five spanwise rows are considered sufficient such that the central row is insignificantly affected by the presence of the spanwise endwalls which are an artifice of the model, and affect both the flow field and the driving gas temperature during the experiments. Data from the middle row data are always reported.

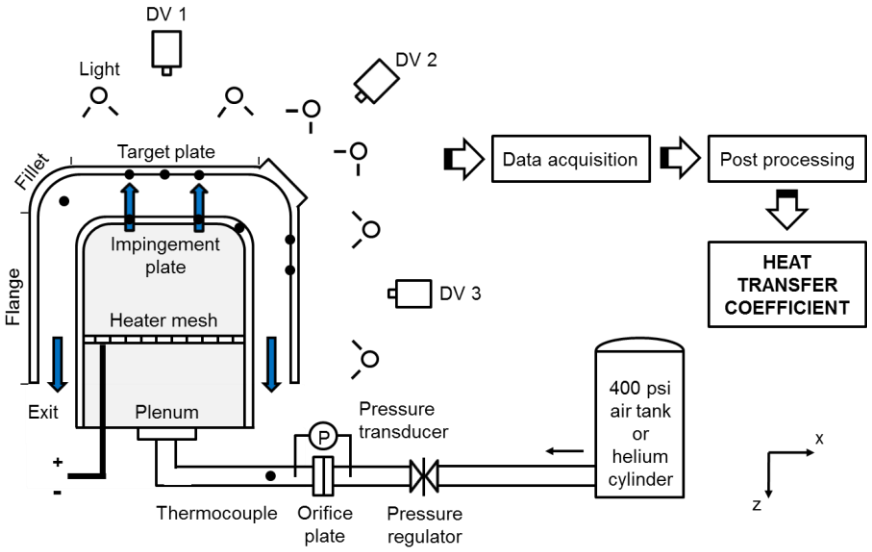

(a)

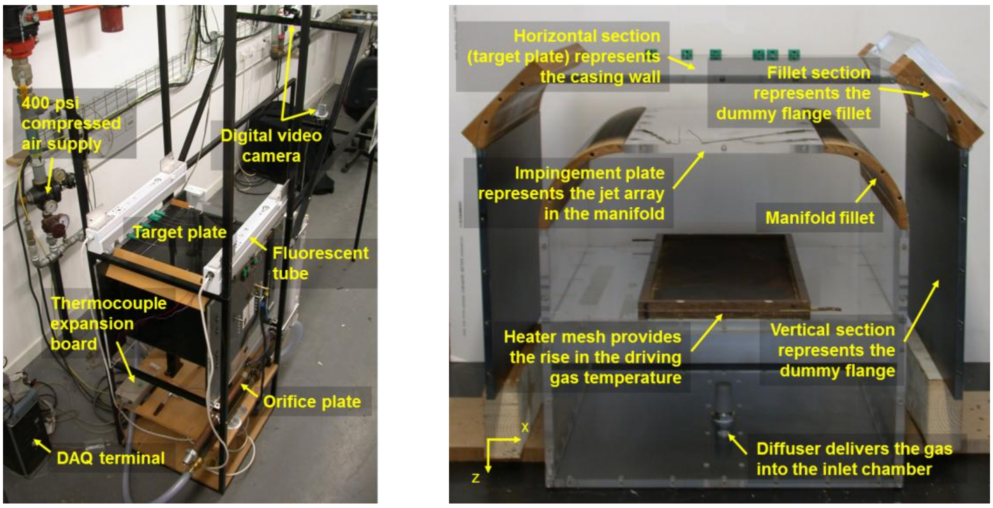

(b)

Figure 3.4 (a) Schematic diagrams of the main components of the external manifold test rig and (b) a photograph of the test section.

The working section as installed in the experimental rig is shown in **Figure 3.4**. Air is supplied to the inlet plenum is from a 400 psi compressed air supply, dropped to inlet conditions through a pressure regulator which is used to adjust the mass flow rate. This is measured using a 51 mm diameter BS1042 orifice meter, connected to HCX differential pressure transducers with ranges 0 - 100 mbar gauge and 0 - 350 mbar gauge.

A series of K-type thermocouples are locally mounted to collect surface and driving gas temperature data: six thermocouples cemented onto target plate and side wall record temperature underneath jets (used for the crystal calibration and local heat flux calculation) and three bead thermocouples pointing at the exit of jets record the driving gas temperature. Data acquisition is via a PC equipped with a 12 bit DAQ driven by Labview software. An expansion board with integral cold junction compensation is used to log pressure transducer channels and thermocouples near simultaneously.

Colour play exhibited by the liquid crystal during transient heat transfer test was recorded using three PAL digital cameras positioned to view the target plate, fillet and dummy wall simultaneously. The cameras were fixed at a constant distance by extension arms sufficiently far enough from each surface that a focused image could be achieved without distortion of the image. Diffused fluorescent light sources provided near uniform lighting on the surfaces with minimal reflections. An example of activated TLCs on the target surface can be seen in **Figure 3.5**.

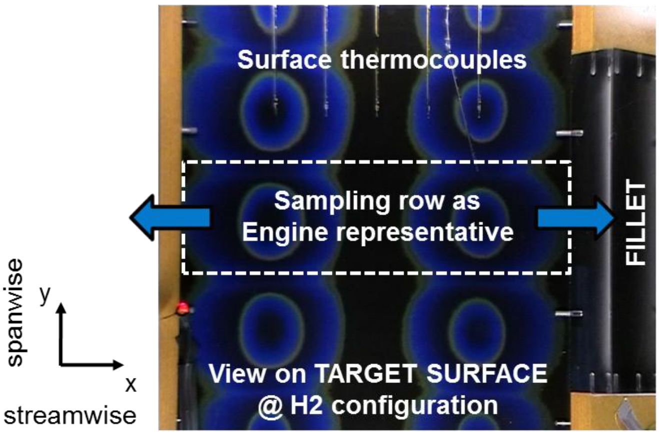

Figure 3.5 Typical liquid crystal activation during the transient test.

Power is supplied to the rig from a Drake 150kVA DC power supply using an upstream mesh heater. A MATLAB code developed by **McGilvray and Gillespie (2010)** was used for post-processing.

Experimental uncertainty was determined at each spatial location using a perturbation method proposed by **Moffat (1982)**. Here errors in the heat transfer coefficient are assessed by finding the partial derivative of the calculated solution with respect to each of the experimental variables. These equations may not be expressed explicitly in terms of *h,* instead numerical partial differentials with respect to each measurand are evaluated at typical operating conditions. i.e. Using the central difference method:

$$\left(\frac{\partial h}{\partial \chi_i}\right) = \frac{H(\chi_i + \delta\chi_i) - H(\chi_i - \delta\chi_i)}{2\delta\chi_i} \tag{3.13}$$

where χ_i represents the parameter of interest and $\delta\chi_i$ represents a small change in this parameter.

In transient narrow band liquid crystal experiments, the uncertainty in the experimental determination of *htc* can be broken into three different components: uncertainty in experimental measurements which feed into the calculation of *htc*; the uncertainty in matching the theoretical intensity history; the uncertainty due to the assumption of one-dimensional conduction in a semi-infinite plate. Possible measurands providing error in the output are: time (s), the material thermal product ($Jm^{-2}K^{-1}s^{-0.5}$), the initial gas temperature (^oC), the driving gas temperature (^oC) and finally any temperature shift in the liquid crystal vs intensity calibration (^oC) in the crystal calibration. The components are considered independent although this is not entirely the case, for example bias errors in the initial temperature and gas temperature will be common mode (and somewhat negating), but will not be common mode with the liquid crystal calibration. The effect of noise in the video signal and the discretization of the matrix of possible *htc* values is captured by using the full data analysis procedure with each measurand appropriately perturbated.

The expected error introduced by the uncertainty in each parameter was found by multiplying the local gradient by the expected error and then dividing by the initial heat transfer coefficient to form a dimensionless fractional error.

$$s_{h_i} = \left(\frac{\partial h}{\partial \chi_i}\right) \times \frac{\Delta \chi_i}{h} \tag{3.14}$$

A measure of the overall error is made by considering the root sum square (RSS) of the component errors. Thus the RSS error is given by:

$$S_h = \sqrt{\sum_{i=1}^{n} \left[\left(\frac{\partial h}{\partial \chi_i}\right) \frac{\Delta \chi_i}{h} \right]^2} \ . \tag{3.15}$$

Table 3.2 shows that the root sum square error in *htc* is under 7.3 % for the highest heat transfer coefficient. Note that the zero contribution to the experimental error caused by an offset in the time data is an artifice of the discrete steps in *htc* used in the global minimization procedure. This step size is also included as a measurement error in the analysis. The measurement error for the full range of heat transfer coefficient is close to this value but rises sharply close to the lowest *htc* measured, due to the low surface temperature response. A maximum error of 16 % is seen at the lowest heat transfer coefficient measured.

Table 3.2 Error contributions and overall uncertainty for the highest heat transfer coefficient level.

Measured parameter	Typical value	Measurement error	Error contribution htc_{highest}
t, (s)	30	± 0.04	0.0 %
Thermal product, ($Jm^{-2}K^{-1}s^{-0.5}$)	569	± 29	4.9 %
T_g, (^oC)	90	± 0.3	0.6 %
T_i, (^oC)	20	± 1	2.8 %
$T_{crystal}$, (^oC)	35	± 0.35	4.5 %
htc discretization	100 levels	± 0.5 %	0.5 %
RSS Error			7.3 %

As noted above there is a possible additional error associated with lateral conduction within the insulating substrate during the transient test. This is insignificant provided

$$\frac{\partial^2 q"}{\partial y^2} \ll \frac{\rho c}{k}\frac{q"}{2t} \ \ \& \ \ \frac{\partial^2 q"}{\partial z^2} \ll \frac{\rho c}{k}\frac{q"}{2t} \tag{3.16}$$

where *y* and *z* are the direction of the lateral axes. These were assessed once the full surface *htc* distribution was calculated. For all cases **Equation 3.16** was satisfied (LHS < RHS by two orders of magnitude) at all points on the surfaces.

3.3 Internal Casing Over-Tip Seal Segment Cavity

3.3.1 Over-Tip Seal Segment Cavity Geometry

Figure 3.6 shows the radial cross section of the hot side of the gas turbine modelled in the vicinity of the high pressure turbine. In the engine modelled, 24 seal segments are circumferentially mounted inside the engine casing via locating hooks. These form an annular shroud surrounding the blade tip which requires cooling, and this is fed from the passage labelled "Over-Tip Seal Segment Cavity" to contain cooling flows. For manufacturing reasons this cavity is formed by several components: the casing, the 24 NGV support rings, and the 24 seal segments. A flow of relatively hot, high pressure cooling air enters the *over-tip seal segment cavity* through a series of small diameter holes on the HP NGV support ring to cool the seal segments, and intentionally or otherwise, to heat the casing.

This flow exits mainly through the cooling passages leading to regions above the blade tip. However, there are a series of unpreventable secondary leakages through gaps between components. HP NGV leakage flows and casing hook leakage flows occur through circumferential disparities and leakage across strip seals. Understanding the effect of these leakage flows to the heat transfer is key to understanding the level of detail required in numerical modelling of this system.

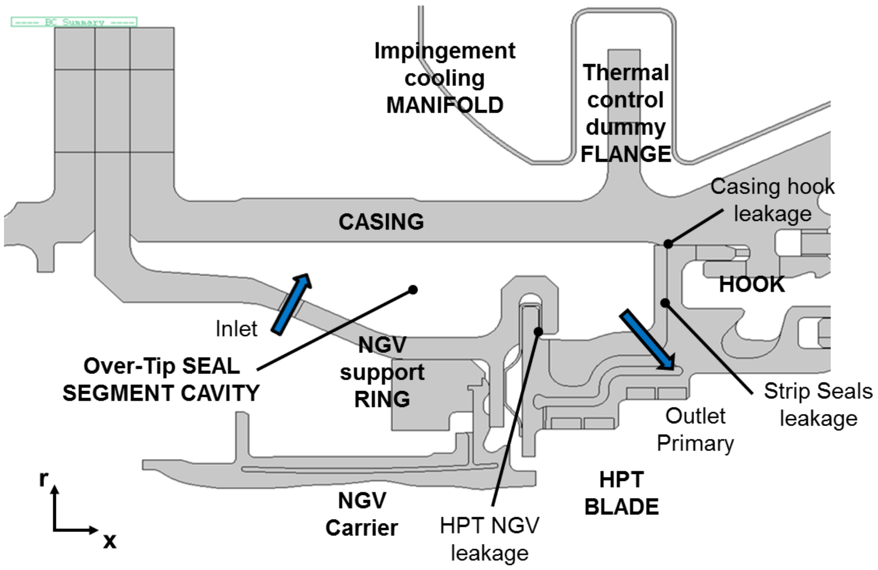

Figure 3.6 Internal Casing Over-Tip Seal Segment Cavity, adapted from (Rolls-Royce, 2011).

3.3.2 Development of Over-Tip Seal Segment Cavity Model

A schematic of the experimental setup used for this thesis is shown in **Figure 3.7 (a)**. The rig consists of a blower, a 51 mm diameter BS1042 orifice meter (not shown), an electrical heater mesh, a PAL type DV camera, a data acquisition system and the test section. Similar dimensional consideration was made as for the external impingement cooling system, however, in this case the primary restriction was the maximum Reynolds number that could be achieved while maintaining incompressible conditions in the test rig. As a result the test section was scaled up by 4.2 from the engine geometry with most of the most geometrical aspects of the seal segment modelled in the test rig. Simplification was made to the inlet plenum, representation of secondary leakage flow paths through HP NGV gap, casing hook gap and inter-segment gap, and primary outlet holes. A side view of the working section can be seen in **Figure 3.7 (b)**. Here it is apparent that all components except for those on the target surface were manufactured from Rohacell, an insulating material. The main target plate and side walls were manufactured from 10 mm thick Perspex.

The test rig allows secondary leakage flow to be opened or closed (simply by taping over exit holes using Kapton tape), allowing different leakage flow scenarios achievable in a real engine to be simulated. This enabled evaluation of the impact of the secondary leakage paths on heat transfer coefficient distributions over the entire internal surface of the casing, as classified in **Table 3.3**.

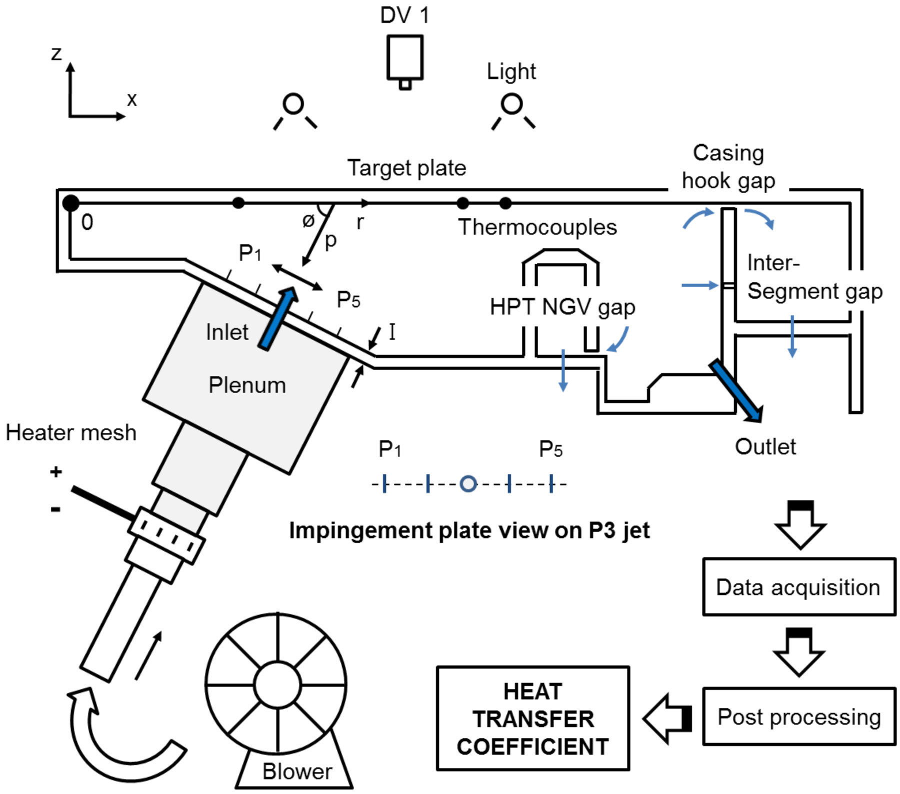

(a)

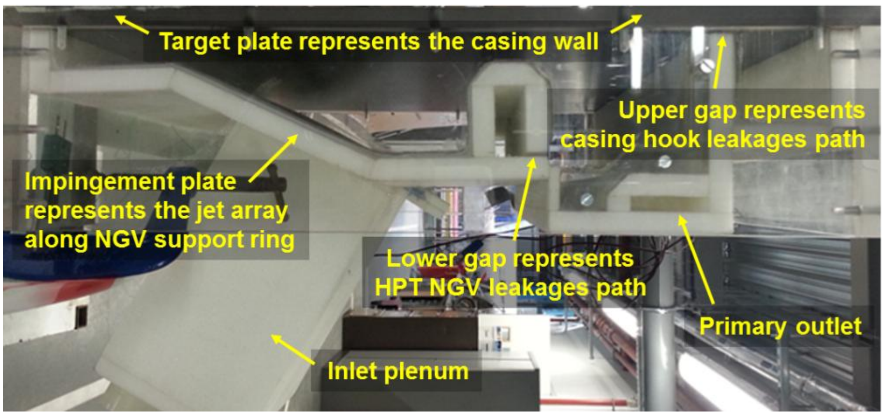

(b)

Figure 3.7 (a) Schematic diagrams of the main components of the seal segment cavity test rig and (b) a photograph of the test section.

Table 3.3 Test matrix for various leakage scenario tested.

Mode	Mode	Inlet	Outlet		
			Lower	Upper	Primary
P_4	**Exp-C**	Re_{jet} = 50,000	Open	Open	Open
	Exp-E		-	Open	Open
	Exp-G		Open	-	Open
	Exp-F		-	-	Open

The entry jet hole and the inlet plenum, are both at an angle of 65 degrees to the target surface, and can be moved along the impingement plate (positions P_1 to P_5), and thus provide various offsets, *p* (between impingement jet and target surface). Five different positions, can be tested to achieve optimum heat transfer level from a continuous clearance control point of view. **Table 3.4** shows the offset tests performed.

Table 3.4 Test matrix for various offset scenario tested.

Configuration	Re	*d* (mm)	*p*/*d*	*I*/*d*	Ø (degrees)
P_1	50,000	2.37	9.6	4.22	65
P_2			11.8		
P_3			14.45		
P_4			17.1		
P_5			18.91		

Note that as for the external cooling manifold, the target surface in the rig model is planar even though in the engine it is clearly a hoop of large radius. The inlet plenum was connected to a variable frequency blower which introduced air through regulated supply. A heater mesh situated upstream of the plenum provides a uniform temperature rise in the driving gas flow at the beginning of a test. Fast response gas thermocouples fixed on a nylon mesh recorded the gas temperature transient accurately, and also confirmed a uniformly heated stream. The target surface was coated with three narrow band liquid crystals, nominally at 30 ^{o}C, 35 ^{o}C and 40 ^{o}C respectively. Thin T-type surface foil thermocouples were fixed onto the surface prior to the crystals being sprayed onto the surface and a black ink backing was applied subsequently for better contrast. The colour display exhibited by the crystals is recorded using a DV camera, while other data are captured using a 16 bit National Instruments cDAQ system with 100 Hz resolution. The camera was fixed at a constant distance by extension arms far enough to provide focus images without distortion. Diffused fluorescent light sources provided near uniform lighting on the surface with minimal reflections. The temperature history available from the thermocouples are used as means of *insitu* calibration of the liquid crystals and also to allow direct point measurement of the local heat flux, allowing validation of the full surface technique. The heat transfer coefficient distributions were obtained by exactly the same technique as described for the external cooling experiments. Some example images from a single test are shown in **Figure 3.8**.

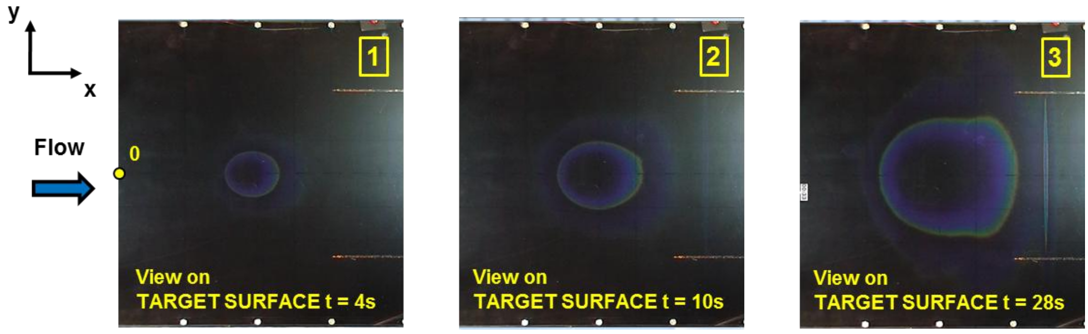

Figure 3.8 Still images of Liquid Crystal colour play, Over-tip segment cavity rig.

It should be noted that unlike for the external cooling rig, the demonstrable Reynolds number range is limited for this test rig to Re_{jet} = 50,000. This is because the very high density at engine cruise and take-off conditions (up to ~20 kg/m^3) leads to extremely high Reynolds number which would equate to compressible flow at atmospheric conditions. Thus, only the idle equivalent condition has been tested to provide validation data. The experimental programme was supported by a parallel CFD campaign in both at rig and engine scale (see Chapter 7). Further simulations not experimentally tested allowed the extension of the study to the high density, high velocity flow fields.

3.4 Summary

The experimental designs used to generate local heat transfer coefficient distributions using the transient liquid crystal technique for the present heat transfer research are summarised in this chapter. First of all, the external impingement cooling manifold is reviewed together with the development of a large scale test rig for the baseline H2 middle section of the cooling manifold configuration. The test rig employed was chosen through the dimensional analysis allowing the appropriate scaling of flow parameters from the engine to the rig geometry. The planar rig consists of two streamwise rows by five spanwise rows of inline array. The data from the middle row which are insignificantly affected by the presence of the spanwise artificial endwalls are considered engine representative.

For the internal over-tip seal segment cavity heat transfer, an expanded 4.2 times scale test rig was built. The developed design represents one of 24 sectors of the annular hot-side seal segment system including the representation of various small exit leakage paths. The inlet circular jet hole in the rig is modular, thereby allowing the impact of different inlet locations to be measured.

Overall uncertainty of measured heat transfer coefficient data using these test rigs has been shown to lie between 7.3 % and 16 %.

Chapter 4 Numerical Analysis of Turbine Casing Cooling system

In this chapter, descriptions of the numerical analysis employed for heat transfer characterisation of the external and internal casing are presented. Extensive use is made of a combined aero-thermal CFD and thermo-mechanical FE modelling technique to understand the thermo-mechanical behaviour of the casing in the presence of an external casing impingement cooling scheme. Insight into the flow field behaviour from the CFD studies is helpful to improve understanding of the drivers of convective heat transfer. Finite element modelling has been used to link the external heat transfer coefficient distributions generated for a wide range of cooling geometries to the displacement of the internal casing at engine representative operating conditions under steady running.

4.1 External Impingement Cooling Manifold Model

4.1.1 Aerothermal CFD Model

Geometry. Numerical simulations were performed to establish both flow fields and detailed application of *htc* distributions over the external casing at engine scale. The baseline computational domain is shown in **Figure 4.1** and consists of a half row of axially spaced impingement arrays of jets extending along the flange wall to the far downstream region. It closely represents the baseline engine configuration **Figure 3.3** as there are no confining circumferential side walls. Direct comparison can be made to the middle row of five spanwise rows modelled in the experimental validation (see **Figure 3.5**). Symmetry conditions were applied on the faces representing the circumferential direction, though as the radius of curvature of the target surface is very large compared to the impingement hole diameter a planar CFD model was used, after **Bunker and Metzger (1990)**.

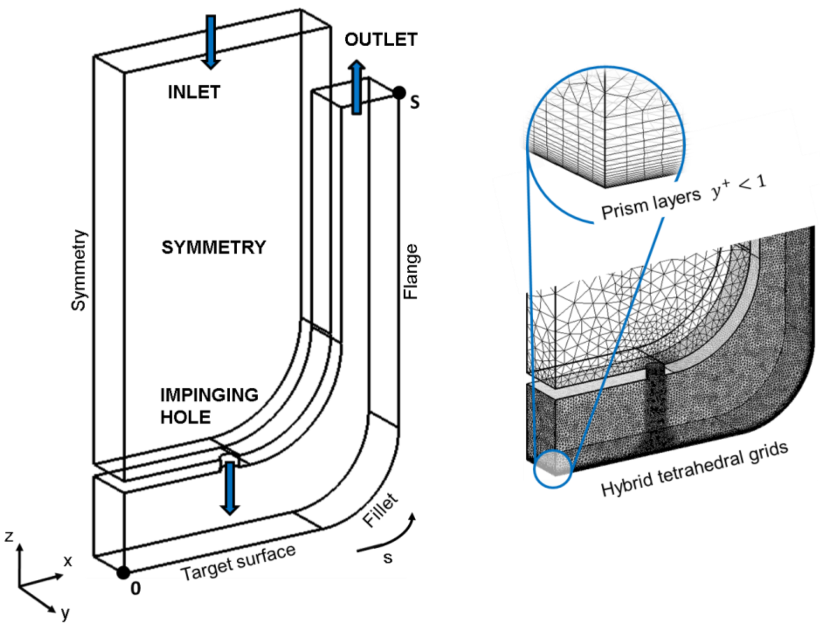

Figure 4.1 Computational domain for standalone external casing heat transfer prediction.

In addition to the baseline *H2* configuration, a range of cooling arrangements was created to determine the best embodiment of an impingement array to achieve effective clearance control. The geometric changes are limited by manufacturing constraints and a desire to maintain the existing flow manifold. The casing impingement cooling geometries investigated are shown in **Figure 4.2** and **Table 4.1**, including details of geometric scaling (x/d, y/d, z/d, and I/d) for streamwise pitch, spanwise pitch, manifold offset and manifold thickness; summarised as:

- Baseline - labelled *H2*: two jets normal to the target plate;
- Jet-to-jet pitch - labelled *Xp1*, *Xp2*, *Xp3*, *Xp4*: changing hole position in the streamwise direction whilst the number of jets in the row is kept at two; the pitch increases for *Xp1* through to *Xp4*;
- Number of jets - labelled *H2, H3, H4, H5*: the number of jets to the target plate is increased in the streamwise row, while the total area remains constant, through a reduction in diameter;
- Inline and staggered arrays of jets - labelled *H3FI*, *H3CI*, *H5CI* and also *H3FS*, *H3CS*, *H5CS*: inline and staggered jet arrays, created by changing alternate hole positions by half a circumferential pitch. These geometries include impingement onto the fillet region of the dummy flanges.
- Arrays of jets on dummy flanges - labelled *H2C*, *H2W1*, *H2W2*, *H2W3*: two jets impinging to the fillet radii or the side face of the dummy flanges.

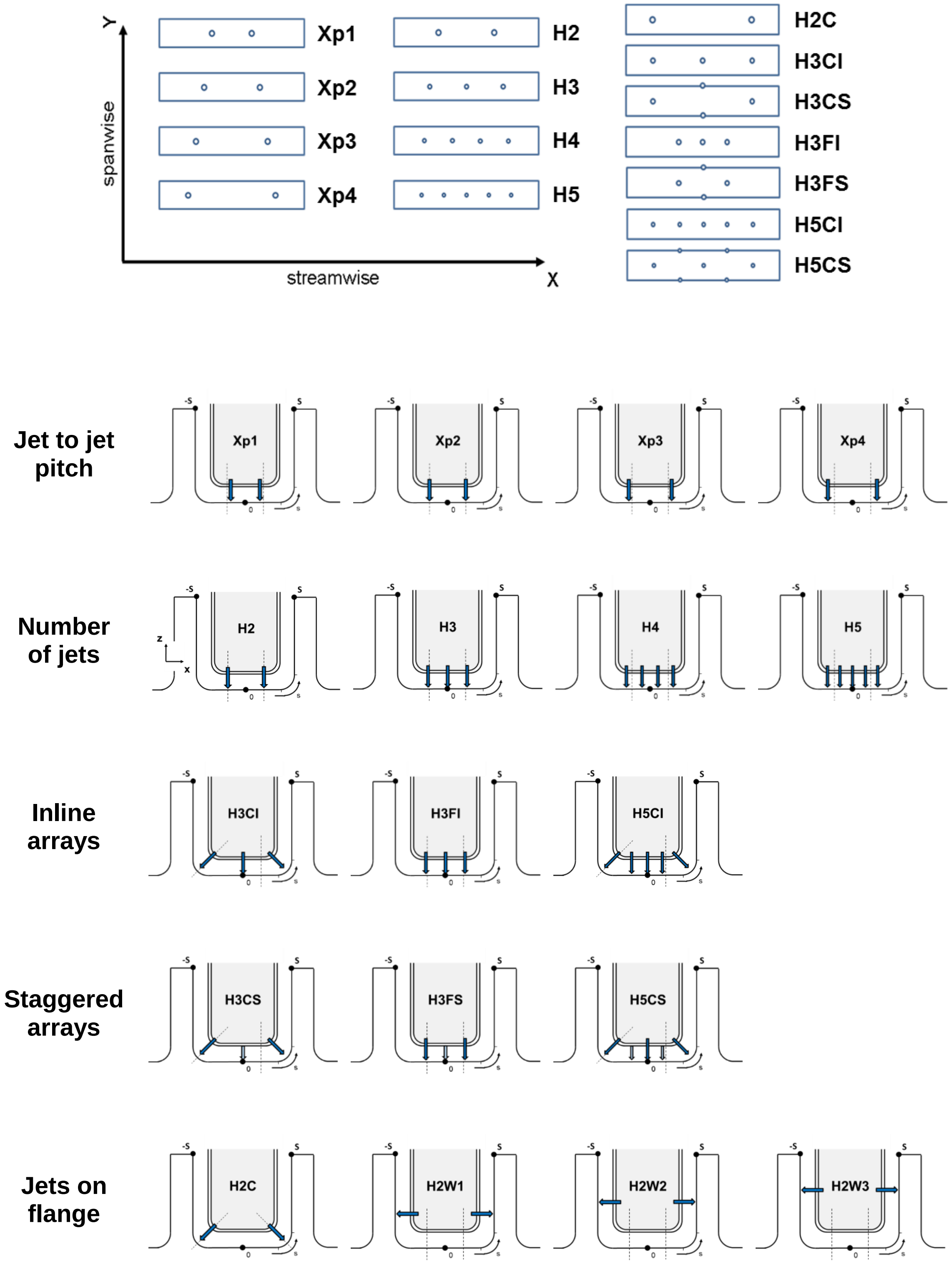

Figure 4.2 Variation in casing impingement cooling geometries investigated.

Note that for the case of *H3CI*/*CS* and *H5CI*/*CS* the pitch of the middle 3 rows is identical to *H5*, however, the outermost holes are placed to point directly at the centre of the external fillet; thus there are no values for these cases in **Table 4.1**.

Table 4.1 Geometrical details of cooling arrangements investigated.

		number of jets in array	*d*	*x*/*d*	*y*/*d*	*z*/*d*	*I*/*d*
Jet to jet pitch	**Xp1**	2	1.21	8.3	5.2	4	0.6
	Xp2	2	1.21	11.6	5.2	4	0.6
	Xp3	2	1.21	14.9	5.2	4	0.6
	Xp4	2	1.21	18.2	5.2	4.5	0.6
Number of jets	**H2**	2	1.21	11.6	5.2	4	0.6
	H3	3	0.99	9.4	6.4	4.9	0.7
	H4	4	0.86	8.2	7.4	5.6	0.8
	H5	5	0.77	7.4	8.2	6.3	0.9
Inline arrays	**H3CI**	3	0.99	7.1	6.4	4.9	0.7
	H3FI	3	0.99	-	6.4	4.9	0.7
	H5CI	5	0.77	-	8.2	6.3	0.9
Staggered arrays	**H3CS**	3	0.99	7.1	6.4	4.9	0.7
	H3FS	3	0.77	-	6.4	4.9	0.7
	H5CS	5	0.77	-	8.2	6.3	0.9
Jets on dummy flange	**H2C**	2	1.21	-	5.2	4	0.6
	H2W1	2	1.21	-	5.2	4	0.6
	H2W2	2	1.21	-	5.2	4	0.6
	H2W3	2	1.21	-	5.2	4	0.6

A robust assembly tolerance was assumed for the manifold, and the standoff distance to target surface is constrained to be four times that of the baseline *H2* diameter for all simulations. The total area of impingement jet holes is constrained; thus the jet diameter is decreased uniformly when the number of jets in a configuration is increased. Sensibly the jet Reynolds number decreases as the incoming mass flow rate is unchanged at each engine condition as shown in **Table 4.2**. It should be also noted that no variation in circumferential spacing has been examined in this study.

Table 4.2 Lists of selected operating conditions and jet Reynolds numbers for the variation in number of jets in numerical calculations.

Number of jet holes	Total area of jet holes	Operating Condition				
		OP0	**OP1**	**OP2**	**OP3**	**OP4**
2	constrained	10000	5710	2360	2120	540
3		8163	4595	1898	1730	440
4		7058	3974	1641	1496	381
5		6315	3555	1469	1338	341
Total coolant mass flow rates in FE casing model, kg/s		0.354	0.172	0.075	0.071	0.017

Boundary Conditions. All the walls of the manifold were considered adiabatic, which is representative of the steady state condition. The target surface (external casing) was set to be isothermal and 50 K higher than the incoming gas. The working fluid was taken to be air which was treated as an ideal gas. A constant mass flow rate inlet boundary condition was set. While this does not necessarily result in a constant feed pressure, because of the low and essentially constant discharge coefficient in the jets the differences are very small. A pressure boundary condition was imposed at the outlet.

Solver and Turbulence Models. Reynolds Averaged Navier Stokes solutions were used in the current study in spite of their known difficulties in resolving some features of impingement flow. The choice was made based on the speed of solution and the likely correct comparison between alternative impingement configurations.

The ANSYS Fluent 12.0 solver was employed in the current study. The SIMPLE scheme for pressure-velocity coupling and a second order upwind scheme for spatial discretization were used. Several different steady-RANS models available in Fluent were implemented to investigate the sensitivity of the predicted local *htc* distribution to turbulence model. These were the realizable *k-ε* model with enhanced wall treatment, the Shear Stress Transport *k-ω* model with low Re corrections and the EARSM models.

Note that the turbulence models were chosen due to their general application previous impingement cooling studies by **Zukerman and Neil (2004)**. It should be noted that the *htc* is calculated from the formula:

$$htc = \frac{q''}{T_{\mathrm{jet}} - T_{\mathrm{surf}}} \qquad (4.3)$$

using the manifold inlet temperature as the reference temperature.

Computational Grids. Hybrid tetrahedral grids consisting of a set of 8 or more layers of prism elements with a 1.2 ratio increase in height from the target surface and tetrahedral elements in the interior volumes of the manifold with fine jet hole resolution were generated to obtain accurate flow and thermal boundary layer data using ANSYS ICEM version 12.0. A mesh sensitivity study was performed by adjusting near wall grids which interfaced with a high grid density in the main flow passage. **Figure 4.3** shows a sample computed result showing *htc* along the passage centreline and span-averaged for the case of the baseline geometry *H2*. The results show the numerical results were essentially independent of the grid when the non-dimensional wall distance for the first cell on the target surface y^+, given by **Equation 4.4**, was 1.5 and below.

$$y^+ = \frac{u_\tau \Delta y}{\nu} \qquad (4.4)$$

where u_τ and ν represent the shear stress velocity and the kinetic viscosity of the fluid and Δy is the wall distance. With higher values of y^+, a region of flow separation near the dummy flange fillet was poorly resolved. Thus y^+ was kept below 1.0 for all simulations. Higher grid resolution was required at higher Reynolds numbers (jet velocities) to achieve the same reported low y^+ values. The total size of mesh required depends on the Reynolds numbers and the cooling arrangement, but all cases lay between 1.3 and 1.8 million cells. The convergence of the simulations was judged based on scaled residuals all of which were required to be below a value of 1×10^{-5}. The solution was only considered to be converged if the integral of the heat transfer coefficient over the target casing surface was also steady at that condition. Furthermore, manual checks were conducted to ensure that an overall mass flux imbalance of less than 0.01 % was achieved.

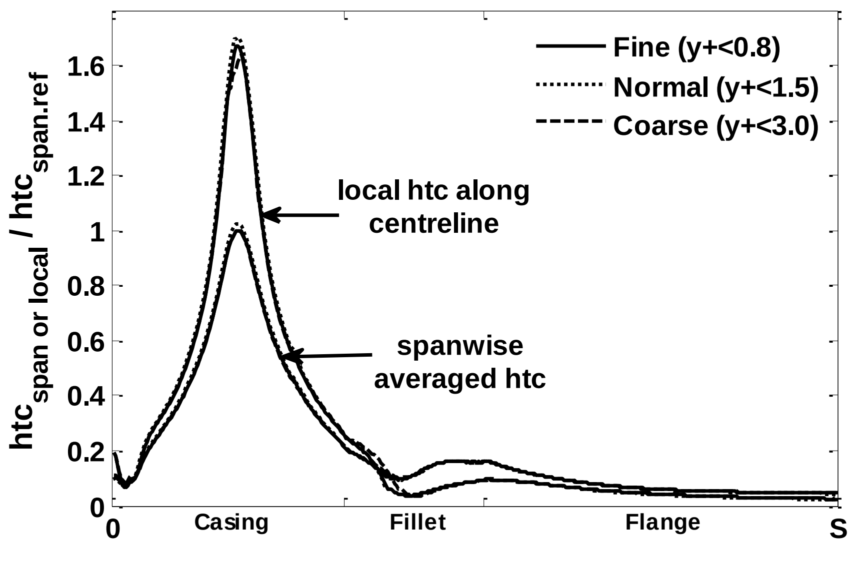

Figure 4.3 Comparison of *H2* solutions showing near grid independent solutions achieved for y^+ < 1.5.

4.1.2 Thermo-Mechanical FE Model for Casing Contraction

The casing contraction capability studies are conducted in the prescribed external casing cooling scheme determined from the CFD analysis and imposed in the FEM using the MATLAB interface within the COMSOL code. The direct PARDISO algorithm is used to solve temperature, stress and displacement for the linear static problem considered. The setup is as described below.

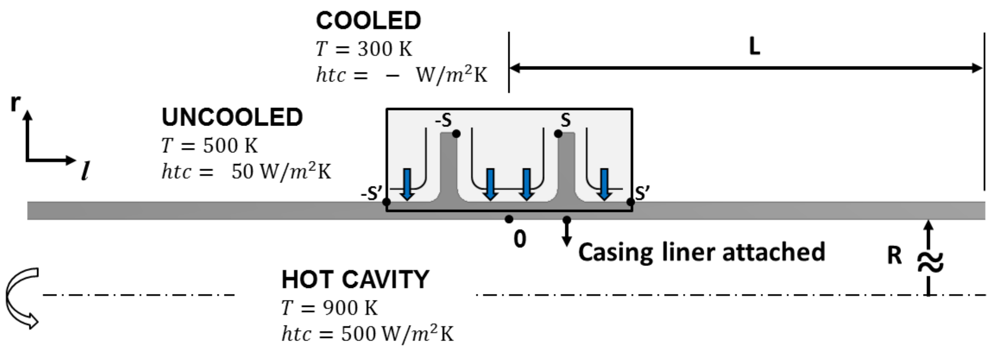

Figure 4.4 Idealised representation of casing FE model.

Geometry. The thermo-mechanical model uses a 2-D axisymmetric cylindrical geometry incorporating the two thermal control dummy flanges representing an axially long casing (L = 400 mm). It is known that the engine casing section near high and intermediate pressure turbine blade is usually cylindrical or conical in shape. The casing radius considered has radius, R = 0.446 m, and thickness th = 0.006 m. The position of a cooling feed from three manifolds in the middle section around the external casing is depicted in **Figure 4.4.** The chosen casing liner attachment point (using an internal hook) is shown directly under one of the web and is used as the reference point from which the casing thermal closure is assessed. The key geometric parameters are summarised in **Table 4.4**.

Table 4.3 Geometrical details of an idealized engine casing representation in mm.

R_{casing}	$2L$	th	H	R_{fillet}	N_{width}	x_{hook}	s'
445.95	800	6	25	5.03	6	21.6	42.4

Boundary Conditions. The *htc* distributions extracted from CFD are mapped across the cooling region (-s` to +s`) symmetrically and used as thermal boundary conditions at engine scale. Over the remainder of the external area a typical ventilation flow for the fire zone of 50 W/m^2K at a nominal temperature of T = 500 K is applied. The internal *htc* is set to a uniform value of 500 W/m^2K with a driving hot gas temperature of 900 K as per a typical high pressure turbine over-tip seal segment cavity level of heating at cruise. While it is recognised that this value will also change over the range of engine operating conditions, a single value is employed to allow the effect of the impingement system to be assessed. The system is convectively dominated and any conduction paths to attached components and radiative heat transfer which accounts for 2.5 - 3 % of the total heat flux are not modelled here. It is constrained mechanically such that there is no rotation of the casing at its extremities (l = L), and axially to zero at one end, otherwise the model is radially and axially free to move. This approximates the constraint imposed by other structural installations in a real engine. From the resulting temperature distribution the corresponding thermal displacement profiles of the casing are found.

Computational Grids. The number of degrees of freedom solved for all cases was 7.9 x 10^3 with a typical 6-node triangular grid consisting of 1.2 x 10^3 elements at 0.97 average symmetric quality. An increase of mesh size by a factor of 1.2 was shown to have negligible influence on the metal temperature, particularly under the cooling section where the temperature gradients recorded are highest, confirming that grid independence solution had been achieved. Material properties of the casing supplied by Rolls-Royce were used assuming temperature independent properties as shown in **Table 4.4**.

Table 4.4 Material properties of the casing applied within the FEM solver.

Properties	Symbol	Value
Thermal expansion coefficient	α	$15.0 \times 10^{6}\ K^{-1}$
Thermal conductivity	k	19.66 W/m K
Poisson’s ratio	ν	0.365
Specific heat capacity	c	537 J/kg K

4.2 Over-Tip Seal Segment Cavity Model

A two stage CFD campaign was employed to model the heat transfer of the casing in both the rig and engine scale segment cavity. The rig scale CFD model supported the experimental programme by confirming how the correct flow distribution and heat loads can best be modelled by the choice of an appropriate turbulence model resulting in a close match of the experimental data set. Further simulations for high velocity flow cases, not experimentally covered, were performed at engine representative scale using the consistent strategy of modelling multiple small sections of the impingement cooling cavity. Note that here all flow regimes at both engine and model scale are essentially incompressible.

4.2.1 Aerothermal CFD Model at Rig Scale

Geometry. The computational domain and the related boundary conditions are depicted in **Figure 4.5**. The domain confidently reproduces the cavity geometry tested including a horizontal discrete gap (referring casing gap) between the target surface and the downstream side set-back wall and a leakage path that models the part where NGV carrier connected. Five geometries, each having different jet hole position along the impingement plate, were considered and created (see **Table 3.4**). A flow enters the cavity through a hole and exits through the primary outlet and the lower and upper gaps.

Boundary Conditions. The working fluid was taken to be air (treated as an ideal gas). The inlet conditions were taken from the experimental case being modelled: an inlet mass flow rate and inlet temperature were set. A constant pressure boundary condition was imposed at each atmospheric outlet. In order to replicate the different exit flows in the measurement, the outlet condition was amended for each case (see **Table 3.3**). All walls were considered adiabatic with the exception of the target surface which was set to be isothermal at the measured initial wall temperature.

Solver and Turbulence Models. All simulations were conducted in the commercial code Fluent using the segregated solver with implicit equations; the SIMPLE method for pressure-velocity coupling; the second-order upwinding scheme. The expected turbulent flow in the impingement cooling system was modelled using two alternative turbulence models: the realizable k-ε model with enhanced wall functions and the Shear Stress Transport k-ω model with low Re correction.

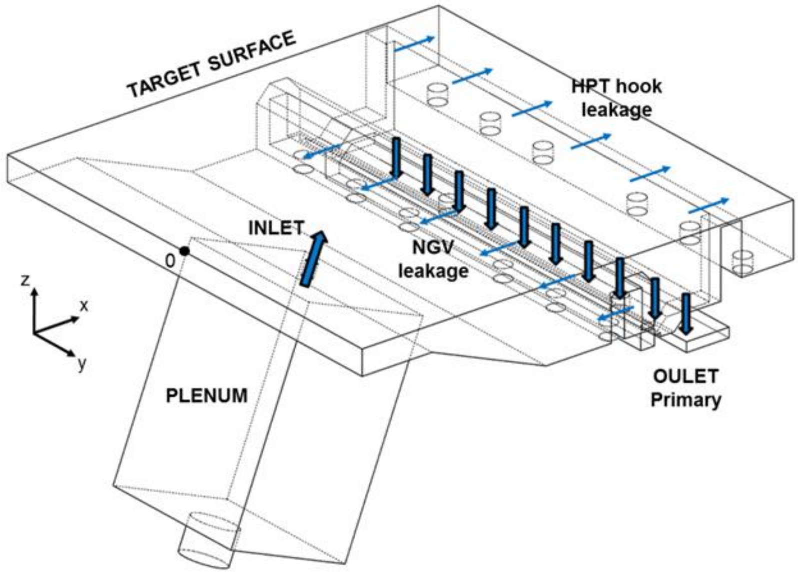

(a)

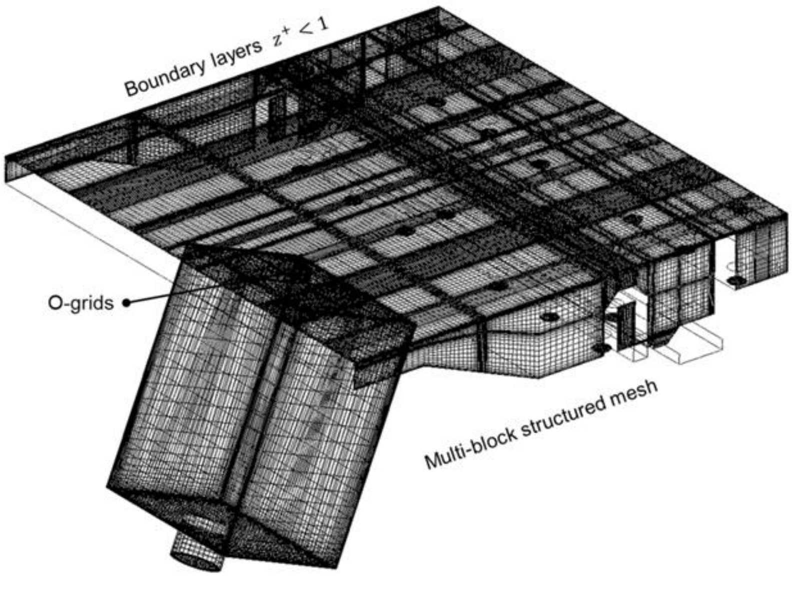

(b)

Figure 4.5 (a) Computational domain and (b) grids for over segment cavity heat transfer prediction at rig scale.

Computational Grids. A structured hexahedral mesh was generated in the domain by means of ICEM CFD multi-block strategies with fine jet hole resolution controlled by the density of the C-grids (half O-grids) and refinement layers near the impingement target surface to obtain accurate thermal boundary layer data. A mesh sensitivity analysis was conducted to show grid independence of the solutions. The total size of mesh was 8.6 million cells segregated into 3658 blocks. Convergence criteria based on the residuals of mass flow rate, velocity components, turbulence components and energy equation were set to be near or below a value of 1×10^{-4}, and manual checks were conducted to ensure that these were steady at that value.

4.2.2 Aerothermal CFD Model at Engine Scale

Geometry. At engine scale**,** the computational domain of the seal segment cavity (see **Figure 4.6**) corresponds to a 7.5 degree circumferential sector above the high pressure turbine of the engine. This includes a half row of the inlet impingement array of jets (24 holes in total). The midplane where the half circular jet exists is set to be a symmetry plane, as is the remaining axial - radial plane.

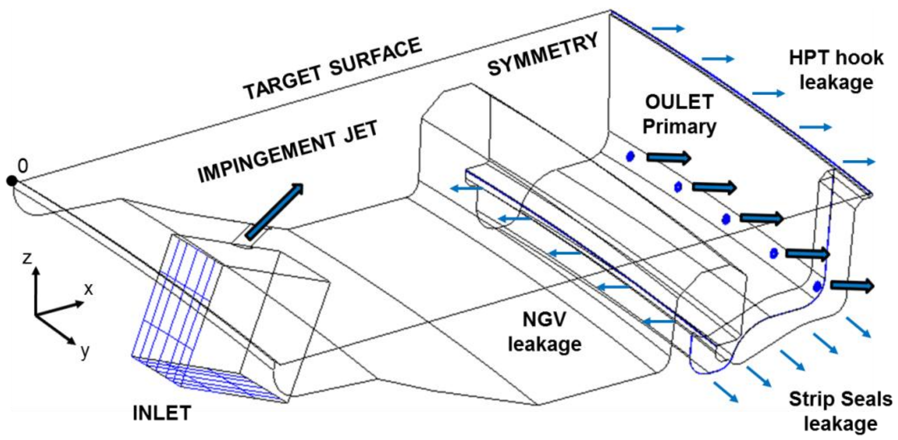

Figure 4.6 Computational domain for over segment cavity heat transfer prediction at engine scale.

Boundary Conditions. All the walls of the seal segment were considered adiabatic with exception of the target surface (inner side of the casing) which was set to be isothermal and 50 K higher than the incoming gas. The working fluid was taken to be air (treated as an ideal gas). Constant inlet mass flow rate and inlet temperature were set. Pressure boundary conditions were imposed at each outlet with targeted mass flow rates. The sensitivity of the local heat transfer coefficient distributions to the different outlet conditions was studied by changing each outlet boundary condition.

Table 4.5 shows the mass flow rate distributions applied. Symmetry boundary conditions were applied on the faces representing the circumferential direction.

Table 4.5 Mass flow rates in kg/s (or percentage of flow distribution, %) at an inlet and outlets of seal segment cavity simulated.

Mode	T_{in}	$\dot{m}_{in}$	$\dot{m}_{out}$ - kg/s or **(%)**			
			HP NGV leakage	Strip seals leakage	HPT hook leakage	Primary
Idle-A	495 K	0.0028 **(100)**	0.000218 **(7.8)**	0.000042 **(1.5)**	0.000910 **(32.5)**	0.001630 **(58.2)**
Idle-F			-	-	-	0.0028 **(100)**
Cruise-A	777 K	0.0076 **(100)**	0.001 **(13.1)**	0.00004 **(1.1)**	0.00232 **(30.6)**	0.004398 **(57.9)**
Cruise-B			-	0.000091 **(1.2)**	0.002673 **(35.2)**	0.004836 **(63.6)**
Cruise-C			0.001011 **(13.3)**	-	0.002345 **(30.9)**	0.004244 **(55.8)**
Cruise-D			0.001440 **(18.9)**	0.000114 **(1.5)**	-	0.006046 **(79.6)**
Cruise-E			-	-	0.002704 **(35.6)**	0.004896 **(64.4)**
Cruise-F			-	-	-	0.0076 **(100)**
MTO-A	939 K	0.0202 **(100)**	0.004099 **(20.3)**	0.000189 **(0.9)**	0.005711 **(28.3)**	0.010200 **(50.5)**
MTO-F			-	-	-	0.0202 **(100)**

Solver and Turbulence Models. Following on from the external manifold studies a decision was made to use the realizable k-ε turbulence model with enhanced wall functions for the present study.

Computational Grids. Considerable difficulty was encountered in generating a useable, high fidelity mesh for this geometry. The cavity is spatially discretized with tetrahedral elements and a set 18 or more layers of prism cells, resulting in a y^+ less than 4.0 on the target surface where a near wall treatment was required. The cell growth ratio was set as 1.2 for smooth transition of the thermal boundary layer. It was checked that there was no sudden change in cell volume between the last prism elements and its tetrahedral counterpart. Great attention was made to ensure good quality of mesh throughout the domain. In particular, the regions near inlet and outlet holes and the vanishingly small leakage paths were given high density elements.

A mesh sensitivity analysis was carried out to confirm grid independence of the solutions. The total size of mesh required depends on the incoming flow condition, but all cases lay between 13 and 14 million elements. The convergence was considered to be achieved based on scaled residuals of below 1×10^{-4} (and exceptionally below 1×10^{-6} for the energy residual), with both mass flow rate and *htc* distributions on the target surface which were monitored throughout the calculations showing no fluctuation with further iteration. Manual checks were also conducted to ensure that these were steady at that value and an overall mass flux imbalance of less than 0.01 % was achieved.

4.3 Summary

Numerical models were created for the external cooling manifold, an idealised engine casing and the over-tip cooling segment cavity. Mesh sensitivity studies confirmed that the mesh size was sufficient to generate accurate heat transfer coefficient distribution predictions for use in the analysis of the thermal control system. The results and discussion of the computational model are presented in the following chapters.

Chapter 5 The Effect of External Casing Impingement Jet Heat Transfer on Casing Contraction

The results of computational modelling of the external cooling system and experimental validation of the heat transfer coefficient distribution on the external surface of the casing are presented in this chapter. Full local heat transfer coefficient distributions under a range of external cooling manifold impinging arrays are presented together with the associated casing temperature distributions, and casing contraction. The data are first presented at fixed manifold to casing offset, for a range of impingement cooling arrangements. The engine casing closure is presented. The effect of changing manifold to casing offset must be understood to allow build tolerance to be specified: this is next presented. Finally, the flow in the system can be modulated to match the closure at different engine operating conditions, the relationship between thermal closure and coolant mass flow rate are predicted and reported.

5.1 Heat Transfer Characteristics of Impingement Cooling Manifold

In this section the results of an experimental study of the baseline cooling configuration are first reported. The equivalent computational studies are then compared to these data to find the most appropriate turbulence model for the remaining modelling. Subsequently a wide range of cooling configurations are explored using a consistent modelling technique.

5.1.1 Experimental Data Comparison and Validation

Figure 5.1 shows a full normalised *htc* map representing the casing walls for the measurement carried out at an average jet Reynolds number of Re = 6000. As the purpose of the experimental test was to validate the CFD, the reference *htc* used for normalisation is the peak value of local *htc* for the baseline *H2* cooling arrangement with the manifold standoff distance to jet diameter ratio of $z/d = 4$ as predicted by the CFD study using the realizable k-ε results at the equivalent operating condition at OP1 (see **Table 4.2**) where Re = 5710 (95.2 % of the experimental Re number). The value used for normalisation at engine scale $htc_{\text{ref, engine}}$ = 2816 W/m^{2}K at engine operating condition, OP1, the equivalent Nusselt number is 136.3, and as all rig scale simulations are conducted at the same temperature, this single value can again be used to scale the normalised data to Nusselt number. For all spanwise, patch or overall area averaged *htc* comparisons the same reference data set is used ($htc_{\text{span.ref}}$ = 1497 W/m^{2}K and $htc_{\text{avg.ref}}$ = 294 W/m^{2}K).

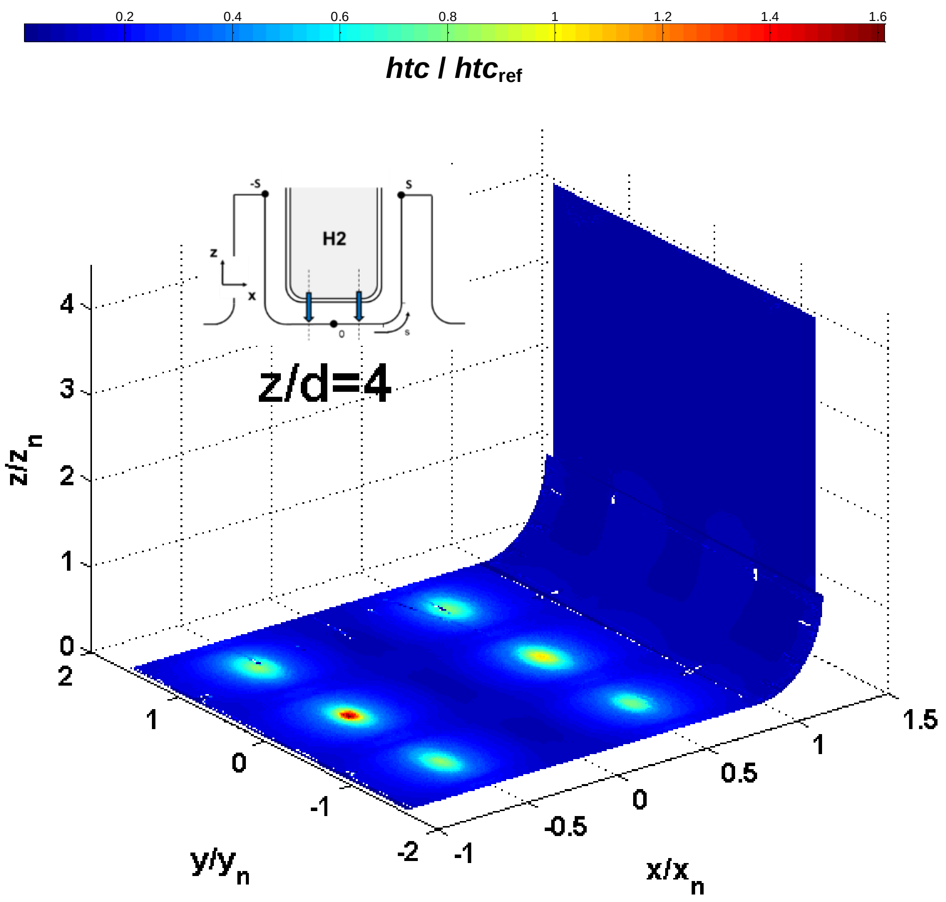

Figure 5.1 Local *htc* / *htc*$_{\text{ref (= H2 } z/d\text{=4.peak.span.realizable k-}\varepsilon\text{.OP1)}}$ distributions, experimental case Re = 6000, equivalent to OP1 in Table 4.2.

All measured and predicted *htc* distributions presented in this chapter can be scaled to engine conditions using the standard convective relationship,

$$htc_{(e)} = \frac{\mathrm{Nu}\, k_e}{d_e} = \frac{htc_m\, d_m}{k_m}\,\frac{k_e}{d_e}$$

so from the local normalised value $\frac{htc_m}{htc_{ref,model}}$ to scale to an arbitrary operating point OP (5.1)

$$htc_{(e)} = \frac{htc_m}{htc_{ref,m}} \times htc_{ref,engine} \times \frac{k_{\mathrm{e,OP}}}{k_{\mathrm{e,OP1}}}$$

This allows the thermo-mechanical model to be used at engine scale.

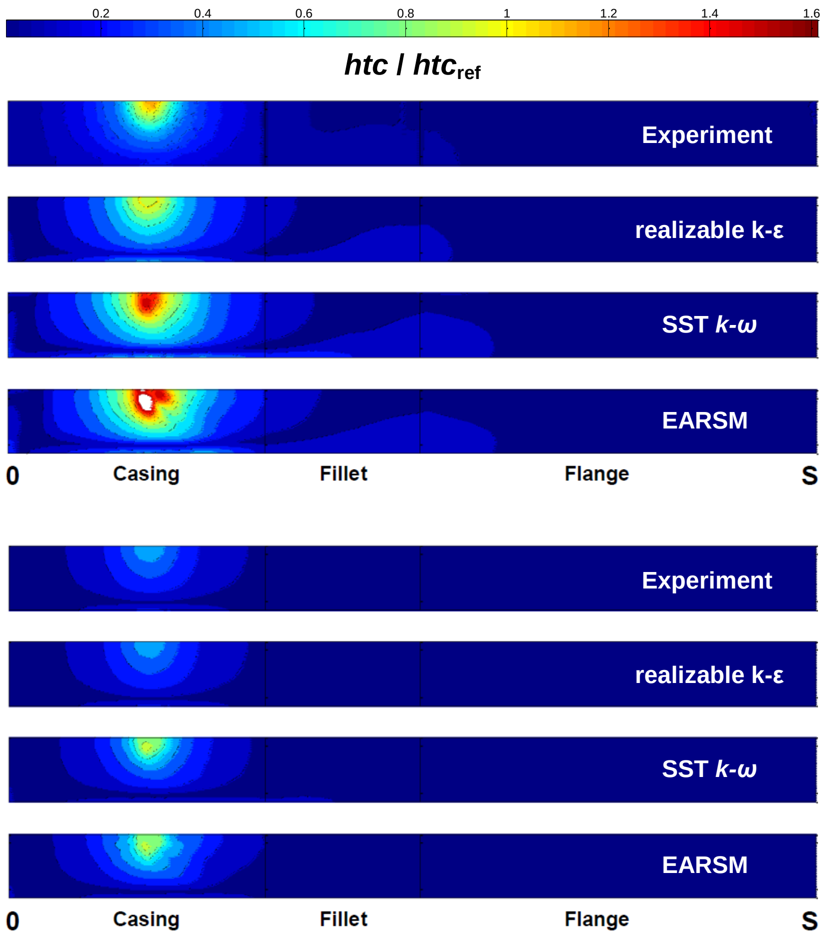

Figure 5.2 Local *htc* / *htc*$_{ref}$ (= H2 z/d=4.peak.span.realizable k-ε.OP1) distributions with different turbulence models employed at OP1 and OP2.

The experimental result in **Figure 5.1** shows typical features of an impingement cooling system with high heat transfer directly under the jets, and in the region of wall jet acceleration. Between the jets in the spanwise direction a feature common in confined impingement, enhancement caused by jet upwash, and reimpingement of a secondary flow is observed between spanwise jets. Here the row pitch (y/d = 5.2) is lower than in the streamwise direction (x/d = 11.7). A striking feature of the flow is the low *htc* directly downstream of the jet axis in the fillet region. This is caused by flow separation and recirculation. The spent flow from neighbouring wall jets forms an upwash jet which is highly turbulated and turns away from the target surface. This swirling flow is initially confined to a region near the impingement holes in the channel, but travels across this surface reimpinging onto the target surface in the fillet region half way between the spanwise rows of holes near the root of the side wall, promoting higher heat transfer which is maintained in the streamwise direction all the way to the exit.

A comparison of the steady-state normalised heat transfer coefficient distributions using three different turbulence model simulations is presented in **Figure 5.2** for the *H2* configuration at the OP1 (or Re = 5710) condition. Numerical results closely represent the central spanwise row of the experimental data.

While the general pattern is similar to the experimental data there are notable differences. First, a consistently lower peak *htc* underneath the jet is seen in the experiment compared to all numerical simulations performed except that using the k-ε turbulence model. Moving axially downstream from the jet axis the CFD results show a local reduction in heat transfer over the fillet area. This appears to be caused by later reattachment of the spent flow from the upwash onto the dummy flange surface compared to the experimental data. Although these areas of *htc* are lower, they cover the majority of the dummy flange and thus affect the overall clearance achieved. The level of over prediction depends on the turbulence model: both the SST k-ω and EARSM based calculation produces 20 - 30 % over prediction, while the realizable k-ε predict averaged *htc* levels close to the experimental measurement.

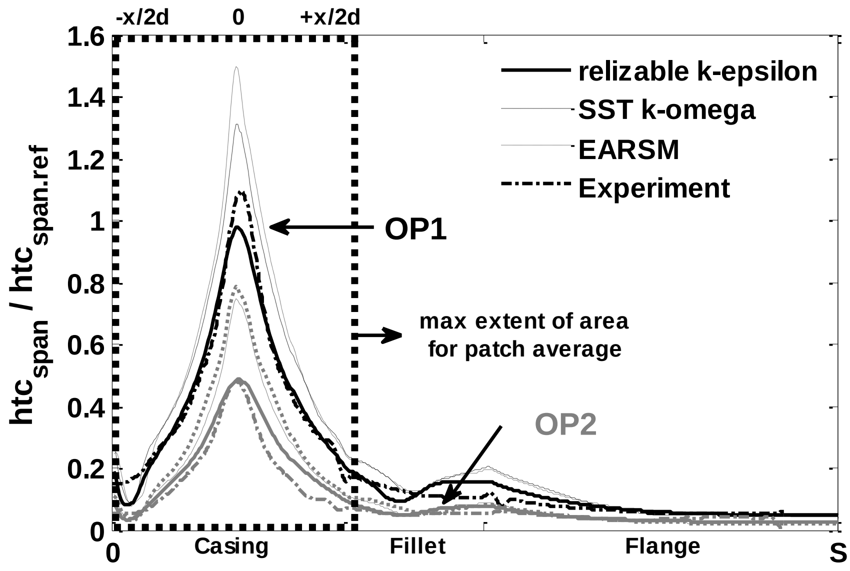

Figure 5.3 Relative performance of spanwise averaged *htc* / *htc*$_{ref}$ (= H2 *z*/*d*=4.peak.span.realizable k-ε.OP1), at OP1 and OP2, for the changing turbulence model.

Figure 5.3 shows a comparison between the spanwise averaged *htc* distributions from the experiment and the numerical calculations again in a normalised format. Spanwise averaged heat transfer distributions typically provide sufficient resolution for engine designers, while full *htc* distributions allow full 3D FE simulation of closure to ensure uniformity is not compromised. The peak of the spanwise averaged <u>*htc*</u> acquired from CFD is under predicted by 17.5 % for the realizable *k*-*ε* model but over predicted by 25.4 % for the SST *k*-*ω* and 33.3 % for the EARSM models respectively. Consistent and very low *htc* is seen towards the top of the flange, at a consistent level in all cases.

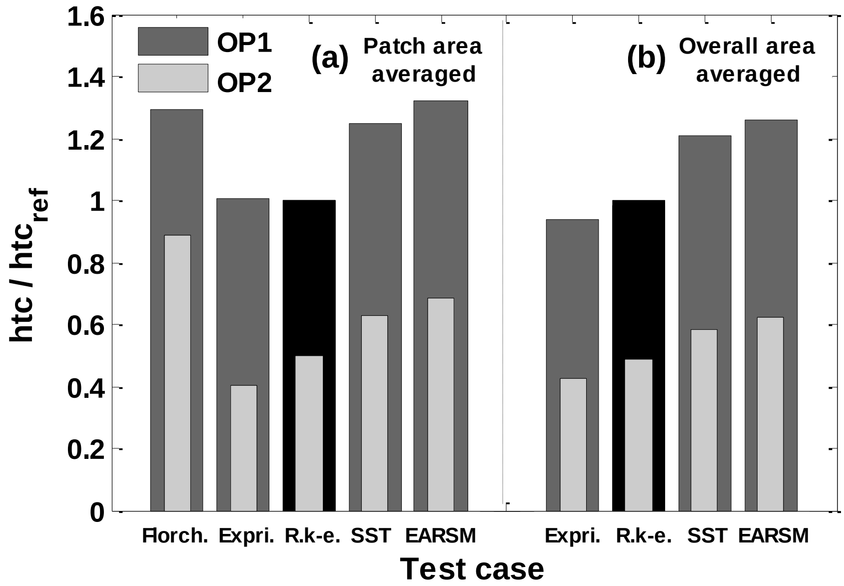

Figure 5.4 Relative performance of (a) patch area averaged *htc* / *htc*$_{\text{ref}}$ $_{\text{(=H2.patch.realizable k-}\varepsilon\text{.OP1)}}$ and (b) overall area averaged *htc* / *htc*$_{\text{ref (=H2.avg.realizable k-}\varepsilon\text{.OP1)}}$ at OP1 and OP2 for the changing in turbulence model.

The relative performance of the turbulence models is quantified in **Figure 5.4** in terms of (a) patch area averaged and (b) total area averaged heat transfer coefficient. The patch averaged *htc* is compared with experimental data from the current study and also the industry standard correlation of **Florschuetz et al. (1981)** who proposed a correlation in the form:

$$\mathrm{Nu_{patch}} = \alpha \mathrm{Re}^m \mathrm{Pr}^{1/3} \left(1 - \beta \left(\frac{z_n}{d}\frac{G_c}{G_j}\right)^n\right) \tag{5.2}$$

with the constants expressed as geometric functions:

$$\alpha, \beta, m, n = C\left(\frac{x_n}{d}\right)^{n_x}\left(\frac{y_n}{d}\right)^{n_y}\left(\frac{z_n}{d}\right)^{n_z} \tag{5.3}$$

Here an averaged Nusselt number to be applied to an area extending $-y_n/2d$ to $+y_n/2d$ by $-x_n/2d$ to $+x_n/2d$, centred on the geometric jet axis is determined in terms of the jet Reynolds number, ratio of the jet to crossflow mass velocity and the main array geometry parameters. Note that Florschuetz' correlation has been widely used as the basis for internal cooling research. However, the geometric parameters and range of Reynolds number expected in the tip clearance control manifold can fall well below the lowest Reynolds number considered valid in their correlation (Re = 10,000), and the array of holes may be substantially more sparse.

The patch area averaged **Figure 5.4 (a)** shows good agreement between the realizable *k-ε* and the experimental results with a difference of less than 1% at OP1 rising to 24 % at the lowest Reynolds number modelled. The deviation from Florschuetz' model is 38 - 43 %. While this is rather high it is to be expected: the Reynolds number lying 60 % below the lower bound of Florschuetz' correlation range. Such over prediction was previously observed by **van Treuren et al. (1996)** who applied the correlation to an array of $z/d = 4$ holes with a moderate crossflow. Patch average *htc* from the realizable *k-ε* model is 20 - 25 % less than that predicted by Florschuetz. The SST *k-ω* and EARSM model nearly match this model being 3 % lower and 2 % higher respectively. However, it is noted that should the pitch be changed the ranking might differ due to the gross over prediction of *htc* in the area near the jet axis, which is then compensated for by under prediction elsewhere in some of the models. The comparison of the overall (whole surface) heat transfer coefficient distribution for different turbulence models, **Figure 5.4 (b)** shows similar trends in the accuracy of each turbulence model. At high Reynolds number, using the realizable *k-ε* model, the error in total overall area averaged is 6 % compared to -1 % for the patch averaged area, but at low Reynolds number the overall are averaged error is 14.5 % compared to 22.4 % for the patch averaged area. Other turbulence models can produce patch averaged and overall area averaged errors lying between 31 - 45 %, (at OP1) or 27 - 68 % (at OP2) dependent on Reynolds number. Thus, the realizable k-ε model was selected for all subsequent numerical analysis reported.

5.2 Relative Performance of Impingement Cooling Arrangements

In this section, the effectiveness of a range of impingement cooling arrangements in typical engine casing closure system is reported. The effects of jet-to-jet pitch, number of jets, inline and staggered alignment of jets, arrays of jets on dummy flange, on an engine representative casing geometry are assessed through comparison of the convective heat transfer coefficient distributions as well as the thermal closure at the point of the casing liner attachment. Constant mass flow rate was used as a constraint at each engine condition, this approximately pertaining to a constant feed pressure when the manifold exit area is constant. Sets of local heat transfer coefficient data generated using a consistent modelling approach were then used to create reduced order distributions of the local cooling. These were used in a thermo-mechanical model to predict the casing closure at engine representative operating conditions.

5.2.1 External Casing Heat Transfer

Again, the primary motivation of this parametric study is to understand how geometric variations affect the casing closure. A first step is therefore to determine the variation in external heat transfer coefficient distribution. Note that a maximised average *htc* will not necessarily result in maximised clearance. The heat transfer results from the numerical simulations are presented in three formats below: first as full field contour diagrams, secondly as spanwise averaged profiles in the streamwise direction and finally total area averaged for OP1 and OP2 conditions. Again, the reference *htc* used for normalisation is the peak value of local *htc* for the *H2* cooling arrangement at operating point OP1. For spanwise, patch or overall area averaged *htc* comparison the same data set is used to provide the reference values.

Streamwise Jet-to-Jet Pitch. **Figure 5.5** and **Figure 5.6** show the general pattern of heat transfer coefficient under the impinging jets as the streamwise jet-to-jet pitch is increased (*Xp1* - *Xp4*). The footprint from each impingement is seen to be essentially independent of the hole position. The region of enhanced heat transfer between jets in the spanwise direction is also similar and produces a moderate rise in local *htc*, though it appears more effective further downstream at increased pitch. Increasing jet to jet distance in the streamwise direction (i.e. moving the jet seen in this half-plane further downstream) causes the jet *htc* foot print to cover a larger portion of the fillet region, however a slight drop in peak *htc* underneath the jet is recorded as its local standoff distance slightly increases due to the fillet curvature of the manifold. Between the jets the *htc* drops as the pitch is increased, most easily seen by comparing spanwise averaged profiles in **Figure 5.7**. The set of total area averaged *htc* data are presented in **Figure 5.8**. For the jet-to-jet pitch studies conducted, configuration *Xp3* (x/d = 14.9) results in the highest total average heat transfer followed by *Xp4*.

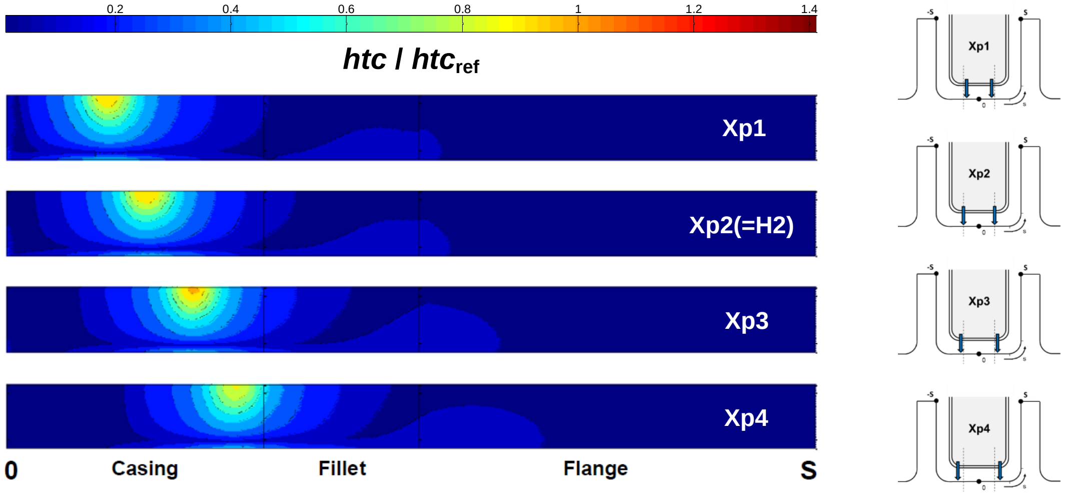

Figure 5.5 Local *htc* / *htc*$_{ref}$ (= H2 *z*/*d*=4.peak.realizable k-ε.OP1) distributions of the variation in jet to jet pitch at OP1.

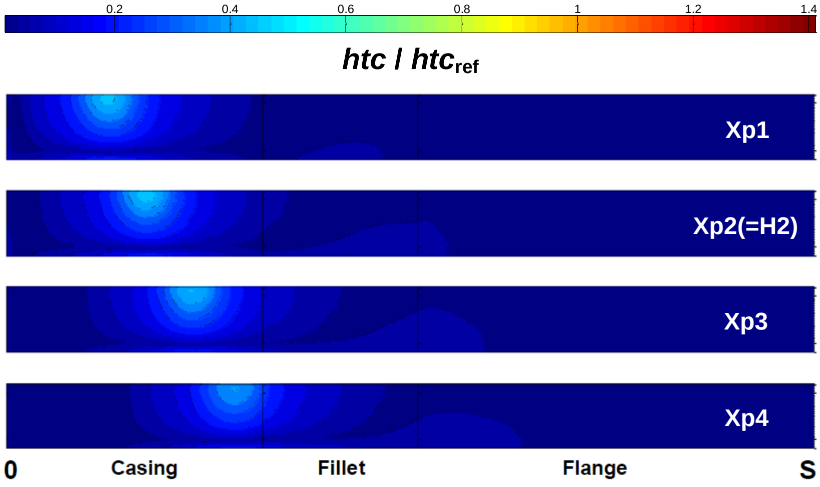

Figure 5.6 Local *htc* / *htc*$_{ref}$ (= H2 *z*/*d*=4.peak.realizable k-ε.OP1) distributions of the variation in jet to jet pitch at OP2.

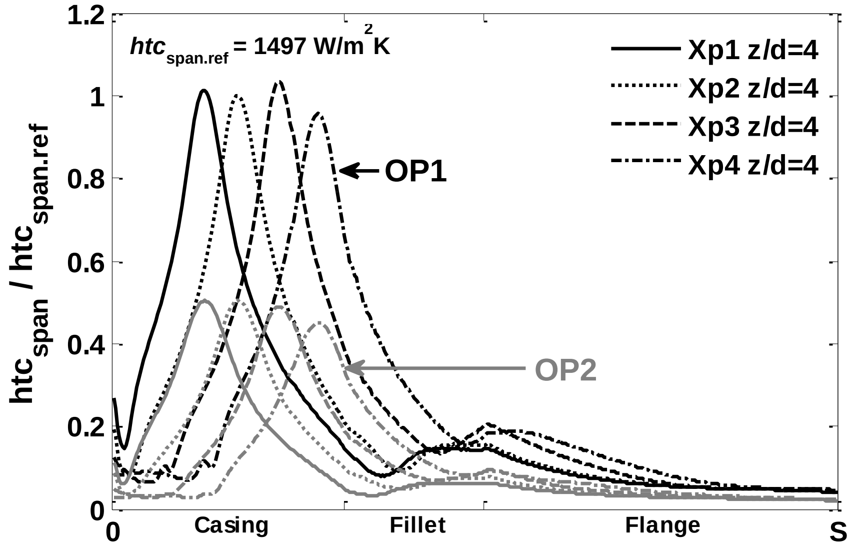

Figure 5.7 Spanwise averaged *htc* / *htc*$_{\text{ref (= H2 } z/d\text{=4.peak.span.realizable k-}\varepsilon\text{.OP1)}}$ distributions at OP1 and OP2, for the variation in jet to jet pitch.

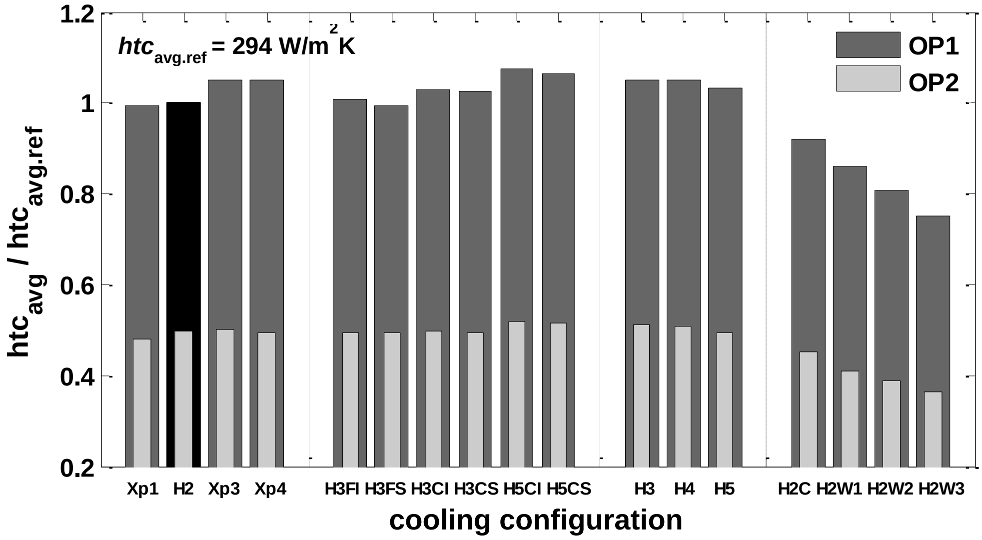

Figure 5.8 Relative performance of overall area averaged *htc* / *htc*$_{\text{ref (= H2 } z/d\text{=4.avg.realizable k-}\varepsilon\text{.OP1)}}$ at OP1 and OP2.

Number of Jets. The effect of the number changing the number of jets while keeping the total cooling hole area constant on the local *htc* distribution is seen **Figure 5.9** and **Figure 5.10** for configurations *H2* to *H5*. As the number of jets is increased, the surface area per jet reduces, and a lower a local peak *htc* is seen at the same operating condition. This reflects the lower Reynolds number from each jet (same velocity, very similar discharge coefficient, but smaller diameter hole). The improved uniformity of coverage, caused by additional jets and recirculation and secondary impingement between jets may, however, lead to a higher total heat transfer than the baseline *H2* case. This is seen for the *H3* prediction with 4.6 to 6.7 % improvement in heat transfer level over the baseline at the two operating conditions as seen in **Figure 5.8**. It is noticeable that tongue of high *htc* at the spanwise location of the upwash region extends farther downstream for the *H3* arrangement than in the *H4* or *H5* cases as shown in **Figure 5.11**. It is surmised that this is because the impingement jet is less degraded by the shear layer in the *H3* case (as *z*/*d* is lower) this results in a faster wall jet and therefore more strongly turbulated upwash flow. Usefully this enhancement effect extends over the full extent of the dummy flange, which it will be shown is desirable for improved closure behaviour.

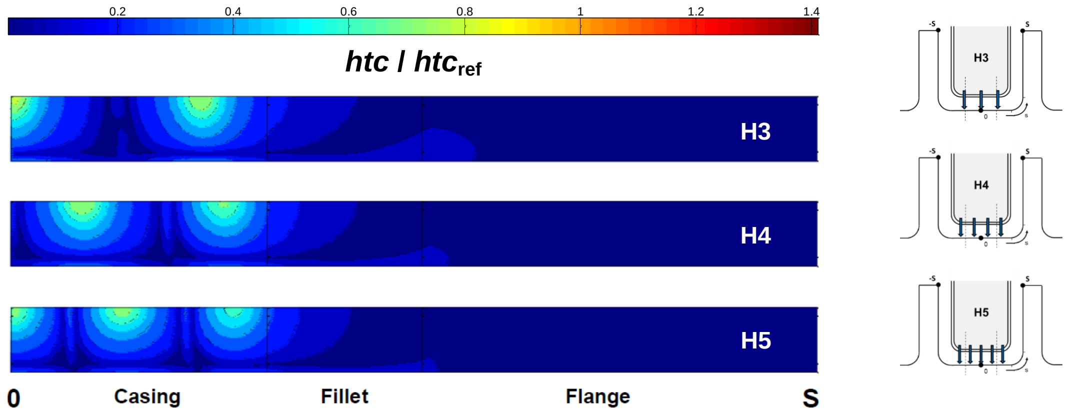

Figure 5.9 Local *htc* / *htc*$_{ref}$ (= H2 *z*/*d*=4.peak.realizable k-ε.OP1) distributions, for different number of rows of jets, OP1.

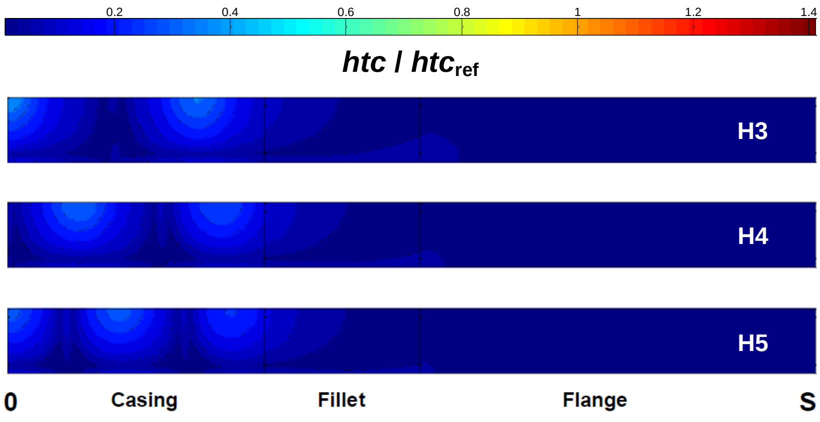

Figure 5.10 Local *htc / htc*$_{ref}$ (= H2 *z/d*=4.peak.realizable k-ε.OP1) distributions, for different number of rows of jets, OP2.

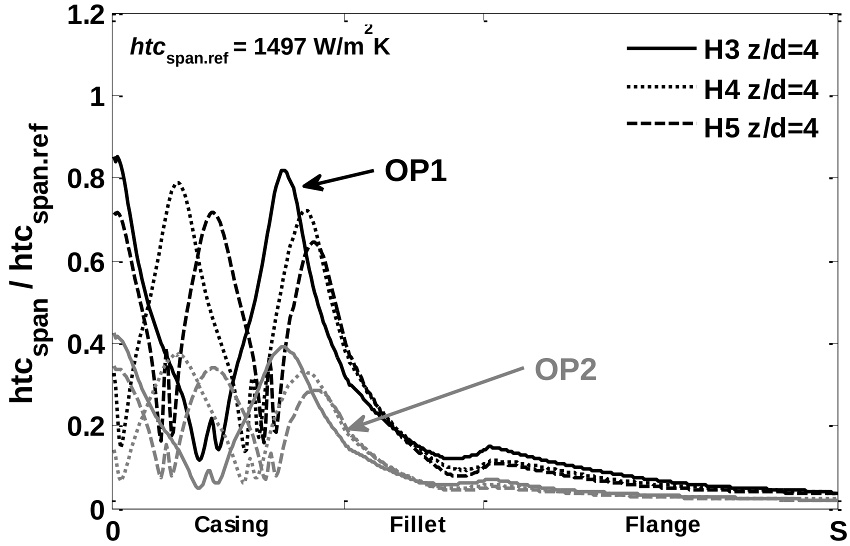

Figure 5.11 Spanwise averaged *htc / htc*$_{ref}$ (= H2 *z/d*=4.peak.span.realizable k-ε.OP1) distributions at OP1 and OP2, for different number of jet rows.

Inline and staggered arrays of jets. **Figure 5.12** and **Figure 5.13** show local normalised *htc* distributions of staggered and inline arrays of either 3 or 5 rows of jets *H3FI*, *H3FS*, *H3CI*, *H3CS*, *H5CI* & *H5CS*. The peak *htc* underneath each impinging jet is lower than the baseline case as the local standoff distance to jet diameter ratio has been increased and the jet area reduced when the number of jets was increased whilst maintaining nominally identical mass flow conditions for a given upstream pressure.

The differences between the overall average *htc* of the inline arrays of jets and their staggered counterparts is barely perceptible with changes seen only in the upwash region midway between jets. The spanwise averaged *htc* distributions in **Figure 5.14** reflect this again by showing mostly identical levels along the casing wall except for the slight difference in the upwash region observed, for which the inline pattern *htc* is higher. This leads to slightly higher total average *htc* levels of 0.6 - 1.3 % seen in **Figure 5.8**.

The configurations *H-C-* include impingement onto the corner fillet radius. *H3CI* has similar behaviour to *H5CI*, but in the former case the overall average heat transfer is considerable lower. Geometries such as *H5CI* and *H5CS* distribute flows more uniformly over the entire target area by adding additional impinging jets onto both the target and fillet region. This increases the overall *htc* compared to *H3CI* and *H3CS* where a larger jet-to-jet pitch is employed. They also outperform the *H3FI* and *H3FS* where impingement is normal to the flat target surface, and the pitch equal to the *H3* configuration.

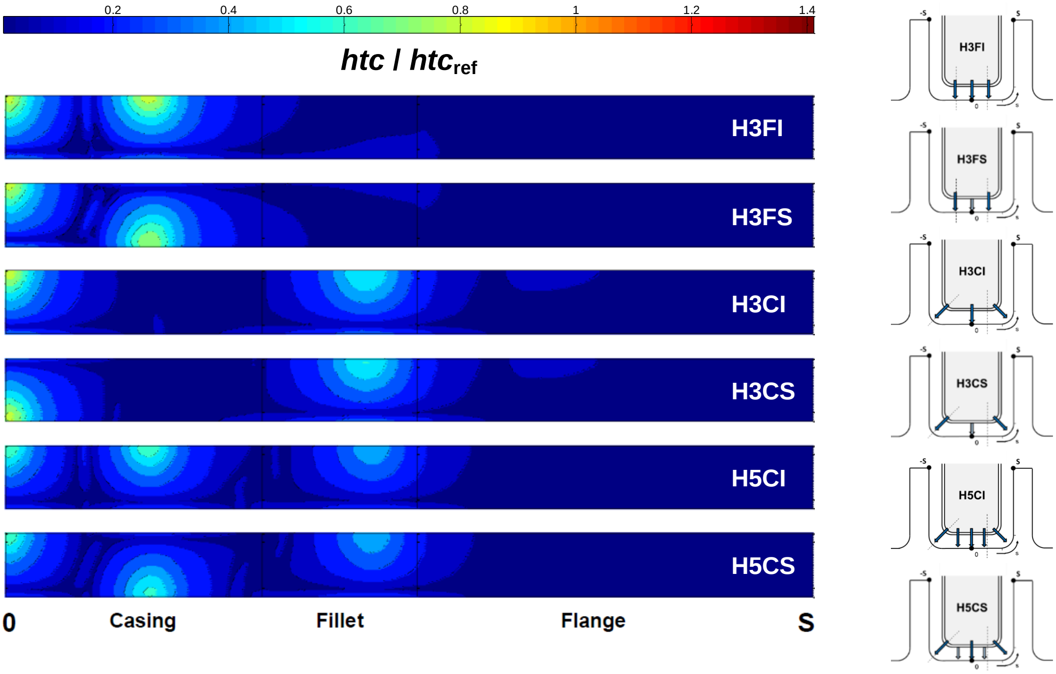

Figure 5.12 Local *htc* / *htc*$_{ref}$ (= H2 *z*/*d*=4.peak.realizable k-ε.OP1) distributions of inline and staggered arrays of jets at OP1.

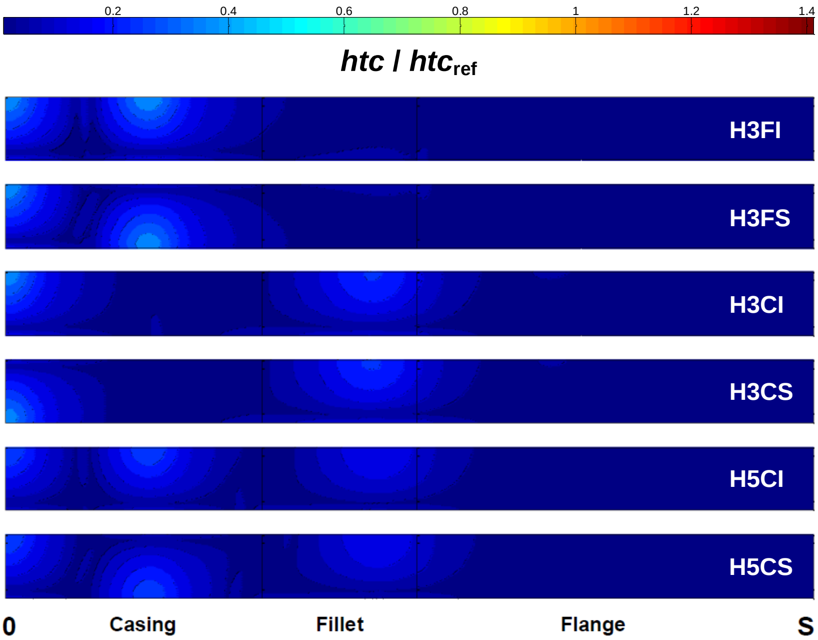

Figure 5.13 Local *htc* / *htc*$_{ref}$ (= H2 *z*/*d*=4.peak.realizable k-ε.OP1) distributions of inline and staggered arrays of jets at OP2.

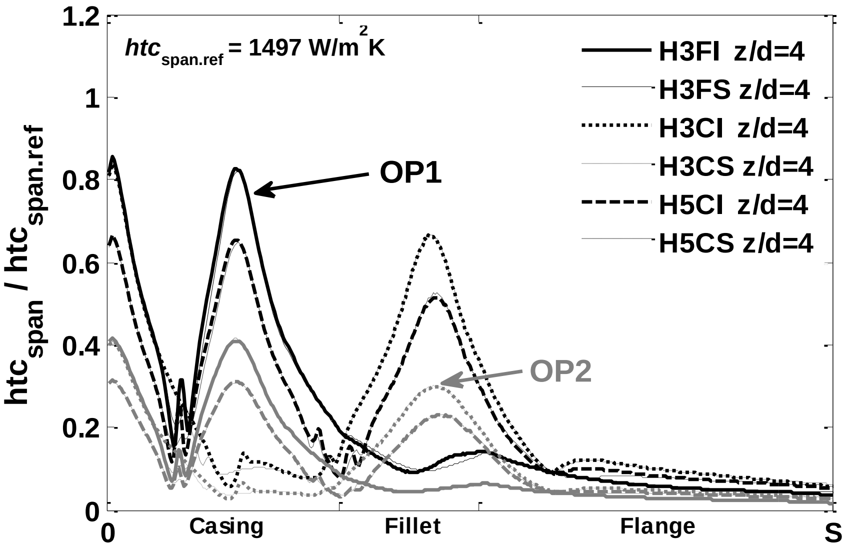

Figure 5.14 Spanwise averaged *htc* / *htc*$_{ref}$ (= H2 *z/d*=4.peak.span.realizable k-ε.OP1) distributions at OP1 and OP2, for inline and staggered arrays of jets.

Arrays of jets on the dummy flange. The importance of the dummy flange in generating casing closure is more clearly highlighted in the FEM results later in the thesis. As a result, a study of the direct cooling of this flange became of interest in the course of the research. **Figure 5.15** and **Figure 5.16** once again show local *htc* distributions normalised by the maximum reference value for OP1 and OP2 conditions respectively, for 4 positions of impingement, moving progressively up the dummy flange (*H2C*, *H2W1*, *H2W2* and *H2W3*). The shape of jet *htc* footprints for the *H2W1*, *H2W2* and *H2W3* configurations are very similar to that of the baseline condition *H2*, but the lower local jet-to-target surface distance between the manifold and sidewall (3.17 times baseline jet diameter as opposed to 4.0 for the baseline) resulted in slightly higher peak *htcs* of 10 - 15 % and a 1 - 1.1 % increase in spanwise averaged *htc* shown in **Figure 5.17** on the flange. The region in the middle of jets directly above the main casing is seen to be very low with the *htc* mostly at an identically low level (regardless of the jet-to-jet pitch in the s-direction). Only configuration H2C affects the region between the two fillets. Whilst *H2C* produced the lowest peak *htc* on the fillet radii, it covers a more extensive cooling area, and appears superior in terms of total area averaged *htc* as shown in **Figure 5.8**. When it comes to the overall performance, the cases of jets on the flange were seen to be have a much lower heat load capability than the other cases presented in this parametric study, it is assumed that much of the flow leaves the domain without using its cooling potential.

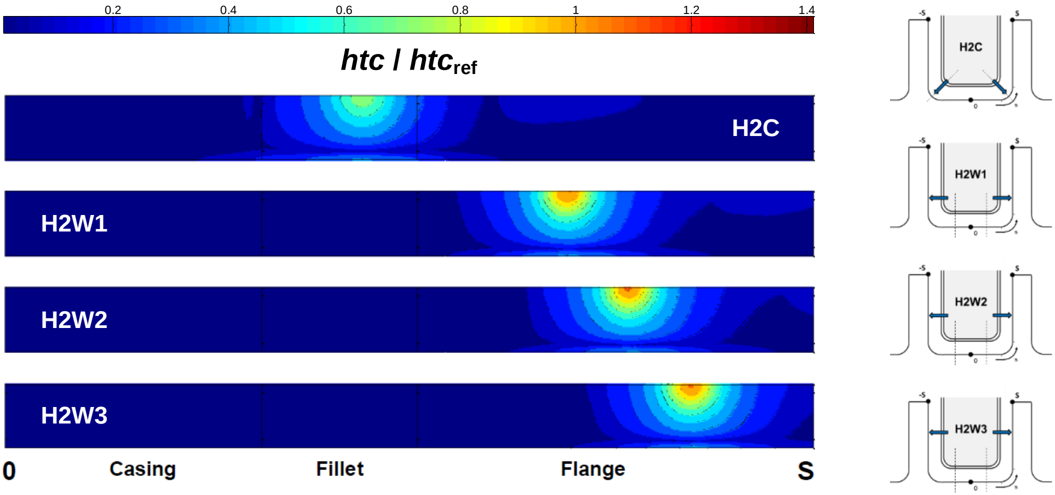

Figure 5.15 Local htc / $htc_{ref\ (= H2\ z/d=4.peak.realizable\ k\text{-}\varepsilon.OP1)}$ distributions of arrays of jets on flange at OP1.

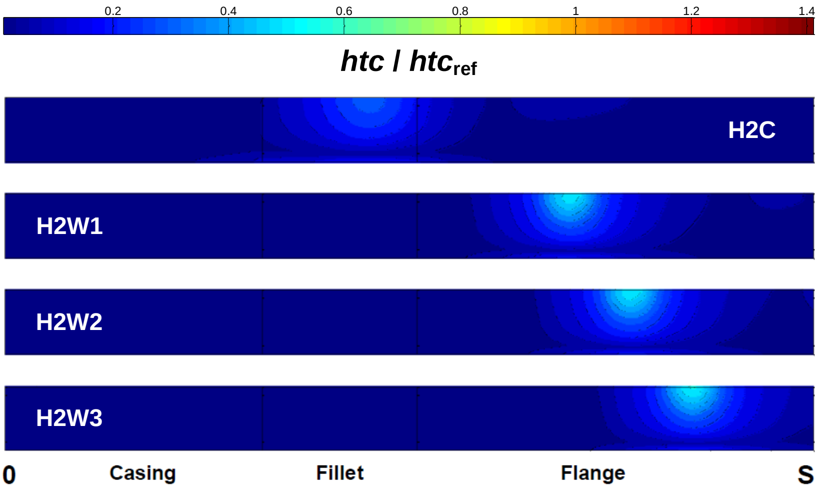

Figure 5.16 Local htc / $htc_{ref\ (= H2\ z/d=4.peak.realizable\ k\text{-}\varepsilon.OP1)}$ distributions of arrays of jets on flange at OP2.

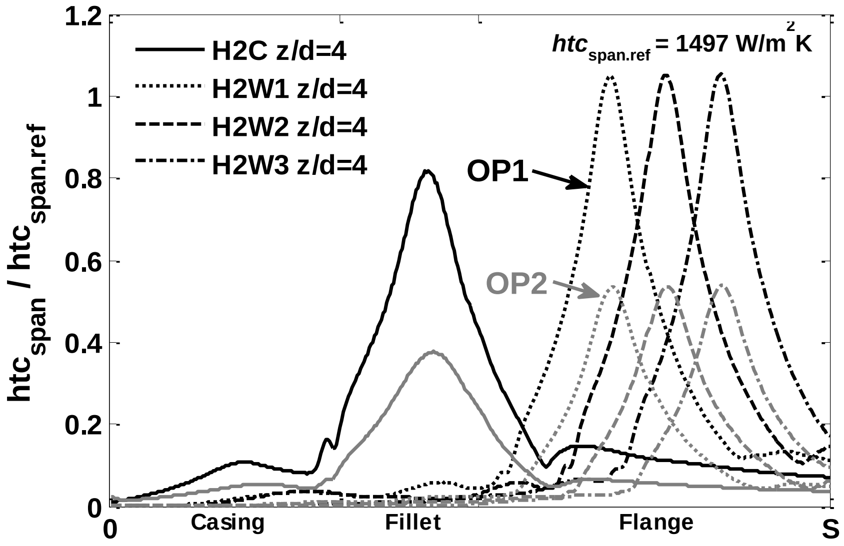

Figure 5.17 Spanwise averaged *htc* / *htc*$_{ref}$ (= H2 *z/d*=4.peak.span.realizable k-ε.OP1) distributions at OP1 and OP2, for arrays of jets on flange.

Overall Performance of all configurations. The full surface area averaged convective heat transfer coefficient is presented as in **Figure 5.8**. As expected for all cases increasing the coolant mass flow rates from OP2 to OP1 results in a rise in *htc*. The variation in *htc* with changing jet-to-jet pitch cases is seen to be less than 6.8 %. Changing the number of holes whilst maintaining impingement onto the flat surface between the flanges resulted in variation of less than 6.7 %. Of the remaining configurations, based on total *htc*, the *H5CI* case is the best option (+9.3 % above baseline at OP1 for the total averaged convective heat transfer); whilst *H2W3* shows by far the worst performance among all of the cases (-25 %). The power relationship between Nusselt number and Reynolds number was determined for each case and found, for all cases to lie between 0.785 and 0.85. On average for all cases $Nu \propto Re^{0.821}$.

5.2.2 Casing Temperature and Displacement Prediction

The spanwise averaged heat transfer coefficient distributions determined above were used to provide external boundary conditions for the idealised engine casing FE model described in section 4.1.2. The local casing temperature and thermal displacement distributions for each impingement cooling configuration could then be determined. These are shown in **Figure 5.18,** where for each condition the displaced shape of half of the casing is shown, along with a contour map of the casing temperature to a common scale in Kelvin. It is notable that the initial condition of the casing is at a smaller diameter than the displaced casing, and this because the nominal geometry is created from cold build conditions. A common way of classifying the effectiveness of a casing cooling scheme is by determining its thermal closure. As the engine heats up the casing expands to plateau level, then shrinks once the cooling is switched on. The closure here is defined as the difference in radial growth between the far field l = 200 mm position and the position of attachment of the casing liner above the HP blade as shown in **Figure 5.19**. The radial contraction resulting from the 0.02 - 0.35 kg/s of the current TCC flows (OP4 - OP0 at engine scale) is in the range from 0.5 - 2.2 mm. The effect of the cooling geometry parameters on closure is now considered further, and for each set of geometric parameters the closure and hook attachment temperature is reported.

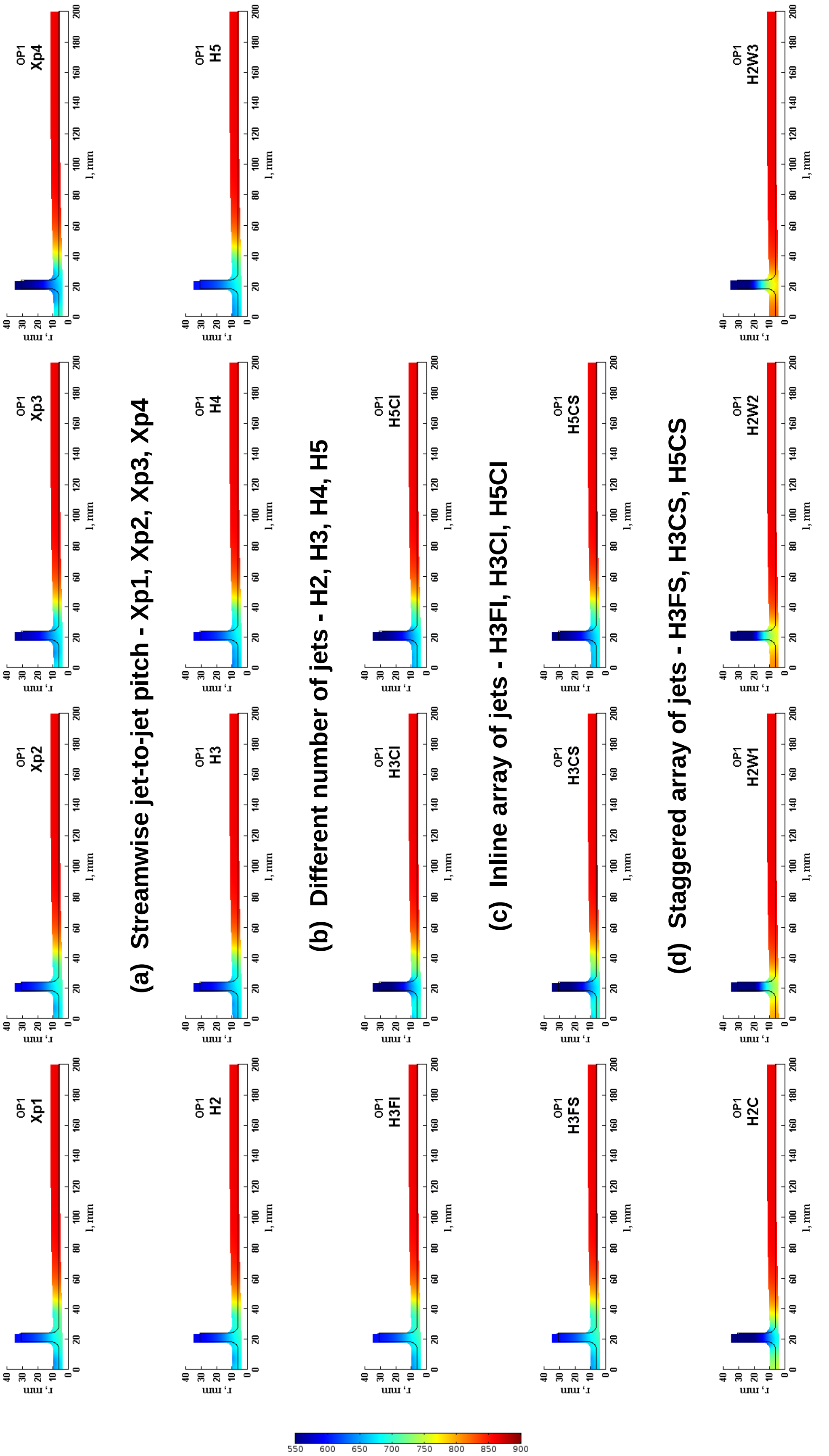

(a) Streamwise jet-to-jet pitch - Xp1, Xp2, Xp3, Xp4

(b) Different number of jets - H2, H3, H4, H5

(c) Inline array of jets - H3FI, H3CI, H5CI

(d) Staggered array of jets - H3FS, H3CS, H5CS

(e) Array of jets on flange - H2C, H2W1, H2W2, H2W3

Figure 5.18 Predicted casing temperature (K) and thermal radial displacement (r,mm) for the variation in impingement jet arrangements at OP1.

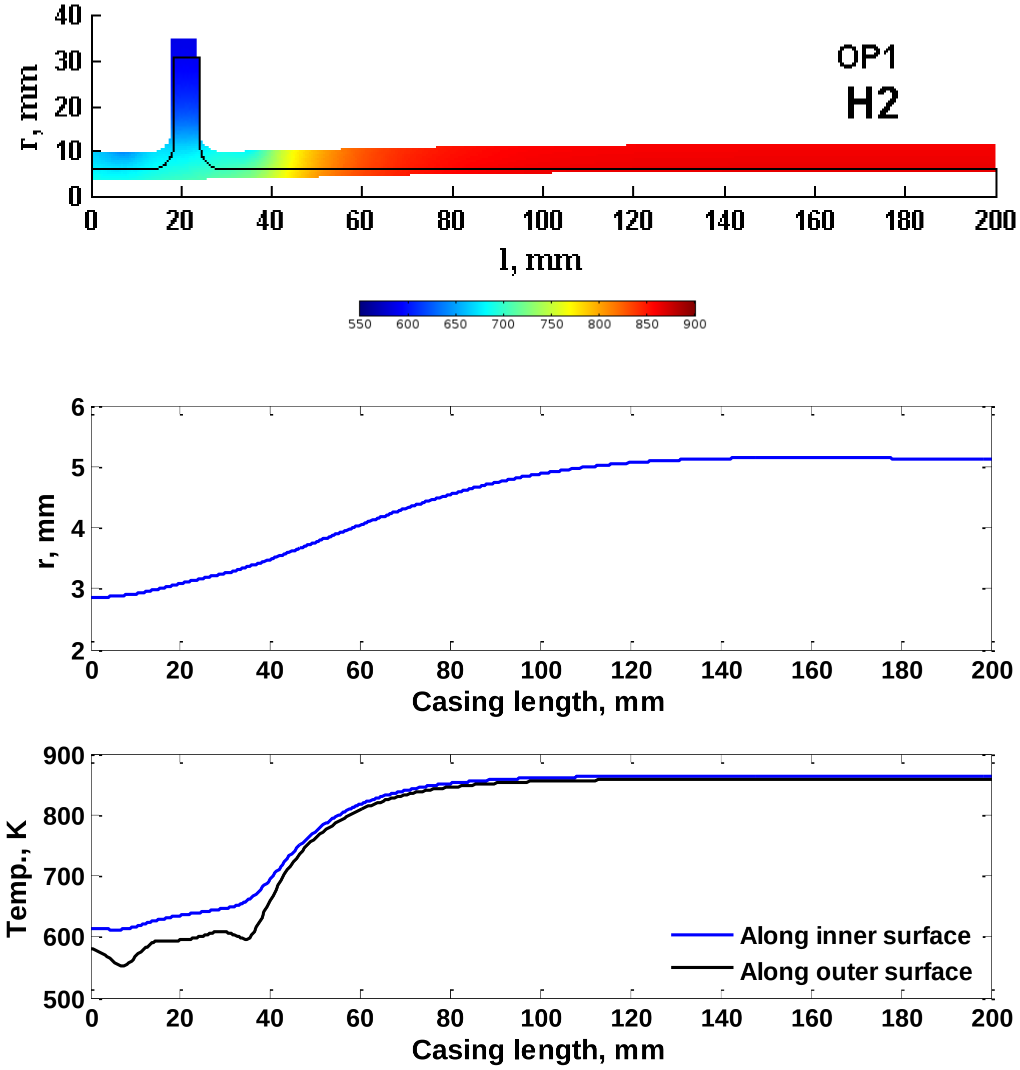

Figure 5.19 Predicted casing temperature (K) and thermal radial displacement (r,mm) for H2 at OP1.

Effect of jet-to-jet pitch. The local casing temperature and relevant thermal closure for the variation in jet to jet pitch are presented as a function of coolant mass flow rate in **Figure 5.20**. Note that in all of the following figures five levels at OP0, OP1, OP2, OP3, and OP4 condition are included, with the levels at OP1 and OP2 highlighted. These are all labelled in **Figure 5.20**, but not in subsequent figures.

As expected more external cooling results in a larger closure. For a given coolant mass flow rate, closure appears to be improved by directing the impingement jet further towards the dummy flange fillet radius. This is indicated by an increase in closure from *Xp1* to *Xp4*. The improvement in casing closure of the *XP4* configuration compared to the baseline *H2* at operating conditions OP1 and OP2 condition is 5.0 % and 5.6 % respectively (0.055 to 0.092 mm). It is notable that this is contrary to the ranking produced based on overall standalone convective heat transfer as shown in **Figure 5.8**, which would suggest that *Xp3* would yield the highest closure.

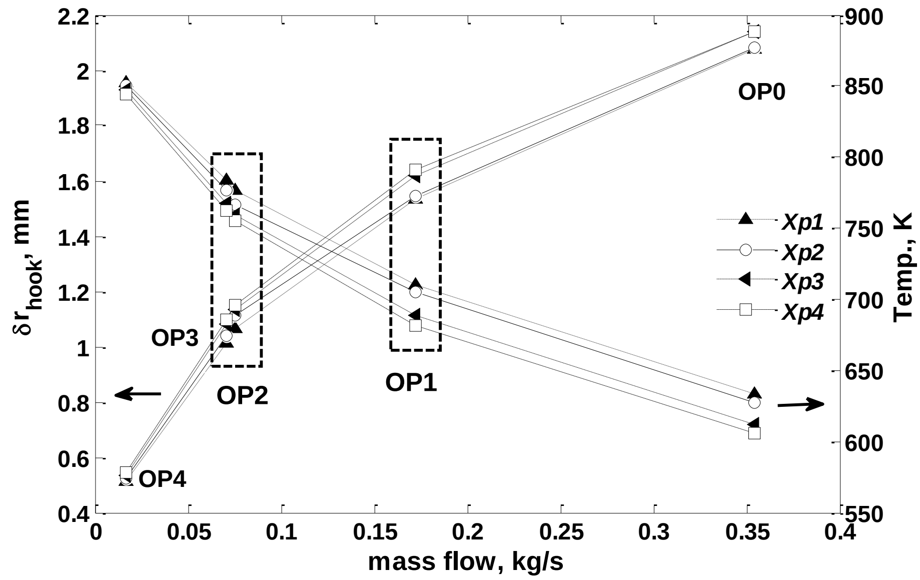

Figure 5.20 Predicted casing temperature (K) and closure (mm) versus coolant mass flow rate, at liner attachment point for jet to jet pitch variation.

Number of Jets. The trend of thermal closure achieved using different number of jet rows is shown in **Figure 5.21**. The closure matches the cooling ranking presented in **Figure 5.8**. In this comparative arrangement where all jets are perpendicular to the surface, three impingement rows provide the greatest closure. The improvement in casing closure of the *H3* array at OP1 is 2.5 % compared to *H2*.

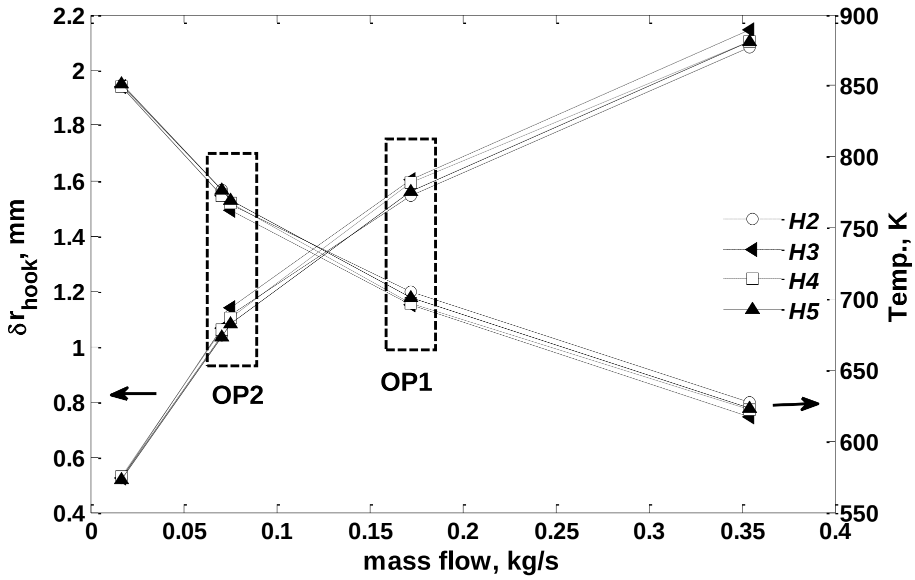

Figure 5.21 Predicted casing temperature (K) and closure (mm) versus coolant mass flow rate, at liner attachment point, for the different number of jets.

Effect of Inline and Staggered Arrays of Jets. The casing closure versus coolant mass flow rate for the equivalent inline and staggered array cooling schemes was nearly identical as shown in **Figure 5.22**, with the *H5CI* configuration consistently producing the highest closure reported. The improvement in casing closure of the *H5CI* arrangement is at OP1 7.0 % or 0.117 mm compared to *H2*.

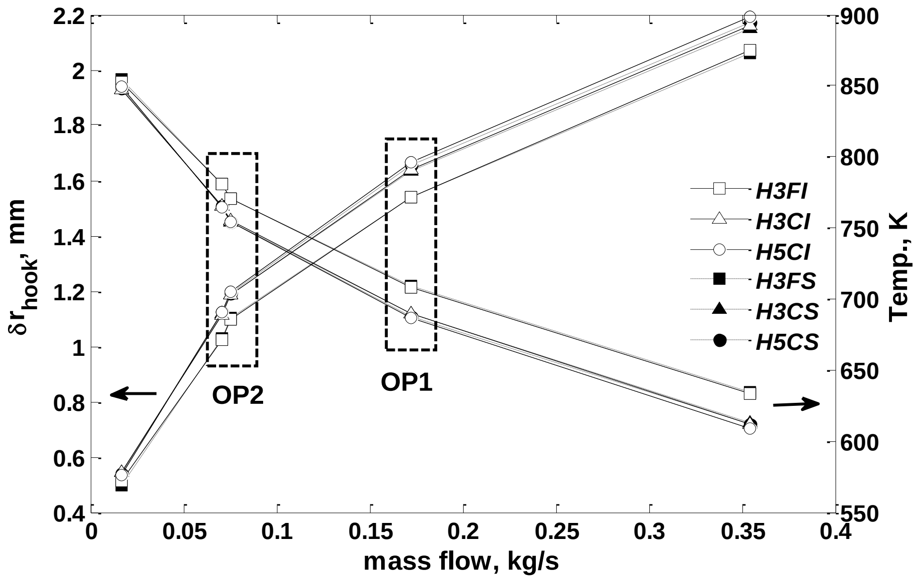

Figure 5.22 Predicted casing temperature (K) and closure (mm) versus coolant mass flow rate, at liner attachment point, for the inline and staggered arrays of jets.

Arrays of Jets Impinging onto the Flange. Unlike the result from the standalone convective heat transfer ranking presented in **Figure 5.8**, the *H2C* fillet radii cooling configuration shows a dramatic improvement in casing closure compared to any of the other flange impingement schemes. On the local temperature distribution it is clear that the flange temperature is lowest for this cooling configuration. As the jets point at regions further up the flange side wall, each case has less impact on the central well region of the main casing, and appears only to cool the area of the flange lying radially outwards from it (downstream). This is unlikely to increase the overall contraction performance as the remainder of the flange is 'fighting' this contraction. It is, then, clearly desirable that jets should be positioned to target the root of flange, this isolates the flange from the heat input at the inside of the casing, and maximises the casing compression caused by the flanges. Unfortunately impingement onto the fillet radii is protected by a patent by **Bucaro et al. (2009)**, so alternative means are required by other engine manufacturers to obtain similar thermal isolation of the flanges.

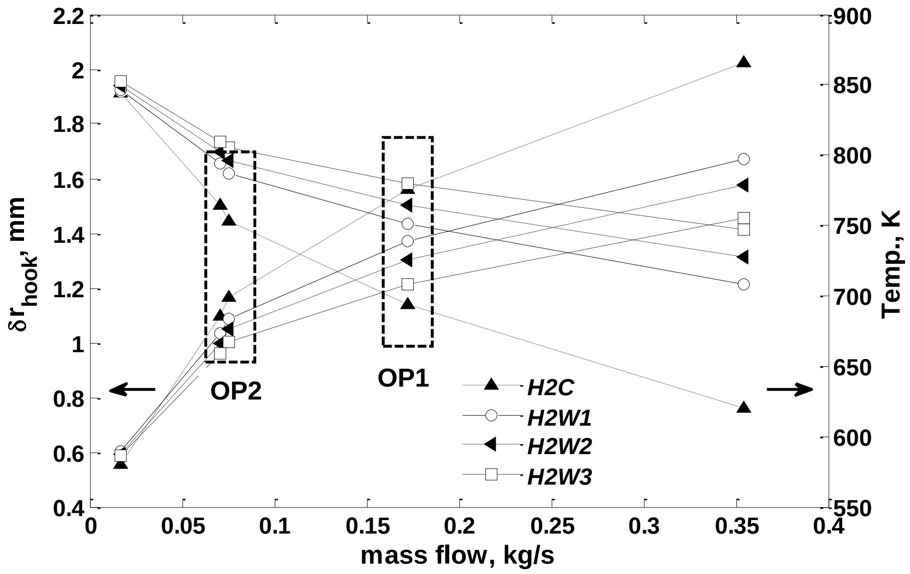

Figure 5.23 Predicted casing temperature (K) and closure (mm) versus coolant mass flow rate, at liner attachment point, for arrays of jets on flange.

Overall Performance. Comparing the ranking of the predicted temperature and radial displacement results, in the main they clearly show the same pattern. The temperature drop at the liner attachment point follows linearly the trend of the thermal closure achieved within each configuration variation as shown in **Figure 5.24** and **Figure 5.25**. The graphs show the relative performance of the range of external cooling arrangements investigated. Notably the striking improvement in temperature drop for *Xp4* does not provide as significant an improvement in closure. The *H5CI* configuration is the best option for both of the convective heat transfer coefficient distributions as well as the thermal closure with 7.0 % or 0.117 mm of possible clearance improvement at OP1 condition compared to the baseline *H2* case; whilst *Xp1* shows the worst performance (-0.9 % or -0.015 mm) among those options (apart from the *H2W* flange series which lie much farther behind). This suggests that a more uniformly distributed cooling scheme is desirable over the entire external region including the fillet; cooling this area effectively constricts the temperature gradient through the dummy flanges, isolating them from heating effects. Note that, for example, for a 50 mm blade span a 0.1 mm increase in casing closure equals to 0.2 % reduction in the operating tip clearance where within a typical operating range of 0.5 - 1.5 %.

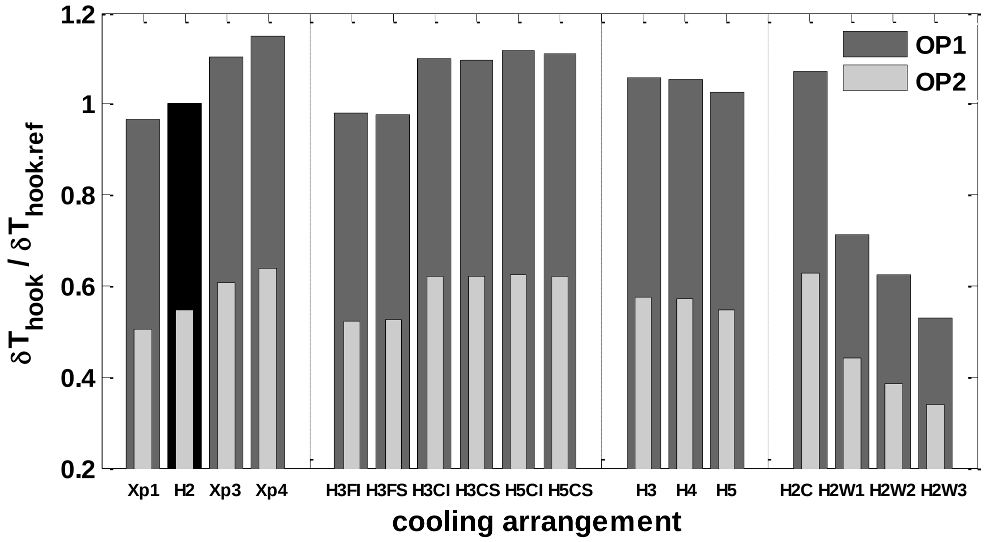

Figure 5.24 Relative performance of casing temperature drop at the liner attachment point by internal hooks, compared to baseline H2 *z/d* = 4 scheme at OP1 and OP2.

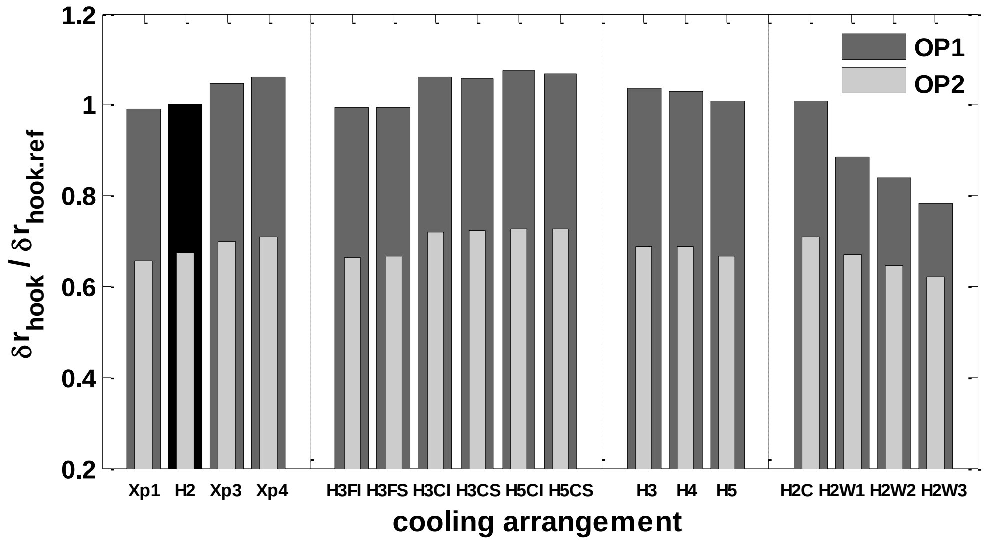

Figure 5.25 Relative performance of casing closure at the liner attachment point by internal hooks, compared to baseline H2 *z/d* = 4 scheme at OP1 and OP2.

5.3 The Effect of Cooling Manifold Standoff Distance

Following the parametric study reported above which was conducted at a single manifold standoff height, three impingement jet arrays i.e. *H2*, *H2C* and *H5CI*, were chosen for further analysis over a range of cooling manifold to target casing standoff distances. Previously it has been suggested that it might be possible to adjust the manifold to target casing standoff (e.g. using spacers of different thickness above manifold mounting features **(Saroi, 2014)**) to allow control of the cooling capacity, and mitigate engine deterioration caused by blade tip and liner wear. A more problematic issue for the jet engine is the likely change in clearance because of build tolerance and changing shape of the manifold during the engine cycle. There are therefore two drivers for understanding this variation in behaviour. For the current configuration the cooling manifold standoff distance, z, is tested in the range 1 to 6 times the baseline jet hole diameter. z_{base}/d = 4 was chosen as the reference offset distance in the previous tests; conventional impingement systems having best performance in the range z_{base}/d = 3 - 4. In order to compare heat transfer capability and effective casing thermal closure, a modelling approach consistent with the previous section is used. **Figure 5.26** and **Table 5.1** show the selected external cooling manifold configurations together with the definition of the jet arrays and relevant coordinates.

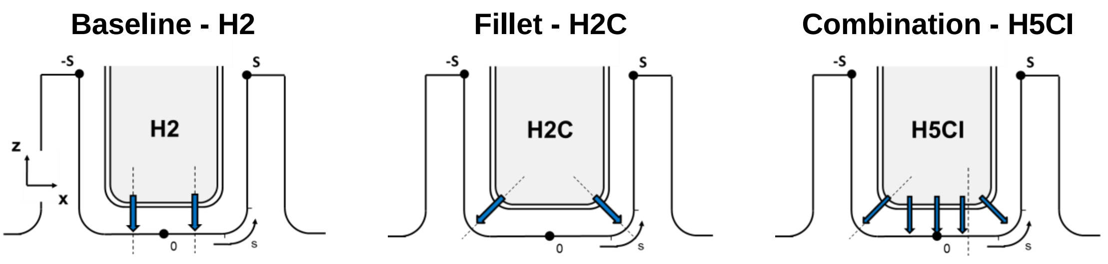

Figure 5.26 Cooling arrangements selected for manifold offset parametric study.

The configurations tested are

- Two jets normal to the target casing wall (baseline), labelled *H2*.
- Two jets directed into the flange fillet radii, labelled *H2C*.
- Combination of impingement onto both the target and the fillet radii, labelled *H5CI*.

Table 5.1 Geometrical details of cooling arrangements and manifold offsets varied.

configuration	d	x(or s)/d	y/d	z/d	z/d_{base}	I/d
H2	1.21	11.6	5.2	1	1	0.58
				2	2	
				3	3	
				4	4	
				5	5	
				6	6	
H2C	1.21	-	5.2	1	1	0.58
		-		2	2	
		-		3	3	
		-		4	4	
		-		5	5	
		-		6	6	
H5CI	0.77	7.1	8.2	1.6	1	0.91
				3.1	2	
				4.7	3	
				6.3	4	
				7.9	5	
				9.4	6	

5.3.1 Flow Field Prediction

Differences in the manifold behaviour at different standoff distances are illustrated by flow pathlines generated for the cooling manifold standoff distance to baseline jet hole diameter ratio z/d_{base} = 1 - 6 at operating point OP1, as shown in **Figure 5.27**.

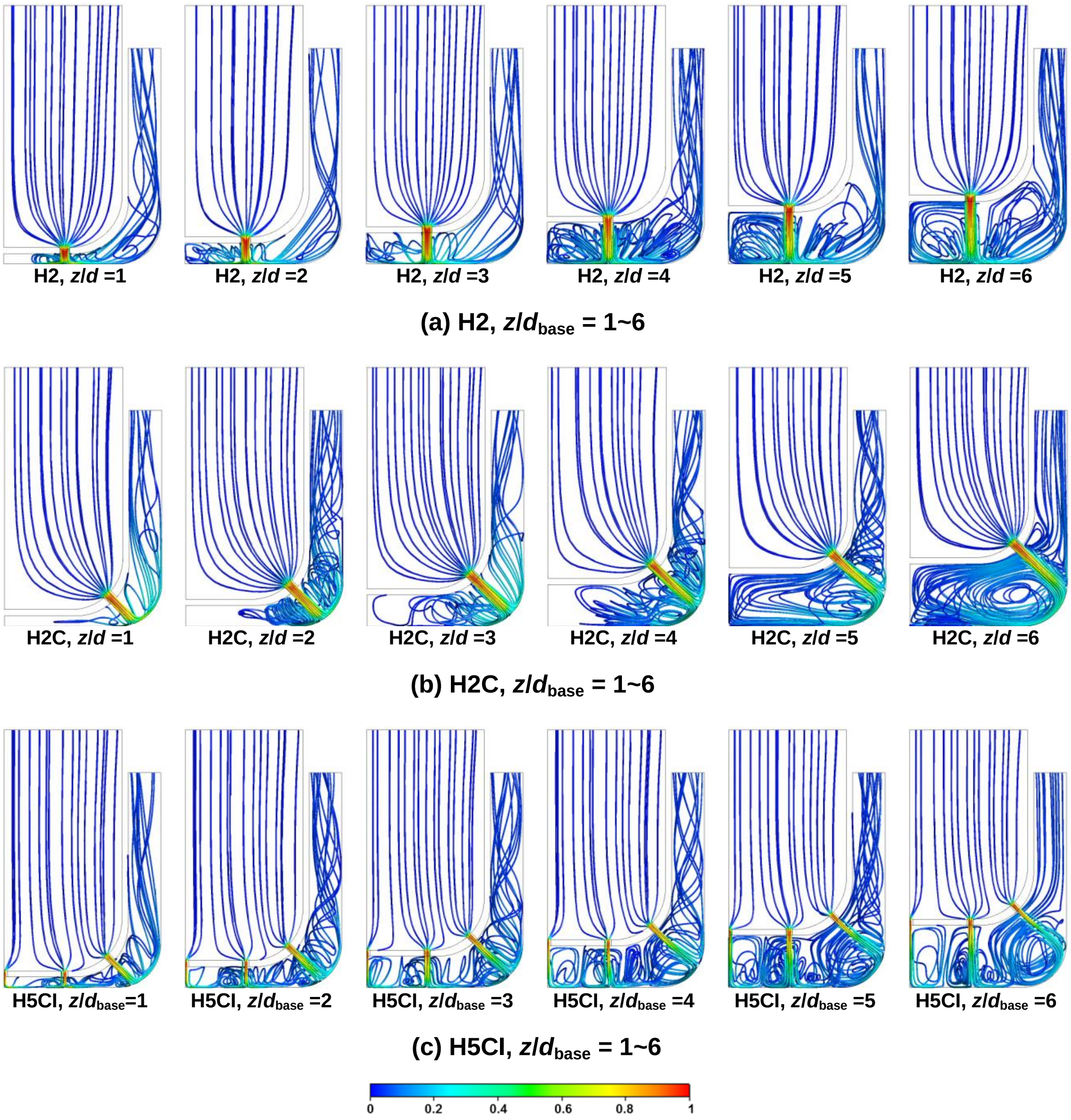

Figure 5.27 Selected streamlines coloured by vel/vel_{max} at OP1.

The pathlines originate from the manifold inlet faces and exit through the side wall channel. (This has constant exit for all standoff heights studied). In general, the jets issued from the short cooling holes (I/d = 0.58 for *H2* and *H2C*, and I/d = 0.91 for *H5CI*) flow towards the casing wall followed by deflection through the stagnation region. At low standoff distances the potential core of the jet is swept downstream and little of the recirculating flow near the centreline of the system can be seen in the pathlines plotted.

Flow interaction in the central region between the streamwise rows of the *H2* arrangement is very low at $z/d_{\text{base}} = 1$, the spent air from the impingement jet turning and exiting into the side channel between the manifold and the dummy flange with insufficient momentum to reach the central axis of the system. Hence the flow in that region is stagnant (no streamlines being seen to reach the centre of the passage). The *H2C* configuration, (b), shows this more dramatically as jet to jet spacing in streamwise direction ($s/d \geq 20$) is almost double that of *H2* while the spanwise pitch is fixed. Essentially no flow from the impinging jets washes the flat outer surface of the casing at $z/d_{\text{base}} = 1$. As the standoff increases $z/d_{\text{base}} > 2$ for *H2* and over $z/d_{\text{base}} > 3$ for *H2C*, the backpressure in the space between the jets drops and mixing occurs between the streamwise jets and surrounding air in the middle. As more holes are placed in streamwise direction, and in particular at the centre of the passage in the *H5CI* configuration, this behaviour is eliminated, and the flow field becomes less sensitive to the standoff distance.

In the *H2* case an upwash fountain is observed between spanwise (circumferential) jets where the hole row spacing (y/d = 5.2) is tighter, and less than half that of the streamwise row spacing (s/d = 11.7). The spent flow from the upwash is channelled between the rows and reattaches to the root of the dummy flange between areas of locally separated flow at the fillet, induced by the main wall jets, and the high fillet curvature. As the standoff distance decreases, the velocity of the upwash flow in the passage increases and this appears to lead to later reattachment of the flow onto the fillet. In contrast, when the jets are directed into the flange fillet, configuration *H2C*, the separation seen in the *H2* configuration is eliminated. This configuration's local jet to the target surface spacing is larger than that of *H2* case for a given manifold standoff distance. Thus a more mixed out jet impinges onto the fillet radii. Note that as the standoff distance is increased the stagnation point of the *H2C* jets on the root of flange is moved onto its upper part, and this changes the primary direction of the recirculation of flow from the jet from upwards towards the exit, to downwards towards the central axis. Thus the flow pattern is strongly geometrical dependent.

The *H5CI* scheme creates more uniformly distributed jets impinging onto both the target and the fillet. As the jet diameter is smaller, these jets are highly mixed out, and for the three largest standoff distances none of the jet potential core remains, thus leading to impingement with gas of lower driving potential. A change in direction of secondary flow with standoff distance is observed for the outer jets in *H5CI* arrangement which impinge onto the fillet radii (as for the *H2C* case, but with relatively lower intensity).

5.3.2 Experimental Data Comparison and Validation

Baseline Configuration *H2*. **Figure 5.28** presents full normalised *htc* distributions on the casing walls at six standoff distances measured experimentally at an average jet Reynolds number of Re = 6000 for the *H2* configuration.

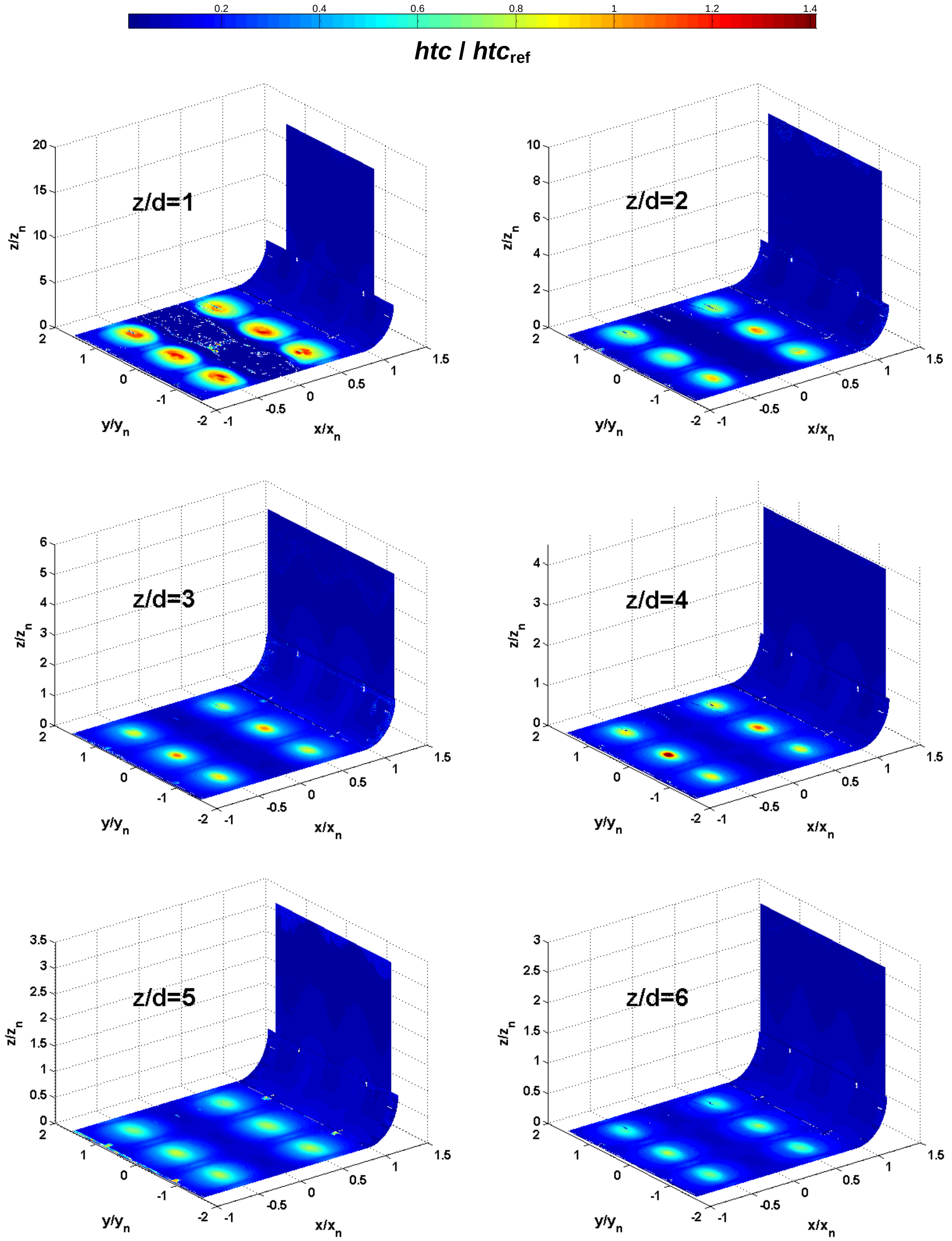

Figure 5.28 Local *htc* / *htc*$_{\text{ref (= H2 }z/d\text{=4.peak.span.realizable k-ε.OP1)}}$ distributions for H2 *z*/*d*$_{\text{base}}$ = 1 - 6, experimental case Re = 6000 (EXP), equivalent to OP1.

Again, all measured and predicted *htc* distributions presented in this chapter can be scaled to engine conditions using the standard convective relationship (see **Equation**

5.1). As the purpose of the experimental test was to validate the CFD, the reference *htc* used for normalisation is the peak value of local *htc* under *H2* baseline scheme with the manifold standoff distance to jet hole diameter ratio of $z/d = 4$ as predicted by the CFD study using the realizable k-ε results at the equivalent operating condition at OP1 where Re = 5710 (95.2 % of the experimental Re number). The value used for normalisation at engine scale $htc_{\mathrm{ref,\ engine}}$ = 2816 W/m^{2}K at engine operating condition, OP1, the equivalent Nusselt number is 136.3, and as all rig scale simulations are conducted at the same temperature, this single value can again be used to scale the normalised data to Nusselt number. For all spanwise or overall area averaged *htc* comparisons the same reference data set is used ($htc_{\mathrm{span.ref}}$ = 1497 W/m^{2}K and $htc_{\mathrm{avg.ref}}$ = 294 W/m^{2}K).

The positions of impingement jets under *H2* arrangement for all offset levels are clearly visible in the heat transfer pattern on the target surface. It can be seen that the peak *htc* underneath the jets decreases with the increasing standoff distance from $z/d = 1$ to $z/d = 6$ apart from $z/d = 3$ and 4 where the order is switched. The author speculateds that this is due to local over acceleration of the jet flow through the middle row of the five spanwise rows in the manifold during the experiment. When $z/d = 4$ these effects are stronger than for the other offset schemes which can be seen in the jet footprints. The largest jet to target spacing $z/d = 6$ in this study provides the lowest local *htc* underneath the jets due to the larger spacing which is likely beyond the extent of potential core while at the lowest standoff distance $z/d = 1$ the magnitude of local *htc* is exceptionally high (1.32 times the value at $z/d = 4$). As the offset decreases, the jet foot print becomes narrower with a steeper decay. For lower standoff distances with $z/d = 1$ and $z/d = 2$, the *htc* in the central well between streamwise rows ($x/d = 11.7$) is reduced due to stagnant flow between jets (as expected by numerical flow result). At $z/d > 3$ the heat transfer coefficient between the jets in the central well region increases to a low but near constant value. The effect of upwash fountains produces a moderate rise in local *htc* between neighbouring wall jets in the spanwise direction in which the pitch is tighter (*y*/*d* = 5.2), and reattachment of the spent flow on the root of the flange enhances local heat transfer coefficients in that region for all offset levels, however the level is higher at higher *z/d*. A larger jet-to-target allows a more coherent impingement footprint to exist on the target surface, albeit at a lower overall level of *htc*, while a smaller standoff distance produces higher intensity impingement, and a large 'dead' region under the centre of the manifold.

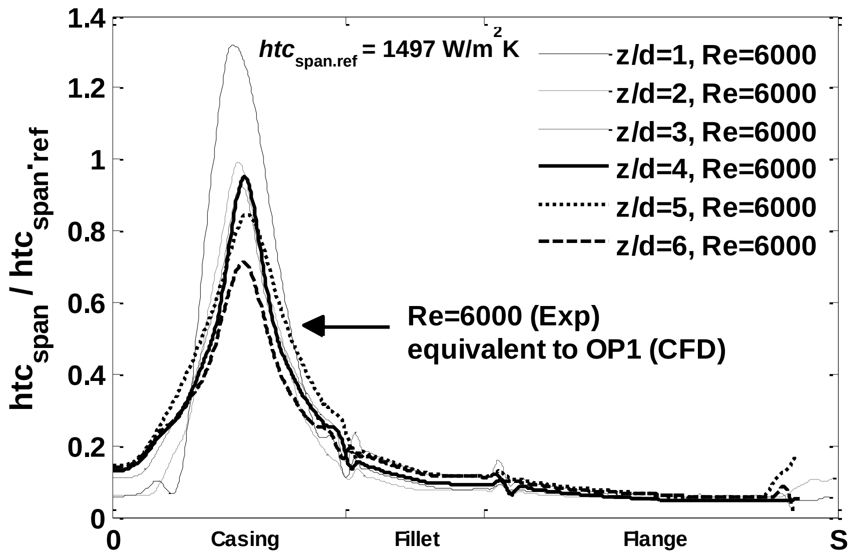

Figure 5.29 Spanwise averaged *htc* / *htc*$_{\text{ref (= H2}z/d\text{=4.peak.span.realizable k-}\varepsilon\text{.OP1)}}$ distributions for H2 *z/d*$_{\text{base}}$ = 1 - 6, experimental case Re = 6000 (EXP), equivalent to OP1.

Figure 5.29 shows the spanwise averaged distributions of the six offset experiments at Re = 6000. As the offset increased from *z*/*d* = 1 to *z*/*d* = 6, both the peak *htc* and the steepness of decay of the *htc* distribution is reduced. As expected at *z*/*d* = 1 and 2 the very low level of heat transfer is seen to increase between the streamwise rows

x/d < 11.7. A common feature at all standoff distances is the very low *htc* at the identical level, is seen on the top of the side wall.

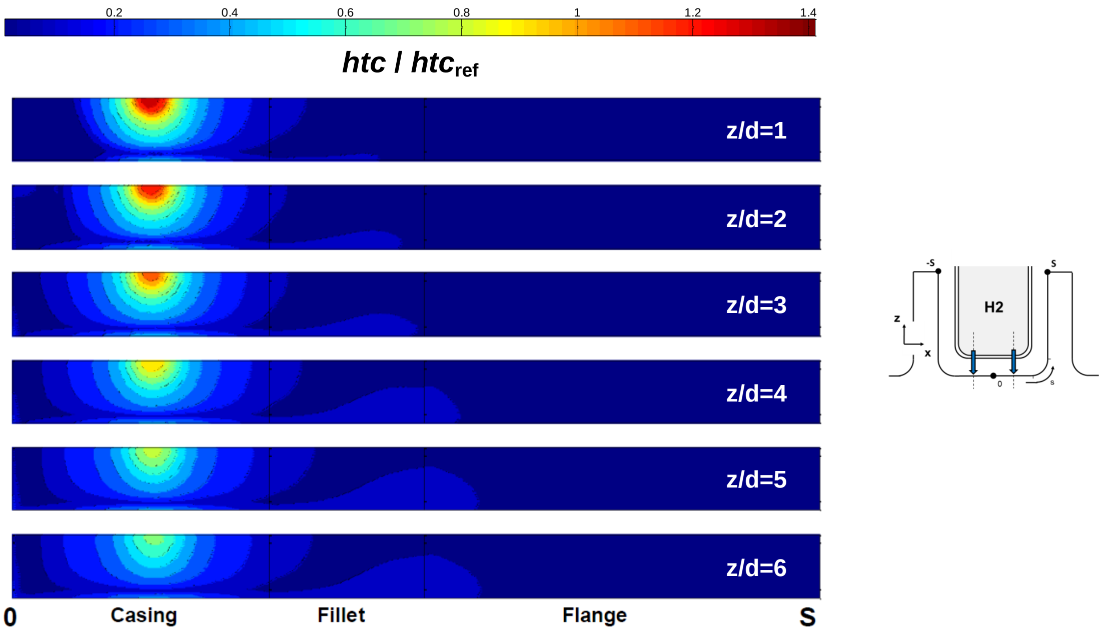

Figure 5.30 Local *htc* / *htc*$_{ref}$ $_{(= \text{H2 } z/d = 4.\text{peak.realizable k-}\varepsilon.\text{OP1})}$ distributions for H2 z/d_{base} = 1 - 6 scheme at OP1 (CFD).

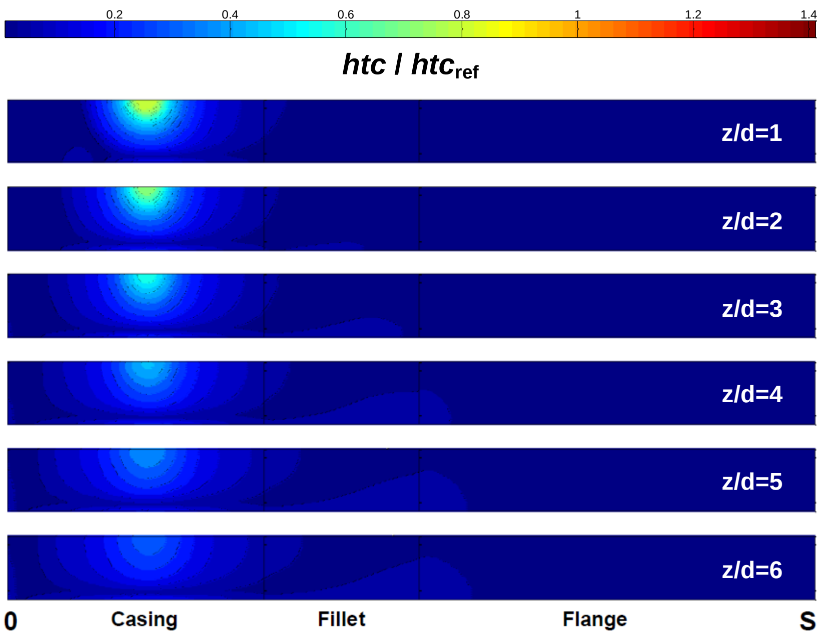

Figure 5.31 Local *htc* / *htc*$_{ref}$ $_{(= \text{H2 } z/d = 4.\text{peak.realizable k-}\varepsilon.\text{OP1})}$ distributions for H2 z/d_{base} = 1 - 6 scheme at OP2 (CFD).

CFD results at OP1, the case equivalent to the experimental data, are shown in **Figure 5.30**. The general trend in the predicted heat transfer pattern resembles the features observed in the measurement data set. The peak of predicted *htc* continuously reduces with increasing standoff distance, but each value is somewhat higher than that of the experiment by up to 30 %. The exceptions are the experiments conducted at z/d = 1 and z/d = 4 where the values are comparable within 5%. At the smallest standoff distance, z/d = 1 the peak CFD heat transfer coefficient is 1.2 times the value at the baseline configuration of z/d = 4, while this is reduced to a factor of 0.6 for the largest standoff distance of z/d = 6. CFD results show a local reduction in *htc* over the fillet area due to lengthier streamwise separated regions of flow compared to the experimental data seen in **Figure 5.28**, also observed is a smaller high *htc* streak on the side wall which also decays along the wall. The CFD study included an additional low Reynolds number OP2 condition as shown in **Figure 5.31**. The level of the heat transfer performance is uniformly lower compared to OP1, however, there were indistinguishable changes in the structure or relative levels of the heat transfer coefficient distributions.

The spanwise averaged *htc* distributions of the *H2* arrangement acquired from CFD are shown in **Figure 5.32**. Compared to the experimental result shown in **Figure 5.29** the prominence of the reattachment of flow at the fillet flange interface is more pronounced in the CFD study. This may be attributed to the reattachment being slowly unsteady in the case of the experiment, and the RANS model being incapable of picking up unsteadiness at this scale. It can be concluded that the peak of the spanwise averaged *htc* is globally over-predicted for most cases by up to 20 % using the realizable k-ε model compared to the experiment.

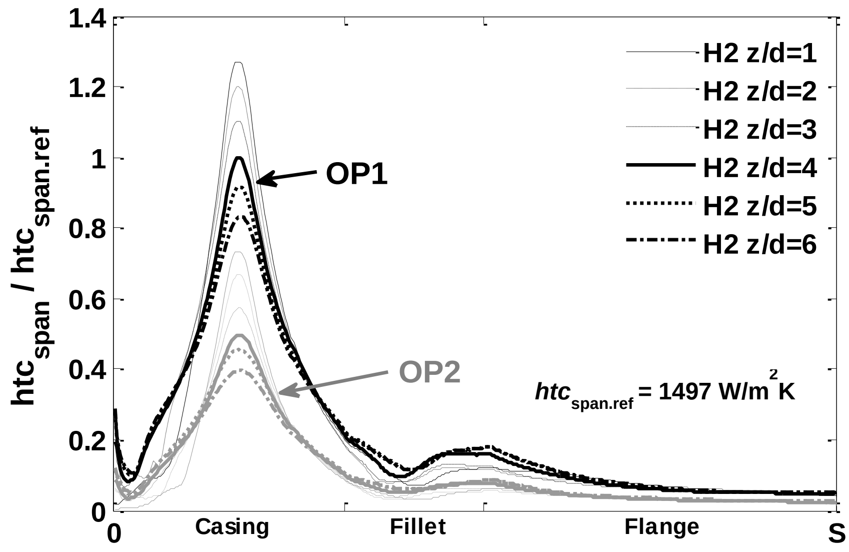

Figure 5.32 Spanwise averaged *htc* / *htc*$_{\text{ref}}$ (= H2 *z*/*d*=4.peak.span.realizable k-ε.OP1) distributions for H2 *z*/*d*$_{\text{base}}$ = 1 - 6 scheme (CFD).

The comparison of the overall (whole surface) heat transfer coefficient distribution for different standoff distances between the experiment (coloured by red) and CFD (by black) for the H2 cooling geometry, **Figure 5.33,** shows similar trends in the performance of each offset apart from *z*/*d* = 1 which is very much higher. It is however unlikely that an offset distance of *z/d* = 1 would be achievable in the engine, and undesirable to implement a scheme where the gradient of heat transfer with changing *z*/*d* would be so high.

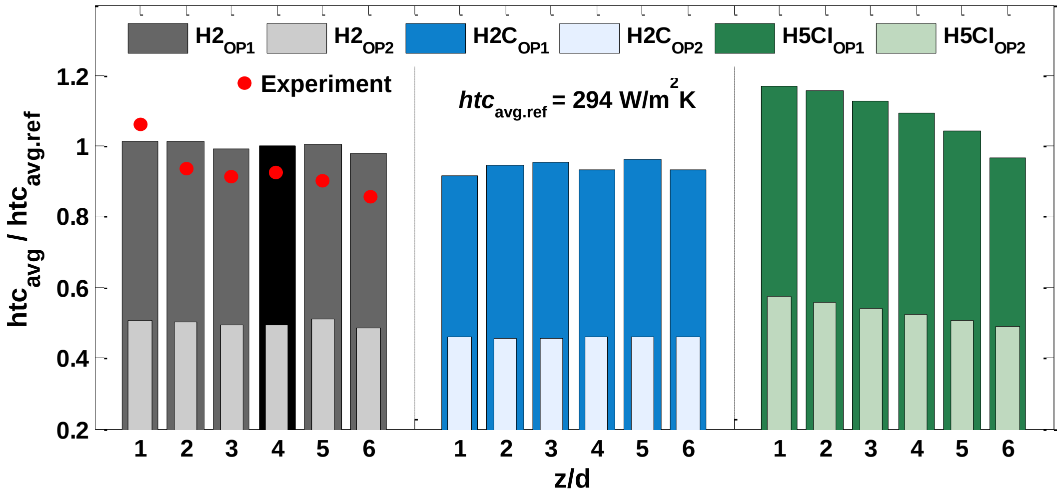

Figure 5.33 Relative performance of overall area averaged *htc* / *htc*$_{ref}$ (= H2 *z*/*d*=4.avg.realizable k-ε.OP1) at OP1 and OP2 – experimental results coloured by red.

5.3.3 External Casing Heat Transfer

Having established that the trend in local *htc* distributions is well captured by the CFD simulations for the baseline case, the results for the two alternative cooling configurations are reported below.

***H2C* Configuration.** **Figure 5.34** and **Figure 5.35** show local normalised *htc* distributions of *H2C* cooling arrangement at the six standoff distances simulated at both OP1 and OP2 conditions respectively. The heat transfer patterns indicate that as the cooling manifold standoff distance increases from z/d = 1 to z/d = 6, the stagnation point moves to the downstream side of the flange (radially outermost) still within the fillet radii area. The peak of local *htc* underneath the *H2C* impinging jets is lower than that of the *H2* baseline arrays at compatible standoff distances and mass flow conditions which is consistent with the larger local manifold to the casing wall offset. At the low offset cases with z/d = 1 and z/d = 2, jets are prone to *'push'* the flow into the exit side wall channel resulting in very little flow recirculating in the central well region and consequently very low heat transfer performance. When the manifold standoff $z/d >= 4$ the reversed angle of the jets starts to direct flow to the middle region, thus increasing its heat transfer coefficients. When $z/d = 5$ and $z/d = 6$, more extensive area of high heat transfer appears on the fillet, but the peak *htc* underneath each impinging jet values are greatly reduced: the jet is beyond the end of its potential core. The spanwise averaged *htc* distributions for *H2C* in **Figure 5.36** reflect most of features seen in the local *htc* maps.

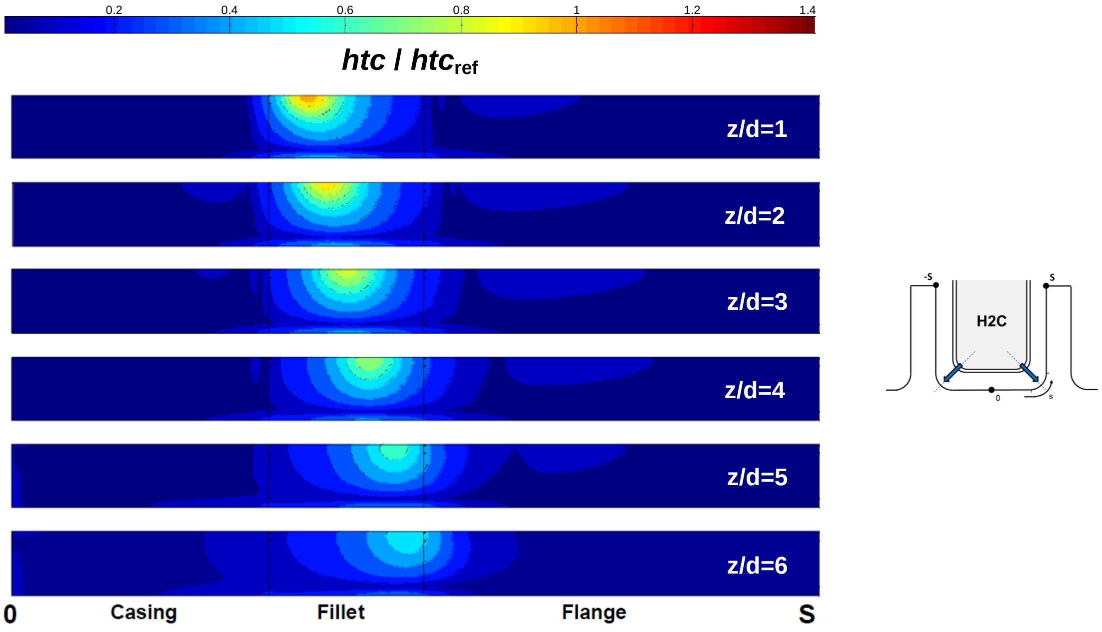

Figure 5.34 Local *htc* / *htc*$_{ref}$ $_{\text{(= H2 } z/d\text{=4.peak.realizable k-ε.OP1)}}$ distributions for H2C *z*/*d*$_{base}$ = 1 - 6 scheme at OP1.

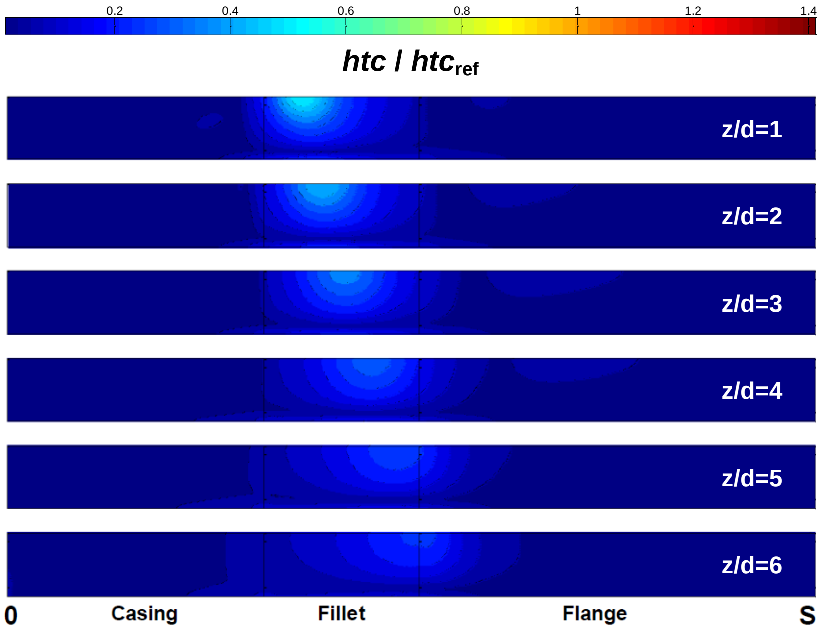

Figure 5.35 Local *htc* / *htc*$_{ref}$ $_{\text{(= H2 } z/d\text{=4.peak.realizable k-ε.OP1)}}$ distributions for H2C *z*/*d*$_{base}$ = 1 - 6 scheme at OP2.

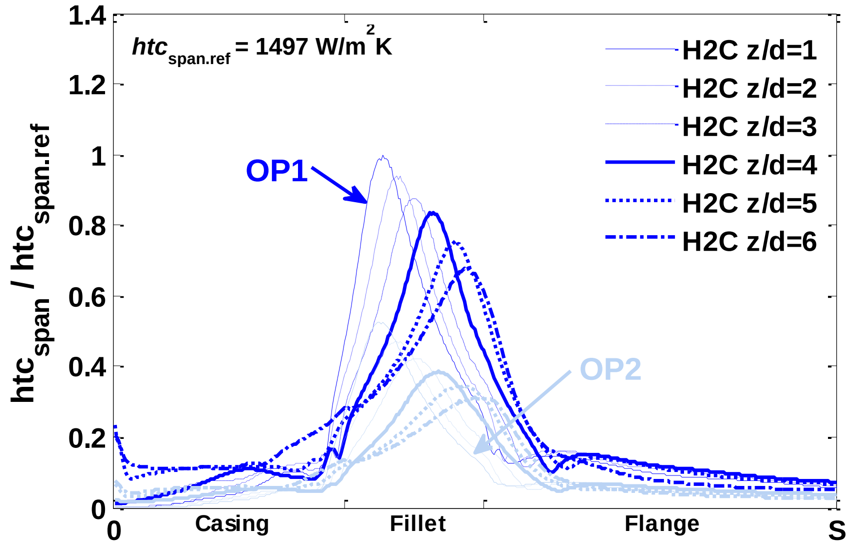

Figure 5.36 Spanwise averaged *htc* / *htc*$_{ref}$ (= H2 *z/d*=4.peak.span.realizable k-ε.OP1) distributions for H2C *z/d*$_{base}$ = 1 - 6 scheme.

***H5CI* Configuration.** **Figure 5.37** and **Figure 5.38** show local normalised *htc* distributions of *H5CI* cooling arrangement for the six standoff distances simulated at both the OP1 and OP2 conditions respectively. This combined impingement scheme produces much lower peak *htc* underneath each jet compared to the baseline *H2* configuration as the local standoff distance to jet diameter ratio has been increased from z/d_{base} = 1 - 6 to z/d = 1.6 - 9.4 (see **Table 5.1**) and the jet area reduced when the number of jets was increased at compatible mass flow conditions and offsets. A repeatable feature in the shape of the *htc* footprint in the central well region was observed for all offset levels and those heat transfer levels are decrease with the increase in the standoff distance. The outer jet locations are identical to the jets of *H2C* and the same changing jet flow direction occurs for each case. This results in similar heat transfer patterns with a smaller area of cooling over the fillet radii. At low offset cases with z/d_{base} = 1 and z/d_{base} = 2 there is no evidence of heat transfer enhancement between the outer jet and its neighbouring wall jet in the streamwise direction. At a manifold to casing wall spacing z/d_{base} = 3 the reversed flow from the outer wall jet is pushed into the upwash region and creates a moderate rise in local *htc*. **Figure 5.39** shows clear evidence of the growth in *htc* over the region when plotted as spanwise averaged *htc*. As expected more rapid decay in the spanwise averaged *htc* underneath each jet in the central well region can be seen as the standoff distance is reduced from z/d_{base} = 6 to z/d_{base} = 1. Unlike the other schemes such as *H2* and *H2C*, the cooling effective area under *H5CI* arrangement is rather uniform due to the tighter jet-to-jet pitch in both the streamwise and spanwise direction.

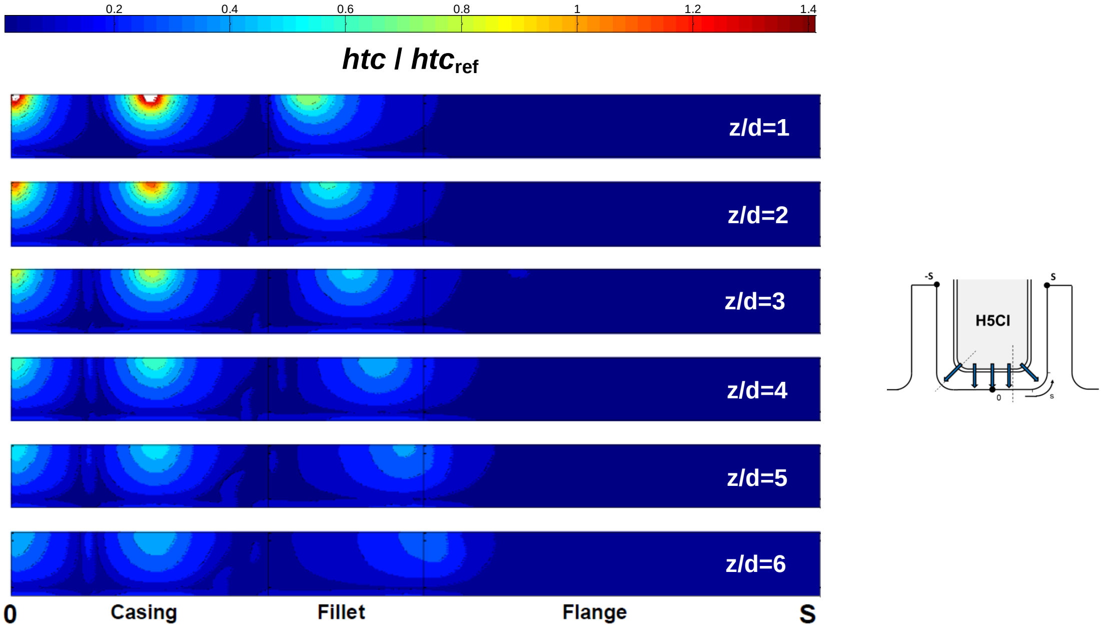

Figure 5.37 Local *htc* / *htc*$_{ref}$ $_{(= \text{H2 } z/d=4\text{.peak.realizable k-}\varepsilon\text{.OP1})}$ distributions for H5CI *z*/*d*$_{base}$ = 1 - 6 scheme at OP1.

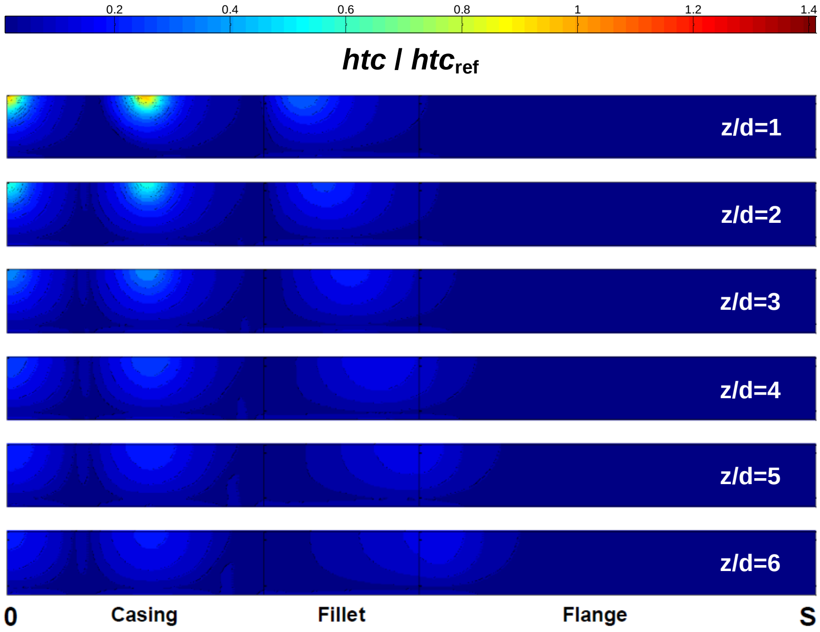

Figure 5.38 Local *htc* / *htc*$_{ref}$ $_{(= \text{H2 } z/d=4\text{.peak.realizable k-}\varepsilon\text{.OP1})}$ distributions for H5CI *z*/*d*$_{base}$ = 1 - 6 scheme at OP2.

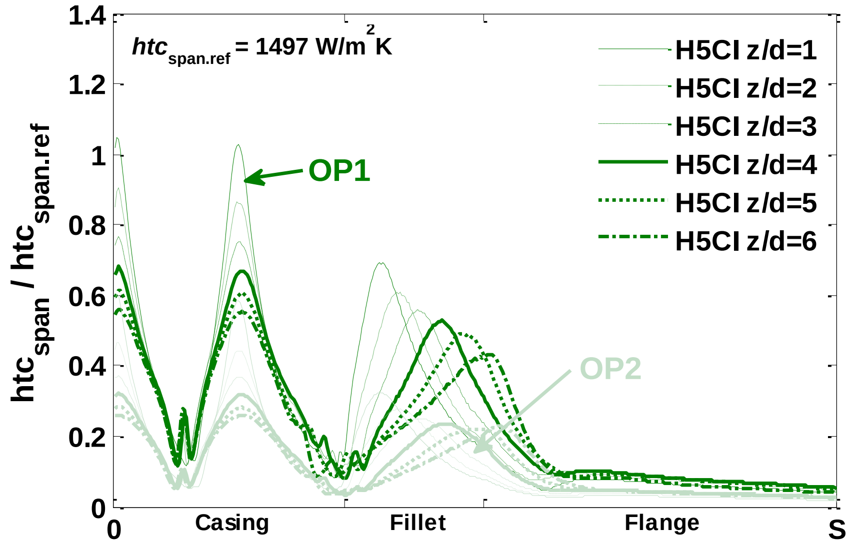

Figure 5.39 Spanwise averaged *htc* / *htc*$_{ref}$ (= H2 *z*/*d*=4.peak.span.realizable k-ε.OP1) distributions for H5CI *z*/*d*$_{base}$ = 1 - 6 scheme.

Overall Performance. Overall heat transfer performance is presented as total area averaged *htc* normalised by the baseline data set in **Figure 5.33**. Note that the graph is directly compatible to the **Figure 5.8** which presents the performance for a range of impingement cooling arrays with the fixed standoff distance z/d_{base} = 4. Once again the increase in the coolant mass flow rate from OP2 to OP1 results in a rise of *htc*. Where the sparse arrays of impinging jets are employed, in particular *H2* and *H2C*, the variation in the overall area averaged *htc* with six standoff distances is low (in the range -2 % to +1.3 % at OP1 and -1.1 % to +1.7 % at OP2 for the *H2* configuration, and -8.4 % to -3.9 % at OP1 and -4.0 % to -3.3 % at OP2 under the *H2C* array). The two arrays employed in this offset study are sparser than typical arrays used for blade cooling designs such e.g. **Florschuetz et al. (1981)**, **Son et al. (2001)**, **Baily and Bunker (2002)**, **Brevet et al. (2002)**, and **Xing and Weigand (2013)** where the cross flow to jet flow mass velocity ratio is an additional governing parameter. In contrast when the denser array of jets of the *H5CI* configuration is used, the overall *htc* varied from -3.3 %

to +17.2 % at OP1 and -0.4 to +8.1 % at OP2. This is surprisingly large compared to the baseline case by a factor of up to 8. The *H5CI* array shows a near linear drop in overall area averaged *htc* associated with increasing cooling manifold standoff distance.

5.4.4 Casing Temperature and Displacement Prediction

The predicted casing temperature and thermal displacement compared to cold build conditions at operating condition OP1, each of the six standoff distances and the three different impingement cooling configurations is plotted against length along the engine casing in **Figure 5.40**. In this figure the displacements look comparable one to another and are considered in more detail below, however there are some striking differences in the temperature distribution:

- in the dummy flanges the temperature is notably lower for both the *H2C*, and *H5CI* cases compared to the *H2* baseline condition;
- between the dummy flanges (*l,s* = 0 - 20 mm) the temperature is lowest for the *H5CI* case with a central impinging jet, followed by the *H2* and *H2C* condition;
- the *H5CI* case has the lowest average temperature at the inner casing over the region *l* = 0 - 40 mm;
- the *H5CI* case has the highest change in temperature with standoff distance.

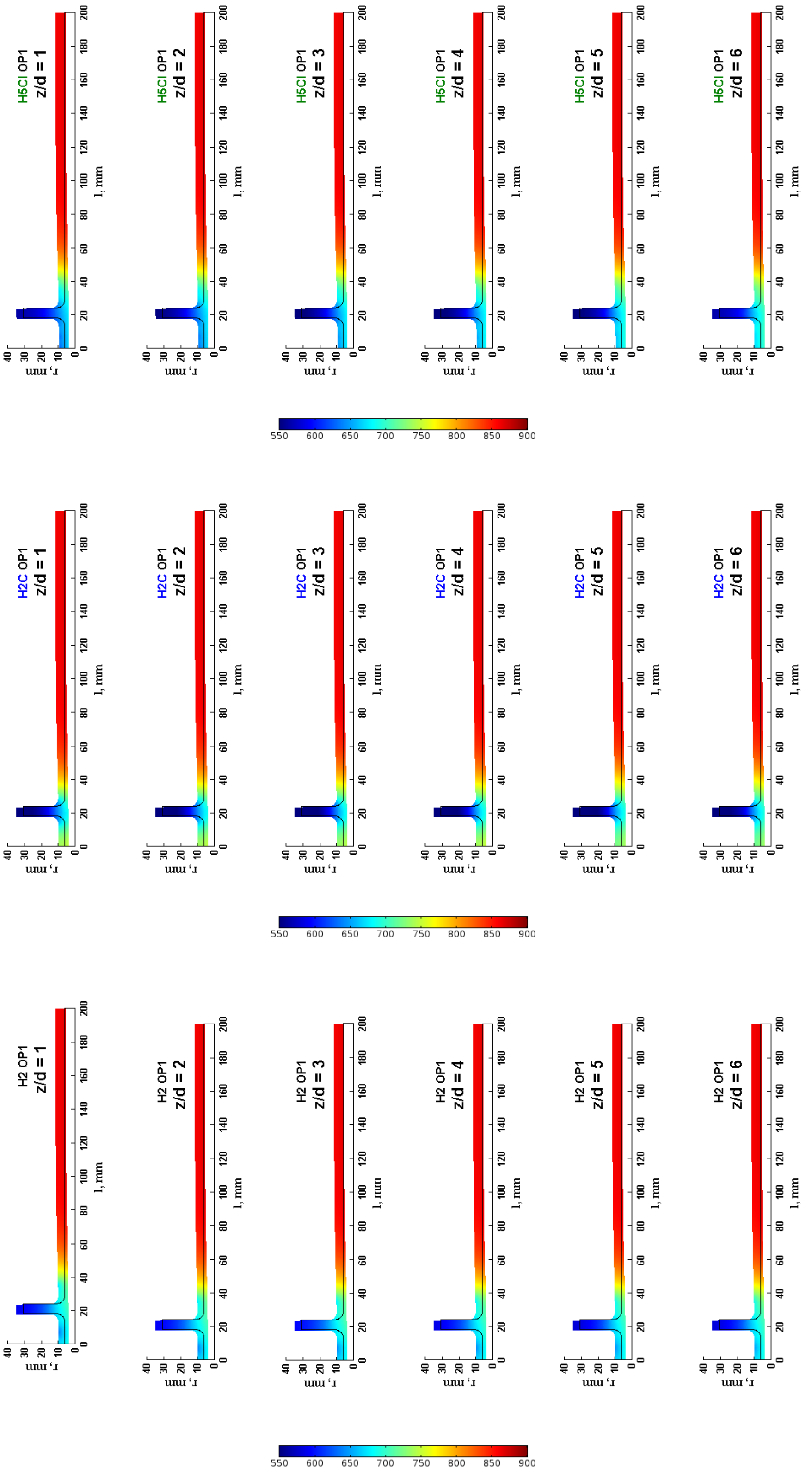

(a) (b) (c)

Figure 5.40 Predicted casing temperature (K) and thermal radial displacement (r, mm), (a) H2 = 1 - 6, (b) H2C = 1 - 6, (c) H5Cl, z/d_{base} = 1 - 6 at OP1.

Figure 5.41, **Figure 5.42** and **Figure 5.43** include all the FEA cases conducted using the applications of *htc* for casing radial closure and metal temperature at the point of the casing liner attachment under *H2*, *H2C* and *H5CI* arrangements respectively. In addition to the operating points reported in detail above a further three operating points have been considered representing in total Idle, Cruise (new), Cruise (engine worn), max take off (new), max take off (engine worn), see **Table 3.1**. The average jet Reynolds number was inferred from the total coolant mass flow rate delivered to the casing cooling manifold, assuming uniform distribution between cooling holes. Going from cold to hot conditions an initial differential growth between the edge of the casing and the centre of ~0.5 mm occurs because of the temperature gradient through the dummy flange when situated in the fire zone. With engine representative coolant mass flow rates of 0.02 - 0.35 kg/s additional casing contractions of $\delta r = 0.5 - 2.1$ mm can be achieved for the baseline *H2* configuration with manifold standoff distance of $z/d = 4$. The equivalent range of contraction for the *H2C* configuration is $\delta r = 0.57 - 2.04$ mm, and for the *H5CI* configuration $\delta r = 0.54 - 2.17$ mm. The maximum contraction achieved was with the *H5CI* configuration, running at $z/d_{base} = 1$, where $\delta r = 0.58 - 2.25$ mm. Again, the difference in contraction achieved is small but significant: the 0.25 mm reduction in tip clearance directly translates to an approximately 0.3 - 0.4 % reduction in specific fuel consumption at cruise **(Rolls-Royce, 2011).**

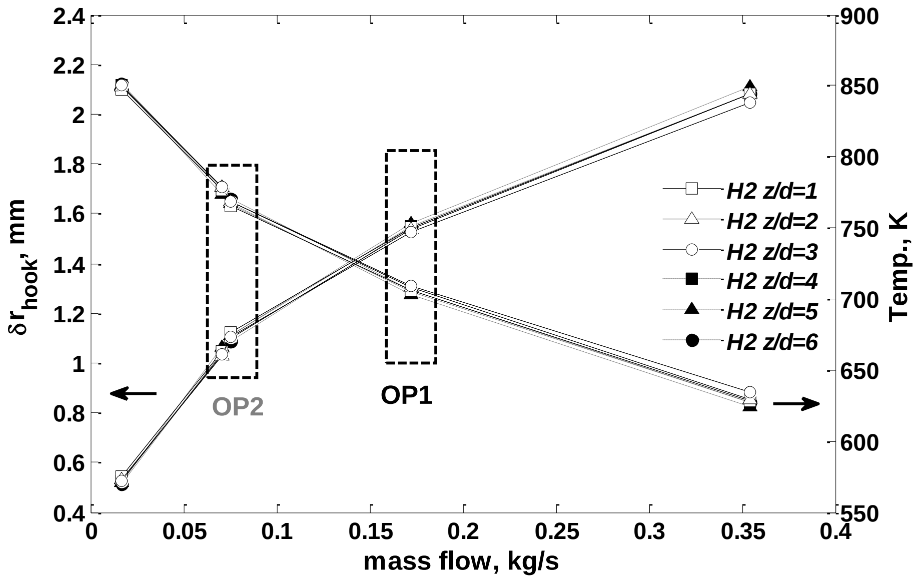

Figure 5.41 Predicted casing temperature (K) and closure (mm) versus coolant mass flow rate, at liner attachment point, for H2 *z*/*d*$_{base}$ = 1 - 6 scheme.

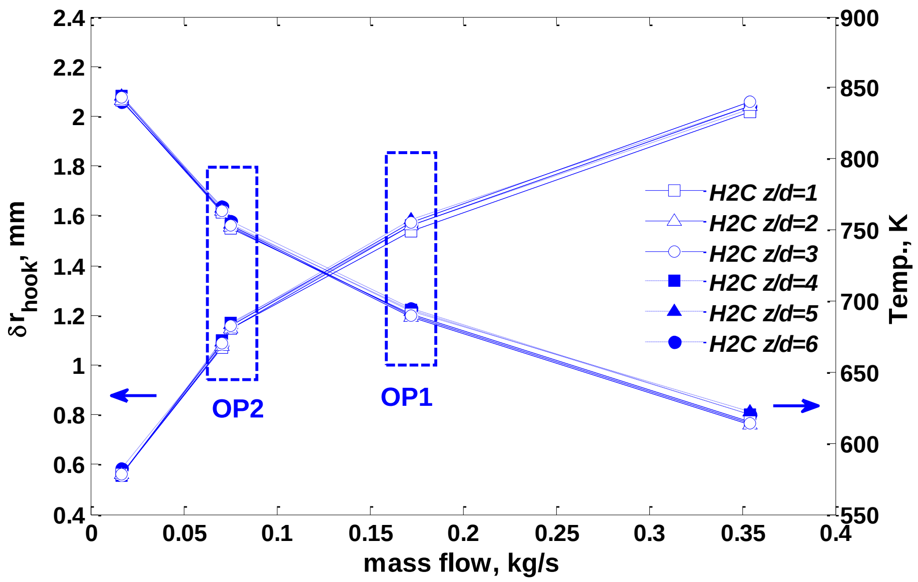

Figure 5.42 Predicted casing temperature (K) and closure (mm) versus coolant mass flow rate, at liner attachment point, for H2C *z*/*d*$_{base}$ = 1 - 6 scheme.

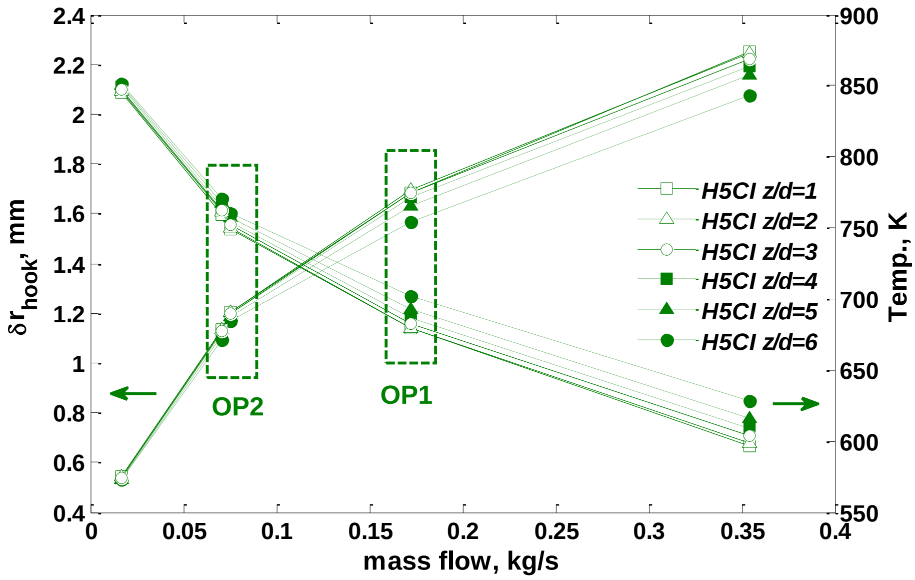

Figure 5.43 Predicted casing temperature (K) and closure (mm) versus coolant mass flow rate, at liner attachment point , for H5CI z/d_{base} = 1 - 6 scheme.

Overall Performance. **Figure 5.44** and **Figure 5.45** show the relative temperature and closure performance at two of the operating condition OP1 and OP2. These are presented in normalized format by comparison to the baseline *H2*, *z*/*d* = 4 data set. Note that the graph is directly compatible to the **Figure 5.25**. The comparative thermal closure variations are -1.4 to 0.8 % over the range of standoff distance for configuration *H2*, -0.6 to 2.2 % for *H2C* and 1.1 to 9.6 % for *H5CI* which is notably much greater. The level of the temperature drop is aligned to the closure trend: -2.7 to 1.3 % for H2, 6.3 to 10.3 % for *H2C*, and 2.0 to 16.4 % for *H5CI*. The higher convective heat transfer underneath the *H5CI* impingement cooling and higher variation in *htc* leads to larger thermal closure, and closure variation. Cooling over the fillet radii in configuration *H2C*, which showed lower overall *htc* levels over the external than those of *H2*, produces slightly larger thermal closure at all offset levels. This is because the benefit comes limiting heat conduction into the dummy flange, which in turn requires less cooling to maintain a low temperature.

Considering manufacturing tolerances such that axisymmetric installation of the annulus manifold causing slight different local standoff distance to external casing, the system with *H2* or *H2C* cooling designs might be better options delivering similar output and less impact to the thermal closure associated with the initial offset intended. However, the benefit in closure of the *H5CI* offers more flexibility in terms of adjusting cooling capacity by physically changing the offset of the manifold during rebuilds over the engine life.

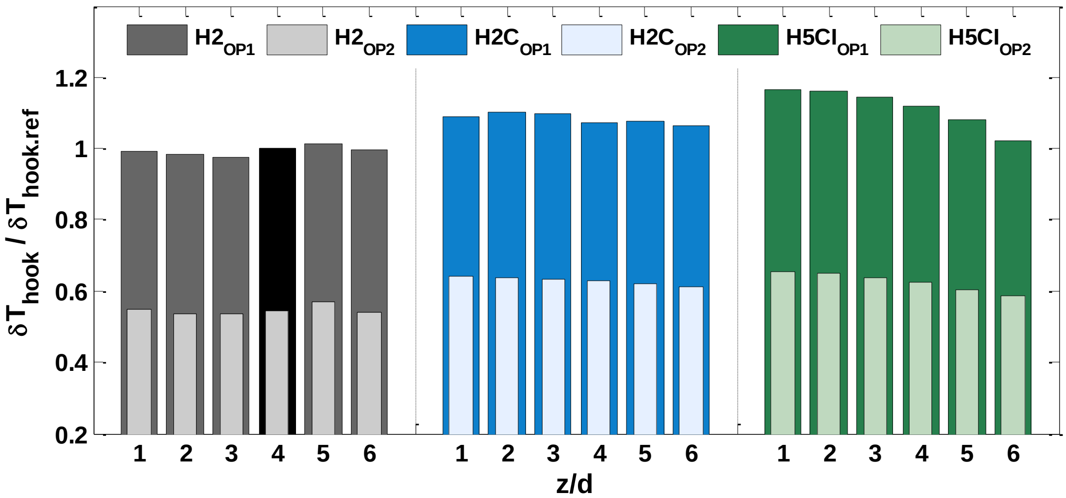

Figure 5.44 Relative performance of casing temperature drop at the liner attachment point by internal hooks, compared to baseline H2 *z/d* = 4 scheme at OP1 and OP2.

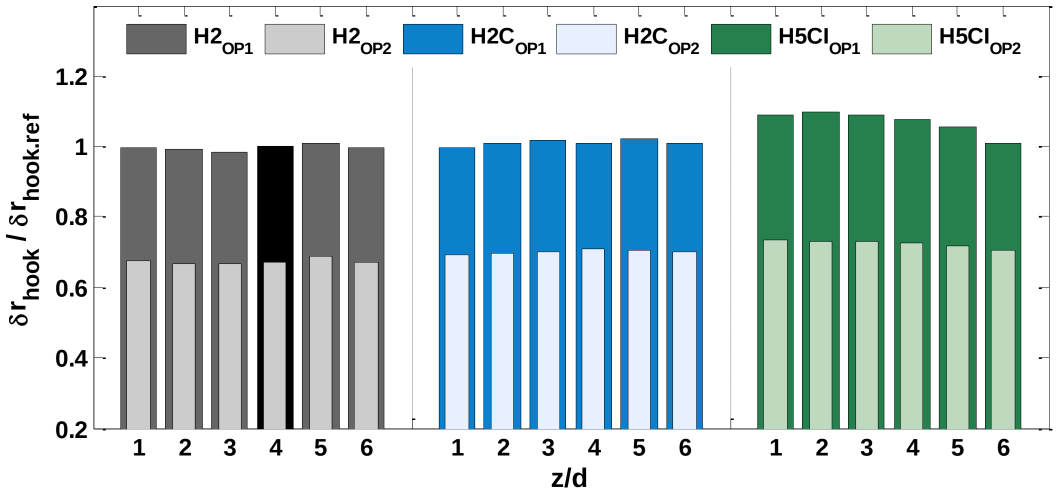

Figure 5.45 Relative performance of casing closure at the liner attachment point by internal hooks, compared to baseline H2 *z/d* = 4 scheme at OP1 and OP2.

5.4 Summary

In this chapter, the effectiveness of a range of impingement cooling arrangements in creating engine casing closure is characterised. The effects of jet-to-jet streamwise pitch, number of rows of jets, inline and staggered jet arrays are assessed through comparison of the convective heat transfer coefficient distributions as well as the thermal closure at the point of the casing liner attachment. The investigation is primarily numerical, however, one geometry has been validated experimentally using a transient liquid crystal technique. Steady numerical simulations using the realizable k-ε, k-ω *SST* and EARSM turbulence models were conducted to understand the variation in the predicted local heat transfer coefficient distribution. A number of conclusions have been drawn regarding the design of the cooling manifold. It has been shown that:

- A combination of impingement onto both the target surface and the flange fillets is desirable.
- The use of inline or staggered arrays of jets causes insignificant changes in heat transfer coefficient.
- The realizable k-ε model produced results closer to experimental results than any other two equation turbulence model investigated.

Finite element modelling has been used to link external heat transfer coefficient distributions generated for a wide range of cooling geometries to the displacement of internal casing at engine representative operating conditions under steady running. From the resulting temperature distribution and sensibly imposed thermal boundary conditions, changes in the expected casing thermal closure against coolant mass flow rates were predicted. The key points observed are:

- Cooling the fillet at the dummy flange constricts heat conduction into the flange creating larger thermal closure.
- Uniformly distributed cooling arrangements lead to better contraction capability at a set coolant flow rate, but at with are more sensitive to the manifold standoff distance.
- Surprisingly for sparse arrays there is very little variation in total average *htc* or contraction observed with changing z/d_{base} over the range 1 - 6, and this suggests that uniformity in the circumferential distribution of casing contraction can be achieved whilst mounting the manifold relative to the casing using a simple pinning strategy at several points around the circumference.

Chapter 6 The Effect of Local Casing Features and External Dummy Flanges on Casing Contraction

In the previous chapter the effect of the external cooling distribution on casing contraction was investigated. In this chapter, the effect of changes to the casing geometry itself is considered. Two main geometric parameters have been investigated: the thickness of the casing and the extent (radial height) and position of the annular dummy flanges. The baseline cooling geometry is employed in these studies, being remodelled in CFD with the same cooling hole configuration where there are substantial changes in the casing geometry. From the results the relative importance of turbine casing and annular dummy flange on casing closure is characterized, and an idealised modification of the design of the dummy flange considered to improve the closure performance.

6.1 Thermo-mechanical FE Casing Model

The effect of external casing thickness and the external dummy flange radial height on casing closure was examined using a consistent FE modelling approach as per Chapter 4. Three casing thicknesses of 6 mm (1.0 × *th*), 4.5mm (0.75 × *th*) and 3 mm (0.5 × *th*) were examined, while the thickness is generally determined from consideration of containment, it is hoped that casing cooling designs will have application in other areas of the engine. In the dummy flange geometry investigation, its radial length was changed from 25 mm (1.0 × *H*) to 12.5 mm (0.5 × *H*), and the number of flanges was increased by a factor of 2. Separate models were constructed for each geometry tested. The findings suggest how the geometric features may be manipulated to obtain an optimised system with for both contraction and weight. **Figure 6.1** shows the parametric variations applied in this study; summarised as:

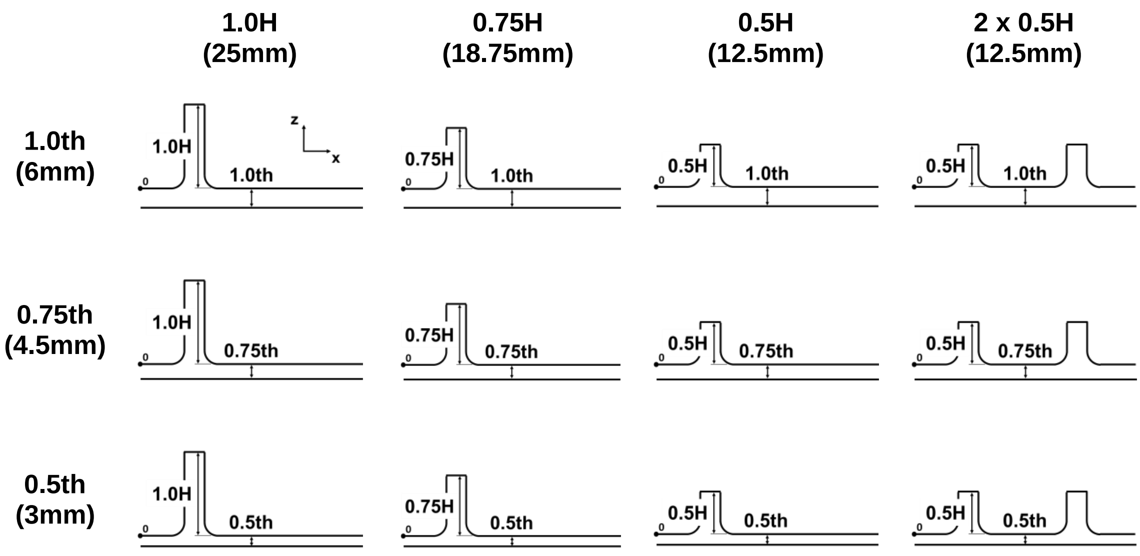

Figure 6.1 Various casing geometries simulated for thermo-mechanical analysis. Note that position 0 represents a centreline of the system.

Note that the casing inner radius, *R*, was constrained at 0.4 m; the baseline casing thickness, *th* = 0.006 m; the baseline height of the dummy flange, *H* = 0.025 m. As before structural boundary conditions were added at the axial extremities of the model to approximate the constraints imposed by structural installations in a real engine such that there is no rotation of the casing otherwise the model is radially and axially free to move.

Thermal Boundary Conditions. The external thermal boundary conditions applied to the cooled region as convective heat transfer that simulate the cooling system were inferred from standalone computational fluid dynamics analyses conducted in Chapter 5. Operating conditions OP2 and OP1 were considered with the *H2*, *H2C* and *H5CI* cooling configurations, see Chapter 5.4, the relevant data are reproduced in **Figure 6.2**. For changing flange height, the data were curtailed, rather than an additional CFD test being conducted. This is considered valid as the flow field is parabolic in that region.

The total average normalised heat transfer coefficient for each of the parametric variations is shown for the full range of manifold offsets z/d_{base} = 1 - 6 in **Figure 6.3**. Once again the reference *htc* is the overall area averaged data for the baseline *H2* cooling arrangement with z/d_{base} = 4 at operating point OP1, taken from realizable k-ε results. The average *htc* shows an increase with reduced flange height as the far downstream region is at the lowest *htc*, however this is in part balanced by the reduction in cooled area associated with the loss of material. The error bars on the black, green and blue data points, in fact represent the range of *htc* as z/d_{base} = 1 - 6, and the z/d_{base} = 4 point has been plotted as an unfilled data marker. The red points represent the averaged data from the three configurations with six different offsets. The reduction in cooled area by downsizing the dummy flange also leads an increase in the averaged *htc* discrepancy over the full range of standoff heights for each cooling configuration, as is apparent from the larger ‘error’ bars in the figure. The increase is by up to a factor of 1.2 for each cooling configuration. The change in casing thickness has no impact on the external heat transfer applied as the total cooled area remains constant, and thus data for 0.5*th*, 0.75*th* and 1.0*th* are overlapped in that format.

The remainder of the external and internal thermal boundary conditions in the model were fixed set out as per in Chapter 4 to allow the effect of the impingement system to be assessed in a consistent format.

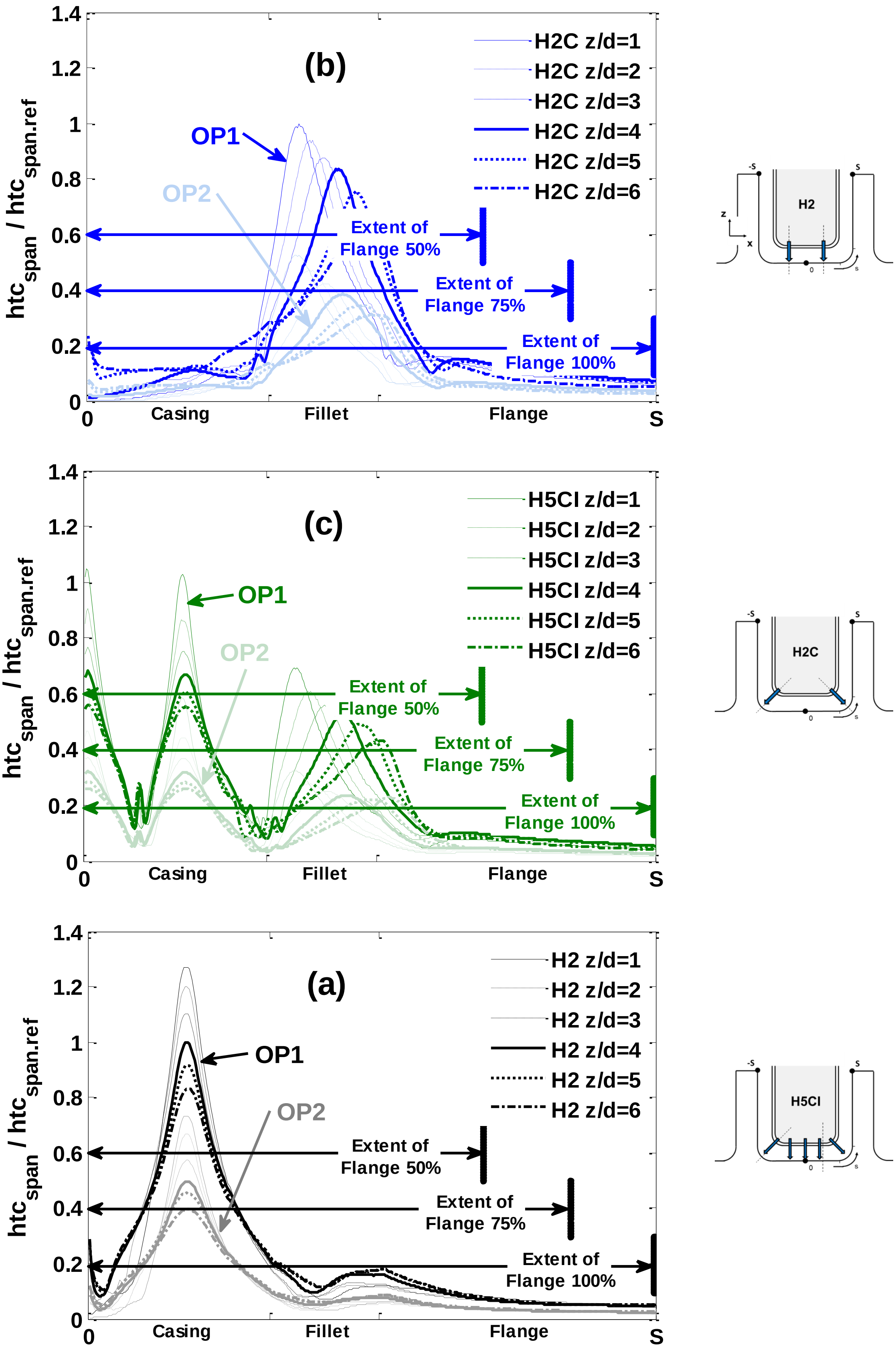

Figure 6.2 Normalised heat transfer distributions applied to the different extents of external casing as thermal boundary condition.

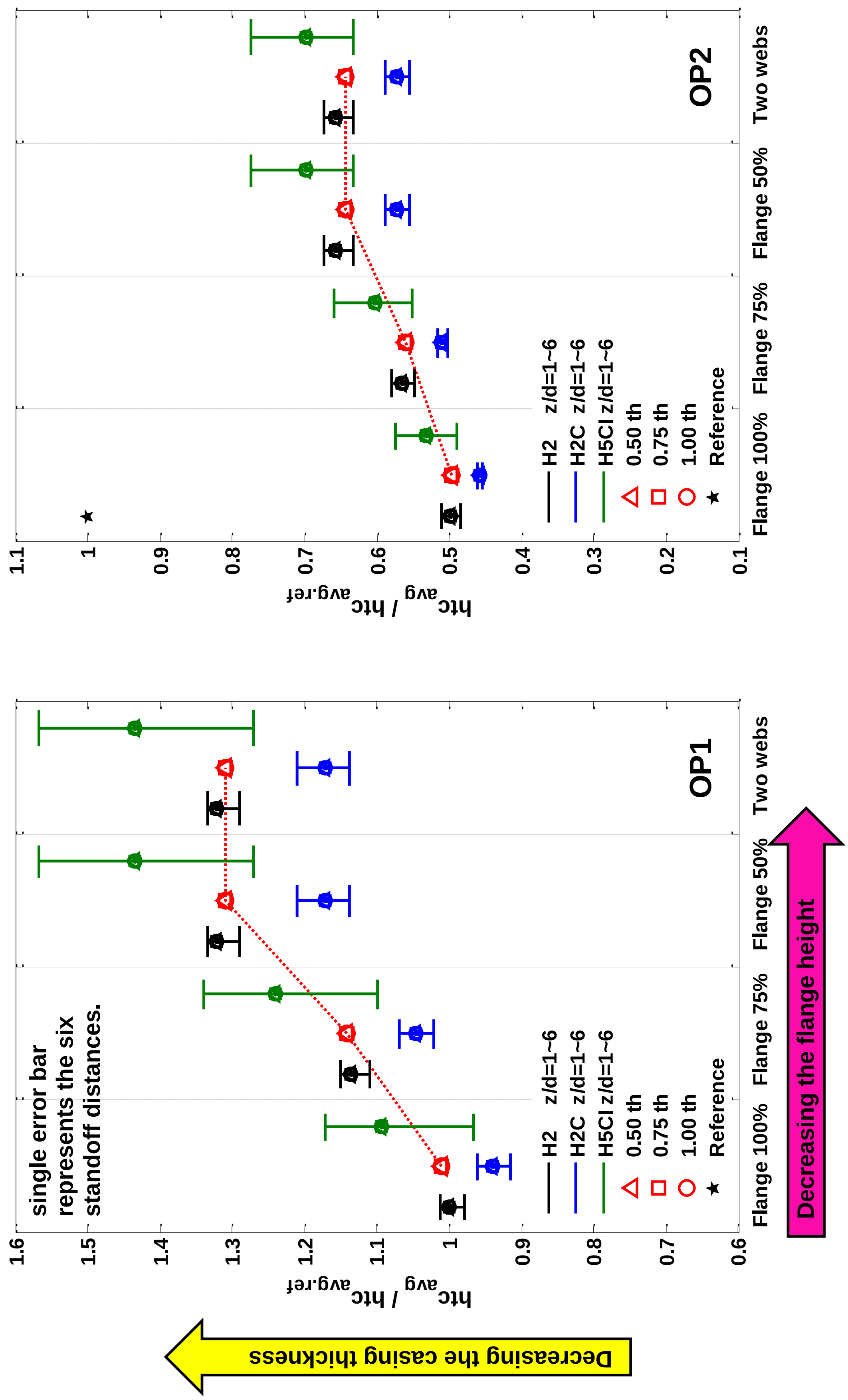

Figure 6.3 Relative performance of overall area averaged *htc* / *htc*$_{ref\ (=\ H2\ z/d=4.avg.realizable\ k\text{-}\varepsilon.OP1)}$ at OP1 and OP2.

6.2. The Effect of Casing Thickness

6.2.1 Casing Temperature Displacement Prediction

Figure 6.4 to **Figure 6.9** show the predicted casing temperature distributions and thermal displacement profiles using the *H2*, *H2C* and *H5CI* cooling configurations with fixed standoff distance of $z = 4d_{\text{base}}$ at operating conditions OP1 and OP2. The change in closure in this graphical format can barely be detected, the magnitude of change being in the order of quarter millimetre scale (which is equivalent to 4.2 % of main casing thickness 6 mm.) What is, however, apparent is the temperature gradient across the domain, and in particular through the dummy flange region. Here considering any of the cooling geometries at either of the operating conditions, the temperature at all points in the flange is adversely affected by curtailing the height of the flange, this reduces the contraction capability of the metal that is left in place. Dividing the total mass of the dummy flange into two flanges one that sits passively in an uncooled region appears to be totally ineffective: the higher temperature of the larger secondary mass of metal (compared to the casing which is has replaced) may in fact pull the casing further away from the axis at the hook attachment point. The general temperature distribution is the same as reported in section 5.4.4. Under the *H2* baseline configuration (see **Figure 6.4** and **Figure 6.5**), the main casing is cooled more than the region near the flange. That region remains relatively hot compared to the *H2C* and *H5CI* configurations as shown in **Figure 6.6** to **Figure 6.9**. On the other hand, the *H2C* configuration effectively constricts radial heat spread through the flange. The *H5CI* cooling scheme shows some aspects of both the other configurations and provides more uniform cooling across the central area and flange.

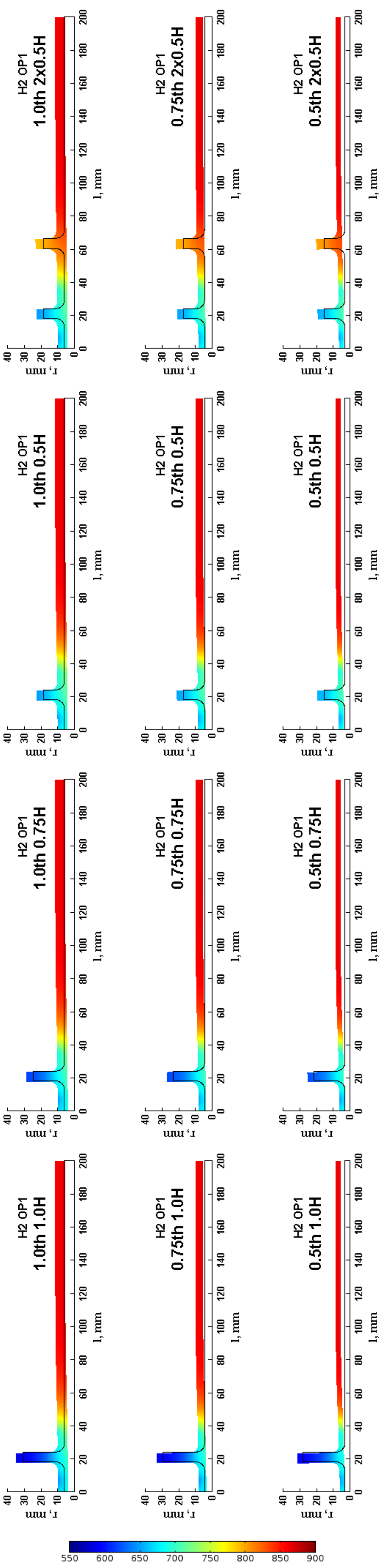

Figure 6.4 Predicted casing temperature (K) and thermal radial displacement (r, mm), H2 *z/d* = 4 at OP1.

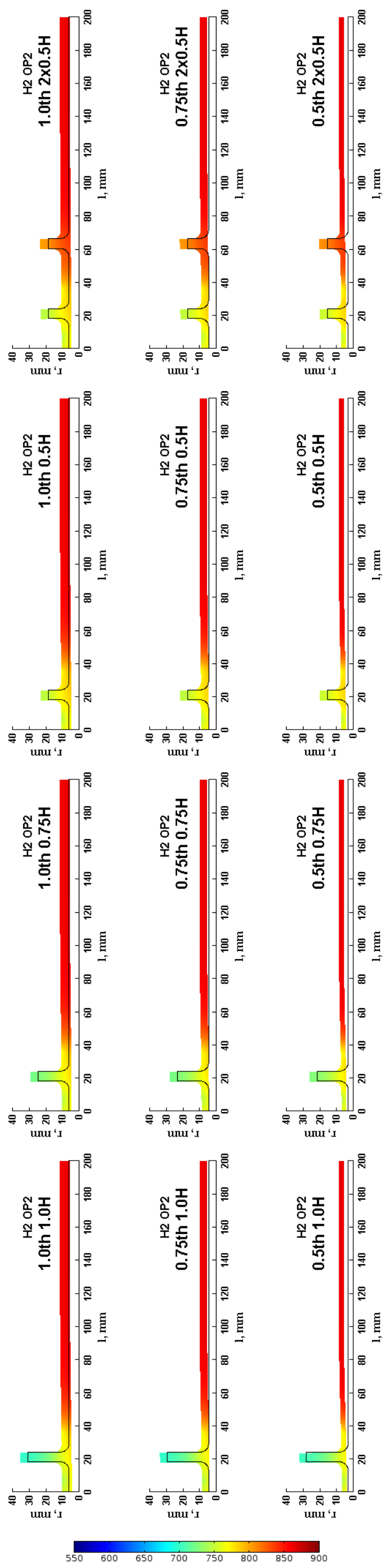

Figure 6.5 Predicted casing temperature (K) and thermal radial displacement (r, mm), H2 *z/d* = 4 at OP2.

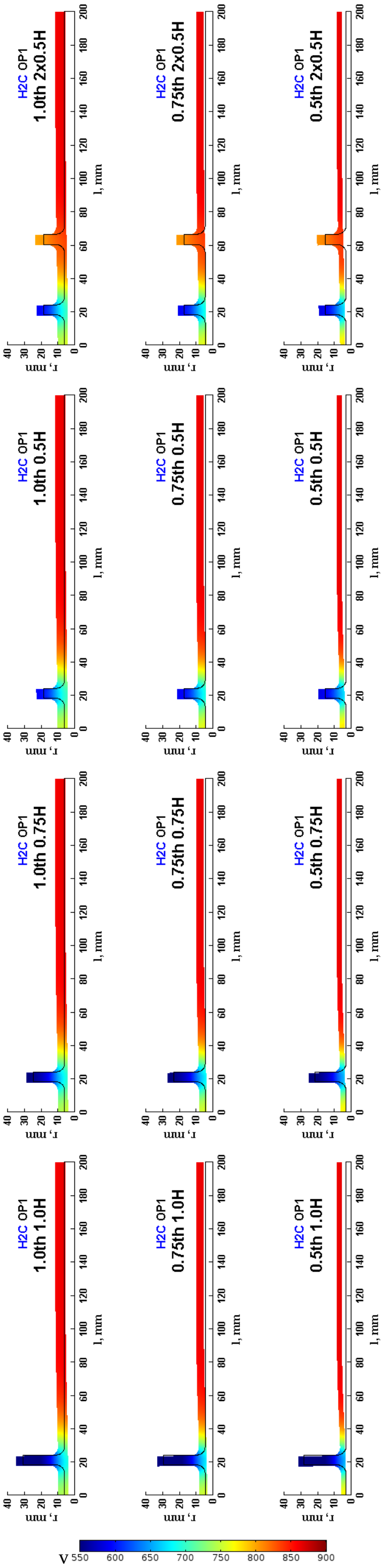

Figure 6.6 Predicted casing temperature (K) and thermal radial displacement (r, mm), H2C *z*/*d* = 4 at OP1.

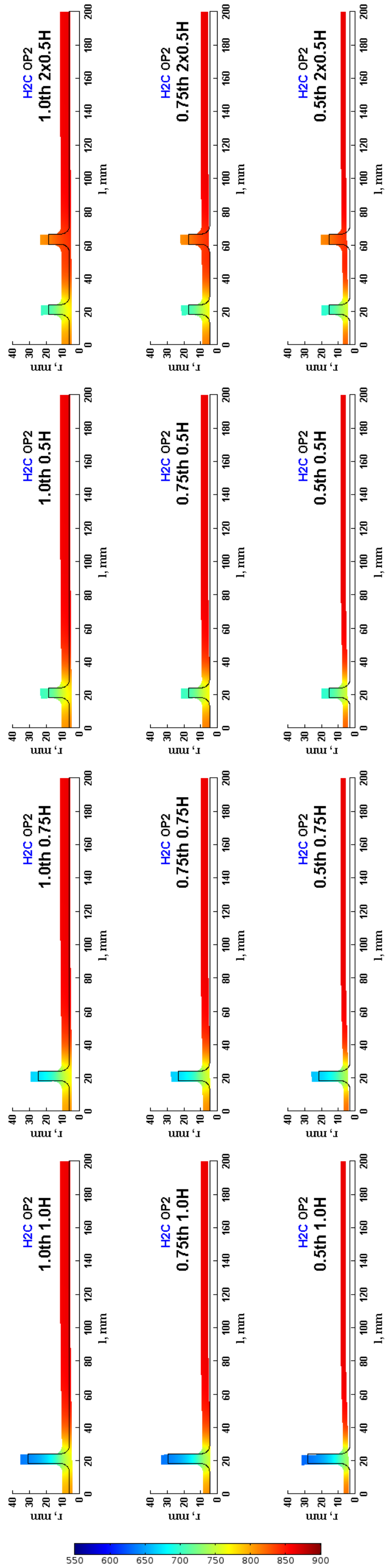

Figure 6.7 Predicted casing temperature (K) and thermal radial displacement (r, mm), H2C *z*/*d* = 4 at OP2.

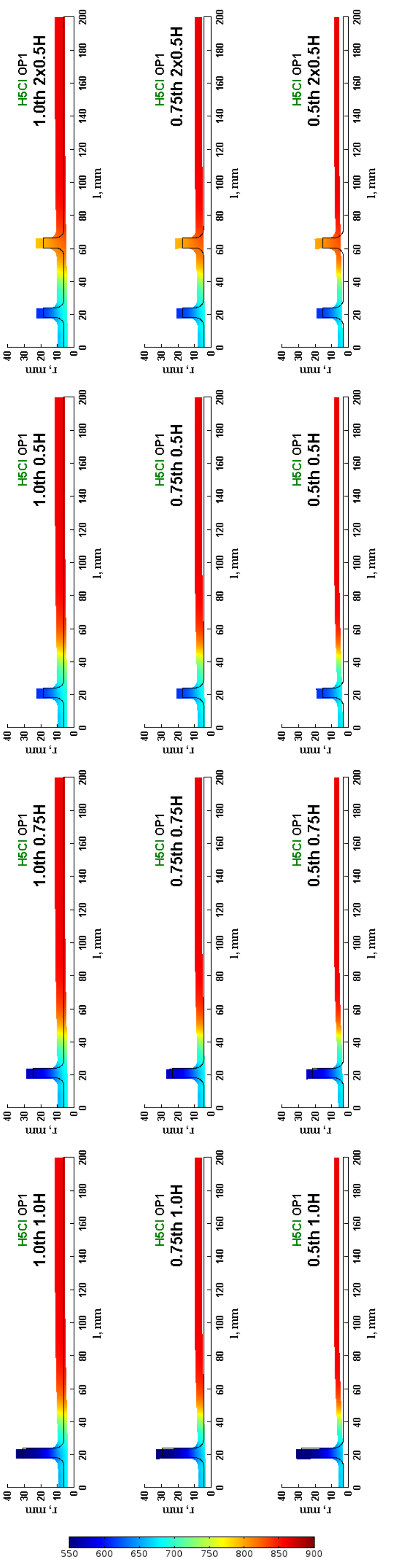

Figure 6.8 Predicted casing temperature (K) and thermal radial displacement (r, mm), H5CI *z/d* = 4 at OP1.

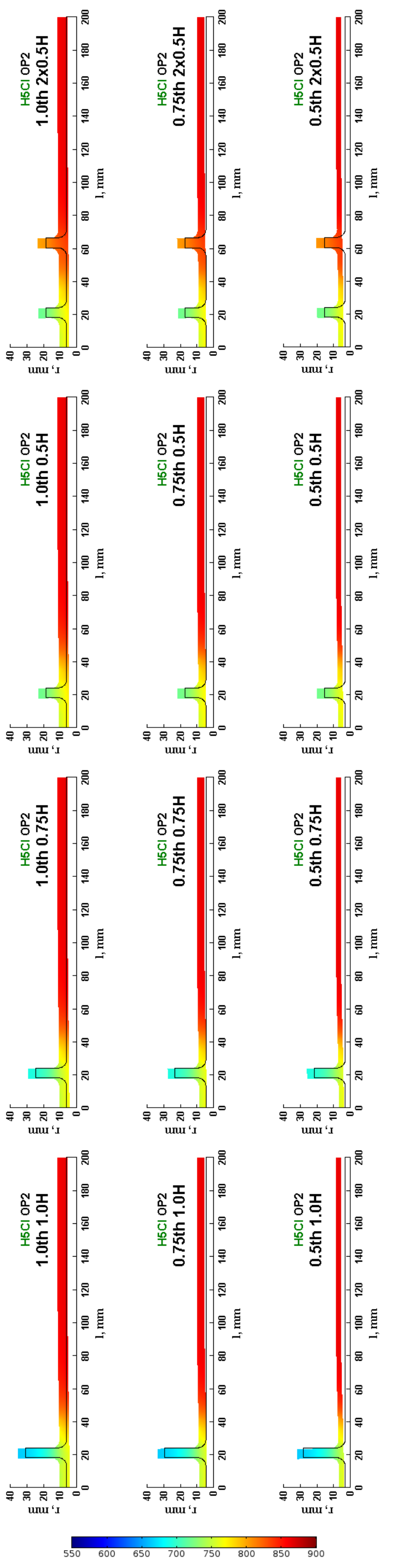

Figure 6.9 Predicted casing temperature (K) and thermal radial displacement (r, mm), H5CI *z/d* = 4 at OP2.

The variable thickness study employed a fixed inner radius casing and with the thickness varying in the range 0.5*th* to 1.0*th* (3 to 6 mm). In the figures presented each row is at constant thickness and each column has a constant thermal control flange height and configuration. Regardless of size of radial extent or number of dummy flanges, the general pattern in regard to the radial extent of main casing is clear. The thinner the casing the larger the overall closure and more dramatic change in the temperature gradient between the inside and outside of the casing.

In a more comprehensive format, **Figure 6.10** and **Figure 6.11** show temperature drop and casing closure which is defined as the difference in radial growth between the far field l = 200 mm position and the position of attachment of the casing liner above the HP blade as per section 5.2.2. The reference data used for the normalisation is the prediction value from the default casing geometry with 1.0*th* and 1.0*H* under baseline *H2* z/d = 4 external cooling scheme operating at OP1. Each error bar represents the six different cooling manifold offset cases from a cooling arrangement (black for *H2*, blue for *H2C* and green for *H5CI*) and in total 216 cases are compared at a single operating condition. The red points represent the averaged value for the three different arrays together with the six standoff distances. Under the *H2* array with full size flanges (first column at black colour in the figure), there is a possible improvement in thermal closure up to 10 % for an initial 25 % reduction in the thickness of the casing (0.75*th*) at OP1 condition. This can be increased to 26 % through when the thickness is reduced to 0.5*th*. Each error bar represents the variation in temperature drop and thermal closure for the six manifold standoff locations and unsurprisingly increases as the casing gets thinner. Cases with the *H2C* arrangement caused larger thermal closure and a cooler temperature at the liner attachment point for all thickness levels simulated compared to the *H2* arrays employed. The 0.75*th* and 0.50*th* size casing thickness with 1.0*H* full size flange then result in a 14 % and 36 % improvement in the casing contraction and a 17% and 30 % lower hook attachment point temperature using the *H2C* cooling configuration at operating condition OP1. As expected the *H5CI* cooling configuration shows improved in thermal casing contraction by up to 19 % for the 0.75*th* casing and 37 % for the 0.5*th* thickness casing at operating condition OP1. When the coolant mass flow rate is reduced to operating condition OP2, the cooling contraction also is reduced, with the reduction scaling similarly for each cooling configuration.

The average temperature drop for the three different cooling configurations together with six offset cases (representing eighteen cases, coloured red) in **Figure 6.10** indicate the full range of temperature and closure change for each cooling and casing combination. Comparing to that of closure shown in **Figure 6.11**, the temperature variation is seen to be smaller than the closure variation. Slight changes in the thickness of the casing result in much larger changes in the thermal contraction at a given normalised temperature.

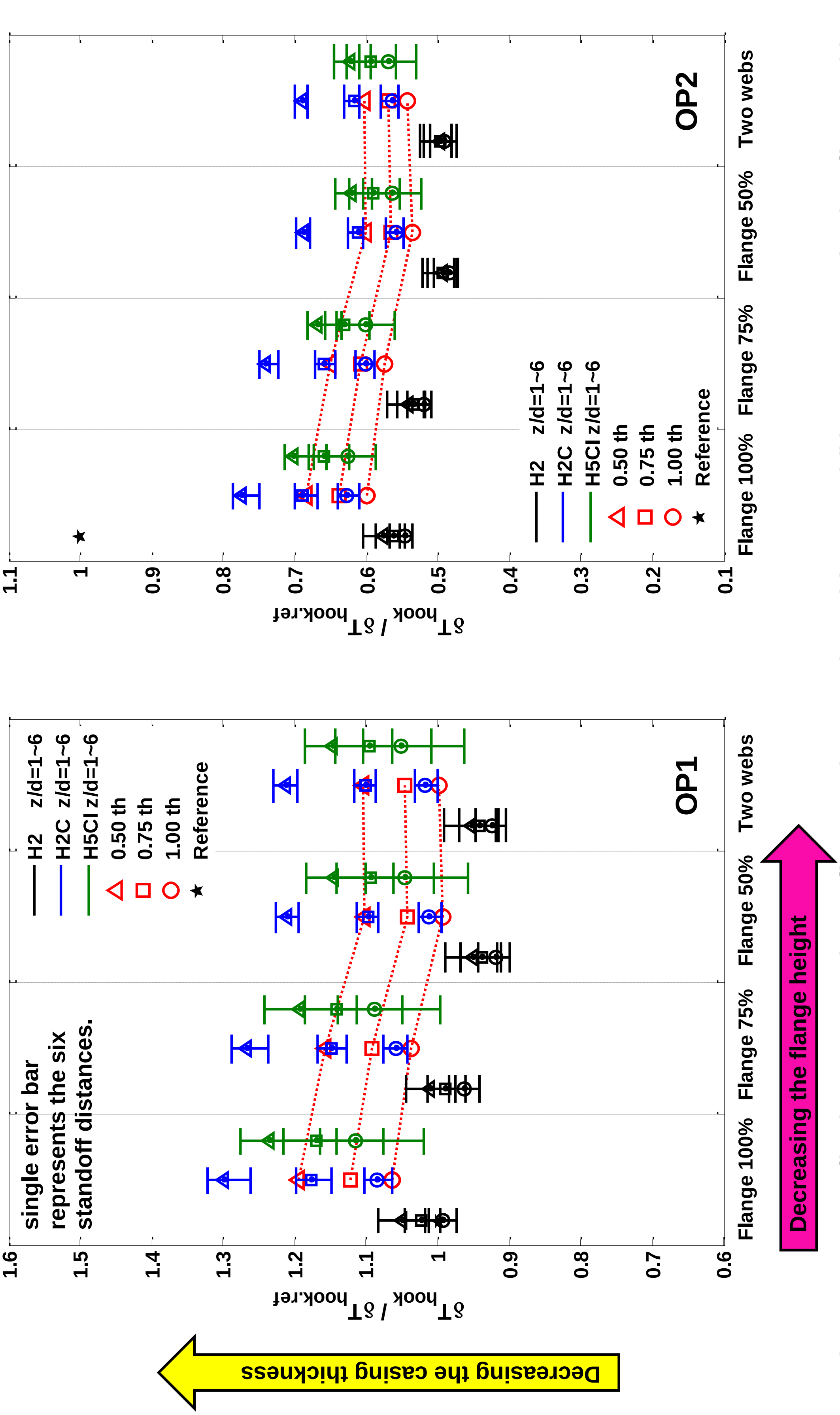

Figure 6.10 Normalised temperature drop at liner attachment point at (a) OP1 and (b) OP2, compared to baseline H2 *z*/*d* = 4 scheme at OP1 employed.

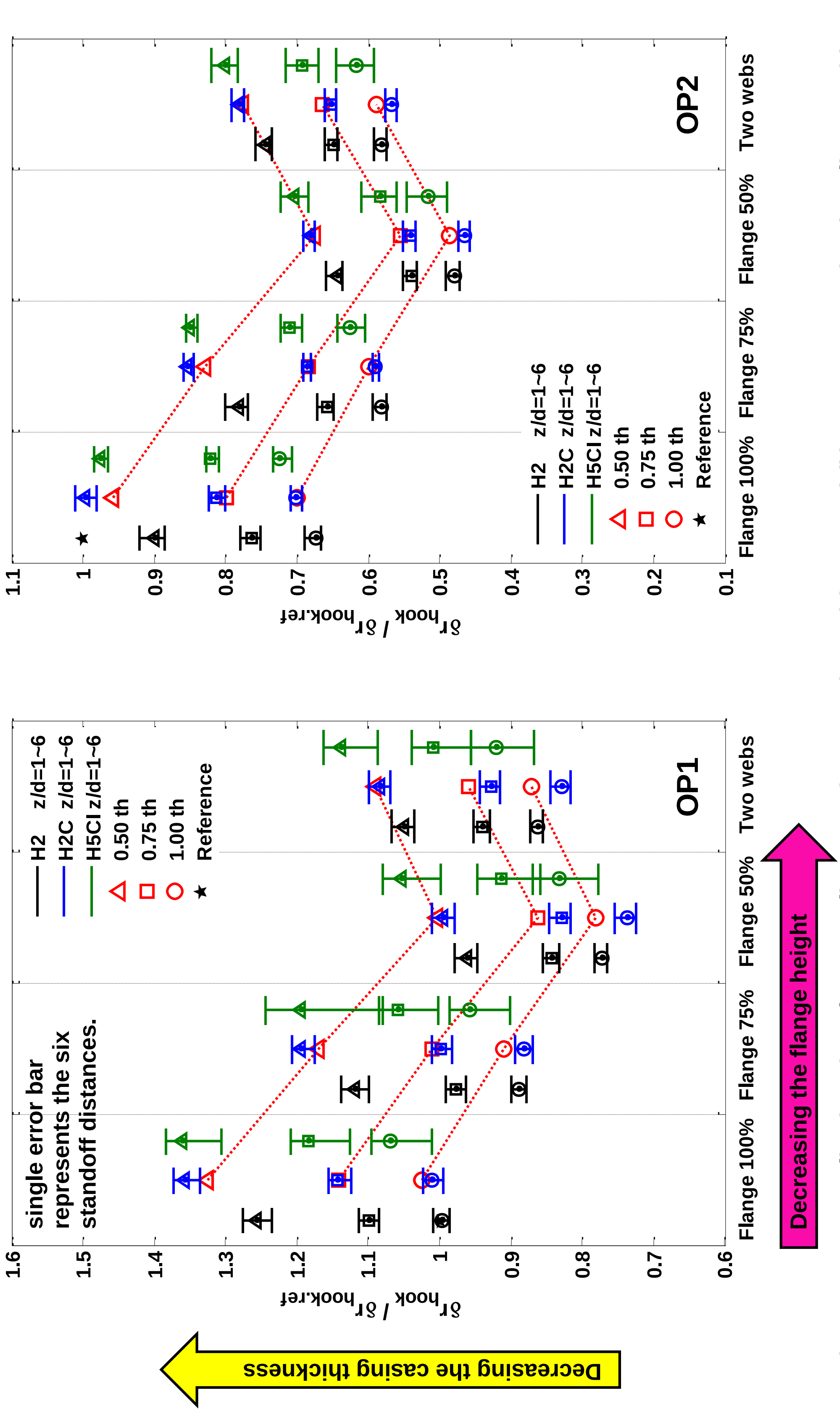

Figure 6.11 Normalised casing closure at liner attachment point at (a) OP1 and (b) OP2, compared to baseline H2 *z/d* = 4 scheme at OP1 employed.

6.3 The Effect of Dummy Flange Extent

6.3.1 Casing Temperature Displacement Prediction

To assess the effect of the dummy flange geometry in **Figure 6.4** to **Figure 6.9**. data from the same row should be compared, giving the same casing thickness but 4 different dummy flange configurations. The effect of changing the radial height of the flange is clear. Downsizing to either 0.75*H* or 0.5*H* cause significant decrease in the steady-state closure in the radial direction. This is because the reduced external cooling area is proportional to the total heat flux level on the surface and hence overall the casing temperature has remained hotter, but also that the flange remains hotter than the full height flange. **Figure 6.10** and **Figure 6.11** show the quantified data. The cooling contraction is reduced by approximately 10 % for the *H2* and *H5CI* cooling configurations and 13 % for *H2C* when the radial height of the flange is reduced by 25 % of its original height. When two half sized dummy flanges are attached to the casing this can be recovered to the level achieved by a flange of height 0.75*H*, though of course with additional weight. The reduction ratio for *H2C* array is somewhat larger because the benefit from the cooled flange is no longer available with shorter thermal mass.

6.4 The Effect of Elliptic Dummy Flange

Parametric study above shows that the dummy flanges play a key role in controlling the thermal closure. The flange acts as cold thermal mass which provides a compressive stress on the casing as it expands through heating. Corner impingement is effective in increasing contraction capability by removing heat from the solid which would otherwise heat the dummy flange. This has the effect of allowing the dummy flange to remain cold without requiring extensive active cooling. Minimising the amount of cooling air required to keep the flange cold by adjusting the flange geometry is therefore an attractive means of improving the tip clearance control system. There is no reason why the thermal control system should not have an arbitrarily shaped flange: indeed in this thesis the flange is deliberately referred to as a dummy flange to indicate that its use is solely for location and assistance in the thermal closure process, and not to provide containment of hot gases. In a recent patent **Kerby (2013)** set out some the cross sections of various thermal control dummy flange which may be used in embodiments of casing cooling system, see **Figure 6.12**. (Some are highly unlikely to be manufactured!) Of course these may also induce flow patterns and pressure changes around the casing.

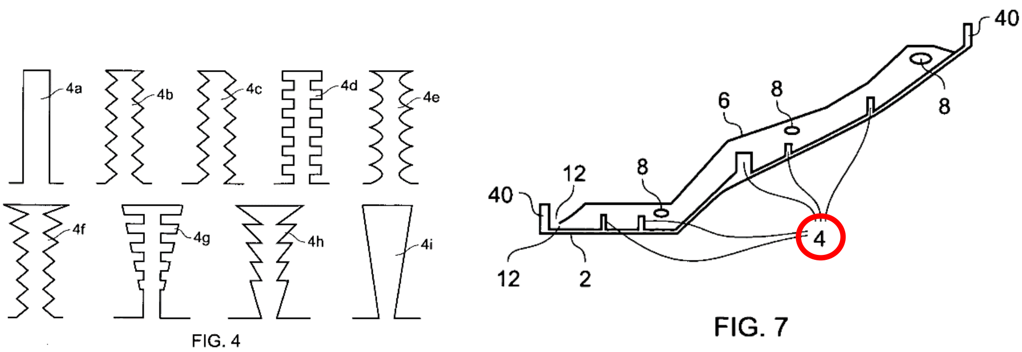

FIG. 4 FIG. 7

Figure 6.12 Various flange features and possible external casing axial positions (4), Kerby (2013)

In this study, elliptically necked dummy flanges at their root fillet were introduced to reduce the conduction path into the flange and accordingly increasing its surface area (see **Figure 6.13**). The author notes that some cartoons depicting such an elliptic indent without claiming its design are embodied in patents by **Bucaro et al. (2009)** and **Estridge et al. (2009)**. One advantage of the adopted design is that it only needs minor modification of the current package in terms of manufacturing capability and creates minor impact on the flow system. In reality, it is noted that a smooth transition to the flange would be required, but this would not invalidate the analysis shown below. Three levels of necking in the root width of the flanges were examined: labelled 1.0*N* (baseline), 0.83*N*, 0.67*N* and 0.5*N*.

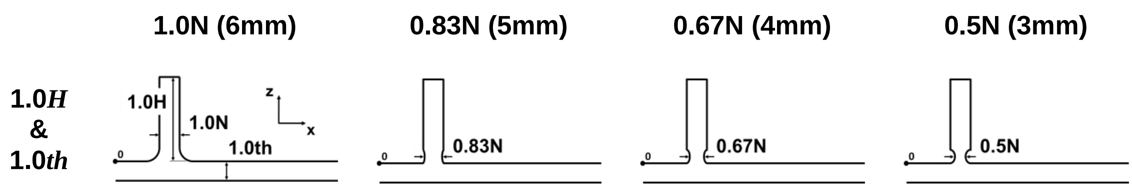

Figure 6.13 Casing models with various elliptic dummy flanges

Note that the baseline *H2* cooling configuration at z/d = 4 was solely used for this study; the *htc* distribution was re-established through CFD simulations for each of the revised geometries and applied onto the casing including modified flange neck design. A newly imposed *htc* distribution is shown in **Figure 6.14**. An additional benefit appears to be a stronger reimpingement of spent flow from the impingement upwash onto the root of the flange in the necked region.

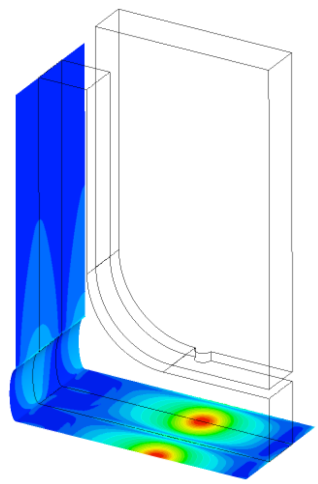

Figure 6.14 Typical impingement *htc* jet foot print over the external surface of 0.83*N* model, indicative data only – blue = low, red = high

6.4.1 Casing Temperature Displacement Prediction

The predicted casing temperature and thermal displacement of the idealised engine casings with elliptic dummy flanges is shown in **Figure 6.15**. The dummy flanges with 0.83*N* 0.67*N* and 0.5*N* elliptical necking show very similar temperature distributions in the central region when compared to the prediction using the baseline 1.0*N* casing geometry. However, moving outwards along the dummy flange from the internal casing surface (which is nearly isothermal below the flange at each condition), the temperature is lower with increased necking of the flange at its root. This is the case for all of the operating conditions OP4 though OP1. The result is not surprising. The necking restricts the heat flow into the flange for a given temperature difference, scaling linearly with the thickness at the neck. Once the heat flow is reduced, the temperature rise of the flange which bathed in slow, cold flow, is reduced. While this should increase the temperature gradient across the neck of the flange, it is insufficient to recover the same heat flow into the flange.

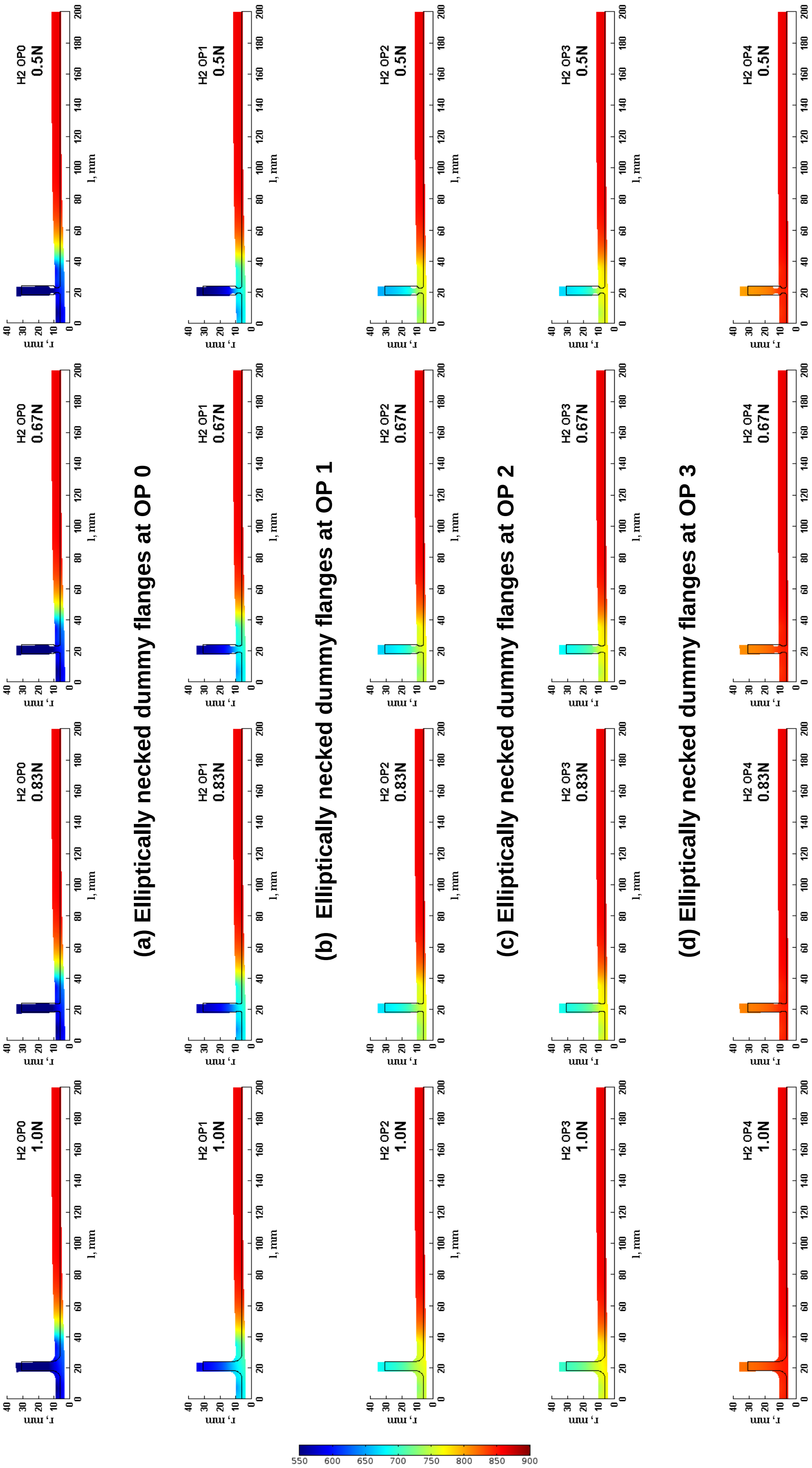

(a) Elliptically necked dummy flanges at OP 0

(b) Elliptically necked dummy flanges at OP 1

(c) Elliptically necked dummy flanges at OP 2

(d) Elliptically necked dummy flanges at OP 3

(e) Elliptically necked dummy flanges at OP 4

Figure 6.15 Predicted casing temperature (K) and thermal radial displacement (r, mm) for 1.0N through 0.5N of elliptic dummy flange models, H2 *z/d* = 4 at OP0 through OP4

Figure 6.16 shows the temperature gradient along the central radial axis of the dummy flanges from the casing inner surface to the top of the flange for the two operating conditions OP1 and OP2. Clearly the flange temperature drops by 30 - 40 K with increased necking of the flange, though the casing temperature is much less affected and the changed heat transfer associated with the necking geometry drops the internal temperature by about 1 K is gained at the edge of root of the flange region regardless of the size of elliptical indent.

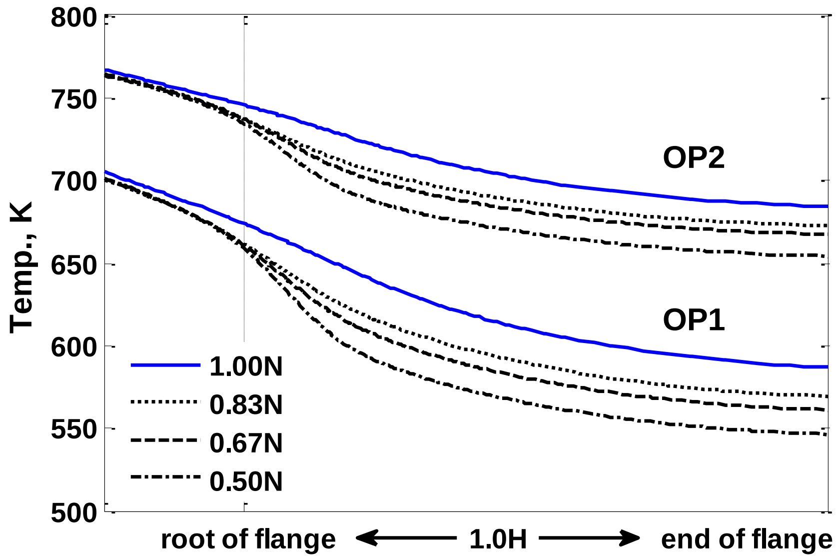

Figure 6.16 Predicted casing temperature (K) along the centroid of elliptic dummy flanges at OP1 and OP2.

The local casing temperature and relevant thermal closure are presented as a function of coolant mass flow rate in **Figure 6.17**. For a given coolant mass flow rate, it can be seen that there is a minor change in temperature at the point of liner attachment associated with the width of the neck. However, there is substantial increase in thermal closure at all mass flow rates, even for the smallest degree of necking considered (0.83*N*).

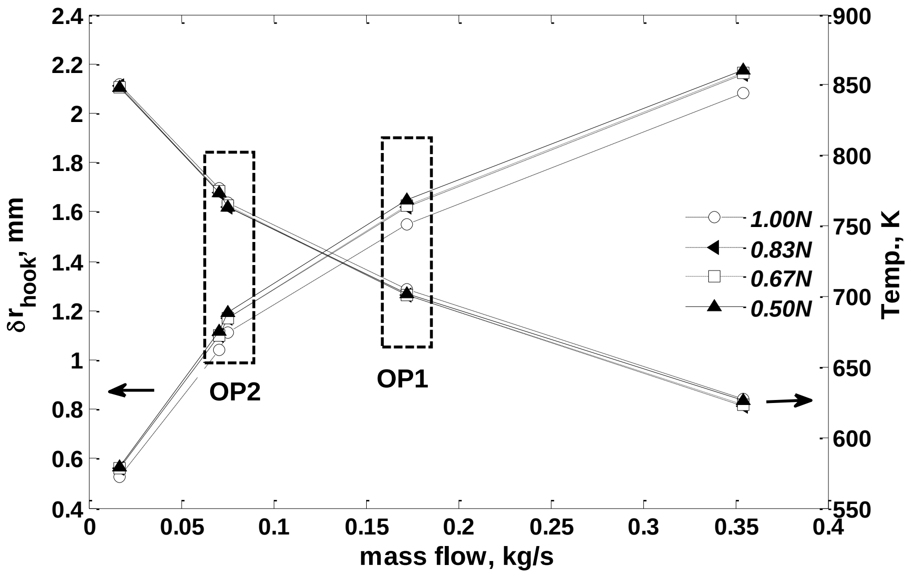

Figure 6.17 Predicted casing temperature (K) and closure (mm) versus coolant mass flow rate, at liner attachment point, for the elliptic dummy flanges.

Figure 6.18 show the relative performance of casing temperature drop and closure at two selected operating conditions OP1 and OP2 in normalized formats by comparing to the baseline 1.0*N* geometry. Note that the graph is directly compatible to the **Figure 5.25** and **Figure 5.45.** In targeting the contraction of the main casing, the option of necking in the dummy flanges at their root fillet shows considerable benefit. An improvement in contraction of ~7 % was seen for the with a 17 % reduction in the width of the flange at its root i.e. 0.83*N*. Further necking gave only slight further improvement in behaviour and would, in any case, be associated with higher thermal stresses and possibly reduced life for the component.

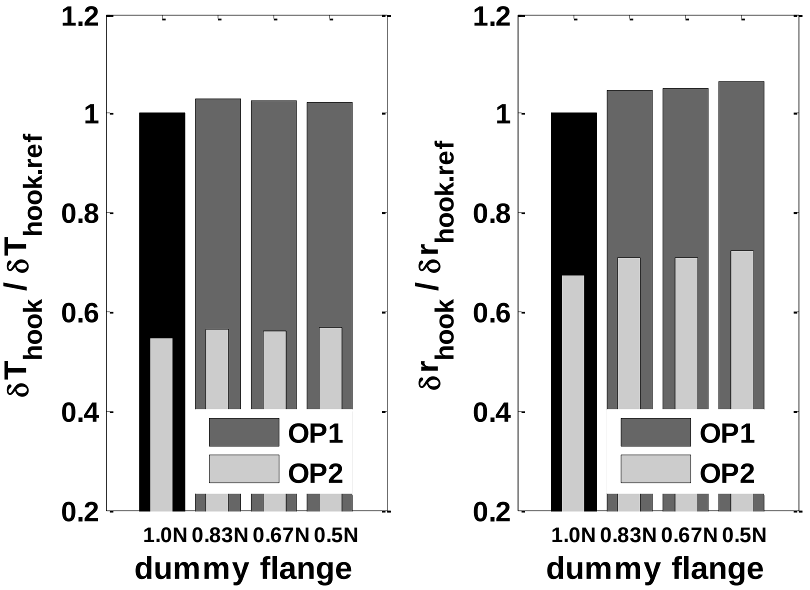

Figure 6.18 Relative performance of casing temperature drop and closure at the liner attachment point by internal hooks, compared to baseline H2 scheme (1.0N) at OP1 and OP2.

6.4 Summary

The effect of local casing thickness and external dummy flange height on casing contraction was characterised using three promising external cooling schemes at two operating conditions. A modelling approach consistent with previous chapters of this thesis was used. For the tested geometries and conditions,

- the contraction of the casing liner was found to be highly sensitive to the casing thickness and the radial height of the casing. Thinner casings and circumferential flanges of extended height resulted in the most effective contraction at a given mass flow rate.
- The height of the dummy flange is important, as a small flange tends not to be able to be maintained close to ambient temperature and therefore fails to counteract the tendancy of the casing to expand.

This can be subsequently maximized with optimized impingement cooling schemes on the external casing. Depending on the requirement for the system either:

- a uniformly distributed cooling scheme such as impingement onto both the casing wall and the flange fillets should be employed to maximise closure, but with a high sensitivity to the manifold to casing offset distance,

  or

- a sparse array of cooling jets impinging onto the flange fillets which provides a lower level casing contraction but is extremely tolerant of installation tolerances.

Some further design changes were made to dummy flange to restrict heat flow into the flange. In general the study suggests:

- it is worth necking the root of the dummy flanges to reduce the conduction path into the flange.
- most of the benefit from necking the flange can be gained with a small constriction of the area (lowest tested being 16.7% of the flange width removed at the narrowest point).

Chapter 7 Heat Transfer Characteristics of Internal Casing Over-Tip Seal Segment Cavity

This chapter describes heat transfer on the internal casing surface, which forms one wall of the over-tip seal segment cavity. The priority here is to understand the fundamental driving mechanism for heat transfer and its level, rather than the management of the tip clearance control. The heat transfer on this surface is a result of the air system designed to cool the liner surrounding the turbine blades, and is not optimised to reduce heat transfer to the case or tune thermal transient response. In the latter part of the chapter, a design permutation is proposed to reduce *htc* on the target surface.

Experimental and computational investigations were carried out using an engine representative geometry and operating conditions (see Chapter 3.3 and 4.2). The cavity is formed from several interlocking components in the engine. The effect of the small leakages between these was examined by setting different cavity exit flow scenarios, thus allowing a simplified modelling approach to be proposed for future work.

In addition, the effect of two parameters, the impingement jet angle and the jet-to-target surface distance *p*, on the internal casing heat transfer were investigated. The geometry permutations show that changing the angle of air entry into the system has a significant impact on the *htc* level and distribution.

The geometry for the current study is reproduced earlier in this thesis in section 3.5. **Figure 3.7 (a)** is reproduced here for easy reference.

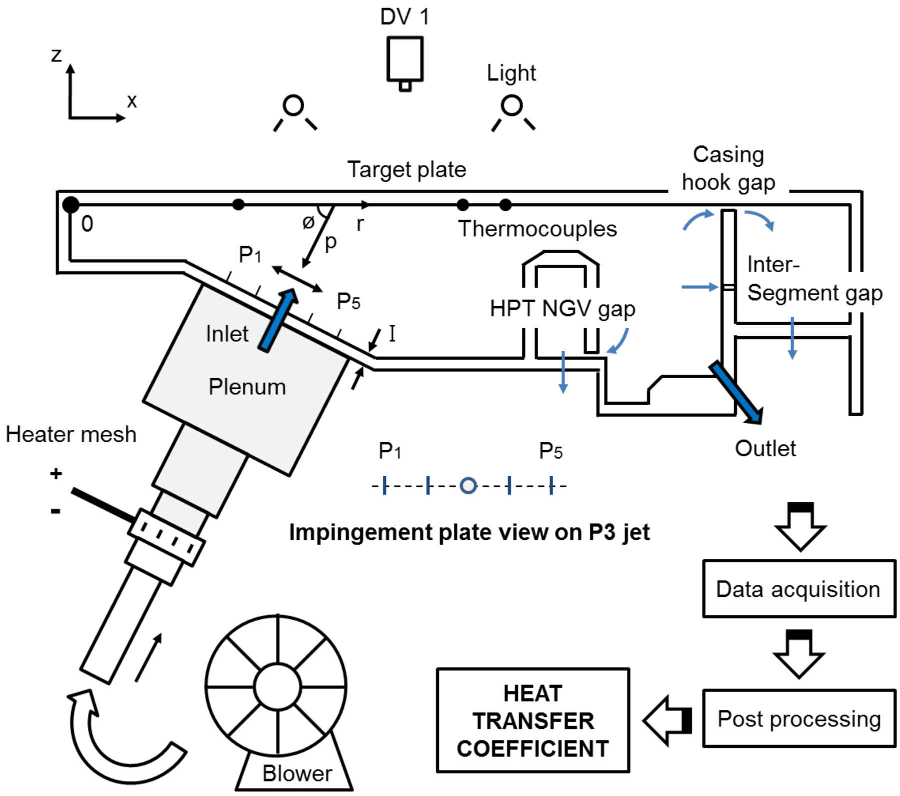

Figure 3.7 (a) Schematic of the over-tip seal segment cavity experimental test rig.

7.1 Experimental Comparison and Validation

The experimental heat transfer coefficient measurements were performed in a large scale defeatured planar rig setting the impingement jet Reynolds number at 50,000 which is indicative of the flow at idle conditions within the engine. (Note again that the very high density at engine cruise and take-off conditions leads to extremely high Reynolds number which would equate to compressible flow at atmospheric conditions. Thus, only the idle equivalent condition has been tested to provide validation data.) This was then supported by a parallel CFD campaign. In addition to confirming modelling validity, engine scale CFD models (presented in the following section 7.2) are employed to incorporate more realistic features such as surface curvature. The experiment and numerical models used are fully described in Chapter 3.3 and Chapter 4.2 respectively.

7.1.1 The Effect of Cavity Leakages

The experiment cavity rig has two exit leakage paths with one primary outlet, and their impact on the target surface *htc* is one of the primary measurements of this study. These results should allow the necessity of modelling these flows to be assessed. **Figure 7.1** presents selected flow pathlines in the cavity rig model for cases where all of the leakage flows are modelled (EXP-C), where the lower set of holes representing the leakage at the interface between the liner and the NGV coverplate are closed (EXP-G), and with the upper holes representing the casing hook and intersegment gaps closed (EXP-E), and finally all leakage flows closed (EXP-F), with all of the flow exiting through the primary outlet. In all cases the total flow rate is fixed, given that the feed pressure in the system is very high and these are unlikely to be the metering flow area in the system.

Very similar flow patterns are seen in the simulations regardless of exit flow conditions. In particular the impingement jet formation on the target surface is not affected by any of the possible exit flow scenarios. It can be seen that a circular jet hits the surface and fans out mainly in the downstream direction. The edge of the jets reaches the sidewalls of the test rigs and turns downwards recirculating within the main over-tip segment cavity. The downstream flow in the axial direction reaccelerates through the upper gap above the NGV coverplate attachment point. When the upper leakage flow path is closed, the flow recirculates in that part of the passage before exiting through the primary exit flow path.

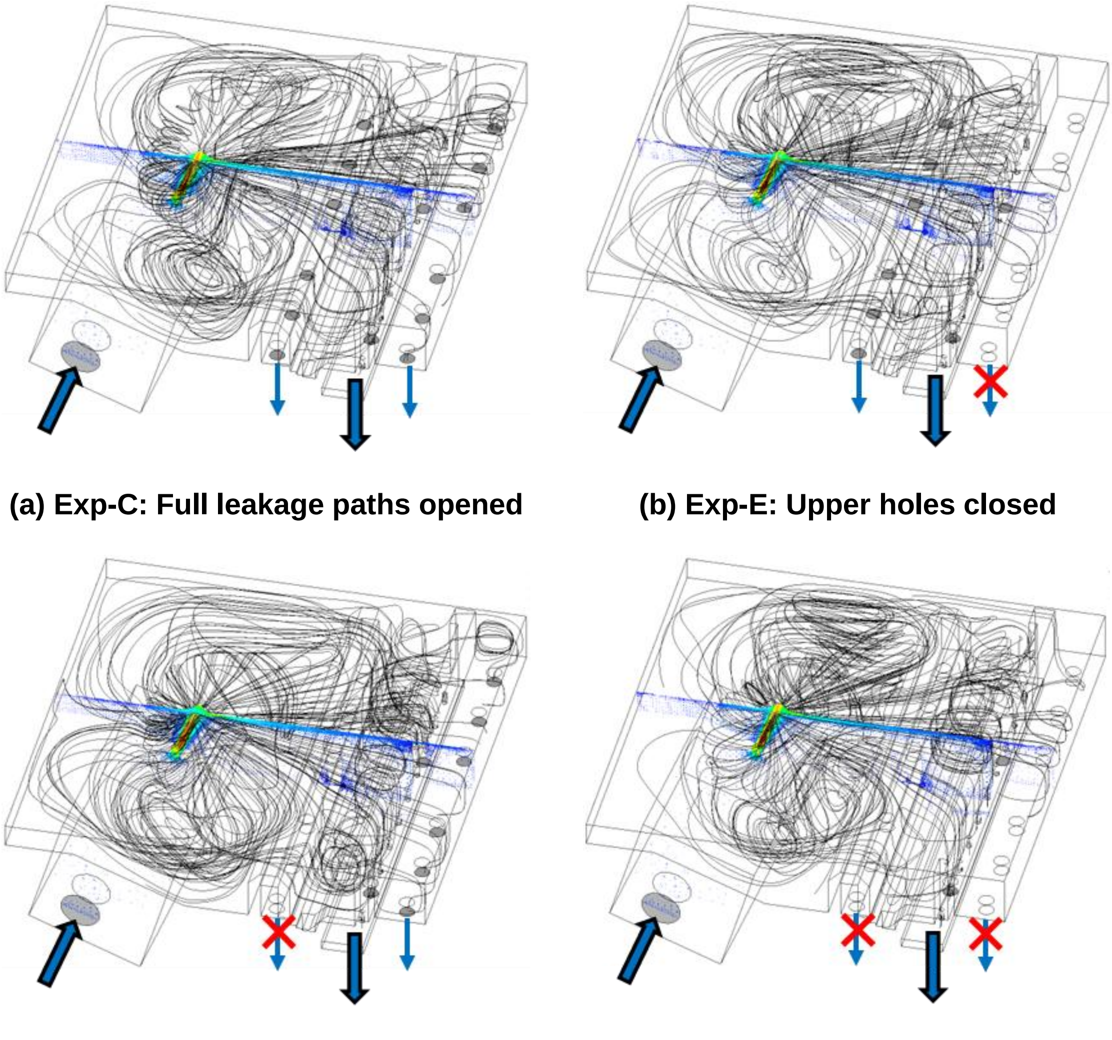

(a) Exp-C: Full leakage paths opened (b) Exp-E: Upper holes closed

(c) Exp-G: Lower holes closed (d) Exp-F: Primary outlet only

Figure 7.1 Flow pathlines for different exit leakage modes in the cavity rig model

Figure 7.2 shows the local normalised *htc* maps for the P_4 impingement flow configuration in the cavity with different leakage flow configurations at Re = 50,000 for both experimental measurements and the CFD prediction. It should be noted that the engine representative part of the passage lies between x/d = 0 - 35.5, and the area downstream is an artifice of the test rig. The reference *htc* used for normalisation is the peak value of local *htc* for the baseline P_4 impingement jet taken from the realizable k-ε CFD simulation with the all leakage paths modelled. At test rig conditions this value is htc_{ref} = 879.3 W/m^{2}K, equivalent to a Nusselt number of 296, and these values can be used to scale the results to both *htc* and Nusselt number. For all circumferential, axial or overall area averaged *htc* comparisons, the same reference data set is used ($htc_{cir.ref}$ = 90.2 W/m^{2}K, $htc_{cir.ref}$ = 90.2 W/m^{2}K, and $htc_{avg.ref}$ = 30.7 W/m^{2}K).

One can see from the experimental results an elliptic heat coefficient pattern showing *htc* decreasing faster orthogonally to the angle of inclination of the jet than in the streamwise direction. The peak *htc* on each target surface is not situated in the geometrical centre of oblique jet impact location at x = 17d, but slightly shifted the upstream side along the axial direction. This is line with the finding so other workers (e.g. **Beltaos (1976)** and **Sparrow and Lovell (1978)**). The shift recorded is roughly at -1d from the geometric axis of the jet. The influence from both circumferential side end walls situated at y = ±21.5d location on local *htc* is minimal showing that the impingement jet acts more like as a single jet, rather than arrays of jets.

The discrepancy in surface *htc* underneath the jet between different exit leakage modes is barely visible both in the experiment and the CFD simulations. Only the region near the entrance of the casing hook gap (at x = 35.5d) is affected by the recirculation of downstream wall jet flow, and causes slight differences in the level of increase in local heat transfer coefficient depending on the exit flow conditions. In the casing hook gap region the flow is accelerated with an associated increase in shear stress along its edge and also an increase in the *htc*. The case where the upper holes were closed produces the lowest *htc* level in this region but is only reduced by 8 % compared to results with the full leakage flows modelled.

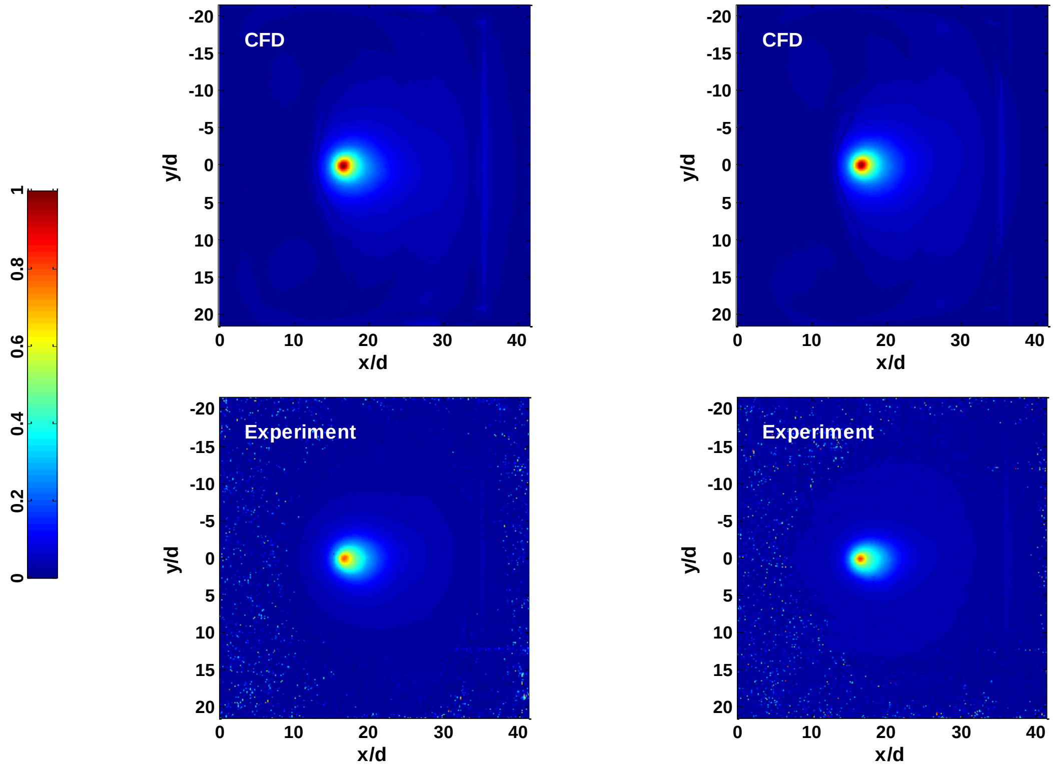

(a) Exp-C: Full leakage paths

(b) Exp-E: Upper holes closed

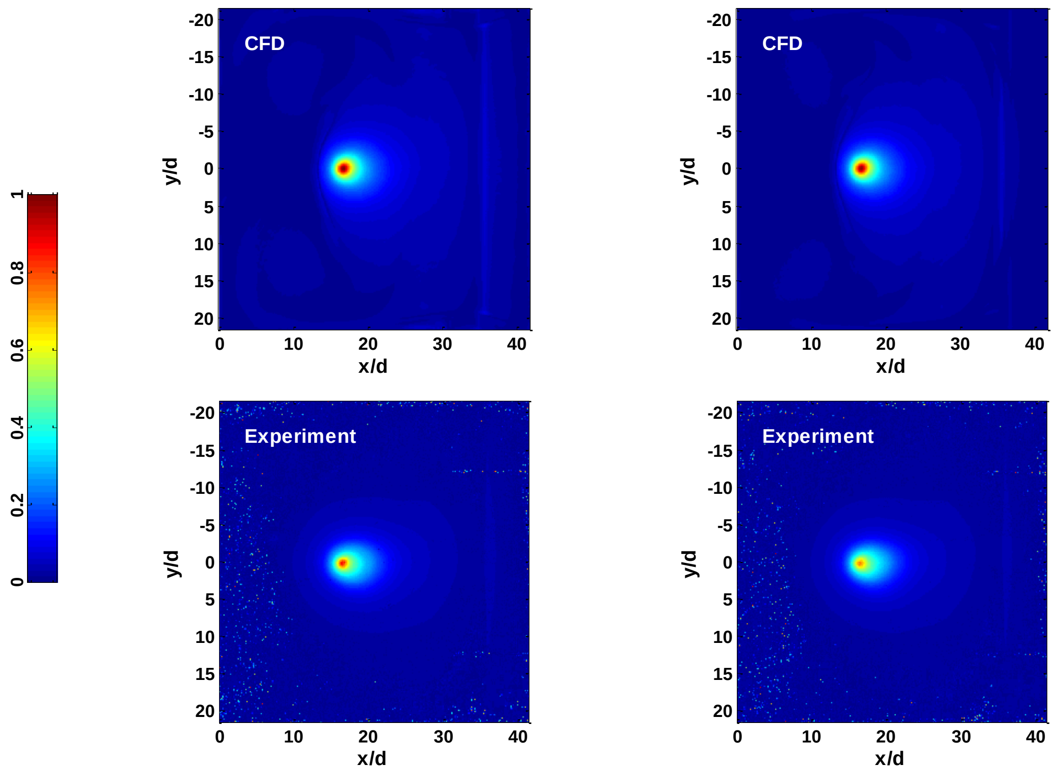

(c) Exp-G: Lower holes closed

(d) Exp-F: Primary outlet only

Figure 7.2 Local *htc* / htc_{ref} (= Exp-C.peak.realizable k-ε) distributions for different exit leakage modes at Re = 50,000 in the cavity rig model.

CFD results closely resemble the measured heat transfer pattern on the target surface, but globally over predict the heat transfer coefficient distribution especially the peak *htc* values underneath the jet (see the axial and circumferential jet centreline comparison plots in **Figure 7.3** and **Figure 7.4**). These were over predicted by up to 40 % and at the downstream edge of the model (x/d → 35.5) by up to 20 %. It is perhaps unsurprising that the jet heat transfer is over predicted as the very long jet axis is associated with mixing of the incoming heating flow with flow in the cavity. In the shear layer at the edge of the jet the CFD is unlikely to capture the mixing accurately. While over prediction of the mixing may cause increased turbulence in the jet, it will also reduce the heating potential of the jet such that over or under prediction of the *htc* cannot easily be predetermined.

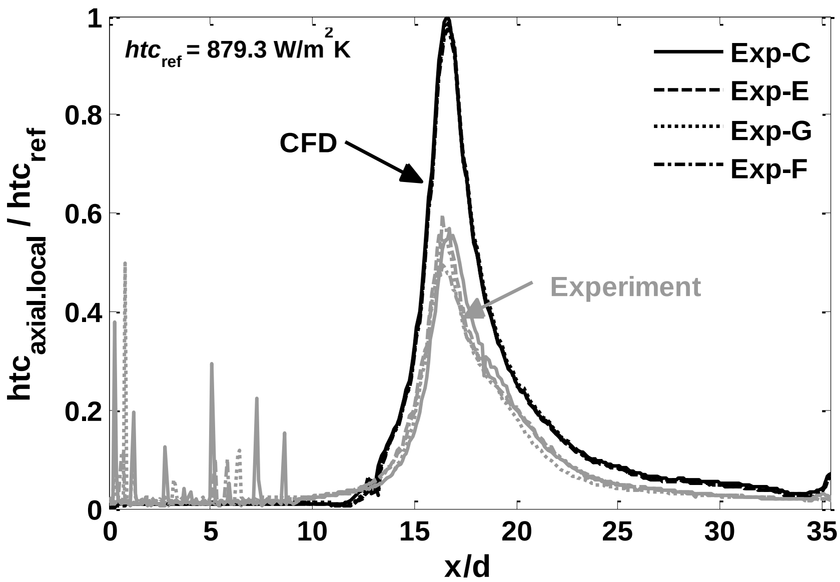

Figure 7.3 Axial jet centreline *htc* / *htc*$_{ref\ (=\ Exp\text{-}C.peak.realizable\ k\text{-}\varepsilon)}$ distributions for different exit leakage modes at Re = 50,000 in the cavity rig model.

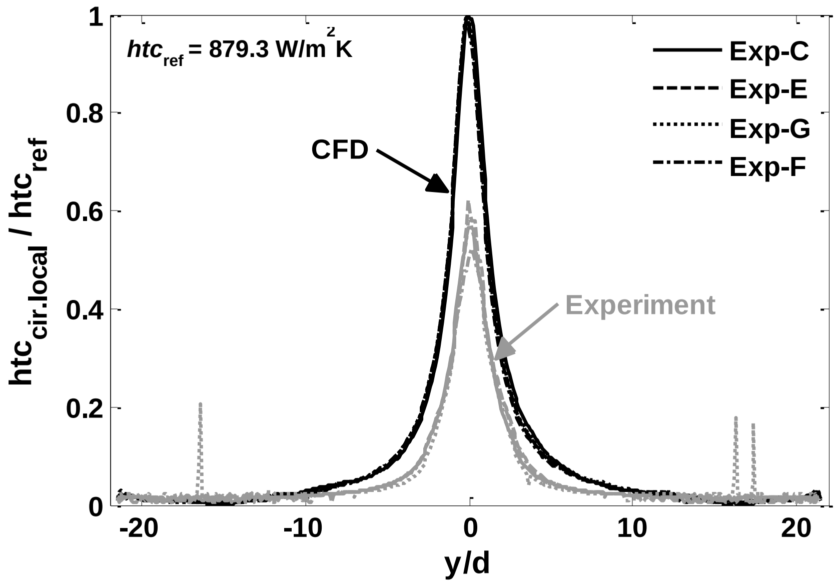

Figure 7.4 Circumferential jet centreline *htc / htc*$_{ref}$ (= Exp-C.peak.realizable k-ε) distributions for different exit leakage modes at Re = 50,000 in the cavity rig model.

Figure 7.5 and **Figure 7.6** show the circumferential and axial averaged *htc* distributions of the P_4 impingement flow in the cavity with different exit leakage flows, again at Re = 50,000 – a representation of the same data. Again, there is only a minor effect on the *htc* caused by blocking either of the sets of holes modelling leakages. The peak of the circumferential or axial averaged *htc* from the CFD prediction data is globally over predicted the measured *htc* for all cases up to 30 %, although the relative distribution with axial or circumferential position is in good agreement.

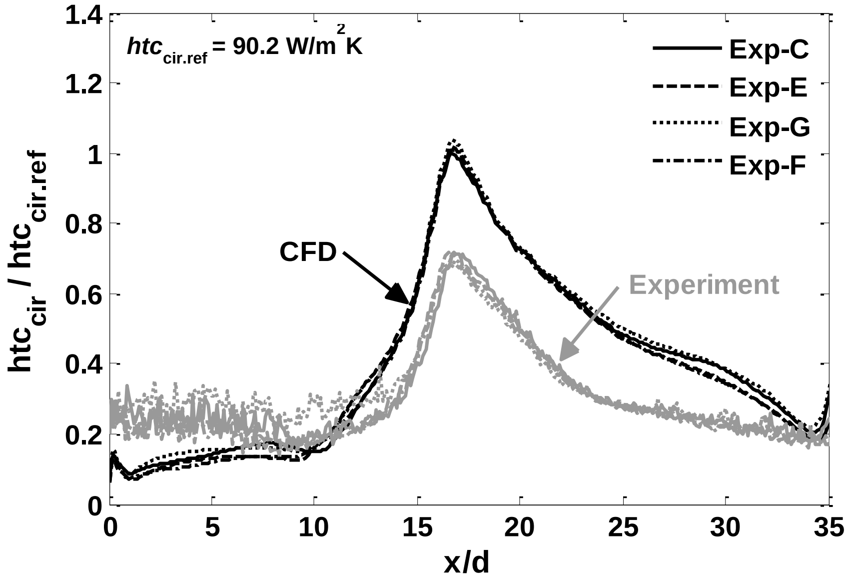

Figure 7.5 Circumferential averaged *htc* / *htc*$_{ref}$ (= Exp-C.peak.span.realizable k-ε) distributions for different exit leakage modes at Re = 50,000 in the cavity rig model.

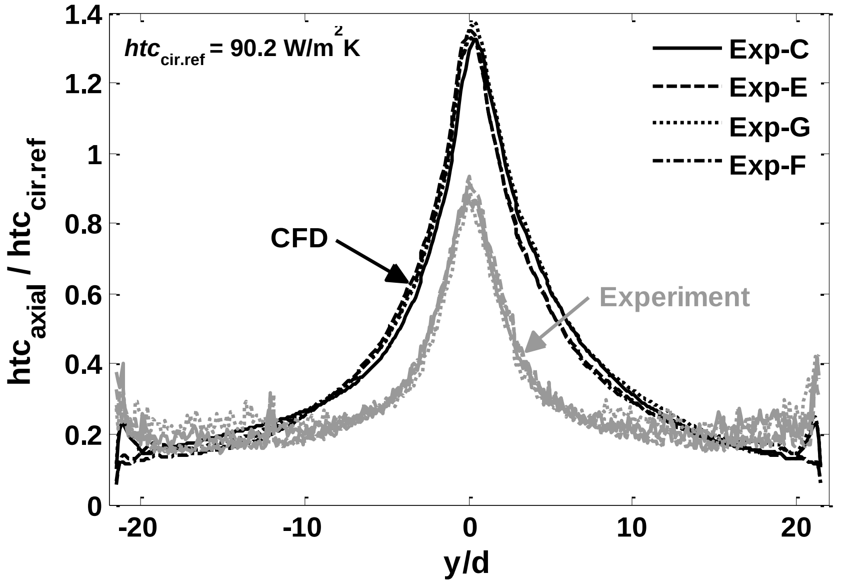

Figure 7.6 Axial averaged *htc* / *htc*$_{ref}$ (= Exp-C.peak.span.realizable k-ε) distributions for different exit leakage modes at Re = 50,000 in the cavity rig model.

The total area averaged *htc* are presented by comparing the baseline data set in **Figure 7.7**. This includes comparison made to the well known **Goldstein and Franchett (1988)** correlation. In the correlation, Nusselt number can be expressed as a function of Reynolds number, *p*/*d* and the angle of impingement jet

$$\frac{\mathrm{Nu}}{\mathrm{Re}^{0.7}} = A\, exp^{-(B+C\cos\phi)(r/D)^m}. \tag{7.1}$$

where r and ϕ are cylindrical coordinates for correlation of contours of constant Nu.

The Nusselt number is then converted to *htc* in the rig condition using the standard convective relationship for direct comparison

$$htc_{\mathrm{rig}} = \frac{Nu\, k_{\mathrm{rig}}}{d_{\mathrm{rig}}} = \frac{q''}{T_\infty - T_{\mathrm{s}}}. \tag{7.2}$$

Note that Goldstein and Franchett correlation is based experiments conducted for jet to target plate spacings between 4*d* and 10*d* and for Reynolds number between 10,000 and 23,000. The coefficients used were linearly interpolated to fit the corresponding geometric condition, ϕ= 65^0 and *p*/*d* = 10.

When the upper leakage path is closed i.e. Exp-E and Exp-F, the area averaged *htc* is somewhat lower than the baseline mode at about 95 % of its value. This has been seen in both measurement and prediction as a similar trend. The over estimation of CFD against the measured data is around 30 %. Notably the use of the Goldstein and Franchett correlation beyond its range of validity has led to a large over prediction of *htc* by 250 %.

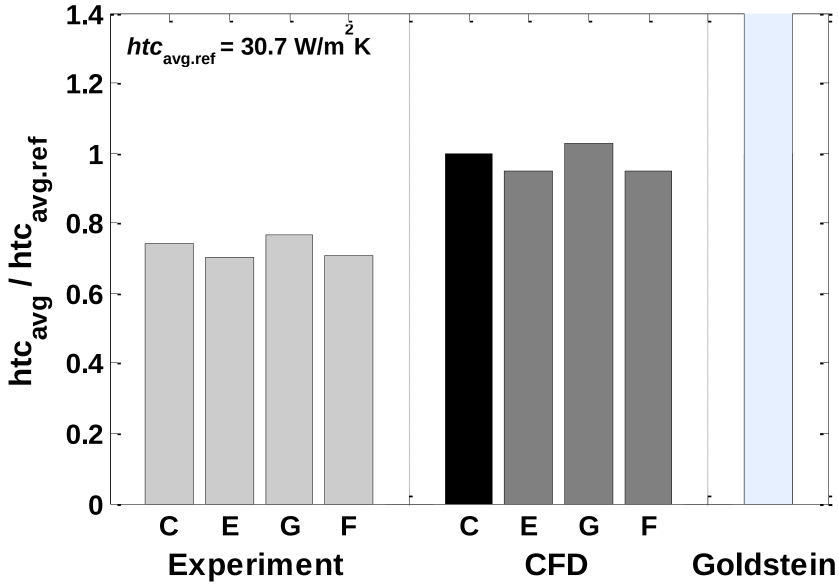

Figure 7.7 Relative performance of overall area averaged *htc* / *htc*$_{ref}$ $_{(=\ Exp\text{-}C.avg.realizable\ k\text{-}\varepsilon)}$ at Re = 50,000 for different exit leakage modes in the cavity rig model.

7.1.2 The Effect of Jet to Target Surface Spacing

Five different positions of the circular jet hole on the impingement plate have been investigated (as shown in **Table 3.4**) to see if it is possible to reduce the *htc* on the casing surface. The inlet jet angle is maintained at 65 degree and only the jet impact location and the jet to target surface spacing are changed which directly affect the *p*/*d* ratio.

Figure 7.8 shows the measured and predicted *htc* maps for the five different positions of impingement flow in the cavity at jet Re = 50,000 condition. The surface *htc* distribution is somewhat affected by the position of the inlet hole along the impingement plate. When the impingement hole is placed in the axially upstream part of the NGV cover plate (P_1, P_2), it is observed that there is higher heat transfer from the impingement jet which is closer to the target surface. The shape of the *htc* footprint is more circular than for the baseline P_4 case, but the region of high heat transfer dies away more rapidly, leaving a lower heat transfer coefficient in the furthest downstream region. As the position of the impingement hole is moved further downstream, the footprint becomes more elliptical and the region of high heat transfer is swept towards the downstream flow outlet areas.

The maximum peak *htc* level was seen at the P_1 jet position due to the shorter jet to target surface distance whilst the baseline P_4 and P_5 produce similar level of peak *htc* which are the lowest among the configurations tested. Note that areas very far from the jet axis where there are very low levels of *htc* could not accurately be experimentally measured, and can be seen as a series of noisy points on the experimental contour plots. Overall, the CFD over predicted the measured *htc* fairly uniformly along the surface by around 30 %, although the distribution with axial position was in good agreement. This indicates that CFD analysis can be used to order the level of *htc* in a future optimisation study.

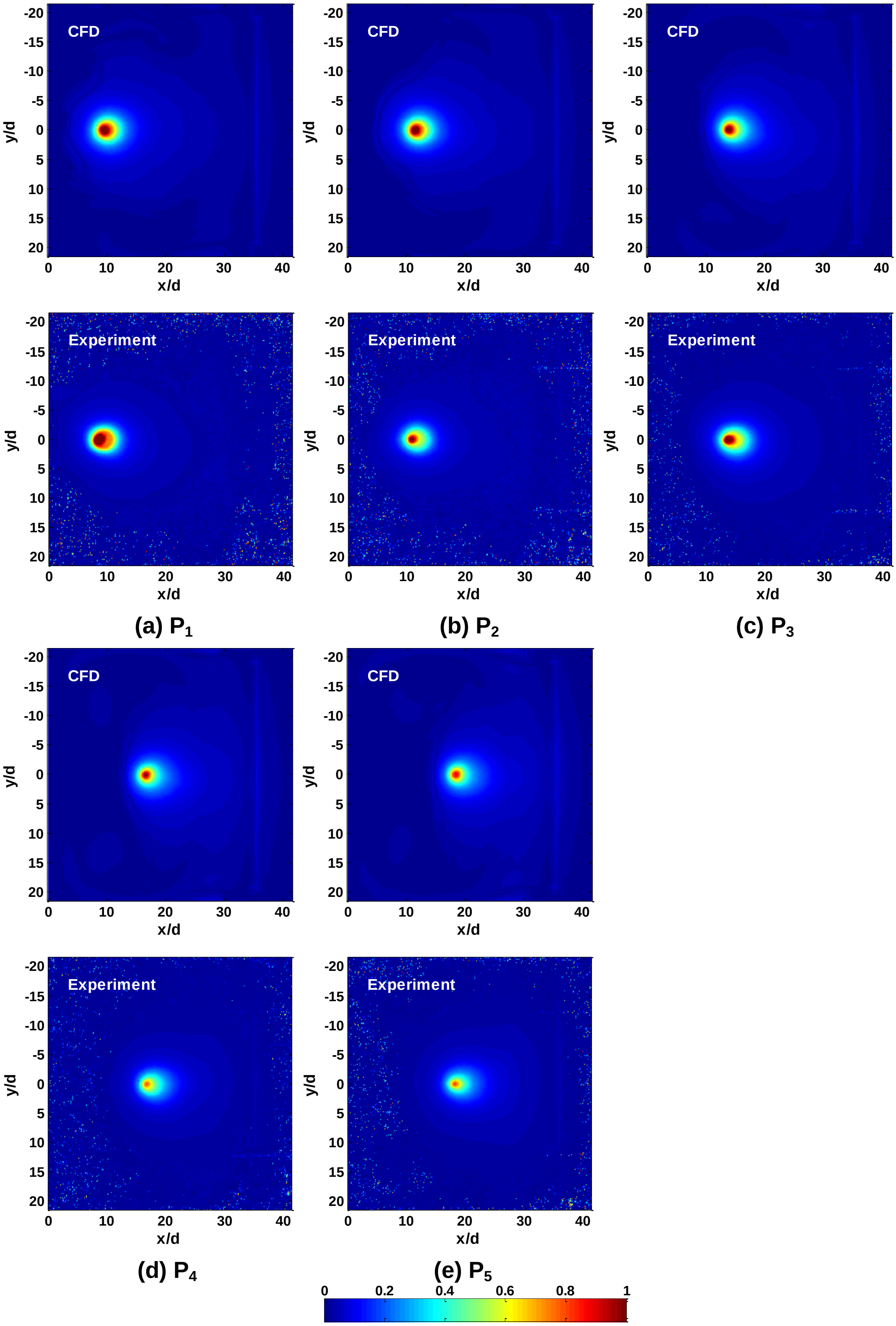

Figure 7.8 Local *htc* / $htc_{ref\ (= Exp\text{-}C.peak.realizable\ k\text{-}\varepsilon)}$ distributions for different position of impingement jet at Re = 50,000 in the cavity rig model.

Figure 7.9 shows the circumferential averaged *htc* distributions. As expected, the peak of the *htc* decreases as the point of impingement occurs further downstream (because the *p*/*d* ratio increases). The level of heat transfer coefficient outside an area $\pm 7d$ around the jet axis are mostly identical for all cases apart from near the downstream edge at $x = +35d$ location.

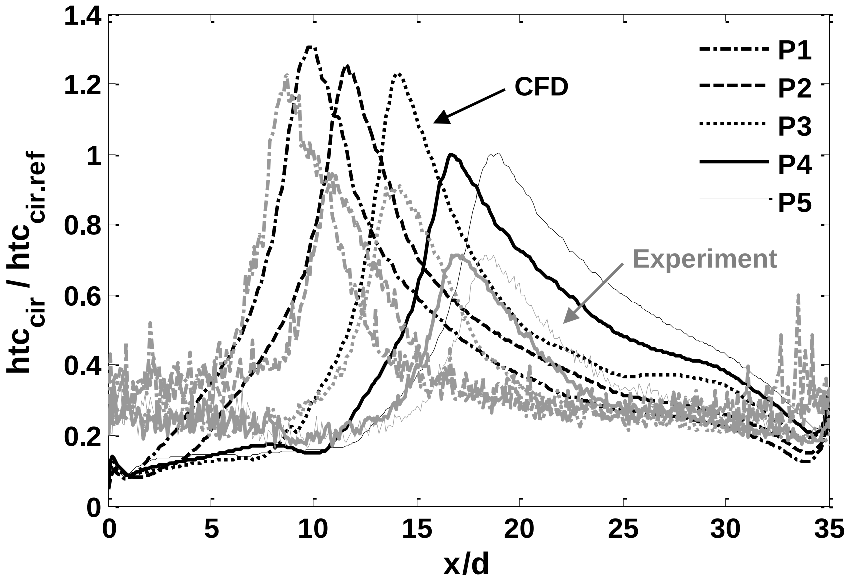

Figure 7.9 Circumferential averaged *htc* / *htc*$_{ref}$ (= Exp-C.peak.span.realizable k-ε) distributions for different position of impingement jet at Re = 50,000 in the cavity rig model.

Comparison also has been made between the overall area averaged *htc* on the target surface in **Figure 7.10**. There is no benefit from moving the location of the inlet holes along the impingement plate compared to the baseline position, P_4. Moving the holes down the plate (P_5) gives no improvement in *htc*, while moving them up the plate, P_1 - P_3 can result in a 20 % rise in the surface-averaged *htc*. The CFD prediction shows very similar trends to the measured *htc*, but the magnitude of the averaged *htc* measured using CFD only changes *htc* by from +5 % to 0 %, even if the CFD somewhat over-estimated the absolute level of *htc*.

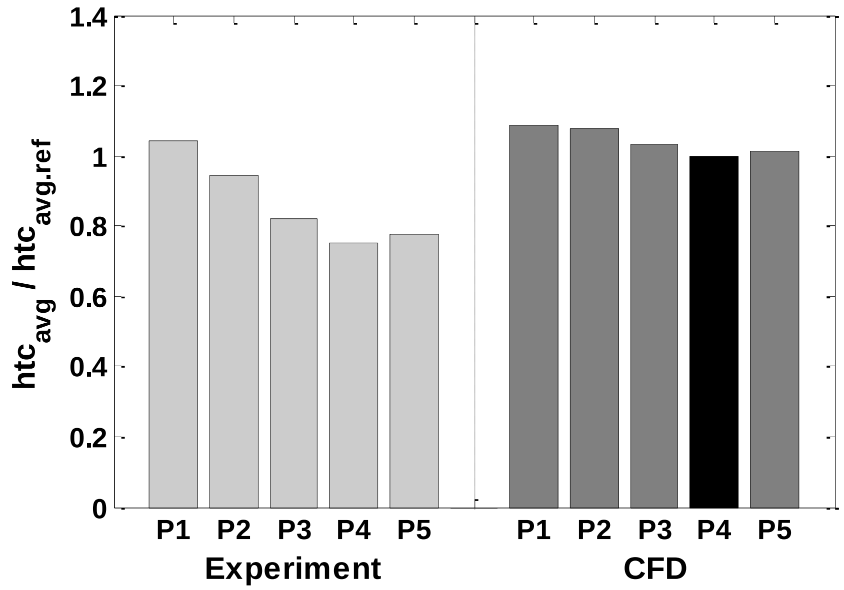

Figure 7.10 Relative performance of overall area averaged *htc* / *htc*$_{ref\ (=\ Exp\text{-}C.avg.realizable\ k\text{-}\varepsilon)}$ for different position of impingement jet at Re = 50,000 in the cavity rig model.

7.2 Cavity Flow Field and Heat Transfer Prediction

Having assessed the validity of the coolant flow, the CFD was rerun at engine scale and operating conditions. Once again the realizable k-ε turbulence model was used for this numerical investigation. This allows the data to be extended to cover all operating conditions, the modelling at engine scale only having remained valid for Re_{jet} < 50,000.

Flow pathlines for the different exit leakage configurations (see **Table 4.5**) in the fully featured half-domain segment cavity with the baseline impingement jet hole position are presented in **Figure 7.11**. The pathlines issuing through the circular jet hole originate from the manifold inlet face. As before the impingement jet targets the upper surface, and then recirculates within the main cavity. The flow exits accelerating through the gap forms by the NGV cover plate attachment hook. In the downstream cavity it further recirculates and exits either into the segment cooling holes or through a further casing hook leakage gap. In this model the sidewalls of the experimental test rig are replaced by symmetry faces, but the flow field is not affected as there is no interaction between neighbouring jets. The overall flow mechanisms at engine scale are quite very to those seen in the previous defeatured rectangular type model of the experimental rig.

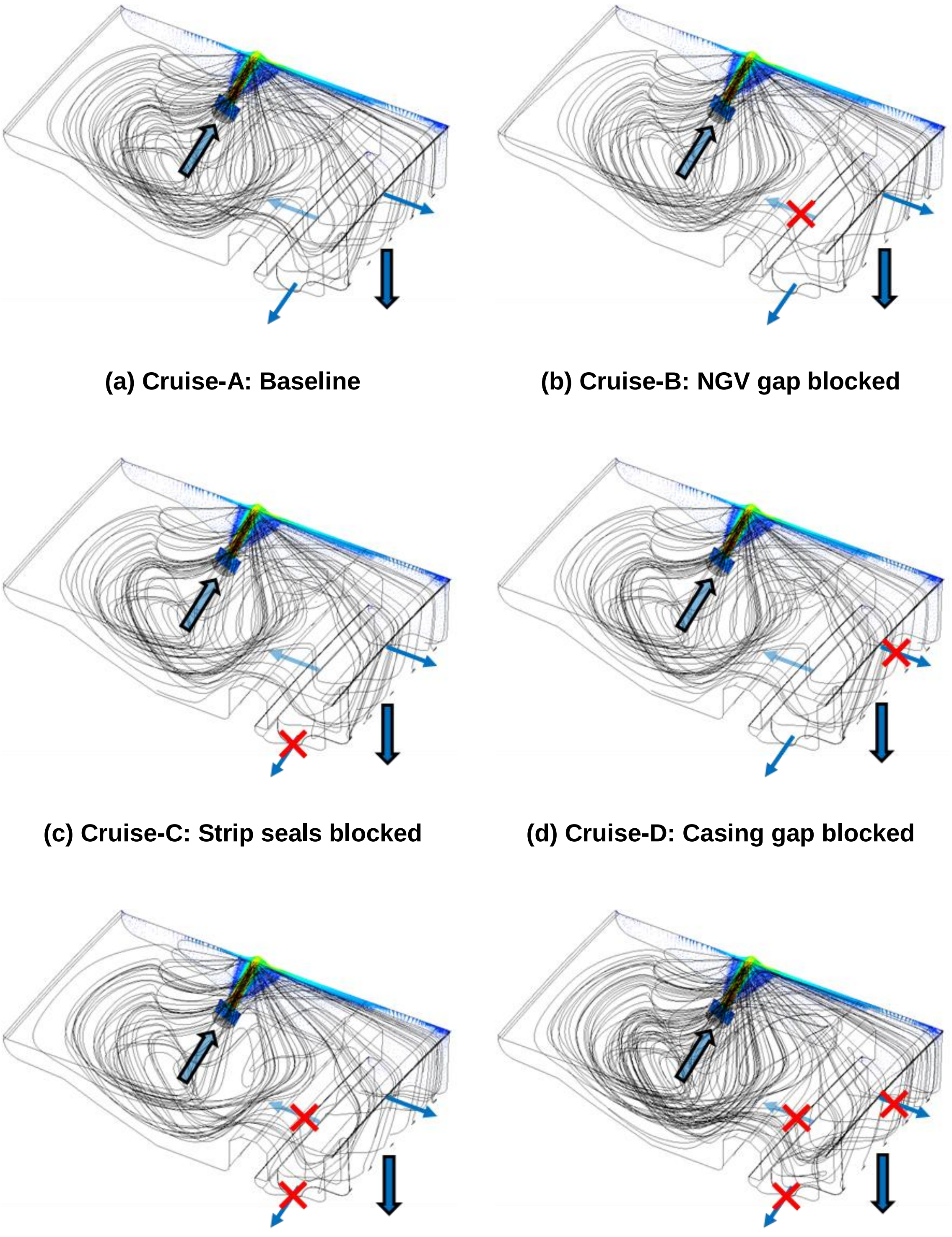

(a) Cruise-A: Baseline

(b) Cruise-B: NGV gap blocked

(c) Cruise-C: Strip seals blocked

(d) Cruise-D: Casing gap blocked

(e) Cuise-E: NGV + strip blocked

(f) Cuise-F: Primary outlet only

Figure 7.11 Typical flow pathlines for different exit leakage modes in the fully featured engine scale cavity model at the baseline hole position.

Figure 7.12 presents local *htc* distributions on the target surface for different exit leakage modes at Re = 114,604 (Cruise conditions). Note that all presented *htc* in engine scale is normalised by the corresponding *htc* at Cruise-A mode (htc_{ref} = 16248 W/m^{2}K for local, $htc_{cir.ref}$ = 1322.5 W/m^{2}K for circumferential averaged, and $htc_{avg.ref}$ = 344.8 W/m^{2}K for area averaged).

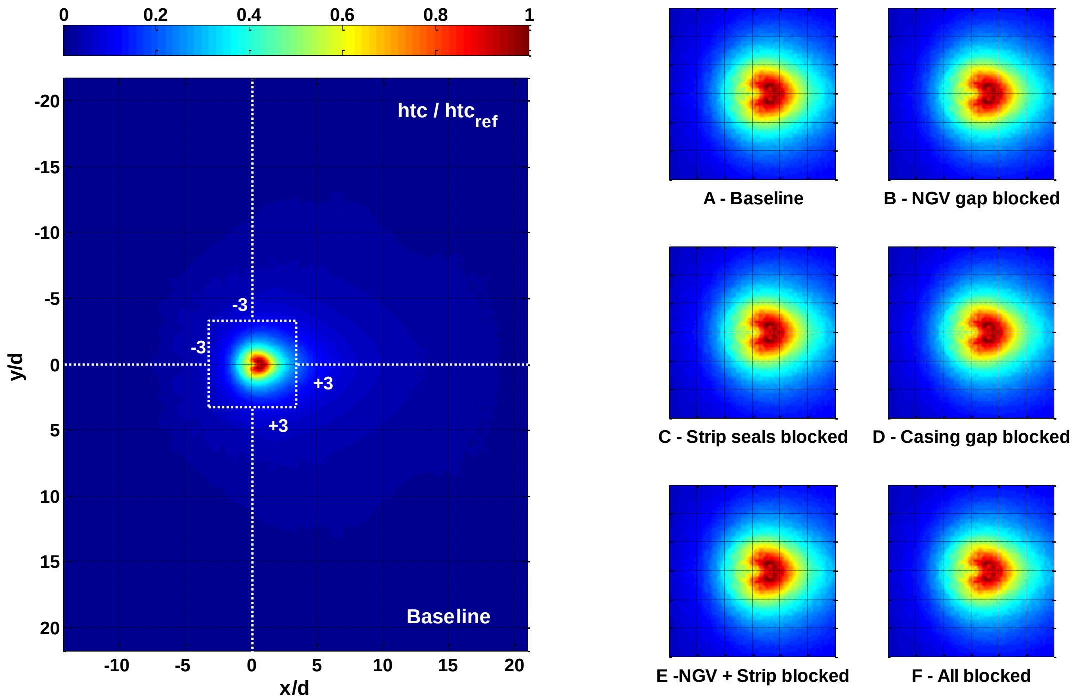

Figure 7.12 Local *htc* / *htc*$_{ref\ (=\ Cruise\text{-}A.peak.realizable\ k\text{-}\varepsilon)}$ distributions for different exit leakage modes at Cruise mode (Re = 114,604).

The *htc* contours shows smooth transition in the axial direction of the jet. This includes *htc* on an area around the geometric centre of the oblique jet impact location cropped for -3 < *x*/*d* < +3 and -3 < *y*/*d* < +3. Contrary to the previous rig models producing elliptic contours, the present engine scale models form a heart-shape *htc* stretching in the axial jet direction with two symmetric heart-shaped peaks identified on either circumferential side at *x*/*d* = +0.8 axial location. This might be because symmetry conditions applied may remove the possibility of unsteadiness along the axis of the impingement jet which would wash out the lower region of *htc* directly along the centreline. The shape of *htc* directly underneath the jet remains nearly identical for all exit flow cases. All of the CFD simulations – even those without all the small exit leakage paths modelled (i.e. with the one inlet and with just the primary outlet main segment flow exit (Cruise-F)) produce a uniform level of oblique jet *htc* foot print, showing that the impact on the impingement heat transfer from the leakage flows is negligible.

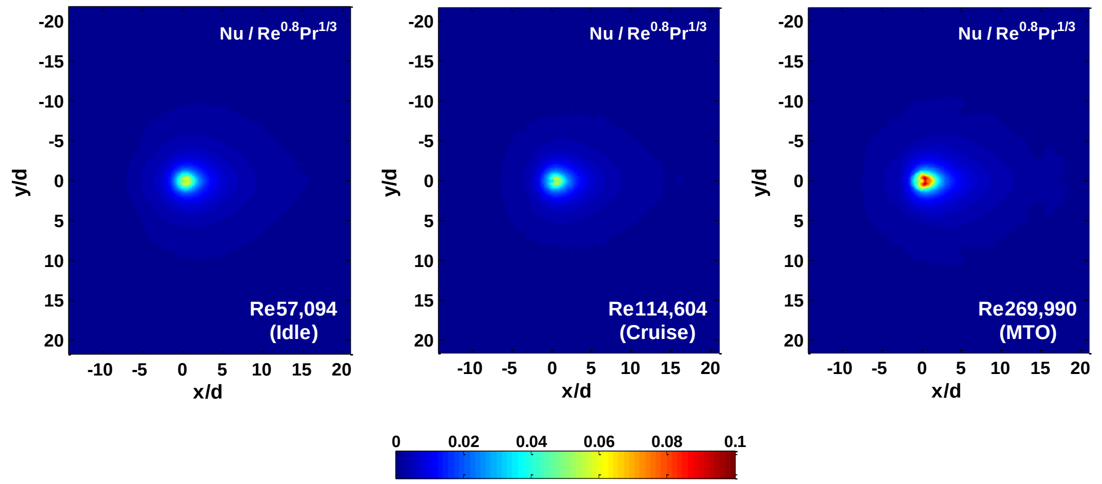

Figure 7.13 Normalised local heat transfer distributions for Idle, Cruise, and MTO condition.

Distributions of $\frac{\mathrm{Nu}}{\mathrm{Re}^{0.8}\mathrm{Pr}^{0.33}}$ for the three cases of Idle, Cruise and MTO are plotted *vs*. Reynolds number in Figure 7.11. Sensibly the Nusselt number scales very nearly as $\mathrm{Re}^{0.8}$, which is typical of an impingement cooling system.

The circumferential averaged *htc* distributions shown in **Figure 7.14** show the full distribution for all exit flow modes with an RMS error of 2.1% between all conditions. However, there is an exceptional difference in heat transfer pattern at the far downstream edge region, x/d > +20.5. When the exit leakage exists at the casing hook gap, the axial spent wall jet is highly accelerated into the gap along this short region, as in the baseline Cruise-A mode. This enhances the local heat transfer on the rear edge of the casing. In contrast, in the Cruise-D and -F exit leakage modes for which the casing hook gap is blocked, there is a rapid decrease in local *htc* due to the spent flow in the region stagnating. All cases which allow the casing hook leakage to pass through the gap (Cruise-B, -C, and -E) show a similar trend as that of the baseline Cruise-A case, regardless of whether any other small exit leakage paths are closed or not. It may be worthwhile modelling this very localised increase in heat transfer as it occurs at the point of attachment of the blade liner, and localised heating here could result in a rotation of the liner relative to the blade. In terms of overall heat transfer, however, it is insignificant.

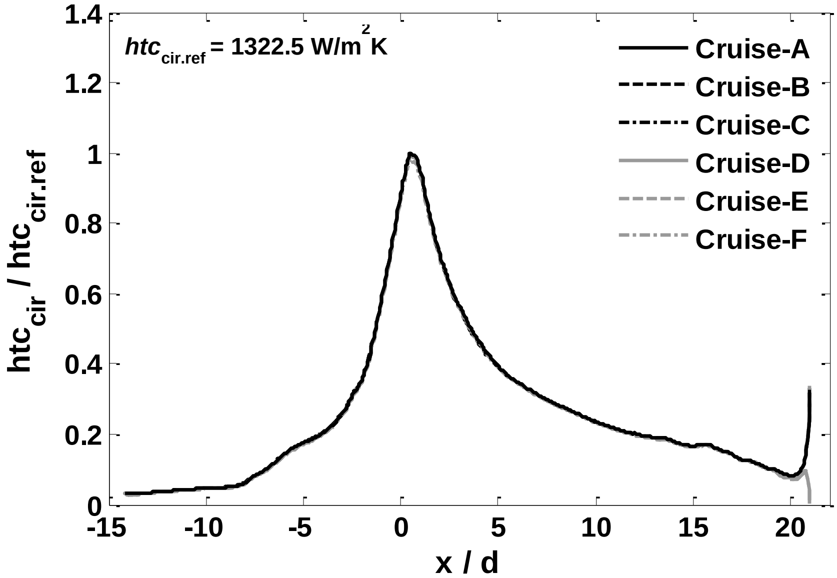

Figure 7.14 Circumferential averaged *htc* / *htc*$_{ref}$ (= Cruise-A.peak.span.realizable k-ε) distributions for different exit leakage modes at Cruise mode (Re = 114,604).

Figure 7.15 shows the axially averaged *htc* distribution at the geometric centreline. Again the peak of the *circumferentially* averaged baseline Cruise-A data is used to normalise the data ($htc_{cir.ref}$) – this leads to values above 1 in the axial direction. There is almost no variation in the results with the RMS error (variation) of 1.7 % being solely to the behaviour at the furthest downstream portion of the cavity.

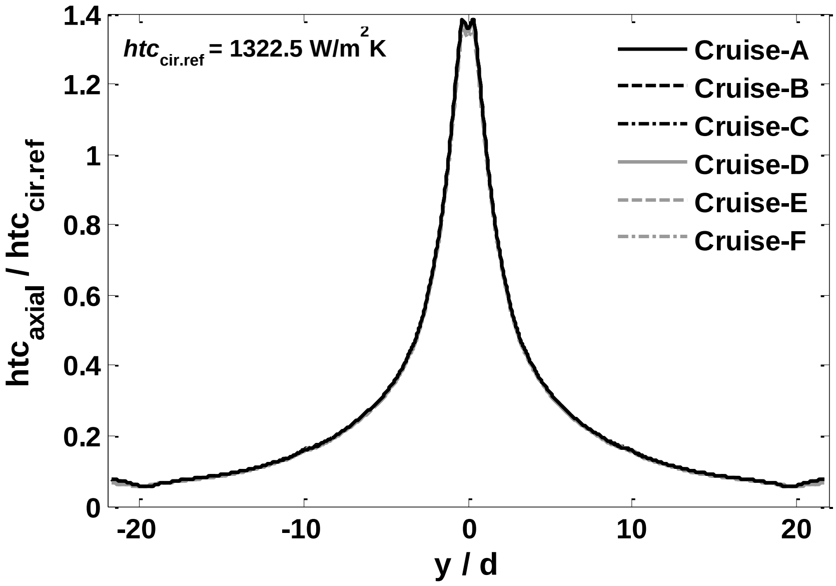

Figure 7.15 Axial averaged *htc* / *htc*$_{ref\ (=\ Cruise\text{-}A.peak.span.realizable\ k\text{-}\varepsilon)}$ distributions for different exit leakage modes at Cruise mode (Re = 114,604).

The key purpose of these latter tests was to generate data over a full range of operating conditions. The total area averaged *htc* are presented in **Figure 7.16**. At Cruise conditions the overall averaged data shows a RSS discrepancy of 1.5 % for the different leakage models tested. For the Idle- and MTO equivalent condition comparison, the fully featured and minimally featured leakage cases are reported. There is a small difference in the overall *htc* in each case of 1.0 % and 4.3 % RSS error respectively. If the far downstream edge region (x/d > +20.5) was not considered, the discrepancy in the area extending *x*/*d* = 0 to *x*/*d* = +20.5 can be reduced to 0.8, 1.1, at idle and cruise conditions but rises to 7.9 % at MTO-equivalent conditions respectively.

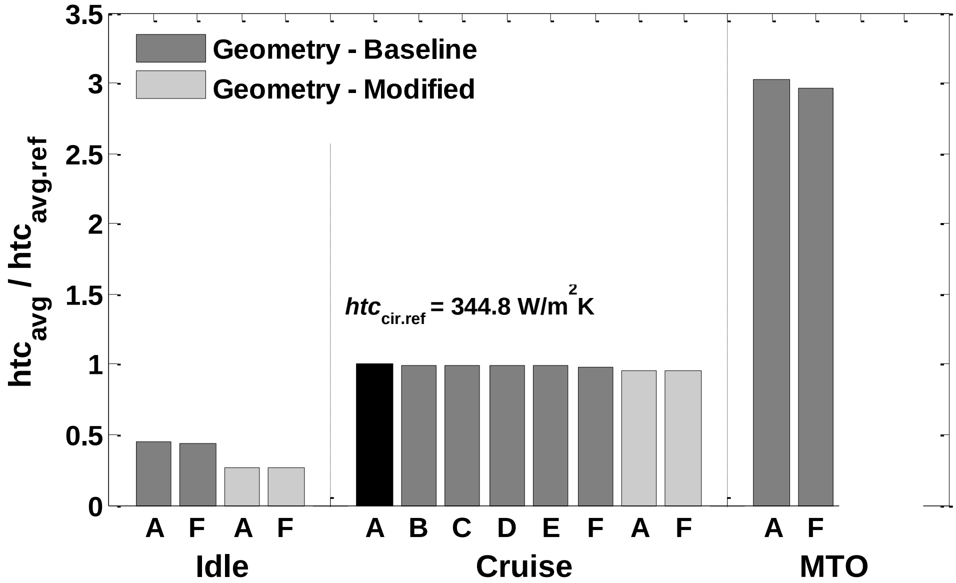

Figure 7.16 Relative performance of overall area averaged *htc* / *htc*$_{ref}$ (= Cruise-A.avg.realizable k-ε) for different exit leakage flows and operation modes.

7.3 Development of Halved Heat Transfer System

On the hot side of the casing reducing the heat transfer coefficient to as low a value as possible is considered desirable (though it is deleterious to the transient behaviour of the system). Reported below are results from an investigation of alternative inlet-hole positions with the aim of reducing *htc* on the target surface by a factor of 2.

A design permutation for the entry jet hole in the NGV support ring was made: the impingement jet angle is increased and moved down along the NGV support ring, so that the impingement jet points further down into the casing gap as shown in **Figure**

7.17. While a relatively lower velocity and more mixed out jet impinges onto the surface as the jet to target surface distance increases, there is a higher velocity downstream wall jet flow at the entrance to the casing gap region as the result of the shorter axial distance from the jet impact location and axial momentum in the injected flow. Now, the main downstream flow of the jet recirculates mainly in the downstream half of the passage, leaving a long residence slow flow upstream.

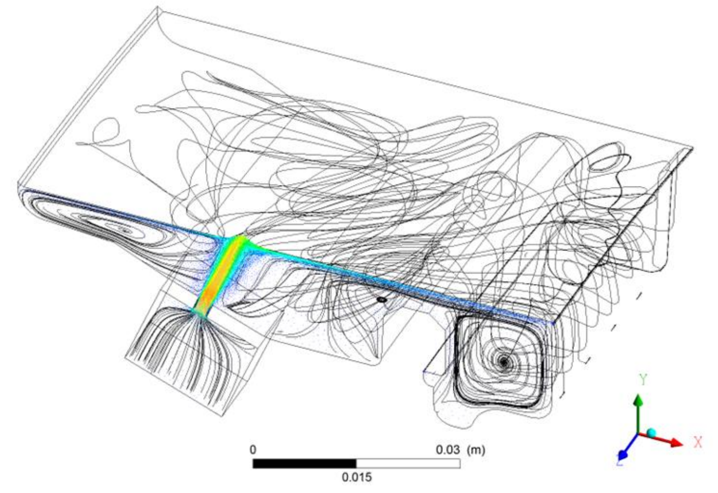

(a) Baseline

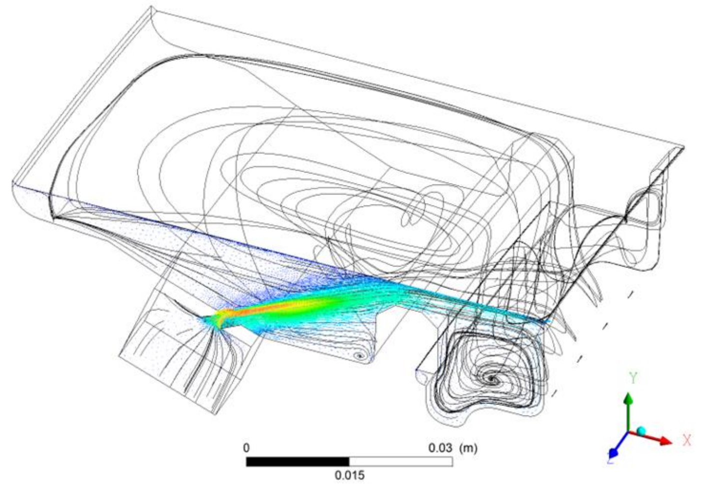

(b) Modified entry hole angle and jet impact location

Figure 7.17 Typical flow pathlines for the fully featured engine scale cavity model with modified entry hole angle and target position.

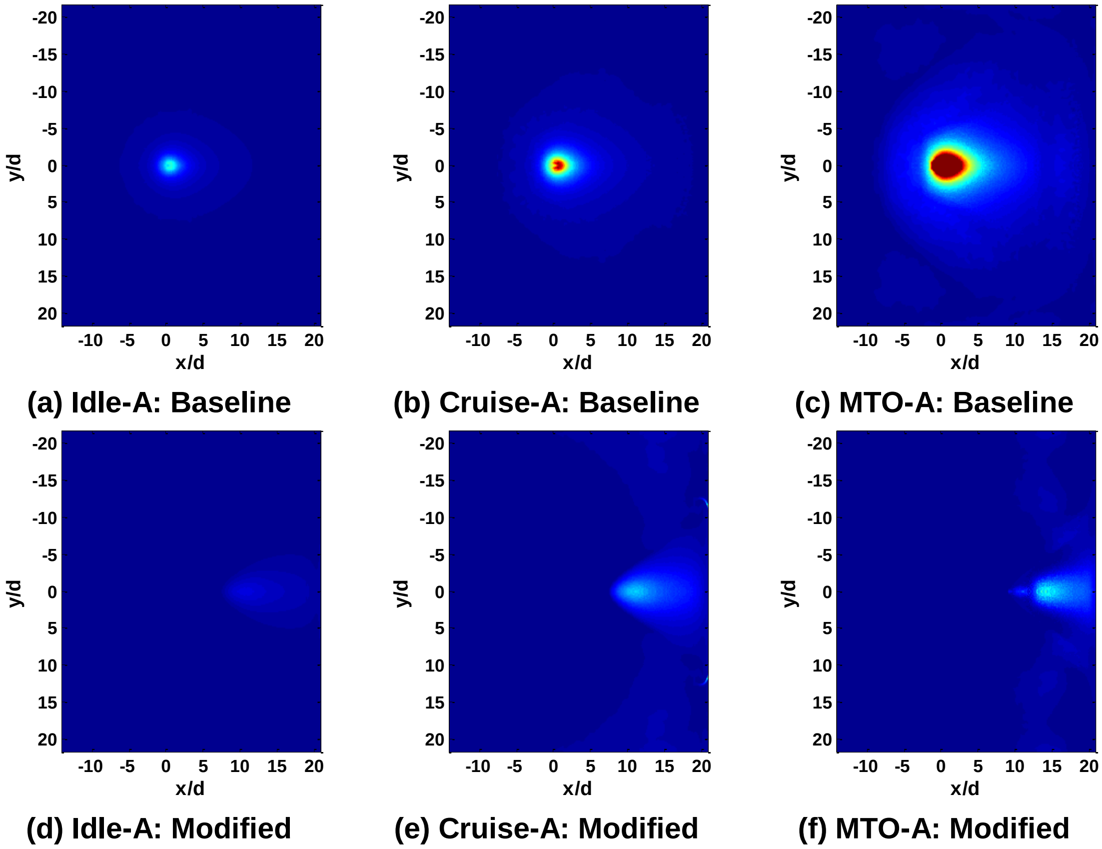

Figure 7.18 Local *htc* / htc_{ref} (= $_{\text{Cruise-A.peak.realizable k-}\varepsilon}$) distributions for different operation modes with modified entry hole position.

Figure 7.18, **Figure 7.19**, and **Figure 7.20** show *htc* distribution comparisons in local, circumferential averaged, and axial averaged format against the baseline data set. The mass flows tested in the modified model are now extended to the idle-, cruise- and MTO-equivalent conditions. It can be seen that the shape of *htc* remains almost identical with the magnitude increasing proportionally to the mass flow rate at the inlet. The change in inlet jet angle has a significant impact on the heat transfer pattern and *htc* value. The jet foot print is dramatically extended downstream along the axial direction of the jet. The recirculation of downstream flow of the jet results in widening fan-shaped distributions with higher *htc* levels on the axially downstream section of the casing. Much lower *htc* levels are seen upstream of the impingement location. The peak of the local *htc*, the peak of the circumferential averaged *htc* and the peak of the axial averaged *htc* are now reduced to 32%, 64.2 % and 70.7 % of the P_4 values respectively. A 54 % reduction in the total area averaged *htc* is seen compared to the baseline configuration as shown in **Figure 7.16.**

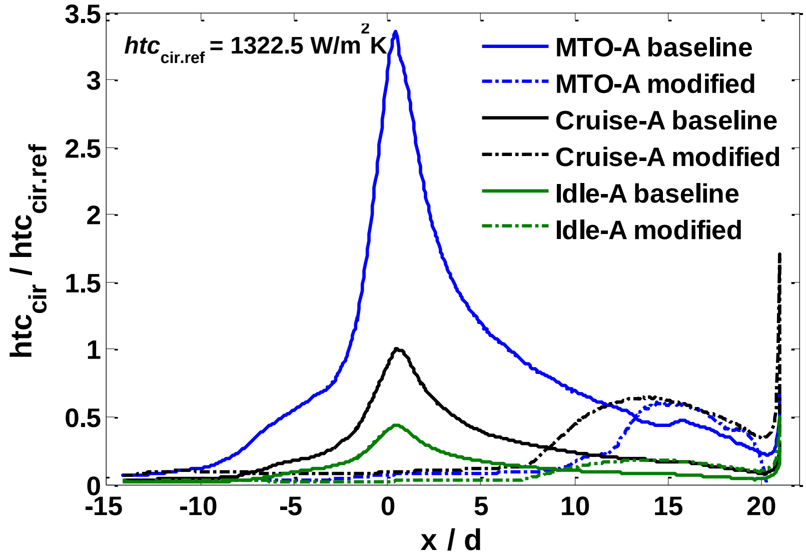

Figure 7.19 Circumferential averaged *htc* / *htc*$_{ref}$ (= Cruise-A.peak.span.realizable k-ε) distributions for different operation modes with modified entry hole position.

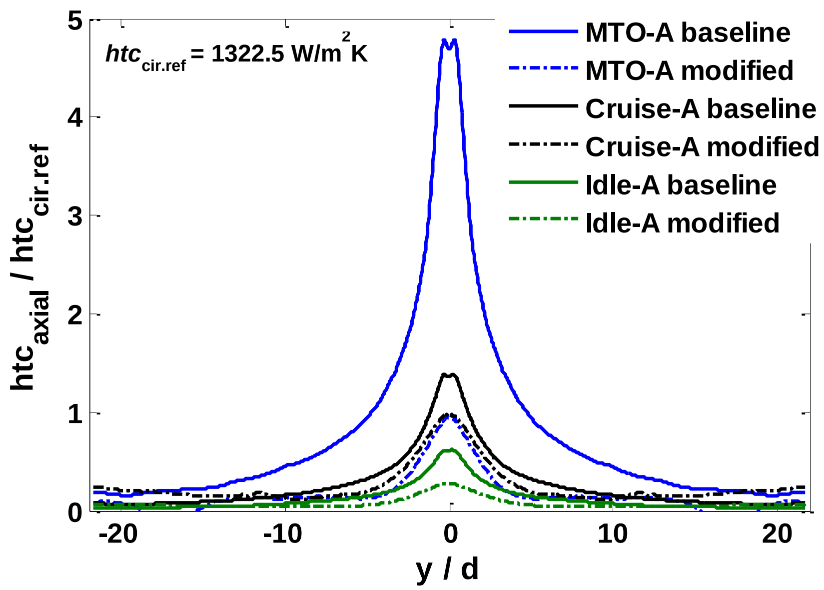

Figure 7.20 Axial averaged *htc* / *htc*$_{ref}$ (= Cruise-A.peak.span.realizable k-ε) distributions for different operation modes with modified entry hole position.

7.4 Summary

The local heat transfer distributions of impingement jet on the casing inner surface within the over-segment cavity were investigated using transient liquid crystal *htc* measurements and CFD numerical modelling. The experimental rig was built at 4.2 times engine scale and run at the idle-equivalent condition, producing the highest available jet Reynolds number while running under incompressible conditions (which always exist in the engine). It was then supported by engine scale CFD models which extended the analyses to higher jet Reynolds representative of Cruise and Maximum Take-Off cases.

The CFD model validation showed that:

- A reasonable replication of *htc* patterns are obtained using a ½ domain model, acturately capturing the position and relative levee of the peak *htc* and distribution with axial and circumferential position;
- The CFD over predicted the measured *htc* fairly uniformly along the surface by around 25 %.

The effect of the cavity small exit leakages on the internal casing heat transfer was examined by setting different exit flow scenarios. This showed that:

- Modelling of small leakages does not affect the heat transfer on the inside of the casing, but a slight localised difference can be seen as a result of the casing gap leakage flow.
- It is unnecessary to model the individual outlet leakages, saving significant meshing time and complexity, providing the total mass flow is represented.

The flow in over segment cavity of the engine is set by other cooling and unavoidable leakage requirement, however, its distribution can be altered to improve the transient behaviour of the engine. By reducing the internal casing *htc*, the thermal clearance control system could benefit against casing expansion leading to significant tip leakage loss. As part of continuing effort to improve the design, several geometry permutations were made. Five different impingement jet to target surface distances were tested by moving them along the NGV support ring so that the jet impact locations are changed. The parametric study result showed that:

- None of options gives a reduction in *htc* compared to a baseline case situated at p/d = 17.1. Moving the impingement location upstream and closer to the casing surface can result in *htc* levels 20 % higher than the best (baseline) case.
- Angling the impingement hole further downstream has a dramatic effect on the *htc* in the cavity, with the axial distribution changed markedly, and the surface-averaged *htc* reduced significantly: the *htc* reductions of 24 % at Cruise and 54 % at Idle were shown.

Chapter 8 Method Evaluation for an Alternative Engine Cooling Design

This chapter covers a case study to demonstrate the capability of the cost-effective combined CFD and thermo-mechanical FE modelling technique. The overall validity of the modelling approach used is difficult to validate in the engine environment, however limited data from a test engine temperature survey became available during the course of the research.

CFD studies to understand the drivers of heat transfer were carried out by the present author. Heat transfer measurement conducted by **Tapanlis (2011)** in a large scale model using the transient liquid crystal technique are used as a reference data set. The results are compared to existing industry standard correlations, which are generally outside the geometric and Reynolds number range of interest. As for the previous designs the heat transfer coefficient distributions are linked to a thermal-mechanical finite element model to provide thermal boundary conditions on a casing for contraction in the presence of the cooling scheme. For one of the geometries tested, a test engine temperature data has been compared to predictions of casing temperature determined using the measured heat transfer coefficient distributions and these show reasonable agreement, confirming the current modelling capability and the applicability of the modelling for the designs reported in Chapter 5.

8.1 Definition of Problem

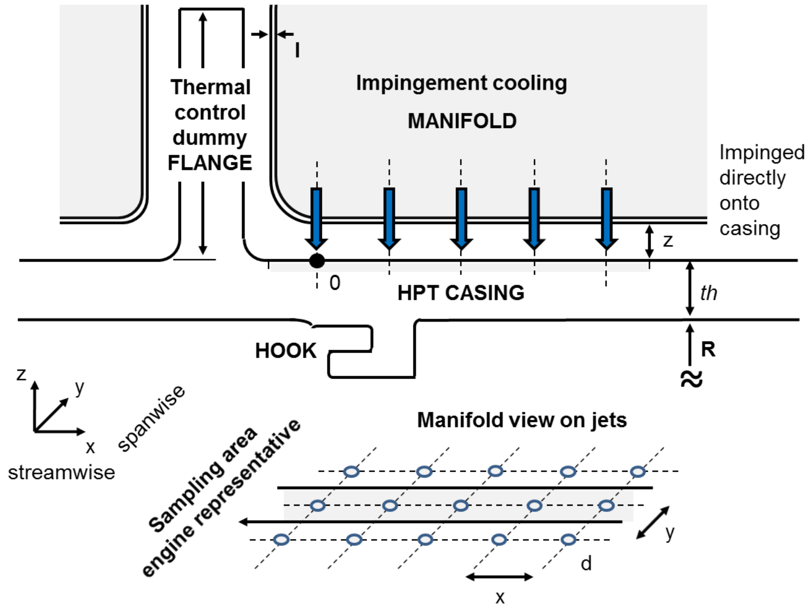

Figure 8.1 Idealized turbine casing cooling configuration with impingement onto the casing wall, adapted from (Ireland et al. 2013).

The external impingement cooling arrangement studied in this chapter matches the original close-packed set of five rows of 1 mm diameter design seen in a Trent 1000 development engine (see **Figure 8.1**). In common with the cooling designs described in Chapter 3 and 5 this application contains a sparse array of short cooling holes flowing at low jet Reynolds numbers (Re = 700 - 11,000) and large standoff distances from the target casing surface (z/d = 4) into a semi-confined passage with multiple exits. Around the circumference of the engine an array of 390 rows of 5 holes, 1 mm in diameter at a spacing x/d = 8.0 (axial), y/d = 5.5 (circumferential) are arranged on the axially downstream side of a dummy thermal control flange. Unlike the previous designs this means that the spent crossflow from the upstream rows of holes can interact with downstream jets, altering the pattern and level of heat transfer coefficient observed.

Unlike most blade cooling designs however, the flow is free to exit both upstream and downstream to the fire zone, and the flow split is determined by the local loss in each of the exit paths. To determine the heat transfer coefficient distributions these splits were set in CFD and experimental models of the cooling system, which, as above was modelled as a short section of the passage which was considered to be planar rather than part of a semi-circular manifold at radius ~ 0.4 m. CFD studies were conducted to characterize the flow field obtained, which in turn is helpful in understanding the drivers of heat transfer.

8.2 Experimental Setup Overview

Experimental measurements were made in a large scale model of part of the cooling system: at approximately ten times engine scale. The measurements were carried out by **Tapanlis (2011)** using the transient liquid crystal technique and those experimental data were compared with numerical prediction. The details of the test rig and the experimental conditions can be found in **Tapanlis (2011)** and **Choi et al. (2014)**, and a brief summary is presented here for completeness.

The impingement test section consists of a 5 by 3 (streamwise by spanwise number of rows) array of 10 mm sharp edged orifices in an inline arrangement (see **Figure 8.2**). The impingement plate was attached to an inlet plenum and offset from the target plate by confining side walls. The rectangular passage created was attached to two exit plena: allowing the flow split (upstream to downstream to be set as 50:50 or 33(L):67(R)).

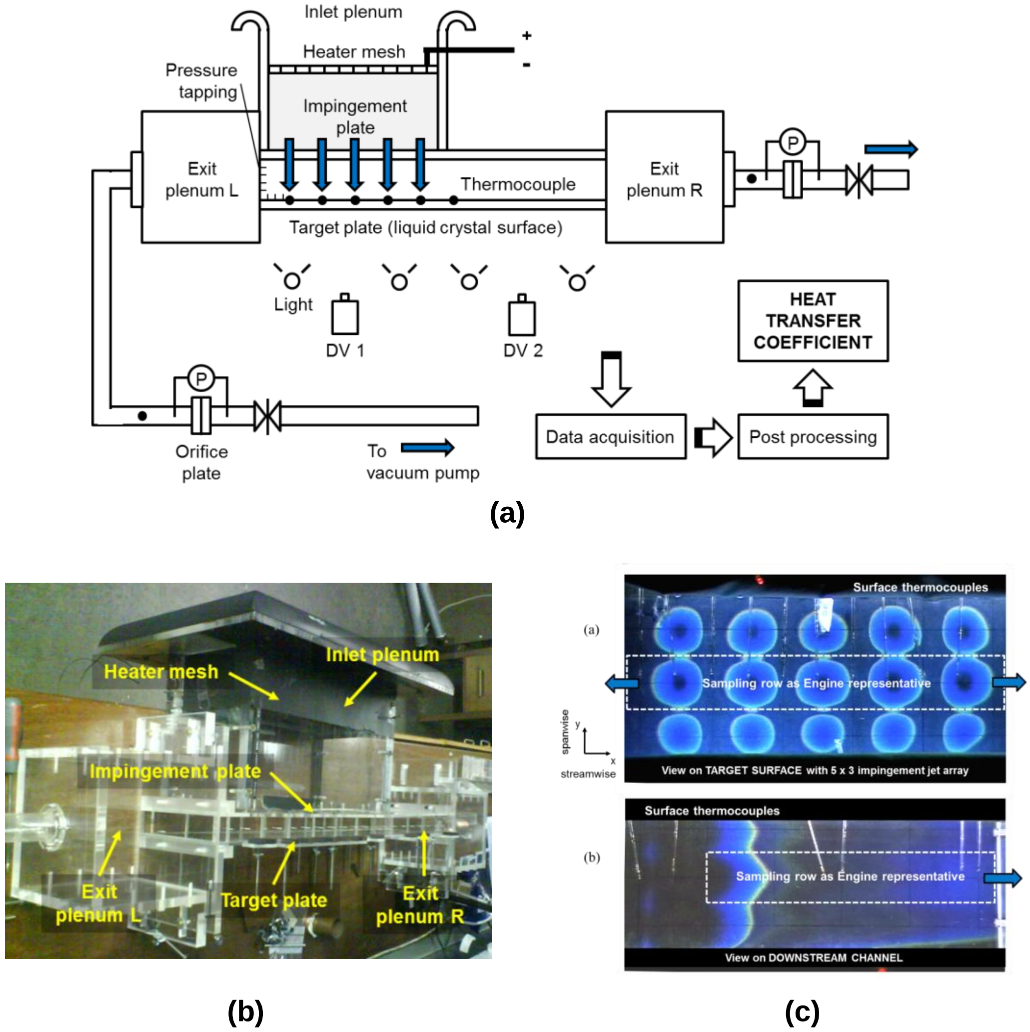

Figure 8.2 (a) Schematic diagrams of the main components of the test rig, (b) a photograph of the test section and (c) a typical liquid crystal activation, the measurement conducted by Tapanlis (2011).

Experimental uncertainty was calculated using a perturbation method proposed by **Moffat (1982)** as per the heat transfer research in Chapter 3. The root sum square error in heat transfer coefficient is under 12.2 % for highest heat transfer coefficient measured and 11.5 % for the lowest.

8.3 Computational Setup and Details

Again, a consistent modelling strategy has been employed to model the behaviour of the engine casing numerically in two stages. First, computational fluid dynamics is used to determine the casing wall heat transfer coefficient distributions, and these are compared to the experimental data and existing industry standard correlations. Second, the external heat loads are used as boundary conditions in a thermo-mechanical finite element model to predict the casing contraction performance in the presence of cooling scheme, and for the validation of available temperature distributions measured in an experimental gas turbine at Rolls-Royce, Derby. The test conditions were chosen to match Idle, Cruise and Maximum Take Off conditions where the total coolant mass flow rates are 0.025 kg/s, 0.145 kg/s and 0.144 kg/s respectively.

8.3.1 Aero-thermal CFD Model

Steady-state numerical models have been set in the commercial code Fluent 13.0.0 using the segregated solver with implicit equations; the SIMPLEC method for pressure-velocity coupling; the second-order upwinding scheme. The expected turbulent flow in the impingement cooling system was modelled using two alternative turbulence models: the realizable k-ε model with enhanced wall functions and the Shear Stress Transport k-ω model. The computational domain contains a single half row of five axially spaced impingement jets and extends far downstream into the channel flow region, as shown in **Figure 8.3**. It closely represents the middle row of the experimental passage, or an engine configuration where there is no confining circumferential sidewall. Symmetry conditions were applied on the pseudo-circumferential faces. All walls were considered adiabatic with the exception of the target surface which was set to be isothermal at the measured initial wall temperature.

The working fluid was taken to be air (treated as an ideal gas). The inlet conditions were taken from the experimental case being modelled: an inlet mass flow rate and inlet temperature were set. Pressure boundary conditions were imposed at the each outlet to create a 50:50 split in the exit flow. A structured hexahedral mesh was generated in the domain by means of ICEM CFD multi-block strategies with fine jet hole resolution controlled by the density of the C-grids (half O-grids) and refinement layers near the impingement target surface to obtain accurate thermal boundary layer data. A mesh sensitivity analysis was conducted to show grid independence of the solutions. The total size of mesh required depends on the Reynolds number, but for all cases lay between 5 and 6 million cells segregated into 104 blocks and assure y^+ values below 1 for the wall function approach in the near wall region. Convergence criteria based on the residuals of mass flow rate, velocity components, turbulence components and energy equation were set to be near or below a value of 1×10^{-6}, and manual checks were conducted to ensure that these were steady at that value.

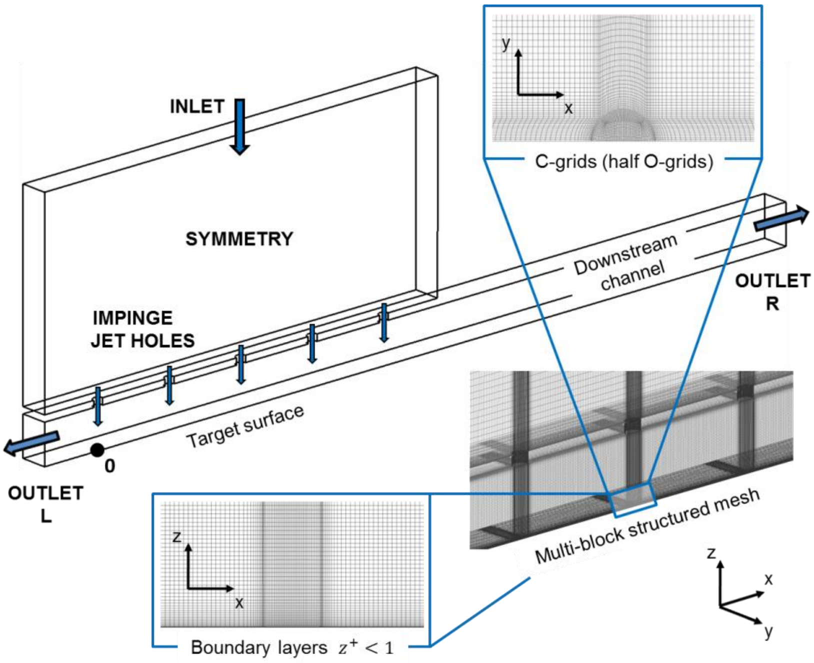

Figure 8.3 Computational domain used for CFD modelling of the impingement jet heat transfer model.

8.3.2 Thermo-mechanical FE Model

The thermo-mechanical model uses an idealized representation of the casing. A 2-D axisymmetric cylindrical geometry incorporating a dummy flange models an axially long casing (L = 400 mm). The position of a cooling feed to the external casing is depicted in **Figure 8.4**. These also include the locations corresponding to the internal hook ($x_{hook}/x_n \sim +1$) where the casing liner is attached and also two thermocouple locations ($x_{TC1}/x_n \sim -1$ and $x_{TC2}/x_n \sim +2$) where data are available from an engine test for comparison. The casing inner radius, R, is 400 mm and its thickness of 6 mm. All analyses were performed using COMSOL Multiphysics 4.2a FEM code with its MATLAB interface.

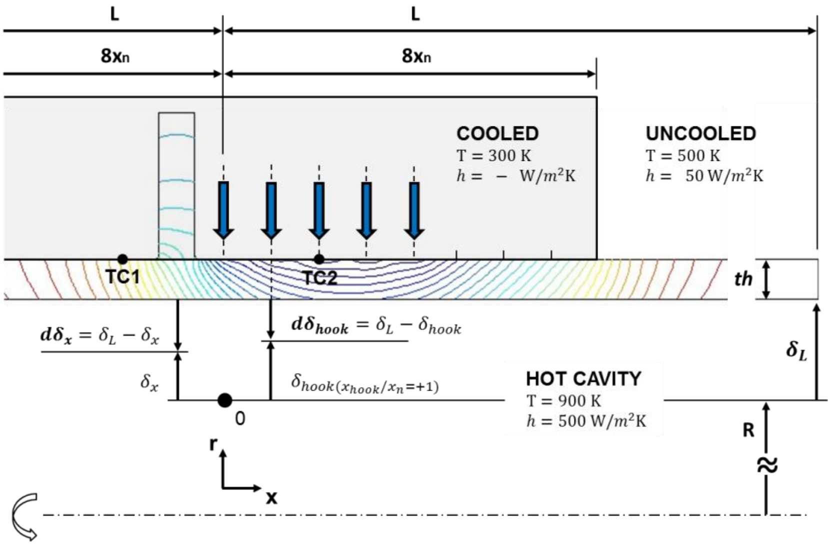

Figure 8.4 Idealized representation of the casing model configuration for thermo-mechanical analysis

Thermal boundary conditions are required over all the external surfaces of the model. The system is convectively dominated and radiative heat transfer and any conduction paths to attached components were not considered here. In the heat transfer zone affected by impingement cooling, spanwise-averaged heat transfer coefficients, h_{cooled}, acquired from both experiment and CFD were mapped onto the target surface between x/x_{n} = -0.5 to x/x_{n} = 8.0 in the axial direction (patchwise averages over this area were applied for some cases). Typical boundary conditions over the model (reported later in this chapter) are shown in **Figure 8.4**. The detailed distributions of h_{cooled} employed in the impingement region are shown in **Figure 8.12**. On the remainder of the cooled external surface from x/x_{n}= -8 to x/x_{n}= -0.5 low heat transfer occurs, and the boundary condition was set as: h = 30 W/m^{2}K at 300 K. The external surface not normally covered by the cooling manifold is subject to heat transfer boundary conditions typical of the ventilation flow: $h_{uncooled}$ of 50 W/m^{2}K at 500 K. Internally a uniform boundary condition is set as $h_{hot\ cavity}$ = 500 W/m^{2}K, at a driving gas temperature of 900 K as denoted in **Figure 8.4**. Note that heat transfer coefficients for the thermo-mechanical model, h_{cooled}, were scaled to engine conditions using the standard convective relationship.

$$h_{\text{cooled}} = \frac{Nu\, k_{\text{cooled}}}{d_{\text{engine}}} = \frac{q''}{T_{\infty} - T_{\text{s}}}. \tag{8.1}$$

The system is constrained mechanically such that there is no rotation of the casing at its extremities, otherwise the model is radially and axially free to move. This approximates the constraint imposed by other structural components in a real engine. The closure results are reported relative to the displacement of an uncooled datum case. The total axial length of the idealized casing model, $2L$ was chosen such that the radial growth at its extremities were uniform for all of the cooling schemes applied.

The fine mesh has been used to capture the thermal gradients under the impingement cooling accurately: a typical triangular grid consists of 2.7×10^3 elements. The mesh quality expressed as degree of element symmetric was 0.96. A reduction of mesh size by a factor of 0.7 was shown to have negligible influence on the temperature field in the solid, confirming that grid independence was achieved for the solution.

8.4 Numerical Characterisation and Assessment

8.4.1 External Casing Heat Transfer

Local heat transfer distributions under an array of impinging jets are presented in two formats below: first as full field Nusselt number contour diagrams and secondly as spanwise-averaged Nusselt profiles in the streamwise (x) direction.

The experimentally measured Nusselt number distributions on the target surface are presented in **Figure 8.5** and **Figure 8.6**, for tests carried out at an average jet Reynolds numbers, Re = 8300, with exit split ratio of 50:50 and 33(L):67(R) respectively. In the case of the 50:50 split, data have also been captured in the confined channel downstream of the impingement array. For the 33:67 split, all three rows of data are displayed for completeness. In the region $-0.5 < x/x_n < 4.5$ the distributions show features typical of impingement arrays, with the highest Nusselt number near the point of impingement, rapidly dropping in a near circular pattern around the jet axis, slight distortion of the jet footprint seen as crossflow builds up in the passage towards the exits.

There are only small differences in the level of Nusselt number when the exit flow split is varied. In fact these lie within experimental error, indicating that the exit flow has little effect on the Nusselt number distributions in this case. This insensitivity is attributed to the low jet to crossflow mass velocity ratio in the current array configuration, a consequence of the large stand-off distances. This leads to near uniform jet Reynolds numbers for each streamwise row, and only slight skewing of the jet axis in the downstream direction moving away from the central jets. This is as expected for a jet to target offset distance $z/d = 4$. This is in notable contrast to the results of **Huang et al. (1998)** who showed at a smaller $z/d = 3$, that changing the exit flow distribution from either 100:0 or 0:100 to a 50:50 exit led to a significant increase in overall Nu.

A moderate rise in local heat transfer coefficient is observed in the upwash regions. These lie at the interface between neighbouring wall jets in the spanwise direction, where the pitch between adjacent rows is tighter ($y_n/d = 5.5$). Here, separation and turning of the wall jet induces small unsteady eddy structures which scrub the target surface.

Notably the outer rows of jets in the experimental results (see **Figure 8.6**) apparently show lower Nusselt numbers than the middle row. This is attributed to two artifices of the experiment: (i) the flow entering the outer rows from the upstream plenum loses driving temperature potential to the plenum walls, and (ii) flow interaction and heat transfer to the passage sidewalls which generate additional secondary flows. For this reason only results from the middle row are considered representative of a circumferentially uniform system. (Tests were performed to ensure that there was no flow mal-distribution between rows of holes in the test rig).

In the confined downstream region $x/x_n > 4.5$ the wall jet enters the channel and shows an initial distribution of axially aligned with the row of jets. This decays in the spanwise direction. This distribution is smoothed as the wall jet diffuses into the passage and a low near uniform Nu is seen far downstream.

The case equivalent to **Figure 8.5**, modelled using CFD, is shown in **Figure 8.7**, for Re = 8300, exit split ratio of 50:50, using the realizable k-ε turbulence model. The general pattern observed is similar to the experimental results. The peak Nusselt number under the jets is somewhat higher, but this is offset by a more rapid decay in the Nusselt number moving away from the jet axes. This may be due to poor capture of the inlet separation of the short sharp-edged impingement holes (I/d = 0.66), leading to local over acceleration of the incoming flow and a smaller effective jet area at the target surface. The shear layer in the jet may also be poorly captured, because of the inherently unsteady nature of these processes and the spreading of the jet as is crosses the manifold to target gap. Most RANS turbulence models are known to have difficulty in simulating this region of the impingement flow field when running under steady conditions **(Zuckerman and Lior, 2005)**.

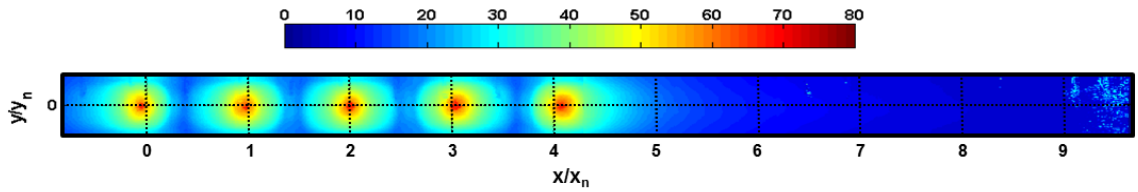

Figure 8.5 Nusselt number distribution on target surface under impingement jet array at Re=8300 with 50:50 exit split (EXP), Tapanlis (2011)

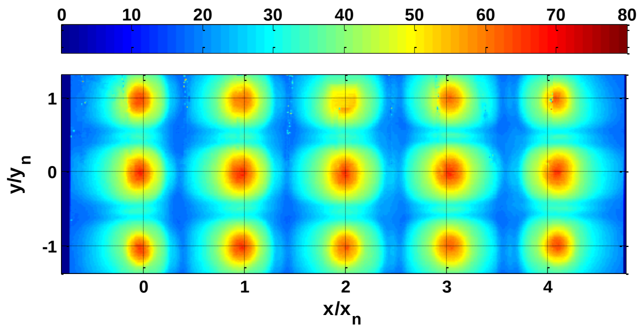

Figure 8.6 Nusselt number distribution on target surface under impingement jet array at Re=8300 with 33:67 exit split (EXP), Tapanlis (2011)

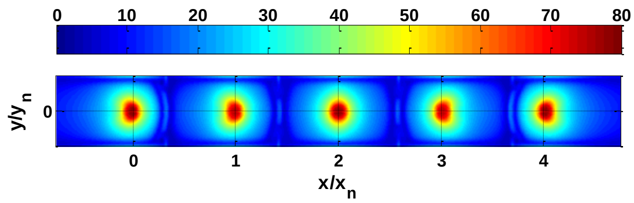

Figure 8.7 Nusselt number distribution on target surface under impingement jet array at Re=8300 with 50:50 exit split (CFD Realizable k-e)

Spanwise Averaged Nusselt Number Distribution. While local Nusselt number distributions allow the casing displacement to be modelled in a full 3-D simulation, appropriately spanwise averaged distributions provide a more useful tool for the engine designer.

Figure 8.9 and **Figure 8.10** show a comparison of experimental spanwise averaged Nu for both flow split configurations, at two Reynolds numbers and the current CFD predictions using both the realizable k-ε and k-ω SST turbulence models. Also included is the equivalent distribution derived from the correlation of **Goldstein and Seol (1991)**. These all sensibly show for all test conditions that the peak value remains located at the axial impinging jet position with troughs approximately midway between successive jet rows. Comparison of the local data and the spanwise averaged peak values shows that the peak of the spanwise averaged value is significantly lower than the maximum local value (~60 %), whereas in the troughs, where the spanwise distribution is near uniform, the average value is very close to centreline results. The detailed distribution is very similar for all cases, however at lower Reynolds numbers there is a notable change in gradient near the jet axis. This is attributed to transition of the wall jet to turbulent flow at a relatively large radial distance from the jet axes in these regimes. The change in exit flow from a 50:50 split to a 33(L):67(R) split has little effect on Nusselt number distribution. At both Reynolds numbers shown, the Goldstein and Seol correlation (which was derived for a single row of impinging jets) matches the shape of the distribution well, but over predicts Nusselt number by between 3 - 5.7 %.

While it is apparent that both the realizable k-ε and k-ω SST turbulence models under predict the heat transfer coefficient in the trough between peaks by an equal amount, the k-ω SST notably vastly over predicts the peak Nusselt number at the stagnation point in all cases.

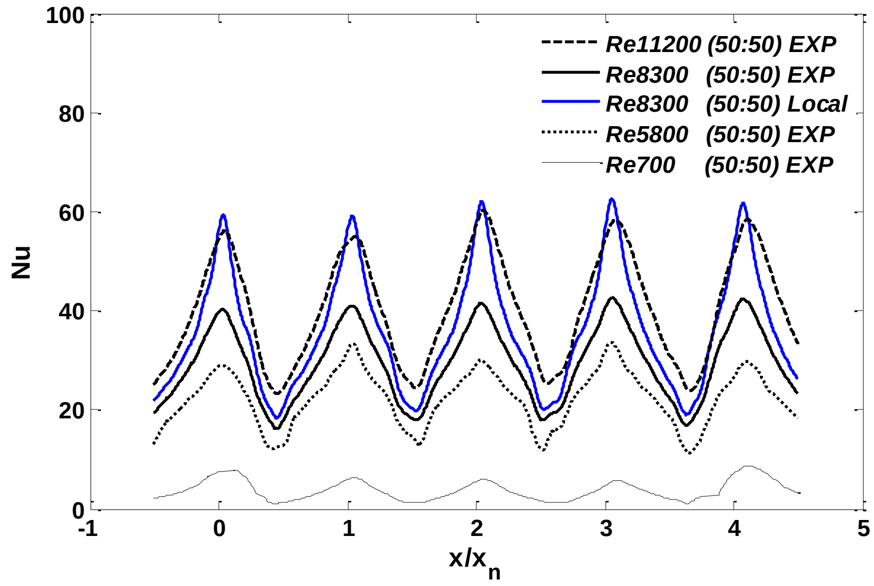

Figure 8.8 Spanwise-averaged Nusselt number distribution with 50:50 exit split (EXP)

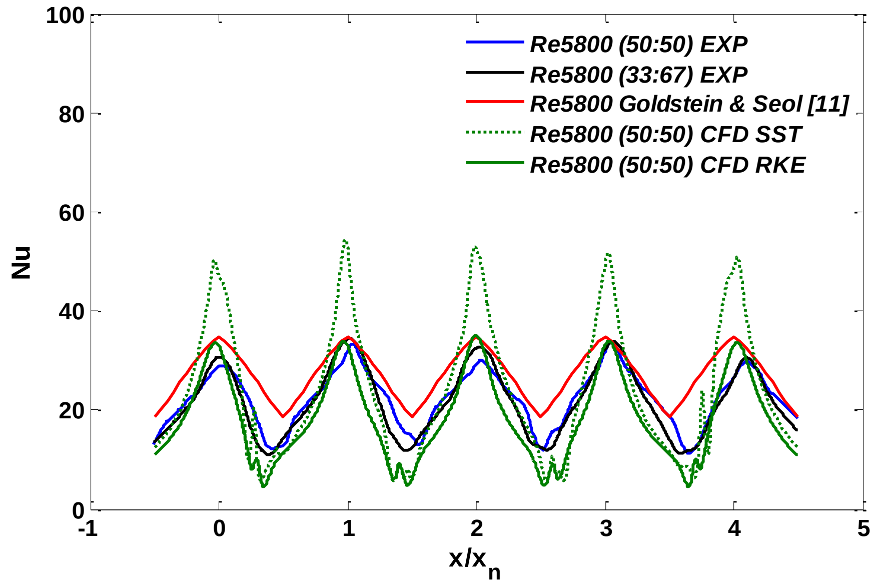

Figure 8.9 Spanwise-averaged Nusselt number distribution at Re=5800

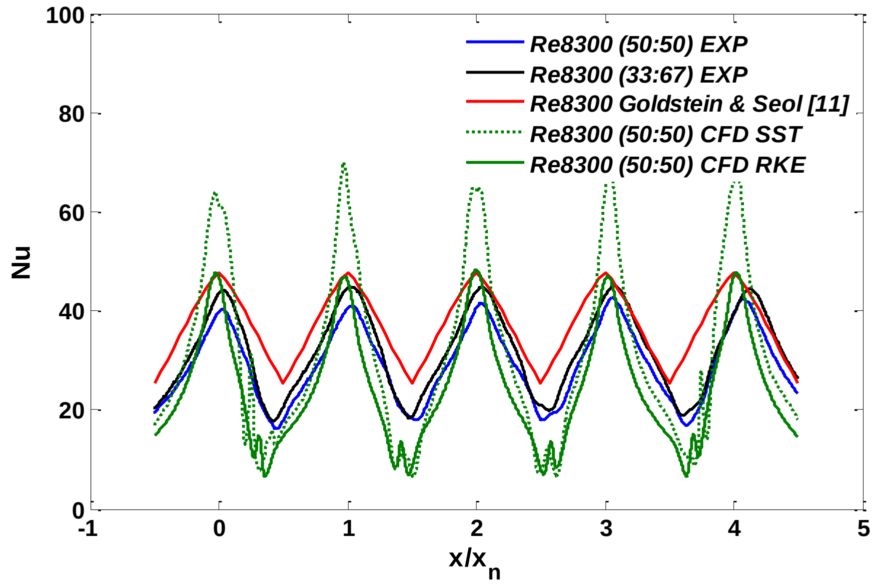

Figure 8.10 Spanwise-averaged Nusselt number distribution at Re=8300

Patch-averaged and Downstream Channel Heat Transfer Correlations. The **Florschuetz et al. (1981)** correlation is widely used as an industry stand patch average impingement Nusselt number in internal cooling passages (see the correlation format in Chapter 5). However the geometric parameters and range of Reynolds number expected in the tip clearance control manifold can fall well below the lowest Reynolds number considered valid in their correlation (Re = 10,000), and the array of holes may be substantially more sparse. Thus the experimental data of the current study were populated into a correlation of this form and the best fit values for the four constants obtained **(Tapanlis, 2011)**. The range of data is somewhat limited, particularly concerning geometric spacing and so the correlation must be treated with some caution. Thus in this chapter only the correlation for the current geometry are reported as:

$$\mathrm{Nu}_{\mathrm{patch},\ \frac{x_n}{d}=8,\ \frac{y_n}{d}=5.5,\ \frac{z_n}{d}=4} = 0.0618\,\mathrm{Re}^{0.72}\mathrm{Pr}^{1/3}\left(1-0.196\left(\frac{z_n}{d}\frac{G_c}{G_j}\right)^{0.010}\right) \tag{8.2}$$

Similarly using the form suggested by **Sarkar and Florschuetz (1992)** for the entrance region of a channel downstream of an impingement array, an updated correlation was obtained (after **Tapanlis (2011)**).

$$\mathrm{Nu_{ch}}(x^{+}) = 0.059\mathrm{Re}_{ch}{}^{0.79}Pr^{\frac{1}{3}}Nr^{3.4}\left(\frac{y_n}{d}\right)^{-5.1}\left(\frac{z_n}{d}\right)^{3.1} exp^{\left[-\left(1.052\left(\frac{y_n}{z_n}\right)\right)x^{+}\right]} + 0.0023\mathrm{Re}_{ch}{}^{0.79}\mathrm{Pr}^{\frac{1}{3}} \quad (8.3)$$

where Nr is the number of row of holes in the array upstream of the channel, $x^{+}=x/2z$, and $\mathrm{Re_{ch}}$ is based on the channel characteristic length $2z$. In both cases, the basic correlations have been extended in terms of the standoff spacing range from their upper bound of 3 to 4.

A comparison of the fit of the newly developed correlation to the experimental data, the Florschuetz et al. correlation and *patch averaged values from CFD predictions* developed for this thesis are shown in **Figure 8.11**, at each Reynolds number the patch averages under each of the 5 rows of jets is displayed. Notably the use of the Florschuetz correlation beyond its range of validity has led to over prediction of Nusselt number by up to 40 %. (This occurs at the highest Re = 11,200 which lies just above minimum valid range of the Florschuetz correlation. However, as z_n/d > 3 and the correlation is a best fit over a much wider range it turns out to be a poor predictor of Nu at this point. The over prediction is similar to that observed by **Van Treuren et al. (1996)** for an array of z_n/d = 4 holes with a single confined crossflow exit.) The realizable *k-ε* model results consistently under predict the patch averaged Nusselt number, while the *k-ω* SST are close to the real value. This ranking of the CFD results should be treated with caution, as it can be seen that the match in average value is dependent on gross over prediction at the stagnation point being balanced by an area weighted under prediction at the edge of each jet (see **Figure 8.12**). If the pitch of the array were to be changed this might not remain the best approximation. The full range of Nusselt number distribution attributed to the region x/x_n = -0.5 to x/x_n = 8.0 used to generate htc_{cooled} is shown in **Figure 8.12**.

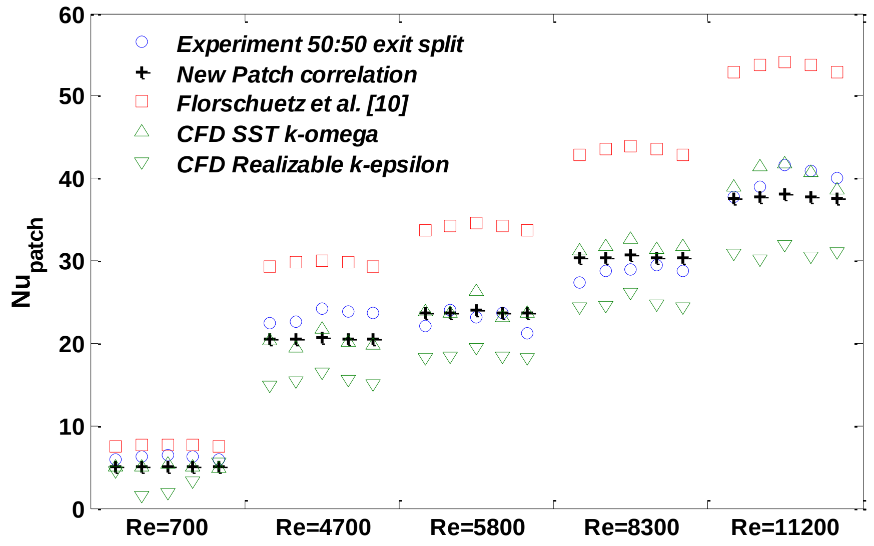

Figure 8.11 Experimental patch-averaged Nusselt number and correlated values under the impingement array with 50:50 exit split.

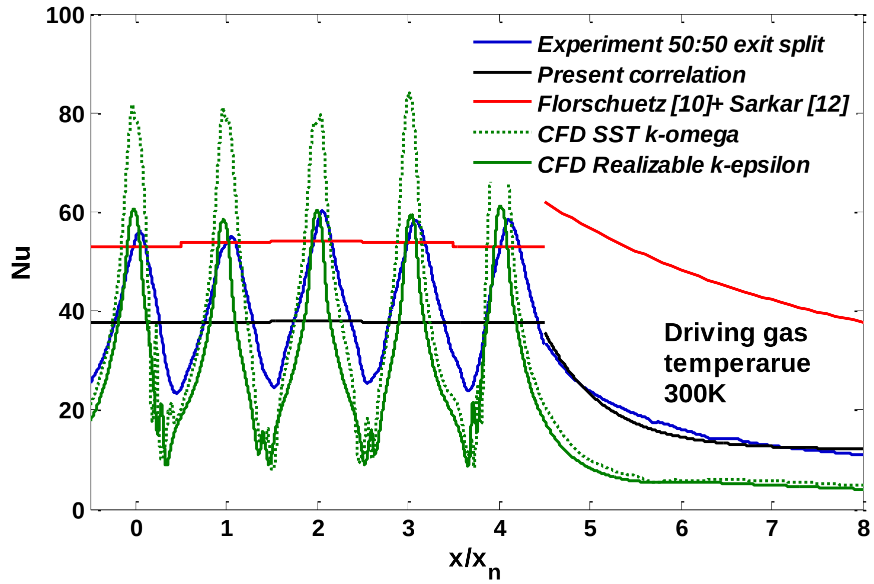

Figure 8.12 Typical thermal boundary conditions applied on the cooled external surface of the model at Re=11000 with 50:50 exit split flow

8.4.2 Comparison with an Engine Casing Thermocouple Survey

Thermo-mechanical analyses have been used to generate steady temperature distributions and radial displacement profiles of an engine casing **Figure 8.13** shows a typical result along the axial length of the casing model, for Re = 11,000 using experimentally generated heat transfer coefficient data as the cooled wall boundary condition. The thermal growth indicated is relative to cold build conditions. Included on the **Figure 8.13** is the expected growth in the absence of active cooling. Notably, the non-symmetric cooling and inclusion of a dummy web has biased the casing closure in the positive *x*-direction with the maximum closure occurring near to $x/x_n = 2$.

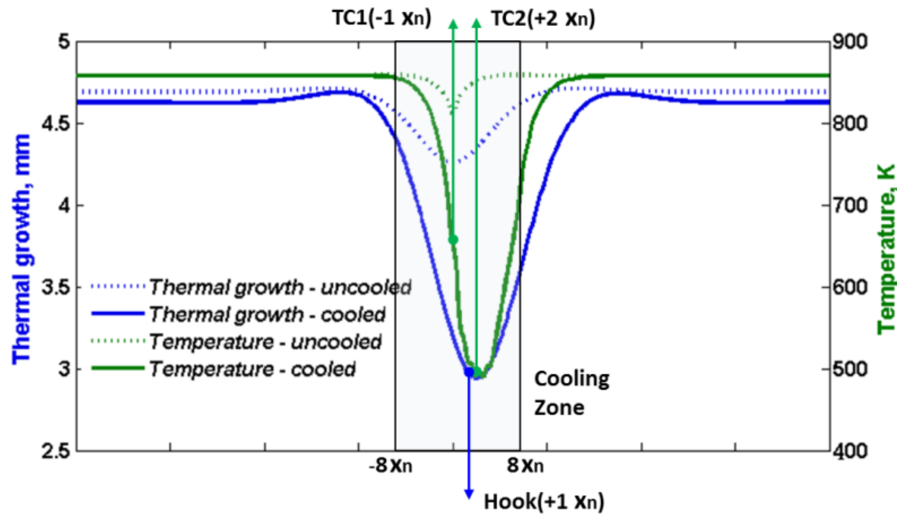

Figure 8.13 Variation of casing model temperature along the external surface and radial thermal growth along the internal surface at Re_j=11,000.

Comparison with an Engine Casing Thermocouple Survey. For one of the geometries tested, data from a test engine casing thermocouple survey, conducted at Rolls-Royce, Derby, have been compared to predictions of idealized casing temperature determined using the measured heat transfer coefficient distributions. In the engine test two thermocouple locations were available to allow comparison to the simplified geometry, these lying at $x_{\mathrm{TC1}}/x_{\mathrm{n}}$ = -2, and $x_{\mathrm{TC2}}/x_{\mathrm{n}}$ = +2 from the centre of the region of interest.

The comparison between the thermocouple measurements and all possible FEA conducted using several *htc* correlations at TC1 is only fair (see **Figure 8.14**). The over prediction of Nu using the Florschuetz correlation sensibly leads to an under prediction of the external casing temperature. For the remaining cases there is good agreement in the mid-range of operating conditions, but the rate of change of surface temperature with coolant mass flow rate is under predicted, suggesting that the power exponent in the Nu correlation is too low. At TC2, however, the agreement is much better (see **Figure 8.15**). This data point lies in the middle of the impingement cooled portion of the casing, and so assumptions concerning the far-field flow are less significant. Here the correlation from the large scale experimental data provides an excellent fit with root mean square (RMS) error of ~4 K at mass flow rates of ~0.2 - 0.3 kg/s typical of cruise condition, but a larger error of ~30 K at the lowest mass flow rate associated with engine idle. This point is close to the blade liner attachment location ($x/x_n = 1$) and indicates that the characterization can provide accurate temperature prediction even where the boundary conditions are idealized within the casing.

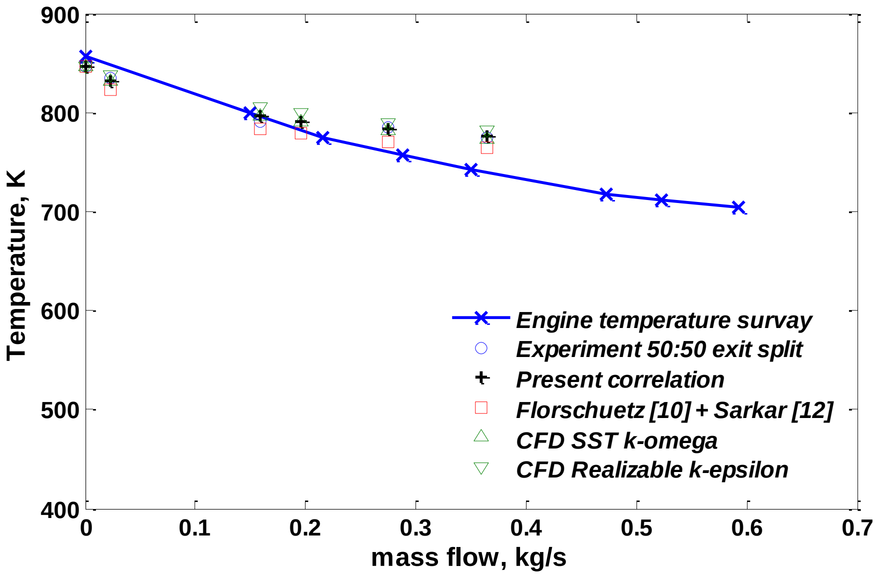

Figure 8.14 Predictions of surface temperature variation *vs*. TCC flow rate at TC1, compared data from engine casing thermocouple survey.

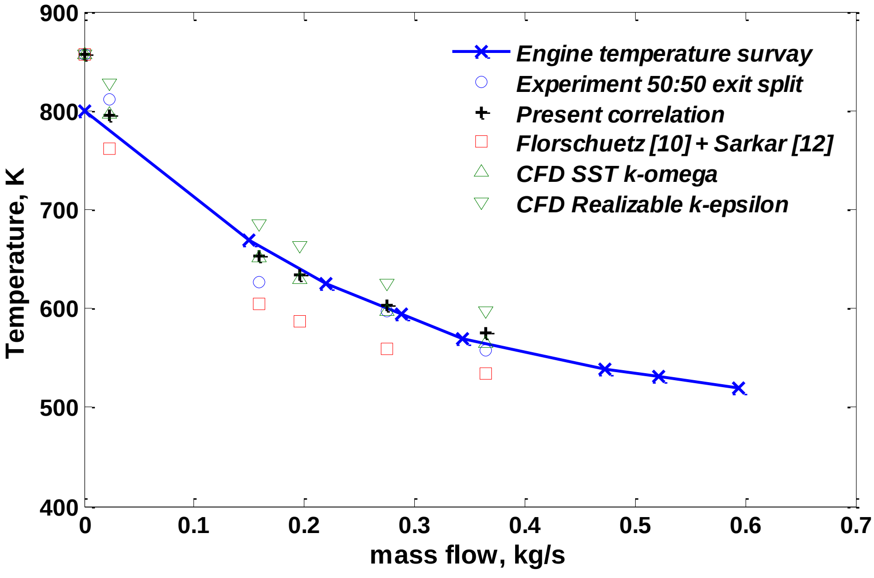

Figure 8.15 Predictions of surface temperature variation *vs*. TCC flow rate at TC2, compared data from engine casing thermocouple survey.

8.5 Summary

Changes in the expected casing closure with external cooling flows were predicted using a set of experimental heat transfer data **(Tapanlis, 2011)** and validated application of heat transfer coefficients on the outer surface of an engine model. A typical engine build cooling manifold standoff distance of z/d = 4 was examined in detail, over a range of average jet Reynolds number Re = 700 - 10000, corresponding to a typical casing cooling system. The mass flow rate ratio of the two opposing exits was set at two values i.e. 50:50 and 33(L):67(R). Local heat transfer coefficients were obtained for both the jet array impingement region and the downstream channel section. The current experimental data were compared with industry standard correlations. The key points observed are:

- For the tested geometries, heat transfer was sensibly unaffected by whether the flow was exhausted through one side of the exit passage or equally in both directions, and the bulk flow field could be predicted using a modified distributed injection model.

The heat transfer coefficients predicted using CFD were linked with an idealized engine casing model. From the coupled CFD and thermo-mechanical simulations performed, it can be concluded that:

- CFD is capable of predicting similar patterns to those observed experimentally, but smaller effective impingement jet foot prints are seen due to poor capture of the inlet separation of the short sharp-edged holes.
- Engine temperatures and casing closure can be reasonably modelled through the application of heat transfer coefficient distribution to an FE model, validated by an engine thermocouple survey.

- A biased thermal closure induced by a single dummy web requires further investigation: the effect of the web is significant and may cause a rotation of the casing.
- The casing closure achieved by this system, 1.6 mm for a mass flow rate of 0.145 kg/s is smaller than in Chapter 5, in spite of a similar number of distribution holes to the surface, and identical driving temperature differences used in the model.

Chapter 9 Summary and Further Work

This thesis deals with a mixture of experimental and numerical modelling of different aspects of a thermal tip clearance control system for a gas turbine engine. The research aims to improve the performance and modelling of such systems in future jet engines, minimising the need for cooling air to provide casing contraction. Significant improvements have been made in the understanding of the thermal response of the casing to realistic thermally induced heat fluxes. The external cooling flow, internal heating and thermal response of the casing have all been investigated. Where experiments complement the numerical studies these have been conducted as a means of validating the numerical approach conducted. A summary of the key findings and conclusions drawn from the research are provided in this chapter along with some recommendations for future work.

9.1 Experimental and Numerical Characterisation of Casing Heat Transfer

The standalone heat transfer distributions of engine representative external and internal casing impingement geometries were measured in large-scale Perspex models using a transient liquid crystal technique. The experimental data were compared with numerical predictions and industrial standard correlations as a part of the experimental validation process. The primary conclusions are:

- Numerical simulations are consistent with experimental measurements of *htc,* while providing detailed flow diagnostics, full surface coverage and esy manipulation of thermal boundary conditions.
- RANS CFD using the realisable k-ε model closely replicates the general heat transfer pattern seen in the experimental cases and replicates the level of heat transfer most closely amongst the turbulence models tested.
- RANS CFD does, however, globally over predict *htc* in the region underneath the impingement jet by up to 30 %.

9.2 External Casing Heat Transfer and Thermal Closure

A range of external impingement cooling arrangements were assessed using a multi-physics approach to assess the best cooling geometry to achieve effective casing contraction. The effects of jet-to-jet pitch, number of rows of jets, inline and staggered jet arrays, and arrays of jets on dummy flange were assessed. In addition, parametric variations in local casing geometric features were examined over a range of manifold standoff distance z/d_{base} = 1 to 6, which may be encountered in a typical engine build. Collapsing results to rank performance of compete cooling solutions provides general design rules for the external cooling manifold and casing geometry including dummy flange. The key findings are:

- Uniformly distributed cooling arrangement such as a combination of impingement onto both the target surface and the flange fillets i.e. *H5CI* is desirable to enhance external heat transfer and casing thermal closure at a given coolant mass flow rate.
- For multiple jet arrays, the cooling manifold to target casing standoff distance z/d can be adjusted to control the contraction capability.
- If sparse arrays are employed (such as *H2* and *H2C*), very slight variation in external heat transfer is observed with the standoff distance allowing build tolerances and engine fixing complexity to be relaxed.
- Cooling the fillet at the dummy flange constricts heat spread in to the flange creating larger thermal closure than cooling either the casing or the flange wall directly.
- Casing thermal closure can be increased without significant change in the external cooling arrangement, by slight necking of the dummy flange at its root.
- This can subsequently be optimized from the improved casing design itself, particularly with thinner case and longer circumferential flanges.

9.3 Internal Casing Heat Transfer

The internal casing heat transfer coefficient distribution inside the over-tip seal segment cavity was characterised. First, the impact of the small exit leakages on heat transfer coefficient onto the entire internal surface of the casing was evaluated. Second a parametric study of the transfer hole position along the NGV support ring was conducted to find out whether an optimum location of the jet in the cavity reducing heat transfer levels obtained. In addition, a further angled transfer hole case was introduced in an attempt to reduce the casing heat peakup. It is concluded that:

- Although each customised cavity design and its modelling strategy are differ, it is most likely unnecessary to model the individual outlet leakages, which could save significant meshing time and complexity, providing the total mass flow is represented. This should allow the cavity to be optimised in a timely manner.
- For a reduction in casing heat peakup in this specific over segment cavity, the inlet hole should be further angled towards the axial direction. A single iteration modelled provided a decrease in surface-averaged heat transfer coefficient levels of up to 25 % with no reduction in flow in the cavity.

9.4 Model Evaluation

It has been possible to evaluate the validity of temperature measurements using the current strategy in a limited way by comparison to a test engine thermocouple survey. This has shown that:

- A reasonable replication of the full scale test can be made through the current modelling technique with good matching of thermocouple data where the locally predicted heat transfer coefficients are applied in the simplified engine casing model.

9.5 Consideration for Future Work

Further studies are required to optimise overall contraction capability and transient response.

- Validation of high temperature clearance prediction in addition to temperature field prediction would provide further confidence in the modelling technique. This should be a priority for future work, given the data now becoming available from a number of hot rigs listed in the literature survey.
- Determining the transient response of the engine casing is of fundamental importance to actually implementing the turbine thermal clearance control system in practice.
- The ability to co-optimise internal and external heat transfer will maximise the transient response of the system allowing tighter clearances.
- A vital complementary component of the research would be to characterise transient heating for step climb clearance alleviation. By heating the casing immediately prior to a step climb manoeuvre, the normal cruise clearance can be further reduced. Better thermal matching of the internal and external cooling flows, could, in fact, remove the requirement for such a process.

.

References

Advisory Council for Aeronautical Research in Europe (ACARE), 2011, "Flightpath 2050 - Europe's Vision for Aviation," European Commission Report.

Ahmed, F., Poster, R., Schymann, Y., Von Wolfersdorf, J., Weigand, B., and Meier, K., 2012, "A Numerical and Experimental Investigation of an Impingement Cooling System for an Active Clearance Control System of a Low Pressure Turbine," ISROMAC-14.

Ahmed, F., Tucholke, R., Weigand, B., and Meier, K., 2011, "Numerical Investigation of Heat Transfer and Pressure Drop Characteristics for Different Hole Geometries of a Turbine Casing Impingement Cooling System," ASME Paper No. GT2011-45251.

Ahmed, F., Weigand, B., and Meier, K., 2010, "Heat Transfer and Pressure Drop Characteristics for a Turbine Casing Impingement Cooling System," ASME Paper No. IHTC14-22817.

Amiot, D., Arraitz, A., Fachat, T., Gendraud, A., Lefebvre, P., and Roussin-Moynier, D., 2007, "Gas Turbine Clearance Control Devices," U.S. Patent No. 7,287,955 B2.

Andreini, A., and Da Soghe, R., 2012, "Numerical Characterization of Aerodynamic Losses of Jet Arrays for Gas Turbine Applications," J. Eng. Gas Turbines Power, 134(5), p. 052504.

Andreini, A., Da Soghe, R., Facchini, B., Maiuolo, F., Tarchi, L., and Coutandin, D., 2013, "Experimental and Numerical Analysis of Multiple Impingement Jet Arrays for an Active Clearance Control System," ASME J. Turbomach., 135(3), p. 031016.

Arkhipov, A. N., Karaban, V. V., Putchkov, I. V., Filkorn, G., and Kieninger, A., 2009, "The Whole-Engine Model for Clearance Evaluation," ASME Paper No. GT2009-59259.

Bailey, J. C., and Bunker, R. S., 2002, "Local Heat Transfer and Flow Distributions for Impinging Jet Arrays of Dense and Sparse Extent," ASME Paper No. GT2002-30473.

Benito, D., Dixon, J., and Metherell, P., 2008, "3D Thermo-Mechanical Modelling Method to Predict Compressor Local Tip Running Clearances," ASME Paper No. GT2008-50780.

Beltaos, S., 1976, "Oblique Impingement of Circular Turbulent Jets," J. Hydraulic Res., 14(1), pp. 17-36.

Bordo, L., Bruzzone, S., Perrone, A., and Traversone, L., 2012, "Prediction of Clearance in Industrial Gas Turbine Validated by Field Operation Data," ASME Paper No. GT2012-69617.

Bozzi, L., Perrone, A., and Giacobone, L., 2012, "Procedure for Calculation of Component Thermal Loads for Running Clearances of Heavy-Duty Gas Turbines," ASME Paper No. GT2012-68184.

Brevet, P., Dejeu, C., Dorignac, E., Jolly, M., and Vullierme, J. J., 2002, "Heat Transfer to a Row of Impinging Jets in Consideration of Optimization," Int. J. Heat Mass Transfer, 45(20), pp. 4191-4200.

Bucaro, M. T., Ruiz, R. J., Albers, R. J., Estridge, S. A., and Wartner, R. F., 2009, "Thermal Control of Gas Turbine Engine Rings for Active Clearance Control," U.S. Patent No. 7,597,537 B2.

Bunker, R. S., and Metzger, D. E., 1990, "Local Heat Transfer in Internally Cooled Turbine Airfoil Leading Edge Regions - Part 1: Impingement Cooling without Film Coolant Extraction," ASME J. Turbomach., 112(3), pp. 451-458.

CFM International, CFM 56-2 Aero Engine - Active Tip Clearance Control, available at http://www.cfmaeroengines.com/engines/cfm56-2, accessed 9/10/2013.

Chambers, A. C., Gillespie, D. R.H., Ireland, P. T., and Dailey, G. M., 2003, "A novel Transient Liquid Crystal Technique to Determine Heat Transfer Coefficient Distributions and Adiabatic Wall Temperature in a Three-Temperature Problem," ASME J. Turbomach., 125(3), pp. 538-546.

Choi, M., Dyrda, D. M., Gillespie, D. R.H., Tapanlis, O., and Lewis, L. V., 2016, "The Relative Performance of External Casing Impingement Cooling Arrangements for Thermal Control of Blade Tip Clearance," ASME J. Turbomach., 138(3), p. 031005. (also ASME Paper No. GT2015-43278)

Choi, M., Tapanlis, O., Gillespie, D. R.H., Lewis, L. V., and Ciccomascolo, C., 2014, "The Effect of Impingement Jet Heat Transfer on Casing Contraction in a Turbine Case Cooling System," ASME Paper No. GT2014-26749.

Cumpsty, N., 1997, Jet Propulsion, Cambridge University Press.

Da Soghe, R., Facchini, B., Micio, M., and Andreini, A., 2012, "Aerothermal Analysis of a Turbine Casing Impingement Cooling System," ASME Paper No. GT2012-68793. (also International Journal of Rotating Machinery, Article ID 103583)

Da Soghe, R., and Andreini, A., 2013, "Numerical Characterization of Pressure Drop Across the Manifold of Turbine Casing Cooling System," ASME J. Turbomach., 135(3), p. 031017.

Da Soghe, R., Bianchini, C., Andreini, A., Facchini, B., and Mazzei, L., 2015, "Heat Transfer Augmentation due to Coolant Extraction on the Cold Side of Active Clearance Control Manifolds," J. Eng. Gas Turbines Power, 138(2), p. 021507. (also ASME Paper No. GT2015-42003)

Dann, A. G., and Thorpe, S. J., 2012, "Loughborough University Turbine Case Cooling Rig Final Report," Department of Aeronautical and Automotive Engineering, Loughborough University, Loughborough, UK, Technical Report No. TT12R10.

Dann, A. G., Thorpe, S. J., Lewis, L. V., and Ireland, P. T., 2014, "Innovative Measurement Techniques for a Cooled Turbine Case Operating at Engine Representative Thermal Conditions," ASME Paper No. GT2014-26092.

Dann, A. G., Dhopade, P., Bacic, M., Ireland, P., and Lewis, L, 2016, "Experimental and Numerical Investigation of Annular Casing Impingement Arrays for Faster Casing Response," ASME Paper No. GT2016-57619.

Denton, J. D., 1993, "Loss Mechanisms in Turbomachines," ASME J. Turbomach., 115(4), pp. 621-656.

EASA, 2013, Type Certification Data Sheet - Rolls-Royce plc Trent XWB series engines, TCDS No. E.111.

Estridge, S. A., Wartner, R. F., and Bucaro, M. T., 2009, "System and Method to Exhaust Spent Cooling Air of Gas Turbine Engine Active Clearance Control," U.S. Patent No. 7,503,179 B2.

Florschuetz, L., Metzger, D., Su, C., Isoda, Y., and Tseng, H., 1982, "Jet Array Impingement Flow Distributions and Heat Transfer Characteristics – Effects of Initial Crossflow and Nonuniform Array Geometry," NASA Contractor Report No. 3630.

Florschuetz, L. W., Truman, C. R., and Metzger, D. E., 1981, "Streamwise Flow and Heat Transfer Distributions for Jet Array Impingement with Crossflow," ASME J. Heat Transfer, 103(2), pp. 337-342.

Florschuetz, L. W., Metzger, D. E., and Truman C. R., 1981, "Jet Array Impingement with Crossflow Correlation of Streamwise Resolved Flow and Heat Transfer Distributions," NASA Contractor Report No. 3373.

Florschuetz, L. W., Metzger, D. E., Takeuichi, D. I., and Berry, R. A., 1980, "Multiple Jet Impingement Heat Transfer Charactistics – Experimental Investigation of In-line and Staggered Arrays with Crossflow," NASA Contractor Report No. 3217.

Florschuetz, L., and Su, C., 1985, "Heat Transfer Characteristics within an Array of Impinging Jets - Effect of Crossflow Temperature Relative to Jet Temperature," NASA Contactor Report No. 3936.

General Electric Aircraft Engines, 2005, "HPT Clearance Control, Intelligent Engine Systems - Phase I," NASA CR-2005-213970.

Gunston, B., 1996, Jane's-Aero Engines.

General Electric Aviation, 2008, "Intelligent Engine Systems, HPT Clearance Control," NASA CR-2008-215234.

Gillespie, D. R.H., 1996, "Intricate Internal Cooling Systems for Gas Turbine Blading," DPhil Thesis, Department of Engineering Science, University of Oxford, Oxford, UK.

Gillespie, D. R.H., Wang, Z., Ireland, P. T., and Kohler, S. T., 1998, "Full Surface Local Heat Transfer Coefficient Measurements in a Model of an Integrally Cast Impingement Cooling Geometry," ASME J. Turbomach., 120(1), pp. 92-99.

Gillespie, D. R.H., Wang, Z., and Ireland, P. T., 1995, "Heating Element," British Patent No. PCT/GB96/2017.

Gillespie, D. R.H., Wang, Z., and Ireland, P. T., 2001, "Heating Element," US Patent 6181874.

Giovannetti, I., Bigi, M., Giannozzi, M., Sporer, D. R., Cappuccini, F., and Romanelli, M., 2008, "Clearance Reduction and Performance Gain using Abradable Material in Gas Turbines," ASME Paper No. GT2008-50290.

Goodro, M., Park, J., Ligrani, P., Fox, M., and Moon, H. K., 2007, "Effects of Mach Number and Reynolds Number on Jet Array Impingement Heat Transfer," Int. J. Heat Mass Transfer, 50(1), pp. 367-380.

Goodro, M., Park, J., Ligrani, P., Fox, M., and Moon, H. K., 2009, "Effect of Temperature Ratio on Jet Array Impingement Heat Transfer," ASME J. Heat Transfer, 131(1), 012201.

Goldstein, R. J. and Franchett, M. E., 1988, "Heat Transfer From a Flat Surface to an Oblique Impinging Jet," ASME J. Heat Transfer, 110(1), pp. 84-90.

Goldstein, R. J., and Seol, W. S., 1991, "Heat Transfer to a Row of Impinging Circular Air-Jets Including the Effect of Entrainment," Int. J. Heat Mass Transfer, 34(8), pp. 2133-2147.

Halila, E.E., Lenahan, D.T., and Thomas, T.T., 1982, "Energy Efficient Engine, High Pressure Turbine Test Hardware Detailed Design Report," NASA CR-167955.

Huang, Y., Ekkad, S. V., and Han, J. C., 1998, "Detailed Heat Transfer Distributions under an Array of Orthogonal Impinging Jets," AIAA J. Thermophys. Heat Transfer, 12(1), pp. 73-79.

Huber, A.M., and Viskanta, R., 1994, "Effect of Jet–Jet Spacing on Convective Heat Transfer to Confined, Impinging Arrays of Axisymmetric Air Jets," Int. J. Heat Mass Transfer, 37(18), pp. 2859-2869.

The International Panel on Climate Change (IPCC), available at https://www.ipcc.ch, accessed 9/10/2011.

Ibrahim, M.B., Kochuparambil, B.J., Ekkad, S.V., and Simon, T.W., 2005, "CFD for Jet Impingement Heat Transfer with Single Jets and Arrays," ASME Paper No. GT2005-68341.

Ireland, P. T., 1987, "Internal Cooling of Turbine Blades," DPhil Thesis, Department of Engineering Science, University of Oxford, Oxford, UK.

Ireland, P. T., and Jones, T. V., 2000, "Liquid Crystal Measurements of Heat Transfer and Surface Shear Stress," Meas. Sci. Technol., 11(7), pp. 969-986.

Ireland, P. T., Newcombe, G., and Mullender, A. J., 2013, "Impingement Cooling Arrangement for a Gas Turbine Engine," U.S. Patent No. 8,414,255 B2.

Jambunathan, K., Lai, E., Moss, M.A., and Button, B.L.,1992, "A Review of Heat Transfer Data for Single Circular Jet Impingement," Int. J. Heat Fluid Flow, 13(2), pp. 106-115.

Justak, J. F., and Doux, C., 2009, "Self-Acting Clearance Control for Turbine Blade Outer Air Seals," ASME Paper No. GT2009-59683.

Kawecki, E. J., 1979, "Thermal Response Turbine Shroud Study," AFAPL-TR-79-2087.

Kirby, S. J., 2013, "Thermal Control System for Turbines," U.S. Patent No. 8,403,637 B2.

Knipser, C., Horn, W., and Staudacher, S., 2009, "Aircraft Engine Performance Improvement by Active Clearance Control in Low Pressure Turbines," ASME Paper No. GT2009-59301.

Lattime, S. B., and Steinetz, B. M., 2004, "Turbine Engine Clearance Control Systems: Current Practices and Future Directions," AIAA J. Propul. Power, 20(2), pp. 302-311. (also NASA TM-2002-211749).

Lewis, L. V., 2014, "Combination of Mechanical Actuator and Case Cooling Apparatus," U.S. Patent No. 8,734,090 B2.

Lewis, L. V., and Bacic, M., 2011, "Rotor Blade Tip Clearance Control," U.S. Patent No. 8,721,257 B2.

Lewis, L. V., and Blidmark, B. E. G., 2013, "Rotor Blade Over-tip Leakage Control," U.S. Patent No. 8,545,175 B2.

Ling. J.P., Ireland. P.T., and Turner, L., 2004, "A Technique for Processing Transient Heat Transfer, Liquid Crystal Experiments in the Presence of Lateral Conduction," ASME J. Turbomach., 126(2), pp.247-258. (also AMSE Paper No. GT2003-38446)

Lucas, M.G., Ireland, P.T., Wang, Z., Jones, T.V., Pearce, W.J., 1992, "Fundamental Studies of Impingement Cooling Thermal Boundary Conditions," AGARD Turkey 1992, paper 14.

Maiuolo, F., Facchini, B., Tarchi, L., Carcasci, C., Da Soghe, R., Andrei, l., and Zecchi, S., 2013, "Heat Transfer Measurements in a Leading Edge Geometry with Racetrack Holes and Film Cooling Extraction," ASME J. Turbomach., 135(3), p.031020. (also ASME Paper No. GT2012-69581)

Metzger, D. E., Florschuetz, L. W., Takeuchi, D. I., Behee, R. D., and Berry, R. A., 1979, "Heat Transfer Characteristics for Inline and Staggered Arrays of Circular Jets With Crossflow of Spent Air," ASME J. Heat Trans., 101(3), pp. 526-531

McElhaney, J., 2008, "Distortion Compensation by Shape Modification of Complex Turbine Geometries in the Presence of High Temperature Gradients," ASME Paper No. GT2008-50757.

McGilvray, M., and Gillespie, D.R.H., 2011, "THTAC: Transient Heat Transfer Analysis Code," Department of Engineering Science, University of Oxford, Oxford, UK, Technical Report No. OUEL2011-05.

Moffat, R. J., 1982, "Contributions to the Theory of Single Sample Uncertainty Analysis," ASME J. Fluids Eng., 104(2), pp. 250-258.

Obot, N. T., and Trabold, T. A., 1987, "Impingement Heat Transfer Within Arrays of Circular Jets: Part 1—Effects of Minimum, Intermediate, and Complete Crossflow for Small and Large Spacings," ASME J. Heat Trans., 109(4), pp. 872-879.

O'Donovan, T. S., and Murray, D. B., 2007, "Jet Impingement Heat Transfer – Part I: Mean and Root-Mean-Square Heat Transfer and Velocity Distributions," Int. J. Heat Mass Transfer, 50(17), pp. 3291-3301.

O'Dowd, D. O., 2010, "Aero-Thermal Performance of Transonic High-Pressure Turbine Blade Tips," DPhil Thesis, Department of Engineering Science, University of Oxford, Oxford, UK.

Park, J., Goodro, M., Ligrani, P., Fox, M., and Moon, H.-K., 2007, "Separate Effects of Mach Number and Reynolds Number on Jet Array Impingement Heat Transfer," ASME J. Turbomach., 129(2), pp. 269-280.

Popiel, C.O., Van der Meer, T.H., and Hoogendorn, C.J., 1980, "Convective Heat Transfer on a Plate in an Impinging Round Hot Gas Jet of Low Reynolds Number," Int. J. Heat Mass Transfer, 23(8), pp. 1055-1068.

Rolls-Royce plc., 2005, The Jet Engine.

Rolls-Royce plc., HPT Casing Configuration on a Typical Large Civil Engine, available at http://www.rolls-royce.com, accessed 9/10/2013.

Rolls-Royce plc., 2011, Annual Report 2011.

Ryley, J. C., McGilvray, M., and Gillespie, D. R.H., 2014, "Calculation of Heat Transfer Coefficient Distribution on 3D Geometries from Transient Liquid Crystal Experiments," ASME Paper No. GT2014-26973.

San, J.Y., and Lai, M.D. Lai, 2001, "Optimum Jet-to-Jet Spacing of Heat Transfer for Staggered Arrays of Impinging Air Jets," Int. J. Heat Mass Transfer, 44(21), pp. 3997-4007.

Sarkar, A., and Florschuetz, L. W., 1992, "Entrance Region Heat Transfer in a Channel Downstream of an Impinging Jet Array," Int. J. Heat Mass Transfer, 35(12), pp. 3363-3374.

Saroi, R., 2014, "Turbine Casing Cooling," U.S. Patent No. 8,668,438 B2.

Son, C., Gillespie, D. R.H., Ireland, P. T., and Dailey, G. M., 2001, "Heat Transfer and Flow Characteristics of an Engine Representative Impingement Cooling System," ASME J. Turbomach., 123(1), pp 154-160. (also ASME Paper No. 2000-GT-0219)

Shultz, D. L., and Jones, T. V., 1973, "Heat Transfer Measurements in Short-Duration Hypersonic Test Facilities," AGARDograph No. 165.

Sparrow, E.M., and Lovell, B.J., 1980, "Heat Transfer Characteristics of an Oblique Impinging Circular Jet," ASME J. Heat Transfer 102(2), 202-209.

Steinetz, B. M., Lattime, S. B., Taylor, S., DeCastro, J. A., Oswald, J., and Melcher, K. J., 2005, "Evaluation of an Active Clearance Control System Concept," NASA Technical Report, NASA TM-2005-213856.

Tapanlis, O., 2011, "Turbine Casing Impingement Cooling Systems," DPhil Thesis, Department of Engineering Science, University of Oxford, Oxford, UK.

Taylor, S. C., Steinetz, B. M., and Oswald, J., 2006, "High Temperature Evaluation of an Active Clearance Control System Concept," NASA Technical Report, NASA TM-2006-214464.

Terzis, A., Bontitsopoulos, S., Ott, P., von Wolfersdorf, J., and Kalfas, A. I., 2015, "Improved Accuracy in Jet Impingement Heat Transfer Experiments Considering the Layer Thicknesses of a Triple Thermochromic Liquid Crystal Coating," ASME J. Turbomach., 138(2), p. 021003.

Van Paridon, A., Dann, A., Ireland, P. T., and Bacic, M., 2015, "Design and Development of a Full-Scale Generic Transient Heat Transfer Facility (THTF) for Air System Validation," ASME Paper No. GT2015-42391.

Van Treuren, K. W., Wang, Z., Ireland, P. T., and Kohler, S. T., 1996, "Comparison and Prediction of Local and Average Heat Transfer Coefficients under an Array of Inline and Staggered Impinging Jets," ASME Paper No. 96-GT-163.

Xing, Y., and Weigand, B., 2013, "Optimum Jet-to-Plate Spacing of Inline Impingement Heat Transfer for Different Crossflow Schemes," ASME J. Heat Transfer, 135(7), p. 072201.

Xing, Y., Spring, S., and Weigand, B., 2010, "Experimental and Numerical Investigation of Heat Transfer Characteristics of Inline and Staggered Arrays of Impinging Jets," ASME J. Heat Transfer, 132(9), p. 092201.

Wang, X. L., Yan, H. B., Lu, T. J., Song, S. J., and Kim, T., 2014, "Heat Transfer Characteristics of an Inclined Impinging Jet on a Curved Surface in Crossflow," ASME J. Heat Transfer, 136(8), p. 081702

Wiseman, M. W., and Guo, T., 2001, "An Investigation of Life Extending Control Techniques for Gas Turbine Engines," IEEE ACC Cat. No. 01CH37148, 5, pp. 3706-3707.

Yan, X., Baughn, J.W., and Mesbah, M., 1992, "The Effect of Reynolds Number on the Heat Transfer Distribution from a Flat Plate to an Impinging Jet," ASME Winter Annular Meeting, Anaheim, USA.

Yan, X., and Saniei, N., 1997, "Heat Transfer from an Oblique Impinging Air Jet to a Flat Plate," Int. J. Heat Fluid Flow, 8(6), pp. 591-599.

Yaras, M. I., and Sjolander, S. A., 1992, "Prediction of Tip-Leakage Losses in Axial Turbines," J. Turbomach., 114(1), pp. 204-210.

Zuckerman, N., and Lior, N, 2005, "Impingement Heat Transfer: Correlations and Numerical Modeling," ASME J. Heat Transfer, 127(5), pp. 544-552.

Zuckerman, N., and Lior, N, 2007, "Radial Slot Jet Impingement Flow and Heat Transfer on a Cylindrical Target," AIAA J. Thermophys. Heat Transfer, 21(3), pp. 548-561.